University of Nottingham
UK | CHINA | MALAYSIA

School of Mathematical Sciences
University of Nottingham

Numerical and Experimental Investigations of Instabilities with Astrophysical Implications

by

August Geelmuyden

A

Thesis

submitted to the

University of Nottingham

for the degree of

Doctor of Philosophy

April 23, 2023

Abstract

Over the past several decades, researchers have explored a family of mathematical analogies that relate inaccessible astrophysical phenomena to systems that can be manipulated in laboratory settings. Now, a variety of these phenomena have been successfully scrutinised in a laboratory setting, allowing for a deeper investigation of these analogies. This thesis presents results from a series of studies of instabilities with astrophysical implications, undertaken in the context of analogue gravity. From the perspective of analogue gravity, vortices in quantum fluids provide space-times with discrete and topological features. It has long been known that a multiply charged quantum vortex will decay into a cluster of singly charged vortices. Recently, it was pointed out that this instability is similar to that of the rotational superradiance of black holes. This relationship is interpreted further, and through numerical observations, a new phenomenon is encountered in the late stages of the decay. Finally, an upper bound on the orbital frequency of a vortex pair is found, and related to the sound wave responsible for the decay of a doubly charged vortex.

On the other hand, the relaxation of compact clusters of quantum vortices involves a complex interplay between vortices and waves, with energy released as sound radiation. By applying techniques from gravitational physics, the study uncovers the emergence of circular sound trajectories, a large-scale feature that enables a straightforward prediction of radiated sound. This phenomenon, called sound-rings, is closely related to the ringdown process of black holes. Furthermore, the linear scaling of the sound-rings with the net charge of the cluster allows them to be located well outside the vortex core.

In a completely different system, we investigate cosmological preheating via the parametric instability appearing from applying a vertical oscillation to two-fluid interfaces. Using methods adapted from field theories, a non-linear model is presented and compared with experimental results and numerical simulations. The appearance of secondary instabilities created by the nonlinear contributions to the primary instability is observed and is well predicted by the model. Experimental results suggest that the analogy with cosmological preheating persists in the nonlinear regime.

Then, in preparation for the next generation of analogue gravity experiments, a new technique of digital holography for the measurement of deformations of fluid interfaces is introduced. Due to partial reflections of the optical beam, coherent light impinging on a fluid interface returns as a multitude of rays. By applying, or exploiting, a tilt of the bed on which the fluid rests, multiple off-axis holograms are formed and can independently be used to measure the interface. The method is realisable with only a few basic optical components and provides a versatile scheme for high-precision measurement of fluid interfaces.

Acknowledgements

I am grateful to my supervisor, Silke, for enabling me to work on the investigations presented here. Her enthusiasm, ambition, and curiosity have been essential in constructing a stimulating research environment. She has gone beyond all expectations in providing constant care and encouragement, which I am immensely thankful for. It has been a privilege to be part of her group and to have had the opportunity to tackle such a diverse set of problems.

It has been an honour to be a part of the collaborations that led to the insights presented in this text. I am especially grateful to Sam, Sebastian and Carlo, whose humbling wisdom inspired me during the countless discussions about condensates and vortex dynamics that took place during the worldwide pandemic. I am particularly grateful to Sam and Vitor for our countless late-night discussions and joint efforts over the years. Their friendship has meant a lot to me, and it has been an honour to learn from and with someone as talented as them. I am confident we will keep collaborating on many future projects.

I would like to extend my gratitude to everyone in the black hole laboratory, Sam, Theo, Zack, Cisco, Sebastian, Vitor, Steffen, Sreelekshmi, Pietro, Patrik and James, for our many discussions, for memorable nights out, for our many discussions, and for generally providing a stimulating working environment. I would like to thank Sam, Theo, Zack, Sebastian and Cisco for warmly receiving me into the group when I first came here. I am especially grateful to Theo and Sam, who have been here for me the whole time, and who have been a constant source of inspiration. I want to thank you for agreeing with me that the universe yearns for a quaternionic description. I would like to express my gratitude to Vitor and Steffen for innumerable hours spent discussing and developing codes in Python together.

To my dearest Ivy, for your love, patience and support. Your care is what has brought me back when my investigations have spiralled. I could not have done this without you.

This work would not have been possible without the constant love and support from friends and family. A special mention goes to Heidi and Bjørn for constantly checking in on me from afar.

Finally, I would like to dedicate this text to my grandfather, and role model, who inspired me to pursue physics in the first place.

Contents

Chapter 1

Introduction

I. The formation of new theories

Every now and then, natural phenomena, for which there is no pre-existing framework of understanding, reveal themselves. When it happens, the race towards the formulation of a new theory begins. We may think of this process as follows. First, a new physical law obeyed by the phenomena is guessed. Then, this new law is incorporated into the theoretical framework, if there is any. If this works, we use the updated framework to make predictions about the phenomenon. Then finally, the guess is evaluated by comparing the predictions with reality. But how does one guess a new law in the first place?

One particularly useful strategy for guessing new laws is to rely on analogies. By assuming aspects of an elusive phenomenon to be similar to some well-known mechanism, the principles and predictions from the known theory can be transferred to the unknown theory. Needless to say, the history of physics is full of this kind of reasoning (see e.g. [1]). For example, in 1746, Leonhardt Euler introduced a theory for light in analogy with the propagation of waves in a frictionless compressible fluid [2], and, in 1769, Joseph Priestley justified the inverse square law of the electrical forces by analogy with the laws of gravitation[3]. In the former example, the shared feature might be taken as the diffraction patterns of light, and in the latter, the absence of electric field amplitude inside charged hollow spheres. In his 1861 paper, James Clerk Maxwell introduces his electromagnetic theory in analogy to incompressible fluid mechanics [4], an analogy which was later reversed to motivate introducing concepts such as hydrodynamic charge [5, 6]. In 1911, Ernest Rutherford introduced a planetary model for the atom [7], and in his 1926 paper, Erwin Schrödinger motivates his wave mechanics through analogies to and in classical mechanics and optics [8, 9]. A more recent example is Jacob Bekenstein's 1973 law for black-hole entropy, which was entirely based on analogies between black-hole physics and thermodynamics [10, 11]. One year later, this analogy was further supported by the discovery of the thermal evaporation of black holes by Steven Hawking [12]. Whereas there is no doubt about the usefulness of analogies in forming and understanding new theories, it is hard not to ponder what facilitates these arguments in the first place. How can theories belonging to entirely different fields of physics be so similar in their mathematical description? Since attempts to answer this question falls far outside the scope of this work, the interested reader is redirected to philosophical treatises such as [1, 13, 14]. Instead, we shall focus on one particular class of exact

analogies that has been much discussed during the past 50 years.

II. Analogue gravity

The early 20^{th} century brought with it the discovery of what is referred to as the two pillars of modern physics: General Relativity and Quantum theory. These theories presented an unrivalled accuracy in the prediction of physics at seemingly opposite scales, from astrophysical objects to the constituents of matter. Moreover, they made it possible to approach philosophical problems such as "why is there something rather than nothing?" and "what is the origin and fate of the universe?" from a quantitative, scientific perspective. Today, a considerable portion of theoretical physicists remain motivated by the promise of a final theory, often referred to as *quantum gravity*, resulting from merging general relativity with quantum field theory. However, the scenarios where such a theory is expected to play an important role tend to be at scales that are not likely to be experimentally accessible in the foreseeable future.

One object for which such a theory is expected to play an important role is the so-called *black hole*. Black holes were conceived just months after Einstein published his general theory of relativity [15], when Karl Schwarzschild introduced a spherically symmetric vacuum solution [16]. Due to the presence of singularities – a genuine singular point at the centre, and a divergent time-coordinate at the so-called *horizon* – this model was not taken too seriously until Chandrasekhar observed that sufficiently massive stars would collapse [17]. By the late 60s, these objects had been widely accepted under the term *black hole*, referring to the understanding of the horizon as the surface from inside which nothing can escape [18]. However, this defining feature was challenged already in 1974, when Hawking proposed that when considering quantum fields near black holes, they cease to be black, and instead radiate a thermal spectrum [12].

Hawking's calculation raised several concerns. On the one hand, the community was now forced to take Bekenstein's analogy [10, 19], between black hole physics and classical thermodynamics, seriously. The central issue was how to reconcile the thermodynamic entropy, related to information and the multitude of microstates, with the black-hole entropy, which was associated with the inverse area of the horizon. On the other hand, there were serious concerns about the technical details of Hawking's prediction. For example, the derivation relied upon extrapolating a free field theory to arbitrarily large frequencies – a regime where the model is expected to fail. This issue became known as the *trans-planckian problem* [20]. Usually, such debates are settled by investigating the validity of the prediction experimentally. However, black holes are elusive and distant, and their predicted temperature of radiation, which scales inversely with the mass of the black hole, is extremely faint for the black hole of stellar origin ($T \simeq 300\text{nK}$ for solar-mass black holes). Therefore, it would seem that the only hope of experimental realisation of this effect in the foreseeable future, would hinge on the existence and discovery of black holes with masses well below the Chandrasekhar limit, e.g. primordial black holes [21, 22].

It was following this discussion that Unruh published his seminal paper titled *Experimental black-hole evaporation?* [23]. In it, he suggests that the same arguments that lead to the thermal radiation of a black hole should hold for sound waves in the vicinity of a sonic horizon. Therefore, consistency would seem to require sonic horizons to emit thermal radiation. The core of the argument is based on a mathematical analogy between the Klein-Gordon equation for the propagation of a massless scalar field on curved spacetime, and the convective wave equation for sound waves traversing a moving fluid.

In its most simple form*, the analogy states that the following two equations [20]

$$\frac{1}{\sqrt{-g}}\partial_\mu\sqrt{-g}g^{\mu\nu}\partial_\nu\phi = 0 \quad \text{and} \quad (\partial_t + \mathbf{v}\cdot\nabla)^2\phi - c^2\nabla^2\phi = 0 \tag{1.1}$$

are mathematically equivalent provided that one identifies

$$\sqrt{-g}g_{\mu\nu}dx^\mu dx^\nu = -c^2dt^2 + (d\mathbf{x} - \mathbf{v}dt)^2\,, \tag{1.2}$$

where c is the propagation speed of waves and g is the determinant of the space-time metric $g_{\mu\nu}$. Here, the first equation in (1.1) is the Klein-Gordon equation for the evolution of a scalar field ϕ on a spacetime with metric tensor $g^{\mu\nu}$, frequently appearing in the context of General relativity and field theory. The latter is a convective wave equation for the scalar field ϕ as it propagates in a medium with background velocity $\mathbf{v}$, often encountered in condensed matter systems. The central idea is that exact mathematical analogies, like (1.1), enable transferring predictions from an experimentally inaccessible system to a system, hereby referred to as the *simulator*, that can be scrutinized in a laboratory. Once established, these analogies provide two-way streets that can be used to transfer predictions and mathematical tools from one field to the other. Note that the analogy (1.1) is kinematic and not dynamical, i.e. it links the movement of a scalar field under the influence of gravity (Klein-Gordon equation), not the movement of the gravitational field itself (Einstein equation). However, the thermal radiation of black holes can be predicted entirely on kinematic grounds and, as such, does not rely on the full evolution of the gravitational field [25].

During the 90s, it was noticed that in the sonic black hole, Hawking radiation is insensitive to the physics at higher frequencies, and was therefore relieved of the trans-plackian problem [24, 26–29]. This ignited interest in experimentally examining the analogue to test if Hawking radiation does indeed take place in the absence of trans-planckian frequencies. Although experimental realisations of sonic black holes were discussed, these systems were difficult to realise [30]. The reason is partly that the speed of sound is dependent on the equation of state, which is not easily controllable, and partly that sound waves travel at inconvenient† speeds for tabletop experiments to exhibit

*This form is in the case of constant density ρ, for an incompressible flow ($\nabla\cdot\mathbf{v} = 0$) with constant propagation speed c. Writing $D_t \equiv \partial_t + \mathbf{v}\cdot\nabla$, the general form that matches (1.2) is $(D_t + \nabla\cdot\mathbf{v})\,\frac{\rho}{c^2}D_t\phi = \nabla\cdot\rho\nabla\phi$, see e.g. [24] for a complete discussion.

†The sonic analogy requires super-sonic flow velocities, which may void a perturbative treatment of the analogy altogether.

horizons. By the early 2000s, another analogy based on the propagation of light in inhomogeneous media, dating back to Gordon's work in 1923 [31][*], had been resurrected in the analogue black-hole discussion [32, 33]. However, also these systems presented challenges as it was hard to obtain the necessary control over the permittivity and permeability of the medium. In fact, around this time it had become clear that black-hole analogies would be omnipresent in condensed matter systems – all that was needed was a convective, non-dispersive and non-dissipative wave equation with an adequate background flow [34]. Then, in 2002, Schützhold and Unruh introduced gravity-driven interface waves as black hole simulators [35]. Despite being classical and two-dimensional, interface waves were a particularly attractive analogue system due to the ease at which the propagation speed, which is proportional to the root of the depth, can be manipulated.

III. Experiments on Gravitational Analogies

During the early 2000s, there had been significant theoretical development toward understanding the necessary ingredients for Hawking radiation. The minimal set of requirements seemed to be (1) the existence of a horizon and (2) the presence of non-negligible quantum fluctuations [25]. However, it was also noticed that the essential mechanism could be investigated by supplying the noise by hand, thus bypassing the need for quantum fluctuations. This effect became known as the *stimulated* Hawking effect, as opposed to its spontaneous counterpart.

Despite the theoretical development, it was first in 2008 that gravitational analogies were studied experimentally [20]. At first horizons were reported observed in a water wave system [36] and in optical fibers [37]. Later, an effective sonic horizon was created in a Bose-Einstein condensate (BEC) [38], horizons for laser pulses in dielectric media [39], acoustic horizons in polariton fluids [40], and spin-precession waves in superfluid Helium-3 [41]. Stimulated Hawking radiation was first observed in fluid interfaces in 2011 [42], and in optical fibres in 2019 [43]. In 2016, noise correlated by the Hawking effect was observed [44], followed by the first observation of spontaneuous Hawking radiation in a BEC [45, 46].

Although the focus was on Hawking radiation initially, it became increasingly clear that a wide variety of experimentally inaccessible astrophysical phenomena could be realised in condensed matter systems. One noteworthy example is the thermal radiation received by an accelerating observer in a vacuum, which is commonly referred to as the Unruh effect [47] and is intimately related to Hawking radiation. Experiments are currently being prepared to realise the Unruh effect in atomic Bose-Einstein Condensates (BECs) [48, 49]. Another prominent example is that of rotational superradiance, or Zel'dovich superradiance [50, 51].

[*] This is the same Gordon as in the aforementioned Klein-Gordon equation.

III.1. Superradiance

Rotational superradiance, the amplification of incident waves by dissipative rotating bodies, was proposed by Zel'dovich [50] in the 70s. The term superradiance was coined by Teukolsky and Press in 1974 [51], when announcing that rotating black holes may amplify incident waves. One striking consequence is the perpetual amplification of these waves if an external reflector is introduced. The result is the instability referred to as the *black hole bomb* [52]. Superradiance is also interesting from an energetic perspective. The amplification of incident waves means that more energy comes out than was put in, i.e. energy can be harvested from rotating black holes. Consensus is that the extracted energy is collected from the rotation of the black hole [53, 54], much like the closely related Penrose process [55]. In light of this, one may wonder, for example, how superradiance would proceed in a system where the amount of rotation can only take certain discrete values.

In fact, an essential ingredient for superradiance is the existence of an ergoregion, a region where the energy of the system can be reduced as a result of increased motion within it. From this perspective, amplification occurs when waves scatter in such a way as to excite negative-energy states in the ergoregion.

Superradiance was first observed experimentally in 2016 for interfacial waves on draining bathtub flows [56]. The phenomenon has since been observed in acoustic systems [57, 58] and optical systems [59, 60]. In fact, it has recently been found that the instability of the quantum vortex is intimately related to the superradiance mechanism [61–64]. This is the topic of chapter 2 in this text. Here, further insight into the dynamical decay of the multiply charged quantum vortex is provided by an alternative perturbative approach. Moreover, we recognise a new phenomenon in the nonlinear regime, where the vortex fails to decay completely and instead enters a period of perpetual decay and re-absorption.

Other examples of phenomena, besides rotational superradiance, recently studied in the context the analogy includes the aforementioned Penrose process [60], as well as Gravitational lensing [65] and black hole Quasi-Normal Modes (QNMs) [66].

III.2. Ringdown

The existence of black hole QNMs was proposed by Vishveshwara in 1970 [67] after a numerical study of gravitational waves scattering off black holes. He observed that the black hole dissipated its energy by emitting damped harmonic waves that were largely insensitive to the details of the incident wave. Since these waves are much like the damped ringing of a perturbed bell, the phenomenon is also referred to as black hole ringdown. The ringdown of a black hole was observed by the LIGO collaboration in 2015 [68] as part of the first detection of the gravitational waves emitted during the merging of two black holes. The observation of the exact frequency of ringdown modes is of importance as they present tests of General relativity [69].

In 2020, it was announced that the interface of draining bathtub flows oscillates at frequencies

analogous to those of black hole QNMs [66]. Black hole QNMs are closely connected to the presence of light rings, i.e. circular trajectories of light. Conceptually, the presence of such an unstable radial fixed-point permits the trapping and slow emission of excitations. The ringdown process describes the relaxation of a black hole towards its resting state. As such, it is unclear to what extent the mechanism carries over to processes that are out of equilibrium. Moreover, ringdown tends to involve azimuthally rotating waves*, and so their emission involves the release, or accumulation, of rotation emitted by the source. It is therefore not clear how ringdown would proceed in a spacetime where rotation is discretized. In chapter 3, we investigate light-ring physics in a relaxing cluster of quantum vortices in two-dimensional BECs, which is a non-equilibrium process in a system with discrete circulation. Here, we shall see that the light-ring, which we call the sound-ring in this case, gives rise to an emergent, large-scale feature, which enables characterising the radiated sound.

The use of mathematical analogies to realise exotic phenomena is by no means restricted to black holes. Most of the phenomena investigated, that did not originate from black-hole physics, are concerned with processes expected to take place in the very early Universe. Some noteworthy examples of phenomena that do not naturally belong to either of these groups include the dynamical Casimir effect [70, 71] and false vacuum decay [72–75].

III.3. Preheating

In the early 1920s, solutions to Einstein's equations for a homogeneous and isotropic universe, known as the Friedmann-Lemaitre-Robertson-Walker (FLRW) metrics, were introduced [76, 77]. To everyone's surprise at the time, these solutions seemed to suggest that the Universe as a whole is not static, but space itself is evolving. When combined with Hubble's observation [78] that galaxies, in every direction, are moving away from us with a speed proportional to their distance, it became clear that the universe must have originated in a compact, hot state, popularly referred to as the *big bang*. This model was further supported by the observation of the Cosmic Microwave Background (CMB) radiation in the 60s[79, 80], which is the afterglow from when the Universe had cooled sufficiently for matter to decouple from the photon-plasma. However, the CMB was found to be almost perfectly uniform, with relative black-body temperature variations of only $\mathcal{O}(10^{-5})$ – a number that was much smaller than what was necessary to facilitate the formation of galaxies. This conundrum was resolved by introducing a cold decoupled species, referred to as Cold Dark Matter (CDM), which resulted in the current ΛCDM model, also called the *cosmological concordance model*, for the origin of the universe (see e.g. Planck 2015 [81]).

There are several theoretical concerns with the cosmological concordance model. For example, it is unclear how causally disconnected regions of the universe could have attained such similar temperatures in the first place, a problem now referred to as the *horizon problem*. Secondly, the universe was found to be almost perfectly flat, which, since the curvature is determined by the total

*Here, azimuthally rotating waves refer to waves that evolve according to $\exp[\mathrm{i}m\theta - \mathrm{i}\omega t]$ for constants m and ω, with t being time and θ being the azimuth angle in the usual cylindrical coordinates.

energy content, raised concerns about fine-tuning; there had to be a reason for the lack of curvature. This became known as the *flatness problem*. In the 80s, a mechanism to alleviate these issues, as well as the absence of magnetic monopoles, was proposed under the name of *cosmological inflation* [82–85]. The idea was to introduce a precursor field, the inflaton, responsible for an initial, temporary exponential expansion, which diluted the fluctuations and curvature of the Universe. The horizon problem is then resolved since regions of space that were causally disconnected at the time of the CMB, had only temporarily lost causal contact during the late inflationary expansion.

During the 80s, it was noticed that at the end of inflation, standard model particles coupled to the inflaton field would be produced, resulting in the re-thermalisation, or *reheating*, of the Universe [86, 87]. However, it was soon observed that this process would likely exhibit instabilities due to parametric resonance [88, 89]. To distinguish this explosive particle production from that of the slow and thermal reheating, it became known as *preheating*.

To illustrate the essential mechanism of preheating, consider a scalar inflaton field ϕ coupled to a light scalar field χ, with coupling $-\frac{1}{2}g^2\phi^2\chi^2$, that is evolving in a flat FLRW background with scale factor $a(t)$. The fluctuations χ_k of χ with physical momentum k/a are then given by [88, 89]

$$\ddot{\chi}_k + 3H\dot{\chi}_k + \left(\frac{k^2}{a^2(t)} + g^2\phi^2(t)\right)\chi_k = 0, \tag{1.3}$$

where $H \equiv \dot{a}/a$ is the Hubble parameter. In simple models of inflation, $\phi(t)$ is expected to oscillate harmonically at a frequency proportional to the mass of ϕ, for which (1.3) takes the form of a damped Mathieu equation for slowly varying $a(t)$.

Already in 2004, it was pointed out that cosmological inflation may be simulated in atomic Bose-Einstein Condensates (BECs) [90, 91]. The idea was further supported by a follow-up study using numerical simulations in 2007 [92]. The same year, the use of ion-chains to simulate expanding universes was proposed [93]. Some years later, it was noticed [94] that the aforementioned observation of the dynamical Casimir effect [71] from 2012, was, in fact, better viewed as cosmological preheating. In the years that followed, both expanding universe cosmology [95] and cosmological particle production [96–98] were successfully simulated in a laboratory setting.

In a theoretical and numerical study of preheating dynamics arising from a two-component BEC [99, 100], it was pointed out that a seemingly fundamental feature of preheating is the emergence of secondary instabilities. In 2019, it was pointed out that classical two-fluid systems can serve as simulators of cosmological inflation [101]. This proposal was the precursor for the results presented in chapter 4 of this thesis. In chapter 4, we present experimental results [102] from a classical simulator for cosmological preheating in a two-fluid system. Here we use the statistical machinery adapted from field theories from the pioneering works [103, 104] to monitor the emergence of secondary instabilities as waves are driven parametrically into the nonlinear regime. As we shall see, our results suggest that aspect of the analogy may persist also in the nonlinear regime.

III.4. The Vision

The analogue gravity program, which has seen numerous theoretical and experimental successes in the past 20 years, has demonstrated that extreme astrophysical phenomena can be simulated in a laboratory environment. The robustness of these simulations extends beyond the original analogy, even when the conditions change, such as when they enter a dissipative, dispersive, or non-linear regime. This has implications for our understanding of modified theories of gravity [20] and suggests that these phenomena are more universal and persistent than previously believed.

It is in this spirit that a new generation of analogue simulators is being prepared, now with the aim of investigating how the astrophysical phenomena unfold when being pushed further into uncharted territory. Here, regimes in which topological, nonlinear and quantum effects are relevant, are of particular interest as lessons from these limits may perhaps aid in the formulation of better models and descriptions.

The main body of this thesis consists of four parts, which are divided into four chapters 2, 3, 4 and 5. In chapter 2, we investigate the relationship between superradiance and the instability of the quantum vortex. Then, in chapter 3, we investigate the relaxation of quantum vortex clusters taking inspiration from the ringdown of a black hole. In chapter 4, the nonlinear parametric resonance of two-fluid interfaces is investigated and compared with cosmological preheating. Then, finally, in chapter 5, we investigate the potential for using the principles of digital holography to measure fluid interfaces.

These four studies are undertaken in preparation for an upcoming series of investigations of how phenomena previously simulated classical hydrodynamics proceed when repeated in a superfluid. Here chapters 2 and 3 investigate superradiance and ringdown in quantum fluids, where vorticity is topological, and circulation is quantised. In chapter 4 a classical hydrodynamic simulator for preheating is investigated, with the intent of repeating the experiment with superfluids, wherein mode populations are quantised. Finally, to observe these effects on the interface of a superfluid, a flexible, non-destructive, high-precision measurement scheme is needed. The theoretical foundation and early testing of such a scheme is presented in the final chapter 5 of this thesis.

IV. Statement of originality

All the chapters of this thesis are accounts of results produced in collaboration. The following is a brief account of my specific role within these collaborations. Chapter 2 accounts for work that resulted in the two published works [63] and [62]. My role in these projects was mainly focused on the non-linear simulations of the GPE and dGPE, and the data-analysis techniques needed to compare with the theory. The results from chapter 3 is presented in the published work [105]. I had a significant role in all aspects of this project. Results from chapter 4 is presented in the preprint [102]. Although I played some part in the early development and implementation of the detection method of chapter 4, I had no role in the actual experiment. My main contribution was to the

model-building and analysis of the experimental data. I played a central role in the development of the detection method presented in chapter 5, which is currently being patented [106].

Chapter 2

Quantum Vortex Instabilities

The following is an account of the investigations that resulted in the two publications *Quantum vortex instability and black hole superradiance* [62] and *Origin and evolution of the multiply-quantised vortex instability* [63] by S. Patrick, S. Erne, C. Barenghi, S. Weinfurtner and myself. In the former, the relationship between the rotational superradiance of black holes and the instability of the multiply quantised vortex is examined. The latter, which builds on the formalism of the former, investigates the fate of the doubly quantised vortex. My role in these projects was weighted towards numerical simulations.

I. Prelude

When a gas of bosonic particles is cooled down to very low temperatures, the system approaches a state in which a considerable fraction of the particles occupy the (quantum) ground state. The result is a macroscopic realisation of a quantum state, referred to as a Bose-Einstein Condensate (BEC). Due to low temperatures involved, it took about 70 years from BECs were first predicted [107, 108] until Bose-Einstein condensation was first observed in a dilute gas of rubidium-87 atoms in 1995 [109].

BECs are macroscopic quantum fluids which exhibit a wide range of exotic phenomena including wave-propagation of heat (second sound) [110] and perfectly inviscid flow. Yet, one of the most remarkable features of BECs, and quantum fluids in general, is the that circulation around vortices is discretized and topologically protected by their phase winding [111]. For this reason, vortices in quantum fluids are typically referred to as quantum vortices. The circulation around a quantum vortex must be an integer multiple of $\kappa \equiv 2\pi\hbar/M$, where M is the mass of the atomic species, and this integer $\ell \in \mathbb{Z}$ is referred to as the charge of the quantum vortex, or the winding number. Experiments [112–114] show that a Multiply Quantised Vortex (MQV), with $|\ell| > 1$, spontaneously decays into a cluster of Singly Quantised Vortices (SQVs), each with $|\ell| = 1$. The usual justification for this is based on the observation that a cluster of SQVs is energetically more favourable than a single MQV, so that any dissipative effect will naturally tear the MQV apart. However, in a non-dissipative system, the decay can still happen due to a dynamical instability [115] arising from the interaction between the surrounding phonons and the MQV. Recently, it has been argued [61] that the dynamical instability of the MQV is closely related to the superradiant amplification [116] of

waves due to the existence of an ergoregion around the MQV. Here, the term ergoregion, which is a notion from black hole physics [117], is used from the perspective of the analogy between vortices and rotating black holes [118]. I fact, rotational superradiance has recently been recognised in a wide variety of systems such as hydrodynamic (classical) vortex flows [56], as well as in acoustic [119] and optical [60] orbital angular momentum beams (see e.g. [120]).

As mentioned in the introduction, the relationship between vortex instabilities and superradiance, or, more precisely, ergoregions, has been pointed out on several occasions in the literature. Early studies focused on the non-dispersive regime and used ad-hoc boundary conditions (BCs) near the vortex axis, where the fluid density drops to zero [121, 122]. These works described the instability as an ergoregion instability, a term coined in the 1970s for describing instabilities of rapidly rotating neutron stars [123]. The word ergoregion, which stems from the Greek word for work (ergon), refers to the possibility for energy to be released by increased movement in this region. An ergoregion instability is related to the perpetual growth of waves in this region that can result from the existence of a mechanism that can transfer energy out of the region.

The ergoregion instability is qualitiatively similar to the black hole bomb [52], see e.g. the black hole bomb instability for massive scalar fields in the Kerr spacetime [124]. Whereas the black hole bomb is the instability that arises when an external reflector is introduced to a superradiating body, the ergoregion instability appears due to the existence of an internal reflector, inside the ergoregion. For this reason, the ergoregion instability has also been referred to as an *inverted black hole bomb* [125].

Recently, it has been shown [61] that the link between the ergoregion and vortex instabilities also carries over to the dispersive regime. Specifically, [61] showed that the vortex instability originates in the vortex core, where the mode has negative energy, thereby identifying the phenomenon as an ergoregion instability and not a BH bomb.

This chapter delves deeper into the superradiant instability of the Multiply Quantised Vortex (MQV). In particular, we introduce a Wentzel-Kramers–Brillouin (WKB) framework which enables us to interpret the underlying mechanism for the process.

By comparison with numerical simulations of the nonlinear, dynamical decay of a doubly quantised vortex ($\ell = 2$), we discover a new vortex state, where the separation distance of the resulting pair of SQVs exhibits slow, repeated modulations. Finally, dissipative decay is considered, where we comment on the asymptotic form of the orbital frequency of the vortex pairs and the significance of their interactions with phonon modes.

II. Quantised Vortices

II.1. The Gross-Pitaveskii Equation

In the limit of large particle numbers and low temperature, a dilute gas of bosonic particles exhibits macroscopic population of the ground state – a phenomenon referred to as Bose-Einstein Condensation (BEC). Considering only point-like interactions, i.e. s-wave scattering, a BEC can be described by the mean-field wavefunction $\Psi(t, \mathbf{r})$, where t is time and $\mathbf{r}$ is the spatial coordinate. The square modulus of the wavefunction can be interpreted as particle density $\rho \equiv |\Psi|^2$ so that if N is the total number of particles in the condensate, then $\int |\Psi|^2 d^3\mathbf{r} = N$. In what follows, we shall focus on two-dimensional condensates, which can be realised by applying strong harmonic confinement along one axis [126, 127], and whose equation of motion takes the same mathematical form as the three-dimensional case [128]. In two-dimensions, the dynamics of Ψ is given by the stationarity of the action [129]

$$\mathcal{S} = \int dt d^2\mathbf{r} \left[\frac{i\hbar}{2} (\Psi^* \partial_t \Psi - \Psi \partial_t \Psi^*) - \frac{\hbar^2}{2M} \boldsymbol{\nabla}\Psi \cdot \boldsymbol{\nabla}\Psi^* - U(\mathbf{r})|\Psi|^2 - \frac{1}{2} g |\Psi|^4 \right], \tag{2.1}$$

where U is an external trapping potential, and g is the two-dimensional interaction parameter and M is the atomic mass of the bosons. Here, g is related to the three-dimensional interaction parameter g_3 through $g = g_3/\sqrt{2\pi a_z^2}$, where a_z is a length scale set by the strength of the vertical confinement. More precisely, if the vertical confinement is of the form $\frac{1}{2} M \omega_z^2 z^2 \Psi$, then $a_z \equiv \sqrt{\hbar/M\omega_z}$ is the harmonic oscillator length (see e.g. [111]). The three-dimensional interaction parameter g_3 is related to the S-wave scattering length a_s via $g_3 \equiv 4\pi\hbar^2 a_s/M$ [111].

For future convenience, we use the parameters M and g along with the ground state energy μ, which may be interpreted as the chemical potential [129], to define the following physical scales

$$\xi \equiv \frac{\hbar}{\sqrt{M\mu}}, \qquad \tau \equiv \frac{\hbar}{\mu}, \qquad \rho_c \equiv \frac{\mu}{g}. \tag{2.2}$$

Here, ξ is the healing length, which appears when balancing kinetic energy with interaction energy, and may be interpreted as the length below which the self-interactions efficiently heal inhomogeneities in the density. Since the wavefunction rotates with μ, i.e. $\Psi \sim \exp(-i\mu t/\hbar)$, the cycle time τ sets a natural time-scale for the condensate. Lastly, the density ρ_c can be interpreted as the density of a uniform ($U = 0$) condensate in the ground state and with negligible kinetic energy [129]. Hereby, all physical quantities will be measured in units of these parameters unless otherwise stated. That is, we set $\mathbf{x}/\xi \to \mathbf{x}$, $t/\tau \to t$, $\Psi/\sqrt{\rho_c} \to \Psi$, $U/\mu \to U$ and $\mathcal{S}/\hbar \to \mathcal{S}$, or, if you like, we set $\hbar = M = \mu = g = 1$. In these units, the action (2.1) takes the form

$$\mathcal{S} = \int dt\, d^2\mathbf{x} \left[\frac{i}{2} (\Psi^* \partial_t \Psi - \Psi \partial_t \Psi^*) - \frac{1}{2} \boldsymbol{\nabla}\Psi \cdot \boldsymbol{\nabla}\Psi^* - U(\mathbf{x})|\Psi|^2 - \frac{1}{2}|\Psi|^4 \right], \tag{2.3}$$

and imposing stationarity of the action with respect to variations in Ψ^* yields a non-linear Schrödinger equation, referred to as the dimensionless Gross-Pitaevskii Equation (GPE)[130, 131]

$$i\partial_t\Psi = \left[-\frac{1}{2}\nabla^2 + U(\mathbf{x}) + |\Psi|^2\right]\Psi. \tag{2.4}$$

If, instead, we impose stationarity of (2.3) with respect to Ψ, we obtain the complex conjugate of the GPE (2.4).

II.2. The Hydrodynamic Formulation

By introducing a change of variables

$$\Psi = \sqrt{\rho}e^{i\Phi} \tag{2.5}$$

referred to as the Madelung representation [132], the GPE (2.4) splits into two separate equations

$$\partial_t\rho + \boldsymbol{\nabla}\cdot(\rho\boldsymbol{\nabla}\Phi) = 0, \tag{2.6a}$$

$$\partial_t\Phi + \frac{1}{2}(\nabla\Phi)^2 + \rho - \frac{\nabla^2\sqrt{\rho}}{2\sqrt{\rho}} = 0. \tag{2.6b}$$

When identifying $\mathbf{v} = \nabla\Phi$, with the velocity field of the condensate, equation (2.6a) takes the form of a continuity equation for the density ρ. Equation (2.6b) takes the form of a Bernoulli equation with an additional term referred to as the quantum pressure. One way to motivate the name *quantum pressure* is to re-introduce dimensions in (2.6b). Then, the quantum pressure term is the only term with $\hbar$ as a prefactor.

II.3. Quantized Vortices

Having identified the velocity field $\mathbf{v}$ with the gradient of the phase Φ of the wavefunction, the velocity field must be irrotational, i.e. $\nabla\times\mathbf{v} = 0$. However, one may always rotate the container, or stir, a substance to enforce a non-zero circulation around a closed loop C. In a BEC, the circulation is zero everywhere except at certain points (2D) or along certain lines (3D), where the wavefunction Ψ vanishes so that its phase Ψ is undefined. These singular points, called quantum vortices, are discretized and topologically protected by their phase-winding ℓ, i.e.

$$\oint_C \mathbf{v}\cdot d\mathbf{r} = 2\pi\ell \text{ for } \ell\in\mathbb{Z}. \tag{2.7}$$

That the circulation is quantized as integer multiples of (in physical units) $2\pi\hbar/M$ is arguably one of the most striking properties of BECs, and quantum fluids in general.

The topological and discrete nature of these vortices, first investigated theoretically by Feynman [133] and Onsager [134], significantly affects the possible flow patterns (vortex lattices, turbulence, etc. [135–137]).

We shall now focus on a stationary condensate in polar coordinates (r, θ) with a central vortex with winding-number $\ell \in \mathbb{Z}$, i.e.

$$\Psi_0(r, \theta, t) = Y(r) e^{i\ell\theta - it}. \tag{2.8}$$

When written this way, it is clear that the discretization of ℓ follows from azimuthal periodicity, i.e. $\Psi(\theta = 0) = \Psi(\theta = 2\pi)$. Here, the e^{-it}-dependence comes from the ground-state oscillation due to the chemical potential, which is 1 in our units. In the absence of a radial flow, i.e. $Y \in \mathbb{R}$, the velocity field around the vortex is

$$\mathbf{v} = \frac{\ell}{r} \mathbf{e}_\theta. \tag{2.9}$$

In what follows, we shall, for simplicity, assume the vortex to rotate in the anti-clockwise direction, i.e. $\ell > 0$.

Inserting (2.8) into the GPE (2.4) for a free ($U = 0$) condensate yields

$$\frac{1}{2r} \partial_r \left(r \partial_r Y \right) + \left(1 - \frac{\ell^2}{2r^2} \right) Y = Y^3, \tag{2.10}$$

whose solutions give the ground state density $\rho = Y^2$ of the vortex solution. In the vortex, the density must be zero, i.e. $Y(r = 0) = 0$, and, far away, the condensate density must tend towards that of a free, uniform condensate at rest, i.e. $Y(r \to \infty) = 1$. We note that at small radii, equation (2.10) asymptotes to Bessel's equation, and a polynomial ODE in the limit $r \to \infty$, allowing us to write down the asymptotics

$$\rho(r) \sim \begin{cases} \rho_0 J_\ell^2(\sqrt{2} r) & \text{as } r \to 0, \\ 1 - \frac{\ell^2}{2r^2} & \text{as } r \to \infty, \end{cases} \tag{2.11}$$

where J_ℓ is a Bessel function of the first kind.

In figure 2.1, the numerically computed density profiles $\rho(r)$ for $\ell = 1, 2, \ldots, 9$ are exhibited. For details on how these profiles are computed, consult appendix B.2.

III. Fluctuations

Now we consider fluctuations of the condensate about the stationary vortex state $\Psi_0 = \sqrt{\rho} \exp(i\ell\theta - it)$ from (2.8) by writing $\Psi \to \Psi_0 + \delta\Psi$ with $\delta\Psi \ll \Psi_0$. When expanding both GPE (2.4), and

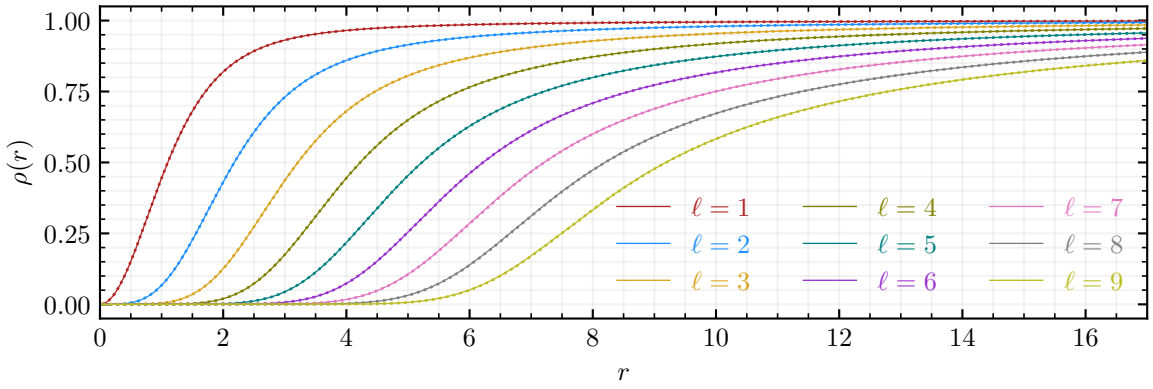

Figure 2.1 (Density profiles of vortices with low winding number) The density profiles $\rho(r)$ for the first 9 non-zero ℓ estimated with two different numerical methods. Densities obtained using the shooting method (appendix B.2.1) are shown as solid lines, and the densities obtained using the damped matrix evolution (see appendix B.2.1) are shown as dotted lines. It is clear that the larger the winding number ℓ, the larger the radius where the vortex core intersects a given density.

its complex conjugate, the linear equations can be collected into a single matrix equation known as the Bogoliubov de-Gennes (BdG) equation [61, 129],

$$i\partial_t|\psi\rangle = \widehat{L}|\psi\rangle \qquad \text{for } \widehat{L} \equiv \begin{bmatrix} \mathcal{D}_+ & \rho \\ -\rho & -\mathcal{D}_- \end{bmatrix}, \qquad |\psi\rangle \equiv \begin{bmatrix} u_+^{(m)} \\ u_-^{(m)} \end{bmatrix}. \tag{2.12}$$

Here, $u_\pm^{(m)}$ is defined through a decomposition of $\delta\Psi$ into azimutal modes*

$$\begin{bmatrix} \delta\Psi(t,r,\theta) \\ \delta\Psi^*(t,r,\theta) \end{bmatrix} = \sum_{m\in\mathbb{Z}} e^{im\theta} \begin{bmatrix} u_+^{(m)}(t,r)e^{+i\ell\theta - it} \\ u_-^{(m)}(t,r)e^{-i\ell\theta + it} \end{bmatrix}, \tag{2.13}$$

and the differential operators are defined by

$$\mathcal{D}_\pm \equiv -\frac{1}{2}\left[\partial_r^2 + \frac{1}{r}\partial_r - \frac{(m\pm\ell)^2}{r^2}\right] + 2\rho + U - 1\,. \tag{2.14}$$

For brevity, the azimuthal index m in $u_\pm^{(m)}$ will often be suppressed, writing $u_\pm$.

The BdG equation (2.12) conserves the norm [61]

$$\mathcal{N} = \langle\psi|\sigma_3|\psi\rangle = \int d^2\mathbf{x}\left(|u_+|^2 - |u_-|^2\right), \tag{2.15}$$

*Notice that the phase of Ψ_0 is factored out of $\delta\Psi$, i.e. a constant $u_\pm$ carries the phase of Ψ_0.

which can be interpreted as the particle content of a given mode. Here, σ_3 is the third Pauli matrix, which enters via the pseudo-unitarity $\sigma_3\widehat{L}^\dagger\sigma_3 = \widehat{L}$ of the BdG operator, and conservation of $\mathcal{N}$ follows from inserting (2.15) into (2.12).

An alternative to the BdG perturbation $\Psi \mapsto \Psi_0 + \delta\Psi$ is to consider fluctuations in hydrodynamic variables introduced in section II.2, i.e. $\Phi \mapsto \Phi_0 + \delta\phi$ and $\rho \mapsto \rho(1+\delta\rho)$ with $\delta\phi \ll \Phi_0$ and $\delta\rho \ll 1$. The linearised form of equations (2.6) then takes the form

$$D_t\delta\rho + \rho^{-1}\nabla\cdot(\rho\nabla\delta\Phi) = 0, \tag{2.16a}$$
$$D_t\delta\Phi + \rho\delta\rho - \tfrac{1}{4}\rho^{-1}\nabla\cdot(\rho\nabla\delta\rho) = 0, \tag{2.16b}$$

where $D_t \equiv \partial_t + \mathbf{v}\cdot\nabla$ is, as usual, the convective derivative. Note that the BdG approach (2.12) and the hydrodynamic approach (2.16) are equivalent, and one can be related to the other through

$$\delta\Psi = \Psi_0\left(\tfrac{1}{2}\delta\rho + i\delta\Phi\right) \quad \text{and} \quad \delta\Psi^* = \Psi_0^*\left(\tfrac{1}{2}\delta\rho - i\delta\Phi\right). \tag{2.17}$$

Exploiting the absence of explicit time dependence, and rotational symmetry of equations (2.16), we may decompose $\delta\Phi$ and $\delta\rho$ into azimutal numbers m and frequencies ω. Introducing the indexing short-hand $a = (\omega, m)$, we separate positive and negative frequencies*

$$\begin{aligned}\begin{bmatrix}\delta\Phi\\ \delta\rho\end{bmatrix} &= \int_0^\infty d\omega \sum_{m\in\mathbb{Z}}\left(\alpha_a\begin{bmatrix}\varphi_a\\ n_a\end{bmatrix} + \alpha_a^*\begin{bmatrix}\varphi_a^*\\ n_a^*\end{bmatrix}\right)\\ &= \int_0^\infty d\omega \sum_{m\in\mathbb{Z}}\left(\alpha_a\begin{bmatrix}\tilde\varphi_a\\ \tilde n_a\end{bmatrix}e^{im\theta - i\omega t} + \alpha_a^*\begin{bmatrix}\tilde\varphi_a^*\\ \tilde n_a^*\end{bmatrix}e^{-im\theta + i\omega t}\right)\end{aligned} \tag{2.18}$$

where α_a are constants. Here, as before, we shall omit the index a whenever convenient. Since equations (2.16) are linear by design, and Fourier modes are orthogonal, each mode satisfies (2.16) independently. These equations follow from the stationarity of the action formed from the following action

$$\begin{aligned}\mathcal{L} =& \frac{\rho}{2}\left(\varphi_a^* D_t n_a + \varphi_a D_t n_a^* - n_a^* D_t\varphi_a - n_a D_t\varphi_a^*\right)\\ &- \rho^2|n_a|^2 - \rho\nabla\varphi_a\cdot\nabla\varphi_a^* - \frac{\rho}{4}\nabla n_a\cdot\nabla n_a^* - \frac{1}{2}\nabla\cdot\left[\nabla\rho\left(|\varphi_a|^2 + \frac{1}{4}|n_a|^2\right)\right].\end{aligned} \tag{2.19}$$

This Lagrangian is invariant under phase rotations $(\varphi_a, n_a) \mapsto (\varphi_a, n_a)e^{-i\epsilon}$, which results in a Nöther-current of the form

$$\begin{aligned}\rho_N =& i\rho\left(\varphi_a n_a^* - \varphi_a^* n_a\right),\\ \mathbf{j}_N =& i\rho\left[\mathbf{v}\left(\varphi_a n_a^* - \varphi_a^* n_a\right) + \varphi_a\nabla\varphi_a^* - \varphi_a^*\nabla\varphi_a + \tfrac{1}{4}\left(n_a\nabla n_a^* - n_a^*\nabla n_a\right)\right],\end{aligned} \tag{2.20}$$

*That $\delta\Phi$ and $\delta\rho$ share coefficients amounts to saying that their phases co-evolve, and differ only by a constant.

satisfying a conservation law

$$\partial_t \rho_N + \nabla \cdot \mathbf{j}_N = 0. \tag{2.21}$$

Inserting the mode definitions (2.13) and (2.18) into (2.17), we find that for $u_\pm$ at a fixed frequency ω,

$$u_\pm = \sqrt{\rho}\left(\frac{1}{2}n_a \pm i\varphi_a\right)\alpha_a e^{-i\omega t}. \tag{2.22}$$

This may be used to identify the conserved quantity (2.20) as the norm $\mathcal{N}$ introduced in (2.15), i.e. $\mathcal{N} = \int \rho_N \, d^2x$.

Before moving on, we may benefit from the observation that the linearised hydrodynamic Lagrangian (2.19) is also symmetric under time translations $t \mapsto t + \epsilon$. This results in the conservation of the energy current ρ_E and $\mathbf{j}_E$, which is related to the norm current through $\rho_E = \omega\rho_N$ and $\mathbf{j}_E = \omega\mathbf{j}_N$.

This reinforces the idea of the norm as the particle number since each quasi-particle in the mode contributes with an energy proportional to ω. Moreover, we see that for positive frequency modes, modes with negative norm have negative energy. Therefore, in the special case of positive frequency modes, we may think of superradiance as the following conceptual mechanism: if a positive energy mode excites a negative energy mode, energy conservation dictates that the positive energy mode must return with larger energy than it had initially.

III.1. The WKB perspective

We now approach the linearised hydrodynamical equations (2.16) using the Wentzel–Kramers–Brillouin (WKB) approximation. At the heart of the WKB method lies the assumption that solutions look locally like plane waves. More precisely, the WKB method is a type of multi-scale expansion where the phase is assumed to vary over much smaller scales than the amplitude. Because we will use this approach throughout this thesis, appendix A has been dedicated to the WKB method.

We start by writing equations (2.16) in terms of the decomposition (2.18), i.e.

$$\partial_r^2\tilde{\varphi} + (\partial_r \ln\rho)\partial_r\tilde{\varphi} + \frac{1}{r}\partial_r\tilde{\varphi} = \frac{m^2}{r^2}\tilde{\varphi} + i\Omega\tilde{n}, \tag{2.23a}$$

$$\partial_r^2\tilde{n} + (\partial_r \ln\rho)\partial_r\tilde{n} + \frac{1}{r}\partial_r\tilde{n} = \frac{m^2}{r^2}\tilde{n} - 4i\Omega\tilde{\varphi} + 4\rho\tilde{n}, \tag{2.23b}$$

where

$$\Omega = \omega - \frac{m\ell}{r^2} \tag{2.24}$$

is the frequency in the co-moving frame. Unfortunately, applying the WKB approximation to equations (2.23) is unjustified close to the core, $r \simeq 0$. The problem is the factors $\partial_r \ln\rho$ that appear

in both equations. Using the asymptotics (2.11) for ρ as $r \to 0$ along with the Bessel asymptotic $J_\ell(\sqrt{2}r) \sim (r/\sqrt{2})^\ell$, we find $\partial_r \ln \rho \sim 2\ell/r$. Because m and ℓ are of the same order, $\ln \rho$ changes over the same scale as the phase (m/r), which violates the WKB assumption of a separation of scales in phase and background.

Salvation comes from the realisation that the offending term can be eliminated by introducing

$$\tilde{\varphi} \equiv \rho^{-\frac{1}{2}} f, \qquad \tilde{n} \equiv \rho^{-\frac{1}{2}} g, \tag{2.25}$$

which reduces the equations in (2.23) to,

$$r^2 \partial_r^2 f + r\partial_r f - \widetilde{m}^2 f = i\Omega r^2 g, \tag{2.26a}$$
$$r^2 \partial_r^2 g + r\partial_r g - \widetilde{m}^2 g = 4\rho r^2 g - 4i\Omega r^2 f. \tag{2.26b}$$

Here, the relation (2.10) for $Y(r)$ has been used to write

$$\widetilde{m}^2 = m^2 + \ell^2 + 2r^2(\rho - 1). \tag{2.27}$$

The factor $1/\sqrt{\rho}$ in (2.25) cancels that contained in Ψ (see e.g. (2.8)), so that the new equations (2.26) can be viewed as an intermediate step in converting the BdG equation (2.12) to the hydrodynamic equation (2.16). The benefit of this rewriting is that there are no derivatives of any background quantities which become large when approaching the origin. Now we can write a WKB ansatz for the waves

$$f(r) \equiv \frac{1}{\sqrt{r}} A(r) e^{i\int p(r)dr} \quad \text{and} \quad g(r) \equiv \frac{1}{\sqrt{r}} B(r) e^{i\int p(r)dr}, \tag{2.28}$$

where $\partial_r(A/\sqrt{r}) \ll pA$, $\partial_r(B/\sqrt{r}) \ll pB$. Here, the factors of $1/\sqrt{r}$ have been taken out of the amplitudes A and B for future convenience. Conceptually, these pre-factors correspond to the geometrical decrease in the amplitude of a wave due to the spreading of energy over a larger circle as the wave moves radially outwards. To leading order, the WKB expansion (see appendix A) of (2.26) gives the dispersion relation

$$\Omega^2 = F(k)k^2 \text{ where } F(k) \equiv \rho + \tfrac{1}{4}k^2 \text{ for } k^2 \equiv p^2 + \widetilde{m}^2/r^2. \tag{2.29}$$

Note that as $r \to \infty$, inserting (2.11) into (2.27) informs us that $\widetilde{m} \to m$ as $r \to \infty$. Therefore, the dispersion relation (2.29) reduces to the well-known Bogoliubov dispersion (see e.g. [138, 139]) in polar coordinates. The dispersion relation has two branches

$$\omega_D^{\pm} = \frac{m\ell}{r^2} \pm \sqrt{F(k)k^2}, \tag{2.30}$$

and modes with $\omega = \omega_D^+$ are referred to as being on the upper branch and modes with $\omega = \omega_D^-$ on the lower branch. We shall soon see that modes on the upper branch have positive norm, and that modes on the lower branch have negative norm.

Being a quartic polynomial in p, the dispersion relation (2.29) has four roots in p for a fixed frequency ω. We label these roots

$$p^{\pm}(r) \equiv \pm\sqrt{-W_+}, \qquad \tilde{p}^{\pm}(r) \equiv \mp i\sqrt{W_-}, \tag{2.31a}$$

$$W_{\pm} \equiv \mp 2\sqrt{\rho^2+\Omega^2} + 2\rho + \tilde{m}^2/r^2. \tag{2.31b}$$

Modes with $\tilde{p}^{\pm}$ are evanescent everywhere, $\tilde{p}^{+}$ grows with increasing r, and $\tilde{p}^{-}$ decays. At large r, modes with $p^{\pm}$ are radially in and out-going propagating plane waves. The direction of propagation is given by the radial component of the group velocity

$$v_g^r = \partial_p \omega_D^{\pm} = \frac{\rho + k^2/2}{\Omega} p. \tag{2.32}$$

To determine the WKB amplitudes A and B (2.28), we consider the next-to-leading order WKB expansion. The result, which can be found in equation (A.9), in appendix A, can be written*

$$\partial_r \left(QA^2\right) = 0 \text{ with } Q \equiv F^{-1}\Omega v_g^r = \frac{\rho + k^2/2}{\rho + k^2/4} p. \tag{2.33}$$

This means that the radial variations of A are given by $A \propto |Q|^{-\frac{1}{2}}$, and B is given by $v_g^r B = iQA$, see equation (A.6) in appendix A.

When the dust settles, we have obtained expressions for the original φ_a and n_a modes given by,

$$\varphi_a \simeq \mathcal{A} \exp\left[i\int p(r)dr + im\theta - i\omega t\right] \text{ for } \mathcal{A} \equiv \left|r\rho F^{-1}\Omega v_g^r\right|^{-1/2}, \tag{2.34a}$$

$$n_a \simeq \mathcal{B} \exp\left[i\int p(r)dr + im\theta - i\omega t\right] \text{ for } \mathcal{B} \equiv i\left|r\rho F\Omega^{-1} v_g^r\right|^{-1/2}. \tag{2.34b}$$

Armed with these expressions, we can write the norm density in (2.20), as

$$\rho_N = \frac{2\rho\Omega|\varphi_a|^2}{\rho + k^2/4}. \tag{2.35}$$

Since ρ, k^2 and φ_a are non-negative everywhere, we see that the sign of the norm density ρ_N follows the sign of Ω. That is, modes on the upper branch (ω_D^+) have positive norm, and modes on the lower branch (ω_D^-) have negative norm. In particular, positive frequency modes can have negative energy, provided they are on the negative norm branch.

*This equation is the motivation for the convenience factors $1/\sqrt{r}$ introduced in (2.28).

III.2. Scattering of WKB modes

If the WKB approximation breaks down in some region, then one WKB-solution may be scattered into one or more of the WKB-solutions on the other side of the failing region. An important example of where this scattering occurs is at radial turning points r_{tp}, which are the locations where a wave stagnates radially, i.e. $v_g^r = 0$ (see section A.3 appendix A for details). From (2.32), we see that this occurs for $p = 0$, and since $W_- > 0$ everywhere, only the $p^\pm$ expressions from (2.31) exhibit scattering. In fact, the $\tilde{p}^\pm$ modes are evanescent everywhere and do not scatter other than potentially at the boundary.

To investigate the turning points r_{tp}, it is convenient to introduce the turnover frequencies,

$$\omega^\pm(r) = \frac{m\ell}{r^2} \pm \sqrt{\rho\frac{\widetilde{m}^2}{r^2} + \frac{\widetilde{m}^4}{4r^4}}, \tag{2.36}$$

which sets the frequency of a mode that stagnates at r. That is, a mode with frequency ω has turning points r_{tp} at $\omega = \omega^\pm(r_{tp})$. See Figure 2.2 for examples of turnover frequencies $\omega^\pm(r)$ for $\ell = 2$ and $m = 1, 2, 3, 4$.

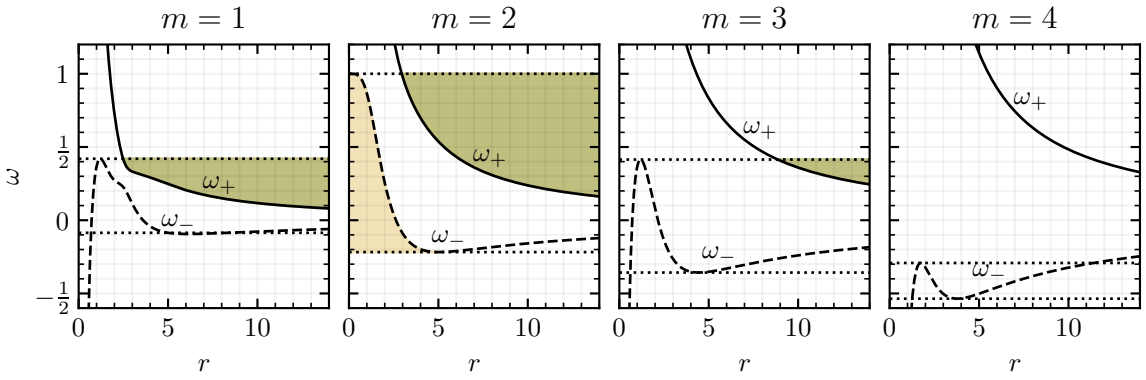

Figure 2.2 (Turnover frequencies) The turnover frequencies ω^+ (solid black line) and ω^- (dashed black line) with $\ell = 2$ for the first four $m > 0$ values. Modes above ω^+ have positive norm whereas those below ω^- have negative norm. Between the two curves (red region) modes are evanescent, and not propagating. In the frequency band between the horizontal black dotted lines, waves can be trapped in a cavity in the vortex core (yellow region) and become (quasi-)bound states. The possibility of there being modes with positive norm at infinity but negative norm in the cavity is what leads to the vortex instability. The frequency range where propagating modes outside ($\omega \geqslant \omega_+$) the core can interact with the cavity modes ($\omega \leqslant \omega_+$) is coloured green. Inverting the vertical axis about $\omega = 0$ and swapping the labels $\omega^+ \leftrightarrow \omega^-$ gives the corresponding plots for the $m < 0$ modes.

Note that $\omega = \omega^+$ is a turning point on the positive norm branch (upper branch) and $\omega = \omega^-$ is a turning point on the negative norm branch (lower branch). If a positive frequency mode $\omega > 0$ has turning points on both branches, i.e $\omega = \omega^-(r_1)$ and $\omega = \omega^+(r_2)$, there exists a scattering process between positive and negative energy modes. A positive energy mode at $r > r_2$ may tunnel through the evanescent region $r_1 < r < r_2$, and scatter into negative energy modes in $r < r_1$. To conserve energy, such a process results in an amplification of the outer, positive energy mode at $r > r_2$. This is the essence of the superradiance mechanism.

Before formulating the exact scattering process, we need to check the asymptotic behaviour of our WKB modes (2.34) as they approach the origin*.

From (2.11), we know that $\rho \to 0$ as $r \to 0$, meaning that the BdG equation (2.12) reduces to the Schrödinger equation in the vortex core. In terms of $u_\pm$, we have

$$\frac{1}{2r}\partial_r\left(r\partial_r u_\pm\right) - \frac{(m \pm \ell)^2}{2r^2}u_\pm + (1 \pm \omega)u_\pm = 0, \tag{2.37}$$

whose solution are of the form

$$u_\pm(r \to 0) = \alpha_\pm J_{m\pm\ell}\left(\varepsilon r\right) + \beta_\pm Y_{m\pm\ell}\left(\varepsilon r\right) \text{ for } \varepsilon \equiv \sqrt{2 \pm 2\omega} \tag{2.38}$$

where $\alpha_\pm$ and $\beta_\pm$ are constants. If the WKB modes (2.34) have the correct limiting behaviour, they should agree with f and g in $u_\pm \sim \frac{1}{2}g + if$ using (2.38) when taking the limit $r \to 0$. For this, we first need to know the asymptotic behaviour of the different values of p in (2.31), which is found to be

$$-W_\pm \overset{r\to 0}{\sim} -\frac{1}{r^2}(\ell \mp |m|)^2 + \varepsilon_\pm^2 + \mathcal{O}(r^2) \text{ for } \varepsilon_\pm^2 \equiv 2 \mp 2\omega\,\mathrm{sgn}(m). \tag{2.39}$$

First, for the evanescent modes $\tilde{p}^\pm \equiv \mp i\sqrt{W_-}$ we have $\tilde{p}^\pm \sim |\ell+|m||/r$ to leading order. Inserting this in (2.33) and (2.34) results in the WKB amplitudes being constant. That is, we have the following scaling relation

$$\tilde{\mathcal{A}}^\pm e^{i\int \tilde{p}^\pm dr} \sim r^{\mp|\ell+|m||}. \tag{2.40}$$

First, if $|m| = \ell$ we have $p^\pm \equiv \pm\sqrt{-W_+} \sim \varepsilon_+$. Inserting this in (2.33) and (2.34), results in the amplitude scaling as $1/\sqrt{r}$. For $|m| \neq \ell$, we find $p^\pm = \pm i|\ell-|m||/r$ to leading order. Substituting this for p in (2.33) introduces an additional factor of $\sqrt{r}$ which cancels that in the amplitudes of (2.34), leaving the amplitudes constant to leading order. That is

$$\mathcal{A}^\pm e^{i\int p^\pm dr} \sim \begin{cases} r^{-\frac{1}{2}}e^{\pm i\varepsilon_+ r} & \text{for } |m| = \ell \\ r^{\mp|\ell-|m||} & \text{for } |m| \neq \ell \end{cases} \tag{2.41}$$

*We have already seen that asymptotic behaviour as $r \to \infty$ is, as expected, that of plane waves with Bogoliubov dispersion.

Notice that since $\varepsilon_+^2 > 2 - 2\omega\,\mathrm{sgn}(m)$, the modes (2.41) are propagating for all $m < 0$, and also for $m > 0$ with $\omega < 1$, and evanescent otherwise.

Since, for $|m| \neq \ell$, the Bessel functions scale as

$$J_{m\pm\ell} \sim r^{|m\pm\ell|}, \qquad Y_{m\pm\ell} \sim r^{-|m\pm\ell|}. \tag{2.42}$$

It is clear that for $|m| \neq \ell$ the WKB modes can be written in the form of the solutions (2.38), i.e. they have the correct limiting behavior.

For $|m| = \ell$, it is a bit more complicated. Whereas the $\tilde{p}^{\pm}$ modes match the Bessel asymptotics (2.42), the remaining two modes $p^{\pm}$ do not match the zeroth order Bessel asymptotics J_0 and Y_0. This can be seen from noting that the amplitude in (2.41) is diverges as $1/\sqrt{r}$, whereas J_0 is regular and Y_0 is only logarithmically divergent, i.e. $Y_0 \sim \ln r$ as $r \to 0$. In fact, that the amplitude in (2.41) diverges for $|m| = \ell$ signals the breakdown of the WKB assumption, and we have to perform an asymptotic matching procedure similar to that discussed in appendix A.4. That is, we consider the asymptotics of the remaining exact solutions for u_- in (2.38) as $r \to \infty$, and match with the asymptotics in (2.41) for $|m| = \ell$. For large arguments, we recover the asymptotic behaviour of the WKB modes,

$$\begin{bmatrix} J_0(\varepsilon r) \\ Y_0(\varepsilon r) \end{bmatrix} \sim \frac{1}{\sqrt{r}} \begin{bmatrix} \cos(\varepsilon r - \pi/4) \\ \sin(\varepsilon r - \pi/4) \end{bmatrix} = \frac{1-i}{2\sqrt{2}} \begin{bmatrix} 1 & i \\ 1 & -i \end{bmatrix} \begin{bmatrix} r^{-\frac{1}{2}} e^{i\varepsilon r} \\ r^{-\frac{1}{2}} e^{-i\varepsilon r} \end{bmatrix}, \tag{2.43}$$

meaning that the J_0 solution contains WKB modes with $\mathcal{A}^- = i\mathcal{A}^+$, whereas the Y_0 solution contains modes with $\mathcal{A}^- = -i\mathcal{A}^+$. Note, however, that since Y_0 diverges at the origin, the amplitudes of these modes must be zero. Therefore the boundary condition for $|m| = \ell$ as $r \to 0$ is

$$\mathcal{A}^-(r_0) = i\mathcal{A}^+(r_0) \tag{2.44}$$

In other words, for $|m| = \ell$ the boundary condition that ensures regularity at $r = 0$ is that of a reflection with a phase shift if $\pi/2$. In fact, if we return to the case of $|m| \neq \ell$, we may use the transfer matrix $\tilde{T}$ from (A.39), along with the condition that the evanescent mode ($\tilde{k}_r^+$) that grows with decreasing r is zero, to find that $\mathcal{A}^- = i\mathcal{A}^+$ at the innermost turning point r_0. That is, the boundary condition (2.44) is valid in both scenarios, with $r_0 = 0$ for the case $|m| = \ell$, and with r_0 being the innermost turning point for $|m| \neq \ell$. When a boundary condition at the origin is necessary, as it is for numerical simulations, then it suffices to observe that for $|m| \neq \ell$, the relations (2.42) and (2.38) requires $u_\pm \to 0$ as $r \to 0$ for solutions to be regular at the origin. That is, for $u_\pm$ with $|m| \neq \ell$, the boundary condition at the origin is Dirichlet, i.e. vanishing amplitude.

To summarise, in this section we have constructed a formalism for the evolution of fluctuations in a condensate with a central ℓ-wound vortex. We saw that fluctuations conserve the norm (2.15), and that using a WKB approximation, we can identify the two branches of the dispersion relation $\omega_D^{\pm}$ with positive (ω_D^+) and negative (ω_D^-) norm. We then considered the scattering of

WKB modes in the presence of turning points, allowing us, by virtue of the formalism discussed in appendix A, to relate amplitudes at any two points in the condensate. Finally, we confirmed that the WKB modes have the correct behavior as $r \to 0$ comparing their asymptotic forms (2.40) and (2.41) to the exact solutions (2.38) in the low-density limit.

IV. The dynamical origin of the multiply quantised vortex instability

IV.1. Open systems

To start, let us consider a multiply wound vortex in an infinite, or open, two-dimensional condensate. That is, a system in which there either is no outer boundary perfectly absorbs impinging waves.

We note that since the $\tilde{p}^+$ mode diverges at infinity and $\tilde{p}^-$ diverges at the origin, and neither of the two scatters, we may consistently set the amplitudes of these modes to 0. This leaves only the $p^\pm$ modes, which for a given frequency ω may have zero, one, two or three turning points (see figure 2.2). If there are no turning points, the wave will be reflected entirely off the origin. Likewise, if there is only one turning point, then the mode is perfectly reflected off this point. Since there are no incoming modes, there are no resonant frequencies in these cases. That is, in absence of incoming modes, a cavity (orange region in figure 2.2) is needed in order to trap modes and facilitate resonance.

Fortunately, the boundary condition (2.44) at the origin, which is needed when there are two turning points, takes the same form as the boundary condition at the innermost turning point r_0, which is needed in the case of three turning points. That is, we may introduce radii $r_0 \leqslant r_1 \leqslant r_2$ such that the $p^\pm$ modes are propagating in the regions $r \in [r_0, r_1]$ and $r \in [r_2, \infty)$, and evanescent in $r \in [r_1, r_2]$. Here, we either identify all three r_0, r_1, r_2 with turning points, or r_1, r_2 with turning points and $r_0 = 0$.

Using the transfer matrices*

$$T \equiv \frac{1}{2} e^{-\frac{\pi i}{4}} \begin{bmatrix} 2i & 1 \\ 2 & i \end{bmatrix} \qquad \text{and} \qquad \tilde{T} \equiv \frac{1}{2} e^{-\frac{\pi i}{4}} \begin{bmatrix} 2 & 2i \\ i & 1 \end{bmatrix} \tag{2.45}$$

derived in appendix A, amplitudes $\mathcal{A}_\infty^\pm$ at $r \to \infty$ can be related to amplitudes $\mathcal{A}_0^\pm$ at r_0 using the

*Note that these matrices are defined differently from those in the published article [62]. In this convention, the evanescent WKB propagator is diagonal, whereas in the alternative notation the propagator must be flipped for the evanescent amplitudes to match on either side. This change in convention is chosen to be consistent with that of the next chapter.

following sequence of WKB propagators and transfer matrices

$$\begin{bmatrix}\mathcal{A}_0^+\\ \mathcal{A}_0^-\end{bmatrix} = \left|\frac{Q(\infty)}{Q(r_0)}\right|^{\frac{1}{2}} \begin{bmatrix}e^{-iS_{01}} & 0\\ 0 & e^{iS_{01}}\end{bmatrix} T \begin{bmatrix}e^{\tilde{S}_{12}} & 0\\ 0 & e^{-\tilde{S}_{12}}\end{bmatrix} \widetilde{T} \begin{bmatrix}e^{-iS_{2\infty}} & 0\\ 0 & e^{iS_{2\infty}}\end{bmatrix} \begin{bmatrix}\mathcal{A}_\infty^+\\ \mathcal{A}_\infty^-\end{bmatrix}, \tag{2.46}$$

where

$$S_{ij} \equiv \int_{r_i}^{r_j} \sqrt{-W_+}\,dr \tag{2.47}$$

and $\tilde{S}_{ij} \equiv iS_{ij}$. Here, S_{ij} is the accumulated WKB phase after propagation from r_j to r_i. From the relation (2.44), the inner amplitudes $\mathcal{A}^-$ and $\mathcal{A}_0^+$ are related by $\mathcal{A}_0^- = i\mathcal{A}_0^+$. Likewise, the amplitudes at infinity are constrained by the absence of incoming waves, i.e. $\mathcal{A}_\infty^- = 0$. As shown in section A.4.3 of appendix A, equation (2.46) permits non-zero amplitudes when supplying the aforementioned boundary conditions if

$$4\cot(S_{01}) = ie^{-2\tilde{S}_{12}} \tag{2.48}$$

For real frequencies ω, both S_{01} and $\tilde{S}_{12}$ are real, meaning that (2.48) can only be solved if the tunneling contribution is infinite, i.e. $\tilde{S}_{12} \to \infty$. In general, one must allow for complex values $\omega_c = \omega + i\Gamma \in \mathbb{C}$ in (2.31b) for solutions to exist. Note that the existence of complex resonant frequencies $\omega_c = \omega + i\Gamma$ means that the resonant modes are either exponentially growing ($\Gamma > 0$) or decaying ($\Gamma < 0$) over time. To distinguish modes of this kind from normal resonant modes, they are referred to as Quasi-Bound States (QBSs) or Quasi-Normal Modes (QNMs). Assuming weak growth rates Γ compared to the oscillation frequency ω, i.e. $|\omega| \ll |\Gamma|$, we may expand the integrated phases S_{01} in (2.48),

$$S_{01}(\omega) = S_{01}(\omega_R) + i\Gamma\partial_{\omega_R} S_{01}. \tag{2.49}$$

Inserting this into (2.48) and separating real and imaginary parts yields

$$\cos S_{01}(\omega) = 0, \qquad \Gamma = -\frac{\log X(\omega)}{2\partial_\omega S_{01}(\omega)} \qquad \text{for} \qquad X \equiv \frac{4 + e^{-2\tilde{S}_{12}}}{4 - e^{-2\tilde{S}_{12}}}. \tag{2.50}$$

Where the first condition determines the oscillatory frequency ω_R, and the second determines the growth, or decay, rate. The oscillatory condition can be seen as a Bohr-Sommerfeld quantization condition (A.44), with additional, non-trivial phase shifts $\pi/4$ supplied at each turning point. The condition for the imaginary part can be interpreted by identifying $T = 2|\partial_\omega S_{01}|$ with the time it takes the mode to travel from r_1, to r_0 and back (see e.g. (A.20) from appendix A.3). Here, $+$ corresponds to a positive norm mode in the region $r_0 < r < r_1$, and $-$ a negative norm mode. Over a full period, the change in amplitude can be written $e^{\Gamma T} = |\mathcal{R}_\pm|$ where $|\mathcal{R}_+| \equiv 1/X$ for the positive norm mode and $|\mathcal{R}_-| \equiv X$ for the negative (see appendix A). Since $X > 1$, the positive norm mode exponentially decays over time, while the negative norm mode grows exponentially.

Numerically estimated solutions to (2.50) are shown in Table 2.1. We find that the $\ell = 1$ vortex is stable, as it should be.

ℓ	m	ω	Γ
2	2	0.3965	2.565×10^{-3}
3	2	0.2476	1.926×10^{-3}
	3	0.6619	7.867×10^{-4}
	4	0.2166	2.398×10^{-7}
4	2	0.1855	1.617×10^{-3}
	3	0.4782	8.759×10^{-4}
	4	0.1172	3.548×10^{-8}
	5	0.4715	1.245×10^{-6}
	6	0.1284	6.886×10^{-13}
	7	-0.2173	3.021×10^{-8}
5	2	0.1505	1.440×10^{-3}
	3	0.3773	8.299×10^{-4}
	4	0.6282	2.665×10^{-4}
	5	0.3237	6.378×10^{-7}
	6	0.6263	7.591×10^{-7}
	⋮	⋮	⋮

Table 2.1 (WKB resonances in open systems) The numerically estimated unstable frequencies $\omega_c = \omega + i\Gamma$ for the first few ℓ computed numerically under the WKB approximation (2.50).

IV.2. Closed systems

We have now seen (section IV.1) how an instability of fluctuations around a multiply wound vortex in an infinite system arises from the interaction between a negative energy mode in the vortex cavity, and a positive energy mode outside. However, it is practically impossible to create truely open systems in a laboratory setting. Instead, one typically has a finite outer boundary r_B of the condensate which is at least partially reflective. Note that this dramatically changes the resonance condition (2.48) in open system as we now have to permit incoming modes in (2.46) resulting from the reflection of outgoing modes at the finite boundary r_B.

To model the outer wall, we shall, for the remaining part of this chapter, focus on the behaviour of the aforementioned instability when the condensate is placed in a finite-sized box-trap U. This external trap U is constructed such that outside the boundary at r_B, the energy cost of a condensate particle is larger than its chemical potential, i.e. $U > 1$ at $r > r_B$. In this chapter, and the next, we shall consider a family of smooth bucket traps of the form

$$U(r) = \frac{U_0}{1 + (U_0 - 1)e^{a(r_B - r)}}, \tag{2.51}$$

where $U_0 > 0$ controls the strength of the trap outside r_B, and $a > 0$ controls the abruptness of the

step (see panel Figure 2.3(a) for the function plotted). The function (2.51) smoothly from $U(r) \simeq 0$ for $r \ll r_B$ to $U(r) \simeq U_0$ for $r \gg r_B$ with the slope at $r = r_B$, which is $a(U_0 - 1)/U_0$, being controlled by the parameter a. It is defined such that U is larger than the chemical potential when $r \geqslant r_B$, i.e. $U(r_B) = 1$. Note that if $a, U_0 \to \infty$, then the trap (2.51) is effectively an infinite wall, i.e. $U = 0$ for $r < r_B$ with $U = \infty$ at $r \geqslant r_B$.

The Outer Boundary Condition

If the outer boundary r_B is distant, i.e. $r_B \gg \ell$, then the equation (2.10) for the density around a stationary vortex can be written in a one-dimensional form

$$\partial_r^2 \sqrt{\rho} \approx 2(\rho - 1)\sqrt{\rho}, \tag{2.52}$$

in the vicinity of r_B. Then, determining the correct boundary conditions at r_B is equivalent to investigating how a fluctuations on a one-dimensional condensate collides with a wall. Using a hard wall $U = \infty$ at $r \geqslant r_B$ with $U = 0$ for $r < r_B$, one must have $\rho(r_B) = 0$. The solution to (2.52) satisfying this boundary condition is

$$\rho \approx \begin{cases} \tanh^2(r_B - r) & \text{for } r \leqslant r_B \\ 0 & \text{otherwise} \end{cases}, \tag{2.53}$$

which changes from the uniform density $\rho \approx 1$ to $\rho = 0$ at r_B over a few healing lengths. This transition arises due to the quantum pressure term in (2.6), and is related to the healing length introduced in (2.2), which is the length scale below which the self-interaction of condensate particles is able to efficiently heal inhomogeneities [111].

To confirm the boundary condition, three different numerical simulations of a right-moving gaussian pulse colliding with a boundary at r_B are considered. First, using a numerical method for simulating the full one-dimensional GPE (see appendix B section B.2.3 for details) with the soft trap introduced in (2.51). This is compared to a simulation of the BdG equation (2.12) (see appendix B section B.2.2 for details) using the background density (2.53) with a dirichlet boundary at r_B, i.e. $\delta\psi(r_B) = 0$. Finally, we consider a simulation of the BdG equation (2.12) with a uniform background density $\rho = 1$, and a Neumann boundary condition at r_B, i.e. $\partial_r \delta\psi(r_B) = 0$. The result, shown in figure 2.3, confirms that the two choices of boundary conditions are equivalent. That is, we can either include the density depression (2.53) in the background density and use a dirichlet boundary condition $\delta\psi = 0$ at r_B, or we can take the uniform density $\rho \simeq 1$ at r_B and use a Neumann boundary condition $\partial_r \delta\psi = 0$ at r_B. For convenience, we shall choose the latter, which, in terms of $\mathcal{A}_B^{\pm}$ becomes*

$$\mathcal{A}_B^+ = \mathcal{A}_B^-. \tag{2.54}$$

*This follows from imposing the Neumann criterion $\partial_r \phi = 0$ on $\phi = \mathcal{A}^+(r_B)e^{ik_r r} + \mathcal{A}^-(r_B)e^{-ik_r r}$ at the boundary $r = r_B$.

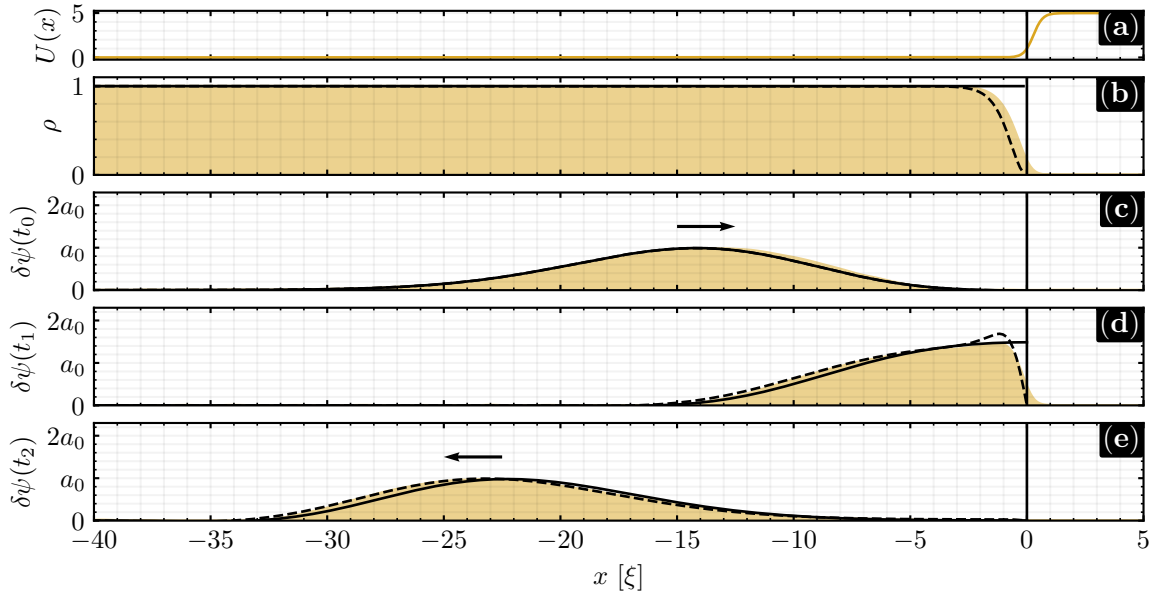

Figure 2.3 (Effective Boundary Condition) A right-moving gaussian pulse of width $\sigma = 5$ and amplitude $a_0 \equiv 0.01$ is reflected off a boundary at $x = 0$ in three different situations: (1) The simulated full GPE evolution (orange) using a soft bucket trap $a = U_0 = 5$ of the form (2.51) as depicted in panel **(a)**, (2) the BdG evolution using the background density (black dashed) $\rho = \tanh^2 x$ from (2.53) with a Dirichlet boundary condition at $x = 0$ and (3) the BdG evolution using a uniform density $\rho = 1$ (black solid) with a Neumann boundary at $x = 0$. In panel **(b)**, the background densities are shown, and in panels **(c)**, **(d)** and **(e)** snapshots of the evolving pulse is shown at three instances $t_0 = 69$, $t_1 = 75$ and $t_2 = 81$. It is clear that evolving pulse using the true background density and boundary conditions (orange) is well approximated by the hard wall BdG (black dashed). Moreover, the agreement of the solid black lines with the black dashed lines means that the boundary is well approximated by a uniform density all the way up to the boundary, and an effective Neumann boundary condition at $x = 0$.

Before computing the resonance condition, we note, as before, that the evanescent modes must vanish at r_B, i.e. $\tilde{\mathcal{A}}_B^{\pm} = 0$. Since it diverges at the origin, and it does not scatter, we must have $\tilde{\mathcal{A}}_B^{-} = 0$. Then $\tilde{\mathcal{A}}_B^{+}$ must also be zero since, if it was not, it would reflect into the forbidden mode $\tilde{\mathcal{A}}_B^{-}$ at r_B.

The Resonance Condition

The formulation of the resonance condition (2.46) in open systems remains perfectly valid in the closed system, provided that the amplitudes $\mathcal{A}_\infty^{\pm}$, and phases $S_{2\infty}$ are instead evaluated at r_B, i.e. $\mathcal{A}_\infty^{\pm} \mapsto \mathcal{A}_B^{\pm} \equiv \mathcal{A}^{\pm}(r_B)$, $Q(\infty) \mapsto Q(r_B)$ and $S_{2\infty} \mapsto S_{2B}$. Therefore, the only missing ingredient in the resonance condition (2.46) is the boundary condition at r_B, which we found in the previous section to be $\mathcal{A}_B^{+} = \mathcal{A}_B^{-}$. Note that in a closed system, we expect a discrete set of normal modes also in the case of only one, or two turning points. As these do not exhibit any instabilities, we shall specialise, as before, to the case of two or three turning points inside the boundary r_B. Recycling the notation from section IV.1, we write $r_0 < r_1 < r_2 < r_B$, so that the matrix that relates amplitudes $\mathcal{A}_B^{\pm}$ at r_B to amplitudes $\mathcal{A}_0^{\pm}$ at r_0 takes the form,

$$\begin{bmatrix} \mathcal{A}_0^{+} \\ \mathcal{A}_0^{-} \end{bmatrix} = \left|\frac{Q(r_B)}{Q(r_0)}\right|^{\frac{1}{2}} \begin{bmatrix} e^{-iS_{01}} & 0 \\ 0 & e^{iS_{01}} \end{bmatrix} T \begin{bmatrix} e^{-\tilde{S}_{12}} & 0 \\ 0 & e^{\tilde{S}_{12}} \end{bmatrix} \widetilde{T} \begin{bmatrix} e^{-iS_{2B}} & 0 \\ 0 & e^{iS_{2B}} \end{bmatrix} \begin{bmatrix} \mathcal{A}_B^{+} \\ \mathcal{A}_B^{-} \end{bmatrix}, \tag{2.55}$$

in direct correspondence to (2.46). Now invoke the boundary condition $\mathcal{A}_0^{+} = i\mathcal{A}_0^{-}$ from (2.44) at the origin, and the Neumann boundary condition $\mathcal{A}_B^{-} = \mathcal{A}_B^{+}$ from (2.54) at r_B. Following the procedure detailed in section A.4.4 of appendix A, the resonance condition in closed systems takes the form

$$4\cot(S_{01})\cot(S_{2B} + \pi/4) = e^{-2\tilde{S}_{12}}. \tag{2.56}$$

Here, the only difference from the resonance condition (2.48) for open systems, is the inclusion of an additional cotangent on the left at the expense of the imaginary unit on the right. If the two propagating regions $r \in [r_0, r_1]$ and $r \in [r_2, r_B]$ are well separated, then $\exp(-2\tilde{S}_{12}) \simeq 0$, so that if only one of the two cotangents in (2.56) are small, then the resonant modes are given by either $\cos(S_{01}) \simeq 0$ or $\cos(S_{2B} + \pi/4) \simeq 0$. That is, the resonance condition decouples into two disconnected cavity conditions, where the first, which is located inside the vortex core, is in agreement with the condition (2.50) found for open systems. We shall refer to modes of this kind as cavity modes, as they are trapped inside the vortex cavity. The second, i.e. $\cos(S_{2B} + \pi/4) \simeq 0$, signals the presence of normal modes outside the vortex core. These will be referred to as phonon modes. Here, the factor $\pi/4$ originates from the absence of a non-trivial phase-shift at the Neumann boundary r_B. In fact, as shown in section A.4.4 of appendix A, if we instead consider a general, reflecting boundary condition of the form $\mathcal{A}_B^{-} = e^{2i\eta}\mathcal{A}_B^{+}$ at r_B for $\eta \in \mathbb{R}$, the result would be that of a phase-shift of S_{2B} by η, i.e. $S_{2B} \mapsto S_{2B} + \eta$.

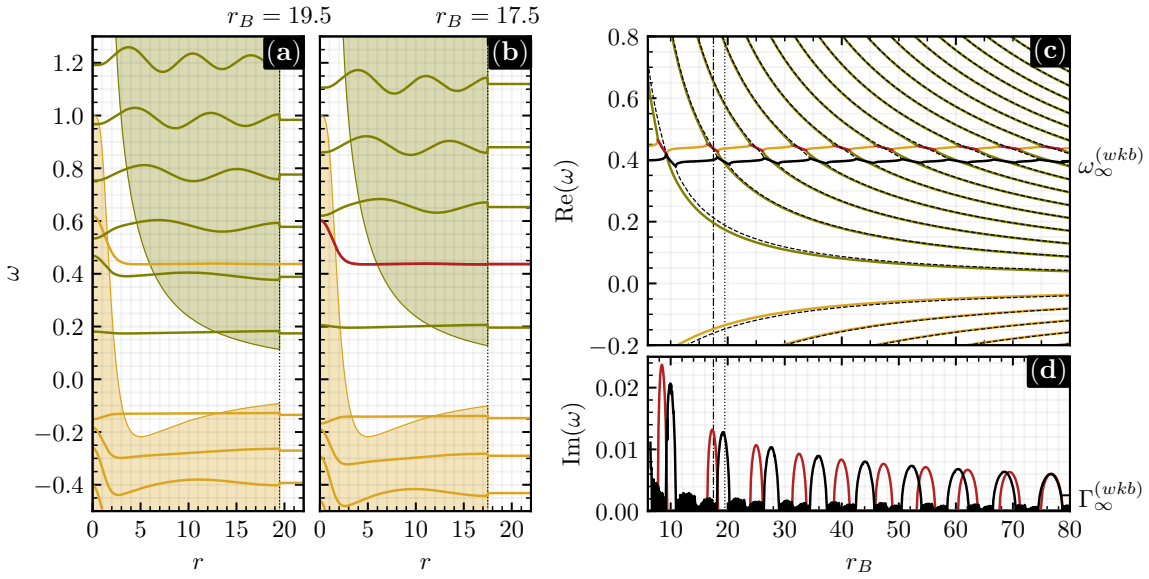

Figure 2.4 (BdG Eigenmodes) Panels **(a)** and **(b)**: The oscillation frequencies ω and mode functions for different eigenmodes of the BdG equation (2.57) for $m = \ell = 2$ and two different sizes $r_B = 19.5$ (stable) and $r_B = 17.5$ (unstable) for panels (a) and (b) respectively. The density fluctuations $\sqrt{\rho_0}\delta\rho = u_+ + u_-$ are drawn around the real frequencies $\mathrm{Re}(\omega)$ and colored according to their norm: green modes have positive norm ($\mathcal{N} > 0$), orange modes have negative norm ($\mathcal{N} < 0$), and red modes have zero norm ($\mathcal{N} = 0$). As in figure 2.2, the orange regions ($\omega < \omega_-$) have negative norm and the green regions ($\omega > \omega_+$) have positive norm. The vertical dotted lines signal the location of the potential boundary r_B. Panels **(c)** and **(d)**: The eigenvalues ω of the BdG equation (2.57) as functions of the trap size r_B. Panel (c) shows the real part $\mathrm{Re}(\omega)$ of the frequencies, and panel (d) shows the imaginary part $\mathrm{Im}(\omega)$. The BdG frequencies are colored as in panels (a) and (b), i.e. red for $\mathcal{N} = 0$ (unstable), orange for $\mathcal{N} < 0$ (cavity) and green for $\mathcal{N} > 0$ (phonon). Vertical black lines highlights the values for r_B chosen in panel (a) (dot-dashed) and (b) (dotted). The solutions to the WKB resonance condition is shown as a black curve, solid for the cavity mode, and dashed for the phonon modes.

Examples of the density eigenfunctions $\sqrt{\rho_0}\delta\rho = u_+ + u_-$ are shown in panels (a) and (b) of figure 2.4 for trap sizes $r_B = 17.5$ and $r_B = 19.5$ respectively. Here, mode amplitudes in the region $\omega < \omega_-$ (orange) contibutes negatively to the norm, whereas amplitudes in the region $\omega > \omega_+$ (green) contributes positively.

Note that when cavity modes and phonon modes are decoupled, i.e. when only one of the cotangents in (2.56) are close to zero, but not both, then the system is stable. If the roots of the cotangents are close, however, then the system does not decouple into two cavities, i.e. $\cos(S_{01}) \simeq 0$ $\cos(S_{2B} + \pi/4) \simeq 0$. Instead, the two cavities interact and, as in the open system, complex frequencies are needed to solve the resonance condition. The resulting unstable modes are a combination of cavity and phonon waves, which permits the outer, positive energy phonon part to grow as it excites the negative energy wave in the cavity. In turn, the cavity mode is further amplified by transmitting positive energy out of the cavity. This perpetual amplification is what causes the instability. Note, however, that the exponential growth is permitted only because the unstable mode is formed in such a way that it has zero norm. In fact, the BdG equation (2.12) can be shown to respect the identity $\mathrm{Im}(\omega)\mathcal{N} = 0$, meaning that any unstable mode with $\mathrm{Im}(\omega) \neq 0$ must have zero norm ($\mathcal{N} = 0$).

To estimate the complex frequencies, we consider, as in the open system, an expansion to linear order of all three phases $S \to S + i\Gamma\partial_\omega S$ for $S = S_{01}, \tilde{S}_{12}, S_{2B}$. The resulting expression for Γ only takes non-zero values when the phase integrals fail to satisfy the resonance condition (2.56) for real frequencies. The frequencies that solve the WKB resonance condition (2.56), are shown (black curve) in panels (c) and (d) of Figure 2.4. For comparison, the BdG eigenmodes are shown in the same panels as red (zero norm), orange (negative norm) and green (positive norm) curves. These curves are found by diagonalising a discrete formulation, using 5-point centered finite difference stencils for radial derivatives, of the BdG (2.12) decomposed in frequency, i.e.

$$\widehat{L}|\tilde{\psi}\rangle = \omega|\tilde{\psi}\rangle \quad \text{for} \quad |\tilde{\psi}\rangle \equiv (\tilde{u}_+, \tilde{u}_-)^T \tag{2.57}$$

with the corresponding eigenfunctions $|\tilde{\psi}\rangle = (\tilde{u}_+, \tilde{u}_-)^T$ where $u_\pm \equiv \tilde{u}_\pm e^{-i\omega t}$ giving the solid lines shown in panels 2.4(a) and 2.4(b). The figure depicts a system which is dynamically unstable for some trap sizes r_B, but not for others. As the system size r_B increases, the density of states increases, and every time a phonon mode in the outer cavity $r \in [r_2, r_B]$ crosses the cavity mode, an unstable region appears.

It should be noted that when (2.57) is solved by $\tilde{u}_\pm$ with a complex frequency $\omega_c = \omega + i\Gamma$ then, since $\widehat{L}$ is a real operator, the conjugate $\tilde{u}^*_\pm$ with $\omega^*_c = \omega - i\Gamma$ is also a solution. That is, the unstable growing mode, hereby labelled $\tilde{u}^\uparrow_\pm$ is always part of a conjugate pair, with the other solution, hereby labelled $\tilde{u}^\downarrow_\pm \equiv (\tilde{u}^\uparrow_\pm)^*$, being an exponentially decaying solution. This mode describes the unstable process in reverse, i.e. the transmission of negative energies from the cavity to the phonon.

From figure 2.4(c), we see that the BdG phonon spectrum (green curves) is very well predicted by WKB (dashed black curves), which can be approximated by $\cot(S_{2B} + \pi/4) \simeq 0$. This is as

expected since the background is slowly changing here. The cavity mode predicted by WKB (black solid line), however, exhibits a clear mismatch with the BdG solutions (solid orange and red). This mismatch, which can be associated with an inaccurate determination of the cavity phase S_{01}, is also expected due to the quickly varying density in this region. Despite this, the WKB resonances still captures all the essential features of the instability and, in particular, the crossing of negative norm modes with positivive norm modes. Therefore, the resonance condition (2.56) may still be used to interpret the mechanism for the instability.

It has been noted in the literature (see e.g. [61, 140]) that for an asymptotically large system, the unstable frequency should asymptote to that of the open system IV.1. This is not at all obvious as imposing open and closed boundary conditions are two completely different procedures. Fortunately, our WKB boundary condition (2.56), which can be rewritten

$$e^{2iS_{01}} + X = -ie^{2iS_{2B}}(Xe^{2iS_{01}} + 1), \qquad \text{for } X \equiv \frac{4 + e^{-2\tilde{S}_{12}}}{4 - e^{-2\tilde{S}_{12}}}, \tag{2.58}$$

can help elucidate this behaviour. For small growth rates, i.e. $|\Gamma| \ll |\omega|$, we may, as before, approximate $S_{2B}(\omega_c) \simeq S_{2B}(\omega) + i\Gamma\tau_B$ with $\tau_B \equiv \partial_\omega S_{2B}$. It follows that the right side of (2.58) becomes exponentially suppressed by τ_B, which can be interpreted as the time it takes the mode to propagate from r_2 to r_B. Since, $\tau_B \sim S_{2B}$, we must have $\tau_B \to \infty$ as $r_B \to \infty$, so that the resonance condition (2.58) for the closed system asymptotes to that of the open system, i.e. equation (2.48). In other words, by the time a once escaping wave has returned from the reflecting boundary, the waves near the core will have grown so much that the returning wave is negligible in comparison.

V. The Evolution of the Doubly Quantised Vortex

We now look more deeply into case of a doubly-wound ($\ell = 2$) vortex in a finite-size bucket trap of the form (2.51) by comparing with numerical simulations of the full non-linear dynamics of the GPE (2.4). In the linear theory presented in the previous sections, there is no mechanism that prevents the unbounded growth of the unstable mode. However, when nonlinearities are taken into account, one expects the unstable mode to eventually become non-perturbative and modify the background on top of which the fluctuations evolve. In particular, the multiply wound phase singularity at the centre should split into singly wound singularities. Armed with the formalism for the origin of the instability discussed in the previous sections, we may now investigate the dynamical decay of the doubly quantised vortex. In so doing, we will identify a peculiar recurrent behaviour of the instability at late times.

V.1. Numerical Simulation

The numerical simulations of the vortex instability proceeds in three main steps: (1) Preparing the initial state, (2) time evolution by numerically solving the GPE (2.4) and (3) extraction of the modes

and tracking the phase singularities.

Because the instability of the multiply wound vortex (2.8) is caused by the exponential amplification of a certain fluctuation about the ground state, it needs to be seeded. In a realistic setup, such an initial seed for the unstable mode is automatically provided by the ever-present background noise. Instead of a full statistical treatment, we shall consider the idealised case of an initial state consisting of a stationary background density ρ perturbed only by the unstable mode, and weakly at that.

Following the procedure discussed in section IV.2 results in a discretized approximation for the stationary background density $\rho(r_i)$ at linearly spaced radial locations r_i, as well as the approximate solutions for the mode functions $|U\rangle = (u_+, u_-)^T$, corresponding to the unstable solution, i.e. the eigenvector whose eigenvalue has the largest (positive) growth rate Γ (see equation (2.49)). The initial state Ψ_0 may then be constructed from

$$\Psi_0(r,\theta) = e^{i\ell\theta}\left[\sqrt{\rho(r)} + \varepsilon u_+(r)e^{im\theta} + \varepsilon u_-^*(r)e^{-im\theta}\right], \tag{2.59}$$

where $\varepsilon \ll 1$ is the initial amplitude of the unstable mode. Note that to prevent artefacts in the numerics, both the density ρ and the BdG eigenmodes $|U\rangle$ are computed, including the density depression at the boundary, and with a Dirichlet boundary condition at the numerical boundary $r \gg r_B$.

The initial phase $\Phi(r,\theta,t_0)$ and density $\rho(r,\theta,t_0)$ for an initial condition of the form (2.59) is shown in panels (a) and (c) of figure 2.5 in the case of an $\ell = 2$ vortex with an unstable $m = 2$ mode with amplitude $\varepsilon = 10^{-3}$.

The state $\Psi_0(\mathbf{r})$ from (2.59) is taken as the initial state for the evolution given by the full GPE (2.4). The cartesian plane is discretized into a linearly spaced mesh of $N \times N$ pixels of separation Δl in each dimension, where Δl is taken to be well below 1 to resolve the vortex core accurately. The time evolution is performed in discrete steps of duration Δt using a pseudo-spectral time-splitting scheme (see B.2.3 for details). Here, a Fourier spectral basis is chosen so that the exponentiated Laplacian ∇^2 from the kinetic term in (2.4) can be efficiently evaluated. For this to work, the numerical boundaries $x, y = \pm\frac{1}{2}(N-1)\Delta l$ of the simulated domain need to extend well outside the potential boundary r_B, so that the wavefunction Ψ is sufficiently periodic. Using this procedure, $8192000 = 16384 \times 500$ timesteps are performed, out of which every 500^{th} frame is stored for post-processing*. The result is a collection $\Psi(x_i, y_j, t_k) \in \mathbb{C}^{N^2 \times N_t}$ of $N^2 \times N_t$ complex numbers.

To extract the evolution of the fluctuations, the cartesian mesh $\Psi(x_i, y_j, t_k)$ is first interpolated onto a polar mesh $\Psi(r_i, \theta_j, t_k)$, followed by a fourier transform in the azimuthal direction. The result is $\psi_{m_j}(r_i, t_k)$, where $m_j \in \mathbb{Z}$ is the j^{th} azimuthal component. Since the relaxed vortex is rotationally symmetric, any population of non-zero azimuthal numbers m automatically gives the fluctuations from (2.13), i.e. $\psi_{m_j}(r_i, t_k) \simeq u_+^{(m_j)}$ with $\psi^*_{-m_j}(r_i, t_k) \simeq u_-^{(m_j)}$ for $m_j \neq 0$.

*The number of data points varies with each simulation.

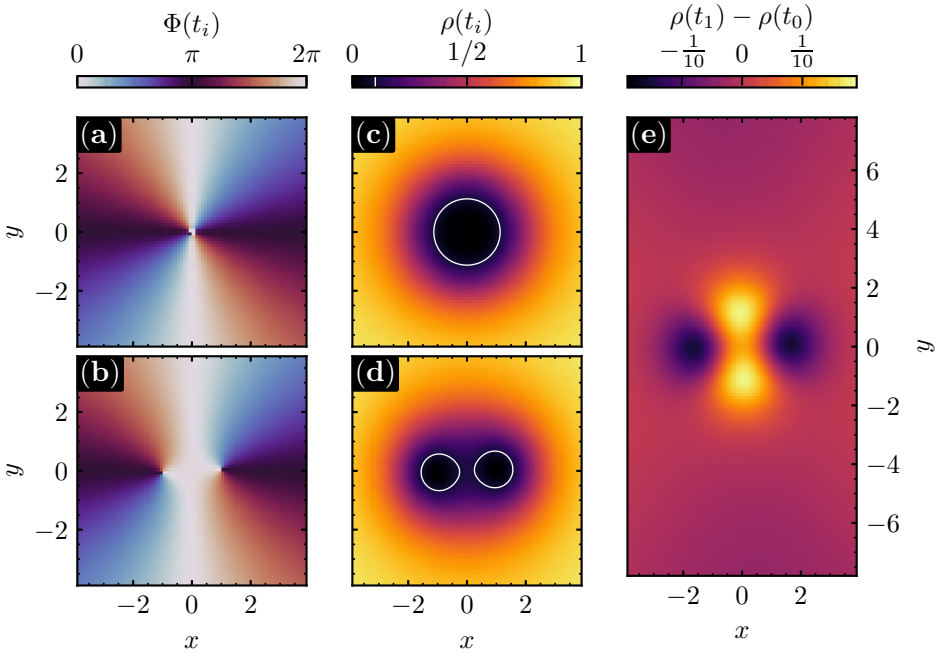

Figure 2.5 (Simulated vortex decay) Numerical simulation of an initial $\ell = 2$ vortex in a trap of size $r_B = 25$ as it decays into two separate $\ell = 1$ phase singularities caused by an unstable $m = 2$ mode of initial amplitude $\varepsilon = 10^{-3}$. Panels **(a)** and **(b)** display the phase Φ of the wavefunction Ψ at times $t_0 = 0$ and $t_1 = 763$ respectively, and panels **(c)** and **(d)** show the density ρ at the same times. In panel **(e)**, the difference $\rho(t_1) - \rho(t_0)$ in density between the two times is exhibited.

As described in appendix B.2.3, the wavefunction ψ is solved with the chemical potential for a uniform condensate factored out, i.e. if $\tilde{\Psi}$ is the actual wavefunction in (2.4), then the solver gives (in units) $\Psi(x_i, y_j, t_k) = \tilde{\Psi}(x_i, y_j, t_k)e^{i\mu t/\hbar}$ for $\mu = g\rho_c$ defined as in (2.2). A correction $\delta\mu$ to the chemical potential (see e.g. (2.2)) $\mu = 1$, which has been approximated by its uniform value up to this point, is estimated by computing the slope in the phase of the $m = 0$ component with time. Although small (typically of the order $\mathcal{O}(\delta\mu/\mu) \sim 10^{-6}$), this correction offers increased accuracy in determining the frequencies. The result is a readjustment of all units in accordance with (2.2), i.e. $\Delta l \mapsto \Delta l/\sqrt{1+\delta\mu}$, $\Delta t \mapsto \Delta t/(1+\delta\mu)$, $r_B \mapsto r_B/\sqrt{1+\delta\mu}$, and, most importantly, $\psi_{m_j}(r_i, t_k) \mapsto \psi_{m_j}(r_i, t_k)\sqrt{1+\delta\mu}e^{-i\delta\mu t_k}$.

We shall now consider three simulations of the GPE, all with potential boundary r_B within the third instability region in figure 2.4(d). One simulation is at the most unstable trap size, i.e. $r_B = 25$ (see figure 2.5), and the two others are equidistant in r_B on either side with $r_B = 25 \pm 0.7$. At early times, the system exhibits a clear exponential growth of the $\psi_{m=2}$ mode. For each simulation, the frequency $\omega_c = \omega + i\Gamma$ of this unstable mode can be extracted from $\psi_2(r_0, t)$ at a fixed radius r_0 in

two steps. First, the growth rate Γ is found from a linear regression of $\ln|\psi_2|$ over the time window that minimizes the error. Second, the real part of the frequency can be found either by locating the dominant peak in the temporal Fourier spectrum of ψ_2, or by a linear fit of the phase-unwrapped $\mathrm{Im}(\ln\psi_2)$. Both approaches give consistent results, and are, as can be appreciated in panels (c) and (d) of figure 2.6, in agreement with the BdG eigenfrequencies computed in IV.2. In other words, the superradiant instability does indeed occur, as predicted, in the fully nonlinear theory.

V.2. Late Stage Modulations

Having confirmed the presence of the unstable modes, we now investigate how it is that these exponentially growing modes lead to the splitting of the doubly quantised vortex into two singly quantised vortices. To avoid confusion, we shall refer to the singly quantised vortices as phase singularities, or proto-vortices, during the early stage of the splitting. This is because at early times the two phase singularities are confined within the same density depression, whereas individual quantised vortices are typically thought of as occupying separate regions of density depression.

Curiously, when simulations of the GPE are left running for a long time, a recurrent behaviour becomes evident. Eventually, the exponential growth of the unstable mode becomes non-perturbative and stops. Instead of remaining large, however, the mode enters a period of exponential decay. Sometime later, the exponential decay seizes, and the exponentially growing mode re-emerges. This behaviour is shown in figure 2.6(a) for the three different trap sizes, $r_B = 24.3$ (red), $r_B = 25$ (blue) and $r_B = 25.7$ (green). Note that at early times ($t \lesssim 1000$), the red and green lines overlap since their growth rates are the same.

From numerically tracing the trajectories of the phase singularities (see appendix B.2.4 for details), the separation distance $s(t)$ between the two singularities is obtained. The result is shown in panel 2.6(b), for the three different system sizes. Here, it is clear that the vortex separation follows the same recurrent pattern as the $m = 2$ mode, albeit on a linear scale. Note, with reference to figure 2.5, that the vortices remain in the shared depressed-density region throughout this entire process, and the density perturbation $|\delta\psi|$ is at most approximately $1/5$ (see figure 2.5(e)). That is, the density perturbations remain perturbative so that the full non-linear dynamics is well approximated by linearised dynamics.

To understand what is going on, first recall that the unstable frequencies in figure 2.4 involve two modes: A growing mode $u_\pm^\uparrow$ and mode $u_\pm^\downarrow \equiv (u_\pm^\uparrow)^*$ that decays at the same rate as $u_\pm^\uparrow$ grows. Initially, the dynamically unstable mode $u_\pm^\uparrow$ grows exponentially, providing an increasingly large $m = 2$ density anisotropy in the vortex core. Eventually, the multiply wound vortex splits into two phase singularities that are guided by the (two) troughs of the unstable mode. As the unstable mode grows further, the two phase singularities spiral outwards, until the singularities are separated by about two healing lengths ($s \simeq 2$). Then, surprisingly, the vortices start to spiral inwards, and the amplitude of the $m = 2$ mode enters a period of exponential decay. During this period, ψ_2 matches the waveform and the decay rate (see decreasing log-linear trends in figure 2.6(a)) of the

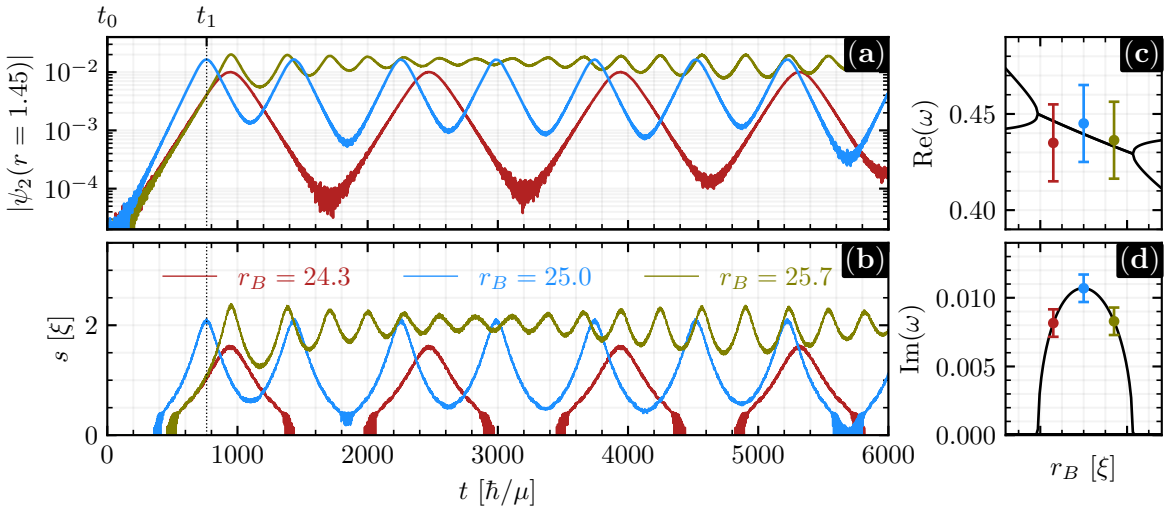

Figure 2.6 (Vortex Modulations) Panel **(a)**: The amplitude of the $m = 2$ mode ψ_2 as a function of time t for three different simulations. The simulations are initialised with the same initial state (2.59) with $\varepsilon = 10^{-3}$, but with different trap sizes $r_B = 24.3$ (red), $r_B = 25$ (blue) and $r_B = 25.7$ (green). The two times $t_0 = 0$ and $t_1 = 763$, for which the $r_B = 25$ simulation is depicted in figure 2.5 are highlighted as vertical dotted black lines. Panel **(b)**: The vortex separation s for the same three simulations as a function of time t. It is clear that the vortex separation exhibits the same kind of recurrent behaviour as the unstable/stable mode. Panels **(c)** and **(d)** exhibits the real and imaginary parts of the frequency obtained from the numerical simulations for the three sizes $r_B = 24.3$ (red), $r_B = 25$ (blue) and $r_B = 25.7$ (green) in comparison with the BdG eigenmodes from 2.4 (black).

decaying mode $u_{\pm}^{\downarrow}$. At some point, which varies greatly across system sizes, the exponential decay stops, the vortices start spiralling outward again, and the $m = 2$ mode adopts the waveform and exponential growth rate of the $u_{\pm}^{\downarrow}$ mode.

The essential physics responsible for the transition from the growing mode $u_{\pm}^{(2)\uparrow}$ to the decaying mode $u_{\pm}^{(2)\downarrow}$ is captured by the following qualitative argument. As the phase singularities are pulled apart by the growing mode, it becomes increasingly hard for them to keep up with the troughs of the unstable mode that guide them, resulting in a reduction of the frequency ω_{cav} of the cavity mode. Eventually, this shift in frequency decouples the cavity from the phonon mode outside, which brings the unstable growth to an end. Since the phonon mode now oscillates at a frequency $\omega_{\mathrm{ph}} > \omega_{\mathrm{cav}}$ faster than the cavity mode, there is a growing phase shift between the two, and when this phaseshift reaches π, i.e. $\int(\omega_{\mathrm{ph}} - \omega_{\mathrm{cav}})dt = \pi$, the waveforms are just right to form a decaying mode $u_{\pm}^{(2)\downarrow}$. At this point, the modes recombine, and the system enters the period of decay. Note, however, that for this argument to hold, the density of phonon states must be sufficiently low for the cavity mode not to couple to any other, lower frequency phonon modes. Therefore, the modulations observed in figure 2.6 are not expected to occur in very large systems, where the density of states approaches the continuum limit.

One might assume that this behaviour is highly sensitive to initial conditions and that any small perturbation might be enough to destroy the effect. While this seems to be the case when the vortex is placed far from the centre of the trap [114], we have found that modulations persist even when the vortex is displaced from the origin a few healing lengths.

V.3. Exchange of energy

The modulations observed in figure 2.6 can be associated with an exchange of energy between phonons and the phase singularities. When phase singularities are separated, incompressible vortex energy is released into the fluctuations as compressible energy. When the phase singularities spiral inwards, the compressible energy is re-absorbed into incompressible energy.

To understand this process, consider a decomposition of the energy

$$E = \int d^2\mathbf{x} \left(\underbrace{\tfrac{1}{2}|\nabla\sqrt{\rho}|^2}_{\mathcal{E}_{\mathrm{qnt}}} + \underbrace{\tfrac{1}{2}|\sqrt{\rho}\nabla\Phi|^2}_{\mathcal{E}_{\mathrm{kin}}} + \underbrace{U\rho}_{\mathcal{E}_{\mathrm{pot}}} + \underbrace{\frac{1}{2}\rho^2}_{\mathcal{E}_{\mathrm{int}}} \right) \tag{2.60}$$

associated with a state $\Psi = \sqrt{\rho}e^{i\Phi}$ in the GPE, into quantum energy $\mathcal{E}_{\mathrm{qnt}}$, classical kinetic energy $\mathcal{E}_{\mathrm{kin}}$, trap energy $\mathcal{E}_{\mathrm{pot}}$, and interaction energy $\mathcal{E}_{\mathrm{int}}$ (see e.g. [111])*. As first proposed by Nore et al.

*Note that the total kinetic energy density is $\mathcal{E}_{\mathrm{qnt}} + \mathcal{E}_{\mathrm{kin}}$, i.e. the sum of quantum energy and classical kinetic energy.

[141, 142], the kinetic energy $\mathcal{E}_{\rm kin}$ may be further split into a compressible part $\mathcal{E}^{\rm c}_{\rm kin}$ and an incompressible part $\mathcal{E}^{\rm i}_{\rm kin}$. Defining $\mathbf{u} \equiv \sqrt{\rho}\nabla\Phi$ and introducing Helmholtz decomposition $\mathbf{u} \equiv \mathbf{u}_{\rm c} + \mathbf{u}_{\rm i}$ with $\nabla \cdot \mathbf{u}_{\rm i} = 0$, the two components of the kinetic energy take the form $\mathcal{E}^{\rm i}_{\rm kin} = \frac{1}{2}|\mathbf{u}_{\rm i}|^2$ and $\mathcal{E}^{\rm c}_{\rm kin} = \frac{1}{2}|\mathbf{u}_{\rm c}|^2$. Numerically, such a decomposition may be obtained from the realisation that if $\mathcal{F}$ denotes a spatial Fourier transform and $\mathbf{k}$ the corresponding wave vector, then $\mathbf{u}_{\rm c}$ is nothing but the projection of $\mathbf{u}$ onto $\mathbf{k}$, i.e.

$$\mathbf{u}_{\rm c} = \mathcal{F}^{-1}\left[\frac{\mathbf{k}(\mathbf{k}\cdot\mathcal{F}\mathbf{u})}{|\mathbf{k}|^2}\right], \tag{2.61}$$

where, in the absence of a mean flow, the $\mathbf{k} = 0$ component may be ignored to avoid zero-division. The resulting time evolution of the total compressible, and incompressible energies $E^{\rm i}_{\rm kin} \equiv \int d^2\mathbf{x}\mathcal{E}^{\rm i}_{\rm kin}$ and $E^{\rm c}_{\rm kin} \equiv \int d^2\mathbf{x}\mathcal{E}^{\rm c}_{\rm kin}$ are shown in panels (a) and (b) of Figure 2.7 respectively.

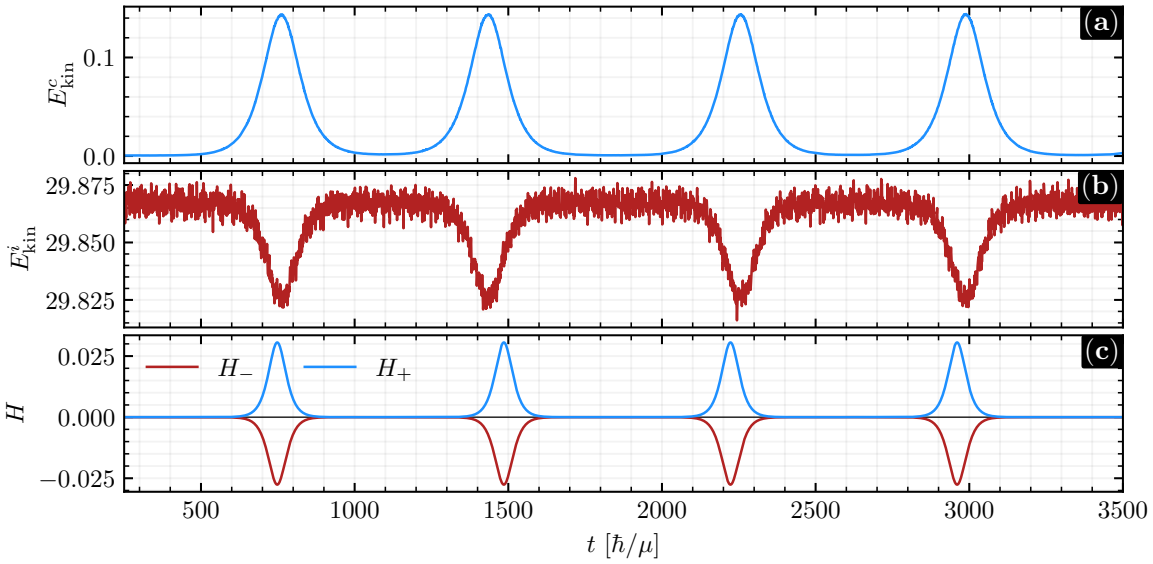

Figure 2.7 (Oscillator model) Panels **(a)** and **(b)**: The numerically computed compressible (a) $E^{\rm c}_{\rm kin}$ and incompressible (b) $E^{\rm i}_{\rm kin}$ energy as a function of time. The synchronisation of the increase/decrease with vortex separation, and the correlation between the two energies, supports the interpretation that the modulations are driven by an exchange of energy between the phase singularities and the phonons. Panel **(c)**: The positive H_+ (blue) and negative H_- (red line) energies of the simple oscillator model for $\Omega = 1$, $\sigma = 1/50$, $g = 1/20$, $c_+ = 0$, and $c_- = 2$. This captures the behaviour of phase-singularities and phonons.

The two energies $E^{\rm c}_{\rm kin}$ and $E^{\rm i}_{\rm kin}$ are clearly correlated, where a temporary increase in compressible (phonon) energy $E^{\rm c}_{\rm kin}$ is accompanied with a decrease in incompressible (vortex) energy $E^{\rm i}_{\rm kin}$. Moreover, the peaks in the compressible energy are exactly where the vortex separation and mode

amplitude reach a maximum (see figure 2.6). This supports the interpretation that the modulations in vortex separation are indeed driven by an exchange of energy between vortex configuration and phonons.

The conservation of the total energy (2.60) within the system is found to be upheld to relative variations on the order of 10^{-7}. Consequently, the temporal noise plotted in the incompressible energies $E^i_{kin}(t)$, as depicted in panel (b) of Figure 2.7, is attributed solely to the exchange or ambiguity of energy distribution among the distinct channels.

To understand the mechanism responsible for the perpetual exchange of energies, consider the following simplified model. Let the vortex movement and phonon modes be represented by two dimensional oscillators at locations $Z_\pm = x_\pm + iy_\pm$ and with (non-interacting) frequencies $\omega_\pm = (\Omega^2 \pm \sigma \pm c_\pm |Z_\pm|^2)^{\frac{1}{2}}$. Here Ω is the central frequency, with σ being the frequency separation of the two modes, and $c_\pm$ controls the nonlinearity, i.e. the amplitude dependence of the frequency. Since the cavity mode has negative energy, we take the excitations of the vortex oscillator $(-)$ to involve negative energies. Introducing the interaction energy $g\mathrm{Re}[Z_+ Z_-^*]$ with $g > 0$, the system is determined by the following Lagrangian

$$\begin{aligned} L =& \tfrac{1}{2}|\dot{Z}_+|^2 - V_+ - \tfrac{1}{2}|\dot{Z}_-|^2 + V_- - g\mathrm{Re}[Z_+ Z_-^*], \\ V_\pm \equiv& \tfrac{1}{2}(\Omega^2 \pm \sigma)|Z_\pm|^2 - \tfrac{1}{4}c_\pm |Z_\pm|^4, \end{aligned} \tag{2.62}$$

where the two oscillators have energies $H_\pm = \pm(\frac{1}{2}|\dot{Z}_\pm|^2 + V_\pm)$. Let us choose $c_+ = 0$ for the phonon, since the frequency is mostly determined by the system size, and $c_- = \varepsilon > 0$ for the vortices, mimicking the decrease in the orbital frequency of the two phase singularities as they spread apart. Note that in the absence of a non-linearity, i.e. $\varepsilon = 0$, $Z_\pm$ oscillates as a linear superposition of the frequencies $\omega_\pm = (\Omega^2 \pm \sqrt{\sigma^2 - g^2})^{\frac{1}{2}}$. In particular, if the frequency separation is lower than the interaction strength, i.e. $|\sigma| < |g|$, then the system becomes unstable as the frequency takes complex values. This is conceptually similar to the appearance of unstable regions in figure 2.4, when the frequency of a $\mathcal{N} > 0$ mode couples close to a $\mathcal{N} < 0$ mode.

In the regime $\Omega \gg \sigma, g, \varepsilon|Z_-|^2$, the Lagrangian (2.62) takes the form

$$L \simeq \Omega \mathrm{Im}\left(z_+ \dot{z}_+^* - z_- \dot{z}_-^*\right) - \tfrac{1}{2}\sigma(|z_+|^2 + |z_-|^2) - \tfrac{1}{4}\varepsilon|z_-|^4 - g\mathrm{Re}[z_+ z_-^*], \tag{2.63}$$

for $z_\pm \equiv Z_\pm e^{i\Omega t}$, where invariance under (common) phase rotations $z_\pm \mapsto z_\pm e^{i\alpha}$ results in a conserved charge $\mathcal{Q} \equiv |z_+|^2 - |z_-|^2$, in direct analogy with the norm (2.15). For exponentially growing/decaying solutions conservation requires $\mathcal{Q} = 0$, meaning that the two oscillators must have equal radii, i.e. $|z_\pm| = R$. Introducing $z_\pm = Re^{i\varphi_\pm}$ with phase difference $\vartheta \equiv \varphi_+ - \varphi_-$, whose equations of motion can be conveniently written as

$$\ddot{\vartheta} + \partial_\vartheta W = 0, \qquad W(\vartheta) = -\frac{(\sigma + g\cos\vartheta)^2}{2\Omega^2}, \qquad R(t) = R_0 \exp\left(\frac{1}{2\Omega}\int g \sin\vartheta(t)\,dt\right). \tag{2.64}$$

This is the equation for the movement of a particle on the circle under the influence of an effective potential $W(\vartheta)$. When the equations are unstable, i.e. $|\sigma| < |g|$, this potential W has two maxima at $\vartheta_\pm = \pi \pm \arccos(\sigma/g)$. From the form of $R(t)$, we see that these unstable equilibria correspond to exponentially growing (ϑ_-) and decaying (ϑ_+) solutions. In particular, if the system is initialised near the exponentially growing point ϑ_- with $\dot{\vartheta} \neq 0$, then ϑ will keep rolling over both peaks. The result is a perpetual switching between exponential growth and decay, as ϑ passes ϑ_- and ϑ_+ respectively. This is precisely the kind of behaviour we observe in figure 2.6. The corresponding energies $H_\pm$ for a numerical solution of (2.64) are shown in figure 2.7(c) in comparison with the compressible/incompressible energy.

Note, however, that this model, unlike our system, contains only two interacting modes. One consequence of this is that modulations in the model are perfectly periodic, which is not the case in the full system 2.6. If other modes are taken into account, i.e. other ω and m modes around the vortex, then energy can be transferred between these channels and we would expect the modulations to lose their exact periodicity.

V.4. Damped Condensates and Experimental Feasibility

Up to this point, we have considered an idealised system with a central $\ell = 2$ vortex in a rotationally symmetric trap, subject to the conservative evolution dictated by the GPE (2.4). In experimental realisations, however, there is always some source of dissipation, either of thermal origin or some other mechanism.

In this section, we briefly consider the evolution of the multiply wound vortex under the influence of weak dissipation, which can be included in the GPE (2.4) by introducing a phenomenological damping parameter $\gamma > 0$ [143, 144], resulting the in dissipative Gross-Pitaevskii Equation (dGPE)

$$i\partial_t \Psi = (1 - i\gamma)\left[-\frac{1}{2}\nabla^2 + U(\mathbf{x}) - 1 + |\Psi|^2\right]\Psi, \tag{2.65}$$

where the additional term -1 appears from the chemical potential having been factored out of Ψ. The inclusion of γ results in energy slowly being removed from the system, forcing the phase singularities to spiral apart and eventually develop separated core regions. That is, γ forces the two singularities to decay completely, resulting in the damped evolution of two well-separated vortices, which is given by the (dissipative) point-vortex dynamics (see e.g. [145, 146]). The point-vortex model, which is valid for well-separated vortices (see appendix C), predicts an orbital frequency $\Omega_{pv} = 2/s^2$ of the two vortices, where s is the vortex separation.

On the other hand, when the vortices are very close, the two cores overlap and the system is better seen as a small fluctuation (cavity mode) on an $\ell = 2$ background. The consequence is that the orbit of the phase-singularities is guided by the troughs of the unstable $m = 2$ mode such that for small s, the orbital frequency is $\Omega_0 = \frac{1}{2}\omega_{inst}$, where ω_{inst} is the frequency of the unstable mode. Here, the factor $1/2$ comes from the fact that the orbital frequency Ω of the troughs/crests

of an azimuthal mode $m \neq 0$ with frequency ω is $\Omega = \omega/m$. Instead of the divergent behaviour of the point vortex model as $s \to 0$, we must therefore have a modification Ω_{pve} of the point-vortex orbital frequency Ω_{pv} such that $\Omega_{pve} \to \Omega_0$ as $s \to 0$, and $\Omega_{pve} \simeq \Omega_{pv}$ for $s \gg 1$. Since $\Omega_{pv} \to \infty$ as $s \to 0$, a natural candidate for this extended model is $\Omega_{pve}^{-2} = \Omega_{pv}^{-2} + \Omega_0^{-2}$.

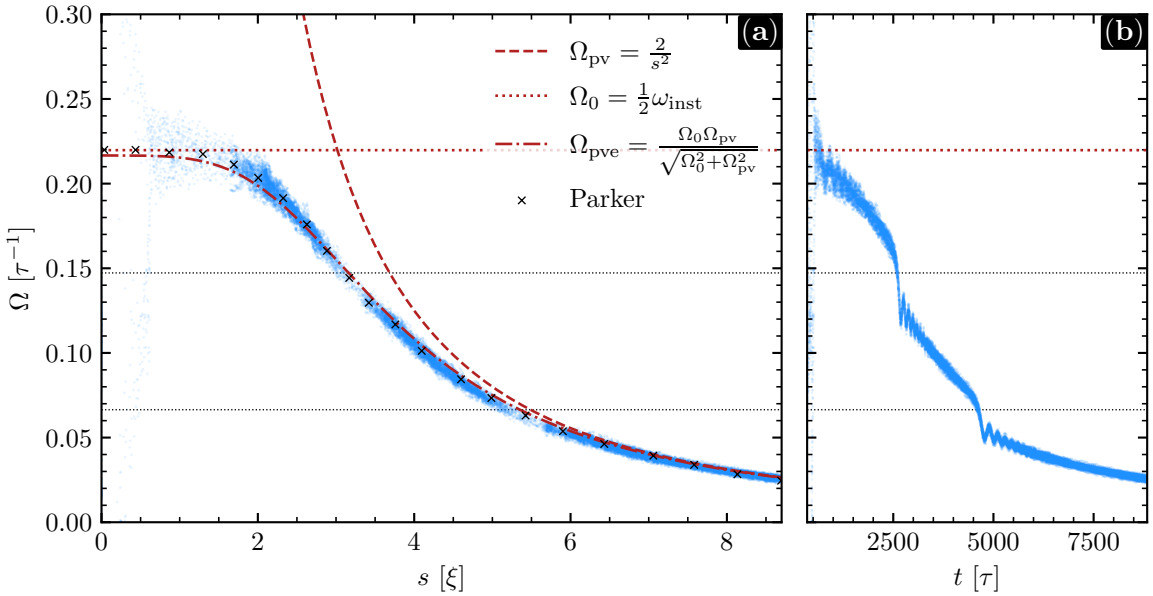

Figure 2.8 (Damped Pair Oscillation) The numerically computed (blue points) orbital frequencies Ω of the two singularities as a function of the distance s between them and the time t is shown in panels **(a)** and **(b)** respectively. At small s, the singularities are guided by the troughs of the unstable cavity mode, with orbital frequency Ω_0 (horizontal dotted line). At large s, the singularities are true vortices which obey the point vortex dynamics Ω_{pv} (dashed red line). The proposed ansatz Ω_{pve} (dot-dashed red line) captures the intermediate behaviour. For comparison, the data is compared with that of Parker [147] (black crosses) who also considered the dynamics of vortices in proximity. The frequencies $\frac{1}{2}\omega_{BdG}$ for other lower frequency phonon modes ω_{BdG} (see figure 2.4) are shown as black dotted lines.

Figure 2.8 exhibits the instantaneous orbital frequencies Ω of the tracked phase-singularities (blue dots) in a simulation of the dGPE (2.65) with size $r_B = 25$ and damping $\gamma = 1 \times 10^{-3}$. The extracted frequencies Ω are shown as a function of vortex separation s and time t in panels (a) and (b) respectively, and are compared with the models Ω_0 (dotted red line), Ω_{ve} (dashed red line) and the proposed extension Ω_{pve} (dot-dashed red line). The prediction obtained by Parker [147], who also considered the dynamics of close vortices, is included for comparison (black crosses).

We see that when the separation s is of the order $s \gtrsim 5$, the orbital frequency of the vortices is well captured by the point-vortex model Ω_{pv}. In the other limit, the orbital frequency clearly

levels off and is bounded from above, by the frequency Ω_0 of the troughs of the unstable mode. Moreover, the purely phenomenological ansatz Ω_{pve} for the extended model, captures the entire process surprisingly well.

As the frequency Ω of the cavity mode decreases, it couples to lower-frequency phonon modes, shown as horizontal black dotted lines in figure 2.8. The result is a faster separation of the vortices aided by the instability arising from the coupling of the two modes. Instead of a perpetual state of modulations, the effective dissipation damps out the modulations, eventually allowing the vortices to continue their spiralling apart. This behaviour can be observed in panel (b) of figure 2.8, where the orbital frequency Ω swiftly passes each phonon frequency (black dotted line), resulting in a brief period of damped oscillations of Ω due to the modulations. Clearly, a sufficiently low density of states is necessary for this phenomenon to occur. That is, one does not expect this behaviour to persist in large systems.

For modulations to be observable in dissipative systems, it is necessary that the damping γ is small. If the time taken by the singularities to spiral in and out, i.e. the period of modulation, is larger than the characteristic time scale set by the dissipation γ, modulations are not expected to be observable. From the results presented in this section, however, it is clear that modulations do persist in dissipative systems. It is therefore expected that this phenomenon will have observable consequences in real experiments where dissipation is important.

VI. Conlusion

In this chapter, we have investigated the dynamical instability of multiply quantised vortices in two-dimensional BECs using three different methods: BdG stability analysis, WKB approximation and nonlinear numerical simulations of the GPE. The WKB method allowed us to identify the origin of the instability as a superradiant bound state local to the vortex core. From a careful consideration of the boundary conditions involved, we then showed that in closed systems, the instability is suppressed for certain trap sizes, which is well known in the literature [61, 114]. However, the WKB method permitted an intuitive explanation for why the limiting behaviour of the closed system is that of the open system. In particular, we noted that the unstable system sizes arise from a resonant coupling between a negative energy mode in the vortex cavity with a positive energy mode outside the vortex (phonon), and that it is the transmission of energy out of the cavity that causes the exponential growth of the unstable mode.

When investigating the doubly-wound vortex ($\ell = 2$) through numerical simulations, we confirmed that the instability predicted from the linear theory is present in the fully nonlinear regime. However, we observed that the initial MQV does not always decay into a pair of SQVs, but that for small systems the phase singularities can form a new state where at late times, the non-linearity in the GPE pushes the singularities back together, resulting in a repeated modulation of their separation. We saw that this behaviour is caused by a detuning of the cavity mode, forcing the unstable mode to

decouple and, soon thereafter, re-connect as an exponentially decaying mode. This behaviour can be associated with an exchange of compressible and incompressible energy, for which we saw that a simplified model of two interacting oscillators captured the essential details of what was going on.

One consequence of this is that the system never enters the regime where one can apply Point-Vortex dynamics [146] since this requires the vortex separation to be much larger than the healing length.

Finally, when considering dissipative systems, we saw that vortices do separate, as expected, but that the modulations persist. From observing the complete decay of the MQV, we saw that the orbital frequency of a co-rotating vortex pair is bounded from above by half the frequency of the unstable mode, i.e. $\Omega \leqslant \frac{1}{2}\omega_{\mathrm{inst}}$. This can be understood from the observation that when the vortices are close together, their orbit is guided by the troughs of the unstable mode. Curiously, in the dissipative evolution, we observed that the two vortices experience multiple periods of modulation, one for each phonon frequency passed by twice the orbital frequency.

It would be interesting to see if this behaviour extends to more general scenarios e.g. clusters of vortices. Then, the resulting dynamics may be more complicated since there are more instabilities in the system, e.g. for $\ell = 3$ there are instabilities in the $\mathfrak{m} = 2, 3, 4$ modes, we also expect these modulations to persist for higher winding numbers.

Chapter 3

The Sound-ring Radiation from Relaxing Vortex Clusters

The following is an account of efforts that resulted in the publication titled *Sound-ring radiation of expanding vortex clusters* [105] by S. Erne, S. Patrick, C. F. Barenghi, and S. Weinfurtner and myself. There is considerable overlap with the previous chapter, but at heart, this project is very different. Whereas the situation investigated in chapter 2 was relatively simple – a rotationally symmetric, central multiply charged vortex – here we investigate the more complex situation of the dissipative relaxation expansion of a compact vortex cluster. Therefore, this chapter is of a more phenomenological nature than the preceding chapter.

I. Introduction

When waves interact with rapidly rotating objects, exotic phenomena may occur. A prominent example is that of rotational superradiance, which was the motivation for the previous chapter 2. Another example is compact gravitational objects exhibiting circular orbits of light, referred to as light-rings [148]. When light-rings are present, the gravitational field significantly affects the propagation of nearby waves. In particular, light-rings are intimately connected to the late-stage relaxation of perturbed black holes, often referred to as black hole ringdown, e.g. following merger events like those recently observed by the LIGO collaboration [149, 150]. If waves are located at the light-ring, they may slowly leak out in a process often, but not always [151], linked with emission of so-called Quasi-Normal Modes (QNMs) [152], which are damped linear oscillations of the system as it strives towards equilibrium. This kind of QNMs is qualitatively different from those encountered when considering vortex instabilities in section IV.1 of chapter 2, in that they describe a relaxation process rather than exponential growth. Like the mechanism for rotational superradiance, however, the usefulness of the light-ring is not in any way limited to gravitational systems. For example, one can identify effective light-rings for the interfacial waves of rapidly rotating fluids, opening the possibility for non-destructive flow measurements [118]. In 2020, the free surface of a draining bathtub flow was reported to oscillate at the effective light-ring frequency [66].

This chapter demonstrates that effective light rings, which we shall call sound-rings, exist around vortex clusters in Bose-Einstein condensates (BECs). Being macroscopic quantum fluids,

BECs exhibit a wide range of unusual phenomena such as the wave-propagation of heat (second sound) [110], perfectly inviscid flow, and discretization of circulation [111]. Therefore it is not clear that the concept of a light-ring, or rather sound-ring in this case, persists in these systems. As we shall see, the notion of sound-rings permits an approximate prediction for the spectrum of sound emitted from relaxing clusters of quantum vortices. In particular, we find that the sound-ring can extend well outside the cluster and that the sound is emitted at frequencies independent of the vortex configuration in the core. The result is the emergence of the sound-ring as a large-scale feature created by the seemingly chaotic movement of vortices in the core.

The findings presented in this chapter are of relevance to the problem of wave-vortex interaction. Most past studies have considered either the properties of a single vortex (e.g. the bending vortex lines [153]) or a large number of vortices of the same circulation (e.g. Tkachenko modes [154]) or different circulations (e.g. turbulence [155, 156]). The vortex clusters examined here represent interesting physics at intermediate scales, which is challenging to approach in the thermodynamic limit.

II. Modelling

We consider a system similar to chapter 2 for large winding numbers ℓ, but with two important differences. Firstly, our focus shall be on the period after which the multiply wound vortex has decayed into a cluster of singly wound vortices. Secondly, we now consider the evolution under stochastic influence, as e.g. provided by thermal variations. That is, we study the non-linear relaxation of a rotating disc-shaped BEC from the perspective of the two-dimensional (2D) Stochastic Gross-Pitaevskii Equation (SGPE) [143, 157],

$$i\hbar\partial_t\Psi = (1-i\gamma)\left[-\frac{\hbar^2}{2M}\nabla^2 + U(\mathbf{r}) - \mu + g|\Psi|^2\right]\Psi + \eta(\mathbf{r},t). \tag{3.1}$$

Here, as in chapter 2, t is time, $\mathbf{r} = (r,\theta)$ is the spatial location in polar coordinates, M is the boson mass, g is the effective 2D interaction constant, μ is the chemical potential, and $U(\mathbf{r})$ is an external trapping potential. The SGPE is a finite-temperature extension of the GPE (see (2.4) in chapter 2) describing the evolution of a coherent state Ψ under the influence of damping $\gamma \geqslant 0$ and stochastic noise $\eta(\mathbf{r},t)$. The inclusion of damping γ (see dGPE (2.65)) represents dissipative particle transfer from the coherent, low energy modes, whose dynamics is given by the state Ψ, to the higher energy modes in the thermal reservoir. The noise η represents the random nature of incoherent scattering in the system. Over long times, the SGPE depicts a condensate in equilibrium with temperature T. The equilibrium, being the state at which dissipation is kept at bay by fluctuations, is given by the fluctuation-dissipation relation

$$\langle \eta^*(\mathbf{r},t)\eta(\mathbf{r}',t')\rangle = 2\hbar\gamma k_B T\delta(\mathbf{r}-\mathbf{r}')\delta(t-t'), \tag{3.2}$$

which imposes a temperature-dependent relation between the variance of the noise η and the damping γ. In what follows, we shall consider a homogeneous damping $\gamma = \text{const}$ and complex Gaussian white noise η with zero mean. However, the exact values for the damping and noise are not expected to affect the result as long as they are both sufficiently small.

Employing the same adimensionalisation procedure as in chapter 2 (see discussion following equation (2.2)), i.e. $\mathbf{x} \mapsto \xi\mathbf{x}$, $t \mapsto \tau t$, $\Psi \mapsto \sqrt{\rho_c}\Psi$, $U \mapsto \mu U$ and $\eta \mapsto \sqrt{\rho_0}\mu\eta$, the SGPE takes the form

$$i\partial_t\Psi = (1 - i\gamma)\left[-\frac{1}{2}\nabla^2 + U - 1 + |\Psi|^2\right]\Psi + \sigma_\eta\eta, \tag{3.3}$$

where the standard deviation σ_η of η has been factored out, such that η denotes an adimensional Wigner process of unit variance [158]. Note that σ_η generally depends on the microphysical parameters of the system. Using this adimensional formulation, the results from analysing equation (3.3) remain applicable for a wide range of parameters. In the following, the numeric values for the damping and noise are chosen to be $\gamma = 2.5 \cdot 10^{-3}$ and $\sigma_\eta^2 \equiv \langle|\eta|^2\rangle = 2.5 \cdot 10^{-3}$. However, the results presented are largely insensitive to the specific values of γ and σ_η provided they are both small, i.e. $\gamma, \sigma_\eta \ll 1$.

As in equation (2.51) of chapter 2, we choose the potential $U(\mathbf{r})$ to be a rotationally symmetric bucket trap of the form

$$U(r) = \frac{U_0}{1 + (U_0 - 1)e^{a(r_B - r)}}, \tag{3.4}$$

but now with a steeper wall $a = 2$ and $U_0 = 10$, and for a fixed location $r_B = 121.5$ of the outer boundary*.

Imagine a rotationally symmetric, multiply wound vortex of charge $\ell = 29$ located in the centre of the aforementioned trap (3.4). Initially, the stochastic noise η provides seeds for all resonant modes in the system. In particular, as seen in the previous chapter 2, azimuthal modes m satisfying $0 < m < 2|\ell|$ may exhibit instabilities. For highly charged vortices ($|\ell| \gg 1$), this produces a complicated competition of exponentially growing modes in the different m channels. Eventually, this instability results in the decay of the central, multiply wound phase singularity into a densely packed cluster of interacting singly wound phase singularities. In the presence of small but non-zero damping $\gamma > 0$, this dense cluster of phase singularities must slowly expand as the system evolves towards a lower energy state. In the process, the rapid movement of the phase singularities inside the core will effectively stir the condensate, resulting in the radiation of density fluctuations, or sound waves, emitted from the cluster. As the system relaxes further, the core will keep expanding, and eventually, the cluster will have developed sufficiently for the vortices to be well separated. At that point, the vortices should effectively decouple from the sound field as they adopt the dynamics of the (dissipative) point-vortex model [146].

*The motivation behind this choice is that the processes investigated in this chapter are significantly more violent, so the outer wall should be taller to prevent shock waves from escaping. The size r_B is taken to be as large as possible, but still small enough for the simulations and analysis to be computationally feasible at the required spatial resolution.

III. The coarse-grained Background

Before we investigate the fluctuations of the sound-field, we must specify a background for the fluctuations. To start, we consider the SGPE (3.1) in terms of hydrodynamic variables $\Psi \equiv \sqrt{\rho}e^{i\phi}$,

$$\partial_t\phi + \rho + U - 1 - \frac{\nabla^2\sqrt{\rho}}{2\sqrt{\rho}} + \frac{1}{2}(\nabla\phi)^2 = \frac{\gamma}{2\rho}\nabla\cdot(\rho\nabla\phi) - \frac{\sigma_\eta}{\sqrt{\rho}}\mathrm{Re}(\eta) \tag{3.5a}$$

$$\partial_t\rho + \nabla\cdot(\rho\nabla\phi) = -2\gamma\rho\left[\rho + U - 1 - \frac{\nabla^2\sqrt{\rho}}{2\sqrt{\rho}} + \frac{1}{2}(\nabla\phi)^2\right] + 2\sqrt{\rho}\sigma_\eta\mathrm{Im}(\eta) \tag{3.5b}$$

Note that this is a natural extension of the hydrodynamic formulation (2.6) of the GPE (2.4), where, in the undamped ($\gamma \to 0$) limit, (3.5a) and (3.5b) take the form of a Bernoulli-like equation and a Continuity equation respectively*.

Although the vortex core contains a large number of moving vortices, all rapidly moving and surrounded by a density depression, we consider an approximate background ρ_0, ϕ_0 given by the coarse-grained, time-averaged quantities. From this perspective, the movement of the individual vortices is averaged out, and one is left with a slowly evolving smooth background. More precisely, for a gently sloped $|\nabla\rho_0| \ll \rho_0$ and slowly evolving $\partial_t\rho_0, \partial_t\phi_0 \ll 1$ free ($U \approx 0$) condensate, the deterministic ($\sigma_\eta \to 0$) hydrodynamic formulation (3.5) requires

$$\rho_0 = 1 - \frac{1}{2}\mathbf{v}^2 \tag{3.6a}$$

$$\nabla\cdot\mathbf{v} = 0, \tag{3.6b}$$

with $\mathbf{v} \equiv \nabla\phi_0$. Hence, the density ρ_0 is reduced by the kinetic energy nearby (3.6a), and the velocity is incompressible (3.6b). Note that perturbative consistency requires $\nabla\mathbf{v}^2 \ll 2\rho_0$.

III.1. The azimuthally averaged velocity field of a vortex cluster

Imagine a collection of N vortices, or phase singularities, with windings $\{\ell_k\} \subset \mathbb{Z}\setminus\{0\}$ located at $\{(x_k, y_k)\} \subset \mathbb{R}^2$. If these vortices originate in the decay of a single vortex of winding ℓ, then one must have $\ell = \sum_k \ell_k$. However, in the decay's early and most violent period, vortex-anti-vortex pairs may be produced, and some vortices may only have decayed partially, i.e. $|\ell_k| > 1$ for some k. That is, we cannot assume $|\ell| = N$, as this holds only for $\ell_k = \mathrm{sgn}(\ell)$ for all k. Assuming the boundary of the system to be far away, the velocity potential ϕ_0 can be approximated as a sum of individual windings

$$\phi_0 = \sum_{k=1}^{N} \ell_k \arctan\left(\frac{y - y_k}{x - x_k}\right). \tag{3.7}$$

*Note that a substitution $\eta \mapsto \eta e^{i\phi}$ has been made in equations (3.5). This is due to the complex gaussian noise being unaffected by a phase rotation.

The velocity field $\mathbf{v} \equiv \nabla\phi_0$ can be conveniently written in terms of complex coordinates $z \equiv x + iy$ as

$$v^* = \sum_{k=1}^{N} \frac{i\ell_k}{z_k - z} \tag{3.8}$$

where $z_k \equiv x_k + iy_k$ is the location of the k'th vortex and $*$ denotes the complex conjugate. As discussed in appendix C, insertion of the phase-ansatz (3.7) into the hydrodynamic GPE leads to the well-known point-vortex model [146], assuming the vortices to be well separated.

For computational convenience, consider a configuration in which the centre of vorticity is located at the origin, i.e. $\sum_n \ell_n z_n = 0$. Now, we may imagine an ordering $0 \leqslant |z_1| \leqslant \ldots |z_M| \leqslant |z| \leqslant |z_{M+1}| \ldots \leqslant |z_N|$ of the vortices in terms of their radial distance $|z_n|$ from the origin, where we shall refer to the largest radius as the cluster size R, i.e. $R \equiv |z_N|$. Note that the index M, being the label of the outermost vortex inside a radius $r = |z|$, generally depends on the radius r. In polar coordinates $z \equiv re^{i\theta}$, the azimuthal average $\langle\cdot\rangle_\theta$ may now be evaluated using the residue theorem

$$\langle ve^{-i\theta}\rangle_\theta^* = \sum_{k=1}^{N} \frac{\ell_k}{2\pi r} \oint_{|z|=r} \frac{dz}{z_k - z} = -\frac{i\ell_M(r)}{r} \text{ for } \ell_M(r) \equiv \sum_{k=1}^{M(r)} \ell_k, \tag{3.9}$$

where $\ell_M(r)$ is the net winding inside a disc of radius r. Recognising the unit vector $\mathbf{e}_\theta \equiv ie^{i\theta}$ in complex coordinates, the azimuthally averaged velocity field can be written as a purely rotating flow

$$\langle \mathbf{v}\rangle_\theta = \frac{\ell_M}{r}\mathbf{e}_\theta \text{ for } \ell_M \equiv \sum_{k=1}^{M} \ell_k \,. \tag{3.10}$$

That is, the azimuthally averaged velocity field of a vortex cluster at a radius r is indistinguishable from that of a central, multiply wound vortex with a charge equal to that of the net charge of the cluster inside r. Indeed, outside the cluster, i.e. $r > R$, this statement holds to second order in perturbation theory, with perturbation parameter $|z_N| \ll |z|$, even without the need for an azimuthal average. That is

$$\mathbf{v} = \frac{\ell}{r}\mathbf{e}_\theta + \mathcal{O}\left(\left|\frac{z_N}{z}\right|^2\right) \text{ for } \ell \equiv \sum_{k=1}^{N} \ell_k. \tag{3.11}$$

The coarse-grained velocity field referred to in equations (3.6) can further be estimated by considering the continuum limit of (3.11) and (3.10). That is, we think of the discrete sum $\ell_M(r)$ as emerging from the integration of a discrete vortex density distribution $\rho_\ell(z) \equiv \sum_k \ell_k \delta(z - z_k)$, where δ is the Dirac delta distribution, on a disc of radius r. Since vortices have the tendency to spread evenly, see e.g. the minimum-energy Rankine vortex of [159], we take the continuum limit of ρ_ℓ to be that of a uniform distribution ($\rho_\ell = \text{const}$) inside R. The result can be written

$$\ell_M \simeq \ell\left(\frac{r}{r_c}\right)^2 \text{ where } r_c \equiv \begin{cases} R \text{ for } r \leqslant R \\ r \text{ for } r > R \end{cases}. \tag{3.12}$$

Inserting this into (3.11), or equivalently (3.10), the coarse-grained velocity field $\mathbf{v}$ adopts the form of a drain-free Rankine vortex $\mathbf{v} = v_\theta(r)\mathbf{e}_\theta$ often encountered in classical fluid mechanics [160], i.e.

$$v_\theta = \frac{\ell}{r}\left(\frac{r}{r_c}\right)^2 = \begin{cases} \ell r/R^2 & \text{for } r \leqslant R \\ \ell/r & \text{for } r > R \end{cases} . \tag{3.13}$$

This velocity field suggests that inside the cluster, i.e. $r < R$, the vortices rotate, with orbital frequency $\Omega_c \equiv \ell/R^2$, as if the cluster was a solid body. Note that this corresponds to Feynman's rule [111, 161], stating that a rotating bucket of quantum fluid constitutes a uniform lattice of vortices to mimic solid body rotation. On the outside ($r > R$), even without the need for coarse-graining, one recovers the irrotational flow indistinguishable from a central, multiply wound vortex. That is, the velocity field outside R is independent of the details inside the core as it depends only on the net winding ℓ of the cluster.

Whereas we may find comfort in the fact that the Rankine velocity (3.13) is consistent with the incompressibility condition (3.6b), it is not applicable for determining the background density $\rho_0 = 1 - \frac{1}{2}\mathbf{v}^2$ from (3.6a) inside the core. This is because the azimuthal average of the velocity magnitude $\langle|\mathbf{v}|^2\rangle_\theta$ is, in general, different from the magnitude of the azimuthally averaged velocity $|\langle\mathbf{v}\rangle_\theta|^2$. Note that the need for calculating this quantity separately arises because the azimuthally averaged velocity is no longer irrotational inside the core, for which the Bernoulli-like equation (3.5a) no longer holds. The following procedure is equivalent to including the integral of $\mathbf{v}\times(\nabla\times\mathbf{v})$ from r to ∞ in the Bernoulli equation, as is standard in classical fluid mechanics.

Going back to the expression (3.8) for the velocity field in terms of complex variables, we observe that

$$\begin{aligned} v^*v &= \sum_{m,n} \frac{\ell_n\ell_m}{(z_n - z)(z_m^* - z^*)} \\ &\simeq r^6 \sum_{m,n} \ell_n\ell_m \left[\frac{\mathbb{I}_{n\leqslant M}}{r^4} - \frac{\mathbb{I}_{n>M}}{(z_n z^*)^2}\right]\left[\frac{\mathbb{I}_{m\leqslant M}}{r^4} - \frac{\mathbb{I}_{m>M}}{(z_m^* z)^2}\right] \\ &= \left[\frac{\ell_M}{r} - \sum_{n>M}\frac{r^3\ell_n}{(z_n z^*)^2}\right]\left[\frac{\ell_M}{r} - \sum_{n>M}\frac{r^3\ell_n}{(z_n^* z)^2}\right] \\ &= \frac{\ell_M^2}{r^2} - 2\frac{\ell_M}{r^2}\sum_{n>M}\ell_n \mathrm{Re}\left(\frac{z^2}{z_n^2}\right) + r^2\sum_{n>M}\sum_{m>M}\frac{\ell_m\ell_n}{(z_n z_m^*)^2} , \end{aligned} \tag{3.14}$$

where $\mathbb{I}_C$ is the indicator function, which is 0 outside C, and 1 inside. Applying the azimuthal average $\langle\cdot\rangle_\theta$ results in the vanishing of all off-diagonal terms as well as the middle term, leaving only

$$\langle v^*v\rangle \simeq \frac{\ell_M^2}{r^2} + r^2\sum_{n>M}\sum_{m>M}\frac{\ell_m\ell_n}{(z_n z_m^*)^2} . \tag{3.15}$$

In the case of a uniform distribution of vortices on the disc $r < R$, only the diagonal terms $n = m$ in the sum contribute, resulting in

$$\langle |\mathbf{v}|^2 \rangle \simeq \left(\frac{\ell}{r_c}\right)^2 \left[2 - \left(\frac{r}{r_c}\right)^2\right] = \begin{cases} \ell^2 \left[2 - (r/R)^2\right]/R^2 & \text{for } r \leqslant R \\ \ell^2/r^2 & \text{for } r > R \end{cases}, \tag{3.16}$$

which, finally, enables us to invoke equation (3.6a) to obtain an expression for the background density

$$\rho_0(r) = 1 - \frac{1}{2}\left(\frac{\ell}{r_c}\right)^2 \left[2 - \left(\frac{r}{r_c}\right)^2\right] = \begin{cases} 1 + \frac{1}{2}(\ell/R)^2 (r/R)^2 - (\ell/R)^2 & \text{for } r \leqslant R, \\ 1 - \frac{1}{2}(\ell/r)^2 & \text{for } r > R \end{cases}. \tag{3.17}$$

Outside the cluster, we find the density, like the velocity field, to be indistinguishable from a multiply wound vortex, see e.g. the density asymptotics (2.11) from chapter 2. Inside the cluster, the density ρ_0 curves off to a constant value of $\rho_0(r \to 0) = 1 - (\ell/R)^2$ at the origin. Note, however, that for very dense clusters the background density (3.17) takes negative values. This nonsensical result can be traced back to a violation of the assumption of a gently sloped background $|\nabla \rho_0| \ll \rho_0$ needed to reach expression (3.6) for the background quantities. We could then go back to (3.1) and use that $\rho_0 \ll 1$ for which we would find, as in (2.11), that in this limit the density is better approximated by $\rho_0 \sim J_\ell^2(\sqrt{2}r)$. For our purposes, however, it will be sufficient to simply set $\rho_0 = 0$ where equation (3.17) predicts negative densitites.

As the cluster expands, i.e. $\partial_t R > 0$, the density (3.17) asymptotically approaches the density of a uniform condensate, i.e. $\lim_{R\to\infty} \rho_0 = 1$. Going backwards in time, however, we observe that as $R \to 0$, one eventually reaches a point at which $\rho_0 \approx 0$ everywhere inside some radius

$$r_m \equiv \frac{\ell}{\sqrt{2}} \tag{3.18}$$

outside R. Since, at this point, the density becomes practically independent of the vortex positions, this is hereby referred to as the minimal cluster size. When the cluster size R is smaller than r_m, the cluster behaves, for all practical purposes, as a single, multiply wound vortex of charge ℓ.

IV. Numerical Simulations

To investigate the details of the decaying, highly wound cluster in the context of the SGPE (3.1), we compare our models with numerical simulations. Because of the stochastic nature of the SGPE, we consider an ensemble $\{\Psi^{(a)}(t, \mathbf{x})\}_a$ of identically prepared simulations. The results presented in this chapter are computed using 51 such realisations, i.e. $a \in \{1, 2, \ldots, 51\}$.

Each realisation $\Psi^{(\alpha)}$ is initialised in the approximate initial state

$$\Psi_0^{(\alpha)}(t, x, y) = \Psi_0 \rho_0 e^{i\ell\theta(x,y)}, \tag{3.19}$$

where ρ_0 is the approximate density (3.17) and Ψ_0 is the numerically obtained ground state for a uniform condensate confined by the trap (3.4) found by long-time evolution of the SGPE (3.1) under the influence of strong damping γ. Note that the presence of damping leads to the relaxation of the vortex core to its exact form over a timescale that is short compared to the overall evolution of the system. Additionally, the transients due to the approximate form of ρ_0 are rotationally symmetric, and, due to the presence of noise and damping, are long gone by the time the vortex has started to decay, i.e. $R \geqslant r_m$.

Each realisation α is spatially discretized $\Psi^{(\alpha)}_{n,i,j} \equiv \Psi(t_n, x_i, y_j)^{(\alpha)}$ into a mesh of $N \equiv 1536$ equidistant points along each axis, i.e. $\{x_i\}, \{y_j\} \in \mathbb{R}^{1536}$, with resolution $\Delta x \equiv x_{i+1} - x_i = 1/5$. The time evolution is performed in discrete timesteps of Δt, i.e. $\Psi^{(\alpha)}_{n,i,j} \equiv \Psi^{(\alpha)}_{i,j}(t_n)$ with $\Delta t \equiv t_{n+1} - t_n$, using a second-order pseudospectral splitting scheme (see appendix B.2.3 for details). Here, the noise η, which is sampled from a central gaussian distribution with unit variance, is added after each timestep, i.e. $\Psi^{(\alpha)}_{n,i,j} \mapsto \Psi^{(\alpha)}_{n,i,j} + \sigma_\eta \eta \Delta t$. Although the stability of the solver generally depends on γ, we choose $\Delta t = 5 \times 10^{-3}$, which is safely within the stable region. From the time evolution, every 200'th frame, leading to a duration $\Delta t = 1$ between frames, is stored for later processing. Periodicity of Ψ, needed for the Fourier-spectral scheme, is enforced by letting the numerical boundaries $x, y \in \{\pm N\Delta x/2\}$ extend well beyond the trap size $r_B \simeq 605\Delta x$.

The density perturbations in a time-window $t \in [t_1, t_2]$ are extracted from a single numerical realisation $\Psi^{(\alpha)}(t, x, y)$ by interpolating the density $\rho^{(\alpha)} = |\Psi^{(\alpha)}|^2$ to polar coordinates and decomposing the result into Fourier amplitudes

$$\rho^{(\alpha)}_m(\omega, r) \equiv \int_{t_1}^{t_2} \int_0^{2\pi} \rho^{(\alpha)}(t, r, \theta) e^{-im\theta + i\omega t} d\theta dt. \tag{3.20}$$

using a two-dimensional fast-Fourier transform.

The typical evolution of the relaxing cluster for a single realisation $\Psi^{(\alpha)}_{n,i,j}$ is illustrated in figure 3.1. In panel (a), the x-coordinate of the vortex trajectories found using a numerical tracking algorithm detailed in appendix B.2.4, is shown as a function of time. Here, we recognise the minimal cluster radius r_m (3.18) (horizontal red dotted line), which is exceeded around times $t \approx 2000$. We identify three qualitatively different regimes, highlighted as coloured regions in red, yellow and blue. In the early stage, referred to as stage I, the vortices in the cluster are confined inside a rotationally symmetric low-density region effectively behaving as a slowly expanding multiply wound vortex. An example of the density ρ and phase ϕ in stage I is shown in panels (b) and (c) respectively. Eventually, the dynamic and energetic instability of the multiply wound vortex [61, 63, 111–113, 115] leads to the decay into a dense cluster of singly wound vortices as the cluster size exceeds r_m. During this period, the stochastic noise η seeds the instability (c.f. chapter 2) and provides the spatial

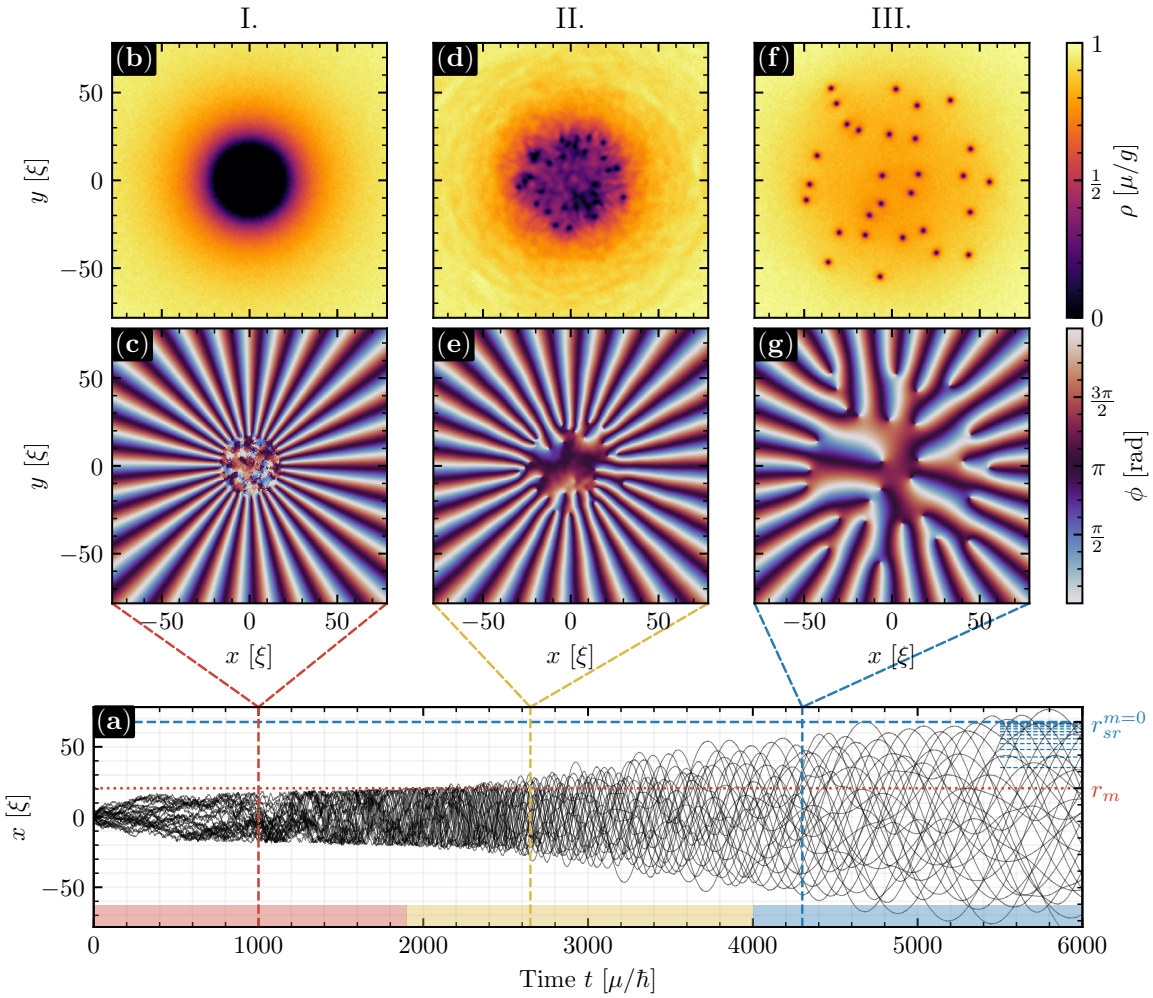

Figure 3.1 (Simulations of a decaying vortex cluster) Panel **(a)**: The x-coordinate of individual vortices over time in a single simulation. The minimal cluster size r_m (red dotted) and the largest sound-ring radius $r_{sr}(m = 0)$ (blue dashed) is shown, together with $r_{sr}(m)$ at $m \in \{-5, -15, -25, \ldots, -65\}$ (short blue dashed). The coloured regions illustrate the time-windows of three qualitatively different stages. Initial multi-wound vortex (I); multi-wound vortex has decayed in many singly wound vortices forming a disordered cluster (II); cluster has expanded (III). Panels (b,c,d,e,f,g): The density $\rho \equiv |\Psi|^2$ (top row) and phase $\phi \equiv \arg(\Psi)$ (bottom row) at times (see horizontal black dashed lines in panel (a)) $t = 1000$ (panels (b) and (c)), $t = 2650$ (panels (d) and (e)), and $t = 4300$ (panels (f) and (g)).

disorder needed to break the rotational symmetry of the system. Indeed, if the simulations were to be performed in the absence of noise, but with damping γ, the only non-rotationally symmetric feature able to provide the symmetry breaking of the initial cluster would be the four-fold discrete rotational symmetry $\mathbb{Z}_4$ originating in the discretisation cartesian plane. In that case, one would find the vortices to maintain a symmetric $\mathbb{Z}_4$ configuration until late times. Including noise, as e.g. provided by quantum or thermal fluctuations, alleviates this problem and leads to realistic vortex configurations. Note also, that whereas the total winding $\ell = 29$ is conserved through the entire simulation, the number of vortices varies greatly during in stage I due to the nucleation of vortex anti-vortex pairs in the low-density region.

As the outermost vortices attain a radius of r_m, density is allowed into the core, and the system transitions to stage II. In this stage, the vortices have started separating sufficiently for density to build up between them. The initial relaxation of this dense cluster of singly wound vortices is accompanied by the radiation of sound-waves from the core [162]. This unrest of the condensate outside the core can be seen in the example of the density and phase during stage II shown in panels (d) and (e) respectively. As we shall soon see, during stage II the individual vortices form time-independent sound-rings extending to radii $r_{sr}^{(m)}$ (see horizontal dashed blue lines in panel (a)) located outside the cluster.

Finally, when the cluster expands beyond the largest sound-ring $r_{sr}^{(0)}$, it enters stage III. In this stage, vortices are sufficiently isolated for their dynamics to effectively decouple from the sound-field.

V. The Evolving Background

Using the numerical simulations introduced in the preceding section, we shall now briefly discuss the adequacy of the coarse-grained background and its evolution in time.

During the late stage III, the slow expansion of large vortex clusters has been experimentally observed to obey a diffusive growth [145]

$$R(t) \simeq \frac{2}{3}\sqrt{\frac{\ell}{\pi}\left(\frac{1}{\rho_0} + 2\pi\ell\gamma(t - t_s)\right)}\,, \tag{3.21}$$

as predicted by a dissipative vortex fluid theory. In figure 3.2, we confirm that if we take the initial time t_s (vertical dotted blue line) to be the time at which the vortices exceed the minimal radius r_m (horizontal dashed red line), then the simulated vortex decay (black lines) is in good agreement with the diffusive expansion model (3.21) (blue solid line).

The sound-ring phenomenon is expected to influence the expansion of the cluster, but a detailed study of this is beyond the scope of this chapter and is instead left for future investigations. It should be noted, however, that if the damping γ is chosen too large, then waves become overcritically damped, and the cluster will expand too fast for the sound-ring phenomena to be relevant.

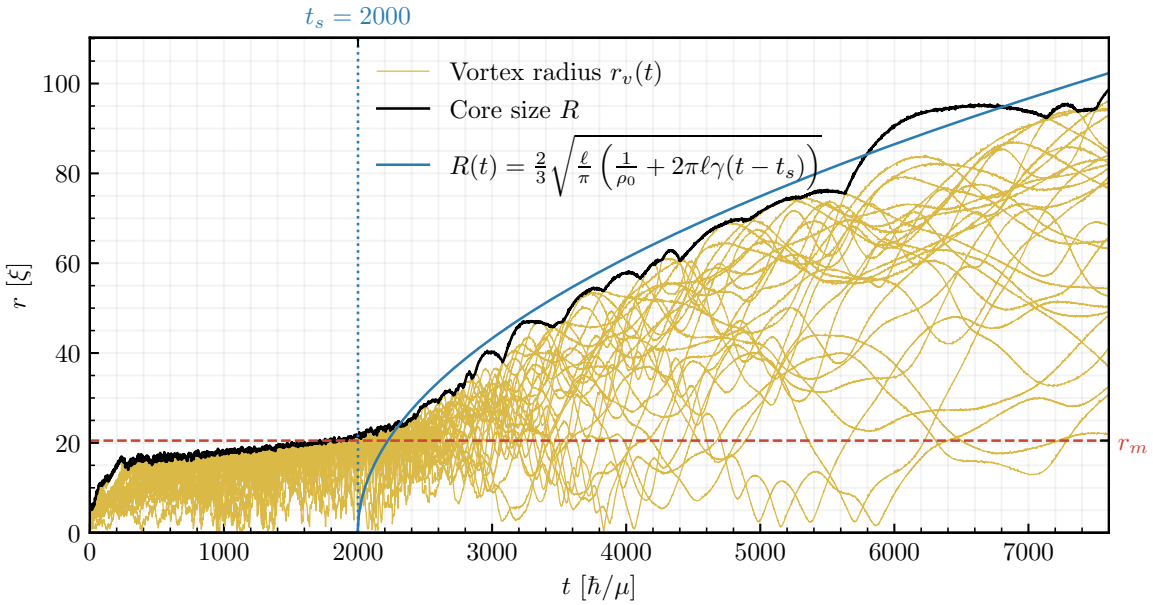

Figure 3.2 (Cluster expansion) The radius $r_v(t) \equiv \sqrt{x_v(t)^2 + y_v(t)^2}$ for each vortex (x_v, y_v) is shown as a function of time t as orange lines with the outermost vortex colored in black. For comparison, the expected evolution $R(t)$ from equation (3.21) is drawn (solid blue line) with initial time $t_s = 2000$ (vertical dotted blue line). The time t_s is chosen to be the time when the vortex cluster exceeds the minimal size r_m (horisontal red dashed line).

To investigate the adequacy of the coarse-grained background, the density $\rho \equiv |\Psi^{(a)}|^2$ and velocity field $\mathbf{v} = \mathrm{Im}\nabla \ln \Psi^{(a)}$ is computed at fixed times and over all realisations a. Transforming the result to polar coordinates, and computing azimuthal averages, results in radial profiles $\rho_0(r)$ and $\mathbf{v}(r)$ that can be compared to equations (3.17) and (3.13) respectively. The result, shown in figure 3.3 for the initial $t_0 = 2391$ and final frames $t_1 = 2902$ of the analysis window, is in excellent agreement with the numerical results outside the cluster. Inside the cluster, the velocity field $\mathbf{v}_\theta$ is well predicted by the Rankine profile 3.3 but slightly weighted towards the rim of the core at early times. That is, at early times, there is a slightly larger vortex population towards the rim of the core compared to the centre. The density ρ_0 in the core is, as anticipated, deviating from the model (3.17) in the low-density region.

VI. Fluctuations

We now shift our focus towards the fluctuations of the condensate around the coarse-grained background by introducing perturbations $\rho = \rho_0 + \delta\rho$ and $\phi = \phi_0 + \delta\phi$, with $\delta\rho \ll \rho_0$ and

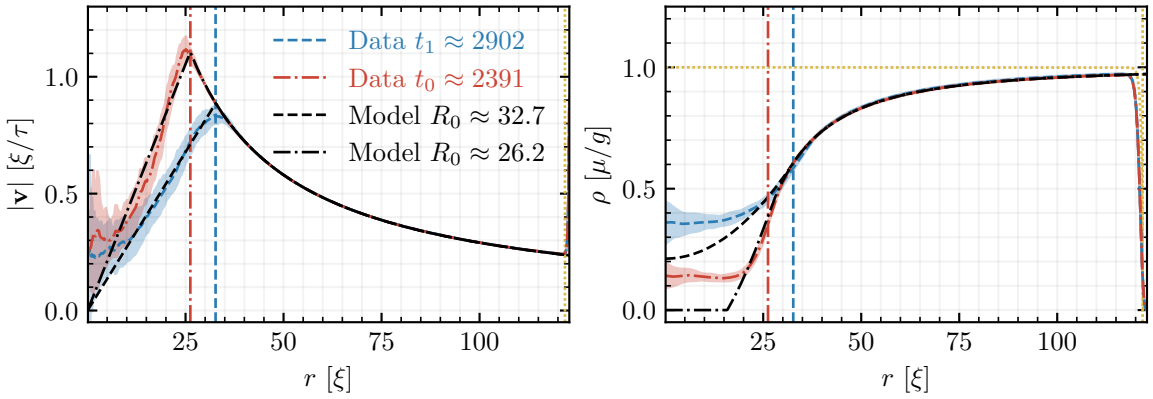

Figure 3.3 (Measured background) Panel **(a)**: Measured velocity fields $\mathbf{v} = \mathrm{Im}\nabla \ln \Psi$ at the initial (red dot-dashed) and final (blue dashed) timeframe as a function of radius r. The ensemble averaged azimuthal mean is plotted with the standard deviation over ensemble shaded. (b) Azimuthally averaged density profile $\rho^{(a)}(r)$ at the initial (red dot-dashed) and final (blue dashed) timeframe. The density is compared to the uniform Thomas-Fermi density $\rho \simeq 1 - U(r)$ (yellow dotted). In both panels, the model is fitted to find the core size R (vertical lines) and plotted as black lines on top.

$\delta\phi \ll \phi_0$, to equations (3.5). Assuming $\gamma, \sigma_\eta \ll 1$, i.e. weak stochastic influence, then the linearised equations take the form

$$(\partial_t + \mathbf{v}\cdot\nabla)\,\delta\rho = -\rho_0\nabla^2\delta\phi\,, \tag{3.22a}$$

$$(\partial_t + \mathbf{v}\cdot\nabla)\,\delta\phi = -\left(1 - \frac{\nabla^2}{4\rho_0}\right)\delta\rho\,. \tag{3.22b}$$

In the limit of long wavelengths, the excitations (3.22) are phonons described by a single Relativistic Klein-Gordon equation (see discussion around (1.1)) on an effective spacetime created by the background flow $\mathbf{v}$. This is the mathematical equivalence that forms the basis of analogue gravity [20]. Here, as in the previous chapter, we shall keep the dispersion.

As in chapter 2, further insight into the sound waves can be obtained using a WKB approximation in equations (3.22), i.e.

$$\begin{bmatrix}\delta\phi\\ \delta\rho\end{bmatrix} = \begin{bmatrix}\mathcal{A}(r)\\ \mathcal{B}(r)\end{bmatrix} e^{i\int k_r(r)\,dr + im\theta - i\omega t}. \tag{3.23}$$

with slowly varying amplitudes, $\partial_r k_r \ll k_r^2$, $\partial_r\mathcal{A} \ll k_r\mathcal{A}$ and similarly for $\mathcal{B}$. Here, the time-independence and rotational invariance of the background (3.13) and (3.17) has been used to decompose the fluctuations into separate frequency ω and azimuthal m components. Whereas this is a

justified assumption outside the core, at $r > R$, it is unwarranted inside the cluster. In each realisation, there are rapidly moving topological defects inside the cluster clearly violating both time independence and rotational invariance. In other words, the validity of the WKB expansion (3.23) inside the core thus depends on whether the specific wave in question is sensitive to the movement of the individual vortices. Intuitively, one would expect perturbations with wavelengths much larger than the characteristic vortex separation to feel only the coarse-grained background, whereas short wavelengths should scatter off the individual vortices.

Inserting the WKB ansatz (3.23) into (3.22), and keeping only leading order terms, results in the local dispersion relation

$$\omega_D^{\pm} = \frac{m v_\theta}{r} \pm \sqrt{\left(\rho_0 + \tfrac{1}{4}k^2\right) k^2}, \qquad k = \sqrt{k_r^2 + \frac{m^2}{r^2}}, \tag{3.24}$$

which is the well-known Bogoliubov dispersion [138, 139] first seen in equation (2.30) of chapter 2, but now with a Rankine velocity profile (3.13) as the background flow. As before, a wave which satisfies the equations of motion must lie either on the upper branch ($\omega = \omega_D^+$) or on the lower branch ($\omega = \omega_D^-$).

Using the WKB ansatz (3.23), a Hamiltonian system for the radial phase space (r, k_r) can be constructed by considering a trajectory of constant phase, i.e. variational stationarity of the WKB phase $\int (k_r dr - \omega_D(r, k_r) dt)$, where the dispersion relation $\omega_D^{\pm}$ appears as a functional Lagrange multiplier constraint [163] (see appendix A.3 for details).

The result is a Hamiltonian flow

$$\dot{r} = \partial_{k_r} \omega_D^{\pm}, \tag{3.25a}$$

$$\dot{k}_r = -\partial_r \omega_D^{\pm}, \tag{3.25b}$$

with the dispersion frequencies $\omega_D^{\pm}$ as the hamiltonian function. Together, equations (3.25) constitute a two Hamiltonian systems, one for ω_D^+ and one for ω_D^-, for each azimuthal number m. Note that by virtue of the symmetry $-\omega_D^{\pm}(m) = \omega_D^{\mp}(-m)$ in the dispersion relation (3.24), considering negative frequencies of $\omega_D^{\pm}$ for some counter-rotating mode $m < 0$, informs us of the behaviour of co-rotating modes $m > 0$.

For counter-rotating modes with positive frequencies, the Hamiltonian system (3.25) for the upper branch (ω_D^+) exhibits an unstable fixed point outside the core (see Figure 3.4). A mode at such a fixed point will stagnate radially at some radius $r_{sr}^{(m)}$ while maintaining its constant angular velocity $\dot{\theta} = \omega/m$. That is, the local phase fronts travel along a circular orbit.

From the approximate time independence of the background, it follows that modes must travel along phase-space trajectories of constant frequency. Therefore, the possible mode trajectories are entirely contained within a single level set $\omega_D^+ = \omega_0$ for some constant ω_0. Consequentially, the phase-space trajectories that intersect the fixed-point (solid black lines in figure 3.4), referred to as separatrices, can be associated with a specific frequency. We shall refer to this frequency as the

sound-ring frequency ω_{sr}, and the radial location of the associated fixed-point as the sound-ring radius $r_{sr}^{(m)}$.

The separatrices defined by the sound-ring frequency ω_{sr} introduce a natural separation of phase-space into three regions of qualitatively different behaviour. First, waves with a frequency larger than ω_{sr}, may propagate freely between the outer boundary r_B and the vortex core, see the orange region in figure 3.4. These modes are hereby referred to as A-modes (A for above). Waves with frequency lower than ω_{sr} may either disperse outward from the sound-ring radius $r > r_{sr}$ (blue region in figure 3.4), or they may be geometrically bound to the outer rim of the cluster (red region in figure 3.4). Waves that are unable to propagate inside the cluster (blue) will be referred to as O-modes (O for outside), whereas waves trapped around the edge of the core (red) will hereby be labelled I-modes (I for inner).

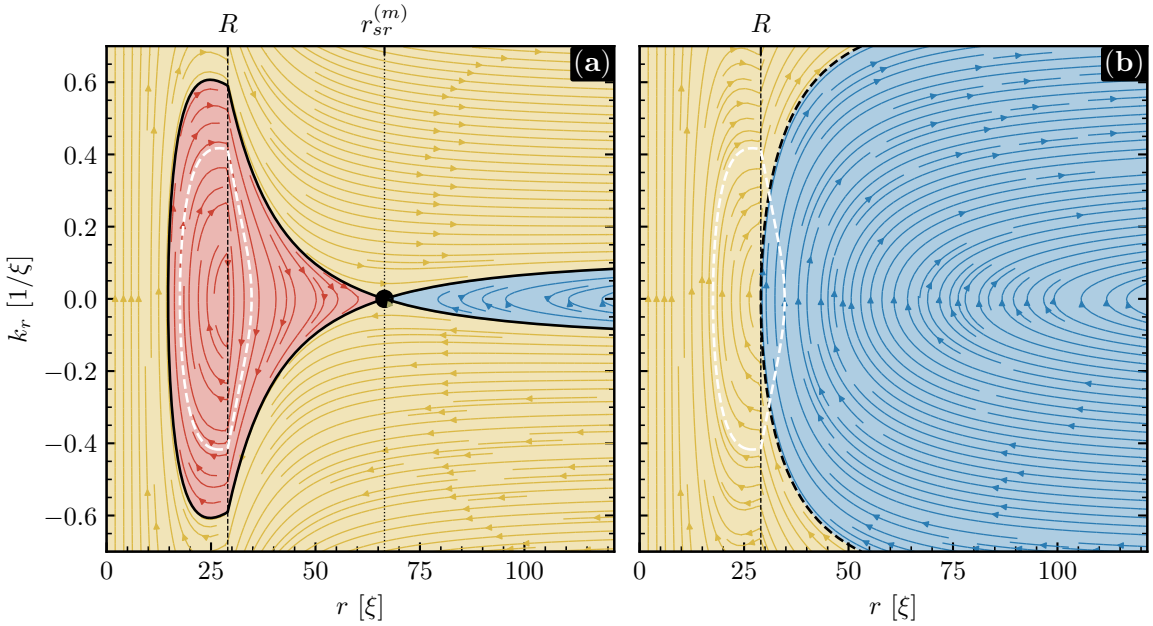

Figure 3.4 (Phase space of waves) The analytical predictions for the effective phase space ω_{D}^{+} of an $|\mathrm{m}| = 15$ mode in an $\ell = 29$ cluster with Rankine radius $\mathrm{R} = 29$ (vertical dashed line) where the arrows indicate the flow of time. Panel **(a)**: the counter-rotating $\mathrm{m} = -15$ phase-space is drawn, with a separatrix (solid black line) indicating the trajectories that intersect the fixed-point (black circle) located at the sound-ring radius r_{sr} (vertical dotted black line). The separatrix defines three regions: (1) A-modes, which can propagate between the cluster core and the outer boundary (orange region), (2) O-modes, which are confined outside the core (blue region), and (3) I-modes, that are trapped at the edge of the cluster (red). In the I-mode region, a white dashed line is drawn around the region inside which there are only negative frequencies. Panel **(b)**: the phase space for co-rotating modes $\mathrm{m} = 15$ is separated in two regions by the frequency with turnover radius at the rankine radius R (black dashed line). This defines two regions (1) waves that can communicate between the core and the boundary (red shaded region) and (2) waves that are confined outside the boundary (blue shaded region). A white dashed curve is drawn around the positive frequency contribution from the negative branch (ω_{D}^{-}).

Before moving on, we will benefit from thinking about what wave behaviour is anticipated from the phase space shown in figure 3.4. First, let us consider an open system, without any noise, and with a cluster that does not expand. If at some instant, waves are excited inside the core, the co-rotating ($m > 0$) components will radiate out effortlessly, whereas only counter-rotating ($m < 0$) frequencies that exceed the sound-ring frequency ω_{sr} can escape to infinity. Modes with frequencies lower than ω_{sr} will be reflected back at some radius smaller than the sound-ring radius r_{sr}. In particular, the closer (from above) the frequency is to ω_{sr}, the longer time it will take the mode to escape. A faraway observer will, therefore, first receive a complicated spectrum of frequencies that depends on the details of the excitation, followed by a long-lived, but gradually decaying signal at ω_{sr}. This slow leakage of waves originating* at the light ring is widely accepted as the main interpretation of the ringdown process for the relaxation of excited astrophysical compact objects[148, 164], although there are some exceptions (see e.g. [151]).

Next, imagine placing a rotationally symmetric reflecting boundary at some finite radius r_B. Now, the escaping waves are reflected back, and the inward-propagating waves interfere with the waves that are still propagating outward, creating standing waves. After the second reflection, the wave either adds to the already established standing wave or subtracts from it. As this cycle repeats, some frequencies will be increasingly suppressed by this interference, while others are amplified, and eventually, one is left only with a discrete collection of resonant frequencies. Because the perturbation originated in the core, however, no wave is excited in the blue regions of figure 3.4. At this point a comment should be made on the validity of the phase space picture. When a wave turns around, at $k_r = 0$, the WKB assumption (3.23) of phases varying much more than the amplitudes is badly violated. Instead, as discussed in detail in chapter 2 and appendix A, one may construct transfer matrices at these turning points, relating propagating WKB modes on one side to evanescent WKB modes on the other. The result is that modes are only partially reflected and with a phase shift of $\pi/4$. The transmitted, evanescent component, which can be seen as a tunnelling amplitude (see appendix A), enables amplitudes from one phase space orbit to bleed into another of the same frequency, but with amplitudes suppressed by their separation. There are two situations in figure A.4 for which this might happen. The first situation occurs for clusters that are sufficiently compact for the negative branch ω_D^- to take positive values, in which case the system may exhibit a superradiating instability as discussed in chapter 2. In panel (a) of figure 3.4, a white dashed line is drawn around the $m < 0$ region in phase space that corresponds to negative frequencies. By virtue of the symmetry $-\omega_D^{\pm}(m) = \omega_D^{\mp}(-m)$, these trajectories are the same as those of the negative branch for $m > 0$ (white dashed contour in panel (b)). However, in what follows we will find ourselves in a situation where the positive frequencies in ω_D^- are lower than the smallest frequency on the positive branch ω_D^+, so that even if modes with $\omega_D^- > 0$ exist, they cannot tunnel into modes on the positive branch.

The second situation that is not captured by the phase space picture is the tunnelling of the

*In our system, the sound-ring/light-ring is populated by radiation trying to escape from inside the cluster. In general, the ringdown modes are said to originate from, or at least nearby, the light-ring itself.

I-modes (red region in panel (a) of Figure 3.4) into the O-modes (blue region) for frequencies that exist in both regions. We shall see that this does indeed happen, resulting in some, although strongly suppressed, counter-rotating resonant modes below the sound-ring frequency. That is, for a stationary, undamped system with reflecting boundary conditions, an excitation that originates in the core is expected to eventually result in a population of resonant modes of type A and I, as well as some frequencies in the O-region of panel 3.4(a).

In reality, there is no sudden excitation in the core, but rather an active stirring by the moving vortices. The presence of noise seeds all regions in figure 3.4, but only weakly compared to the sound radiated from the cluster. Moreover, the damping reduces the population of resonant modes that are not continuously sourced from the cluster. Although slow, the expansion of the cluster introduces a drift in the resonant modes. However, the sound ring, being located safely outside the cluster during the early stages, remains static during the entire process.

To determine the location of the sound-ring, we first observe from (3.25a) that a wave stagnates radially, i.e. $\dot{r} = 0$, whenever $k_r = 0$. As in (2.36) from chapter 2, this motivates the introduction of the turnover frequencies

$$\omega^{\pm}(r) = \frac{m v_\theta}{r} \pm \sqrt{\rho_0 \frac{m^2}{r^2} + \frac{m^4}{4r^4}}, \tag{3.26}$$

being the frequency of waves that stagnate at the radius r. For positive frequency counter-rotating waves ($m\omega < 0$), the turnover frequencies $\omega^+(r)$ on the positive branch can exhibit a local maximum which determines the location of the sound-ring

$$r_{sr}^{(m)} = \sqrt{\tfrac{1}{2}(6\ell^2 - m^2) + \ell\sqrt{6\ell^2 - m^2}}, \quad \omega_{sr} = \omega^+(r_{sr}). \tag{3.27}$$

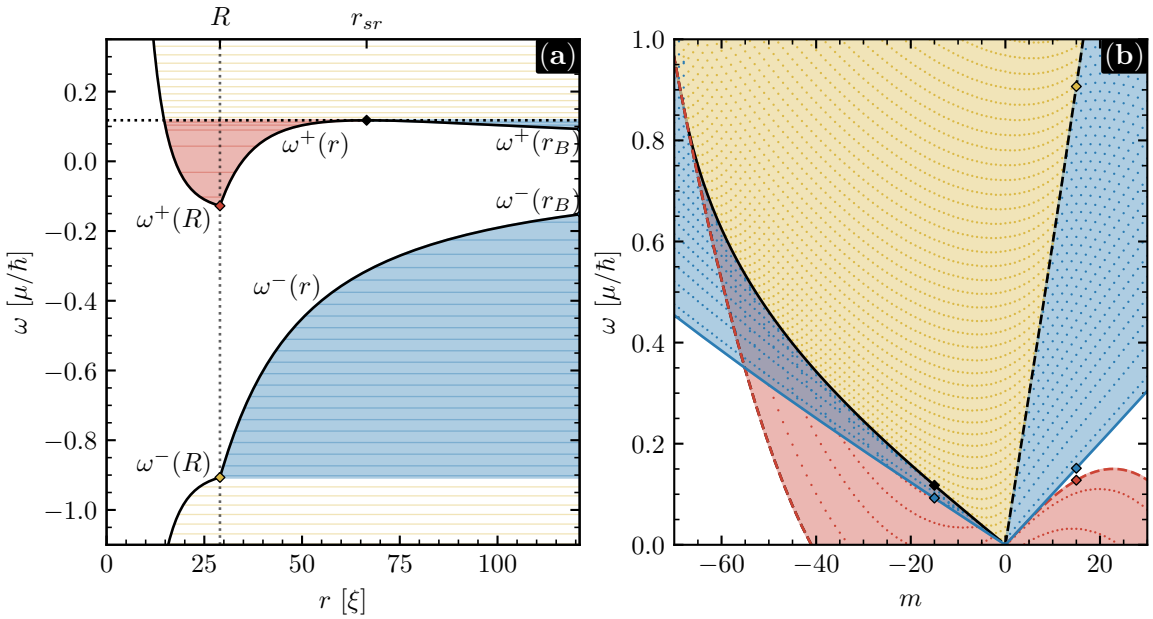

Figure 3.5 (Anatomy of the spectrum) Three qualitatively different regions shaded for $\ell = 29$ with $R = |\ell|$: I-modes (red), O-modes (blue), and A-modes (orange). Panel **(a)**: the effective potential $\omega^{\pm}(r)$ (solid black line) for $m = -15$. From the symmetry $-\omega^{\pm}_{D}(m) = \omega^{\mp}_{D}(-m)$, negative frequencies inform us of $m = +15$. Frequencies at three key radii are labelled: the Rankine radius R (vertical dotted line), the sound-ring radius $r^{(m)}_{sr}(\ell)$ and the potential boundary r_B. Coloured horizontal lines are drawn at the resonant frequencies predicted using the WKB approximation. Panel **(b)**: allowed frequencies ω over azimuthal number m for all radii r in the system. For a single $m = \pm 15$, this corresponds to the middle panel projected onto the frequency axis. Here, the solid black line gives the sound-ring frequencies ω_{sr}, and the dashed black line is the frequency $\omega^+(R)$ of waves with a turning point at the Rankine radius. The solid points signal which modes stagnate at the sound-ring (black), counter-rotating at the core (red), co-rotating at the core (yellow) and at the boundary (blue) for $|m| = 15$.

Here $r_{sr}^{(m)}$ is the radius of the sound-ring and ω_{sr} is the frequency of the wavefront which orbits the system at this radius (see panel (a) of figure 3.5). Note that the sound-ring radius $r_{sr}^{(m)}$ only exists provided that $R < r_{sr}^{(m)}$. Importantly, ω_{sr} is the lowest positive frequency needed for a counter-rotating wave to travel freely from inside the vortex cluster to the potential boundary. Moreover, since the effective Hamiltonian is locally flat at the sound-ring r_{sr}, i.e. $\partial_r \omega^+|_{r=r_{sr}} = 0$, waves which are created in this region will linger around r_{sr} before eventually dispersing [165].

Note that the sound-ring is completely determined by ℓ and $|m|$ and that it only exists when the cluster is sufficiently compact, i.e. $R < r_{sr}$, and only for azimuthal modes with $|m| \lesssim \sqrt{6}|\ell|$. For a singly wound vortex ($|\ell| = 1$) the sound-ring is of the order of the healing length $r_{sr} \sim 1$.

The same coloring of regions as in figure 3.4 are used in figure 3.5, and the white region correspond to modes that are evanescent. Here, the frequencies $\omega \geqslant \omega^+$ gives the counter-rotating spectrum in figure 3.4(a), whereas the negative frequencies $\omega \leqslant \omega^-$ correspond to the co-rotating phase space in panel (b).

If the radial direction is projected out from $\omega^\pm$ for all m, we are left with panel (b) of figure 3.5. Here, the solid black line is drawn along the sound-ring frequencies, and the solid blue line gives the frequencies of modes that stagnate at the potential boundary r_B. On the co-rotating side, for which there is no sound-ring, a dashed black line at $\omega^+(R)$, delimiting the A-modes from the O-modes, is drawn along the frequencies that stagnate at the rim of the cluster. Counter-rotating ($m < 0$) modes that stagnate the edge $r = R$ of the core are drawn as a dashed red line. Note that the negative frequencies appear as co-rotating positive frequencies, as seen from the red region for $m > 0$. As the cluster expands, the dashed lines change their locations, while the solid lines do not. The result is that in the co-rotating spectrum, O-modes are continually being promoted to A-modes, whereas in the counter-rotating spectrum, they remain fixed.

Several brief observations should be made. Firstly, the I-modes in the co-rotating spectrum, which carry negative energy, do not overlap with O-modes for the depicted core size ($R = 29$). An overlap of these regions exists for smaller core sizes or larger trap sizes, for which a superradiating instability can occur, leading to large mode populations in this region. Secondly, we observe that, due to dispersion, the sound-ring seizes to exist when $r_{sr}^{(m)} \leqslant R$ which happens for sufficiently large azimuthal numbers $|m|$. For azimuthal numbers larger than this threshold, the counter-rotating spectrum exhibits the same qualitative behaviour as the co-rotating spectrum. Thirdly, in the counter-rotating spectrum, there is an overlap of regions I and O, which are precisely the frequencies for which tunnelling may occur between regions I and O. The result is that in this region, I and O modes are not naturally separated due to their interaction and one should instead refer to them as joint IO-modes. The WKB resonance condition for I and O modes takes the same form as that used for closed systems in chapter 2, i.e.

$$\underbrace{\cot\left(\Phi_{12}\right)}_{\text{I}-\text{modes}} \underbrace{\cot\left(\frac{\pi}{4} + \Phi_{3B}\right)}_{\text{O}-\text{modes}} = \exp\left(-2\Phi_{23}\right) \quad \text{for} \quad \Phi_{ab} \equiv \int_{r_a}^{r_b} |k_r| dr, \tag{3.28}$$

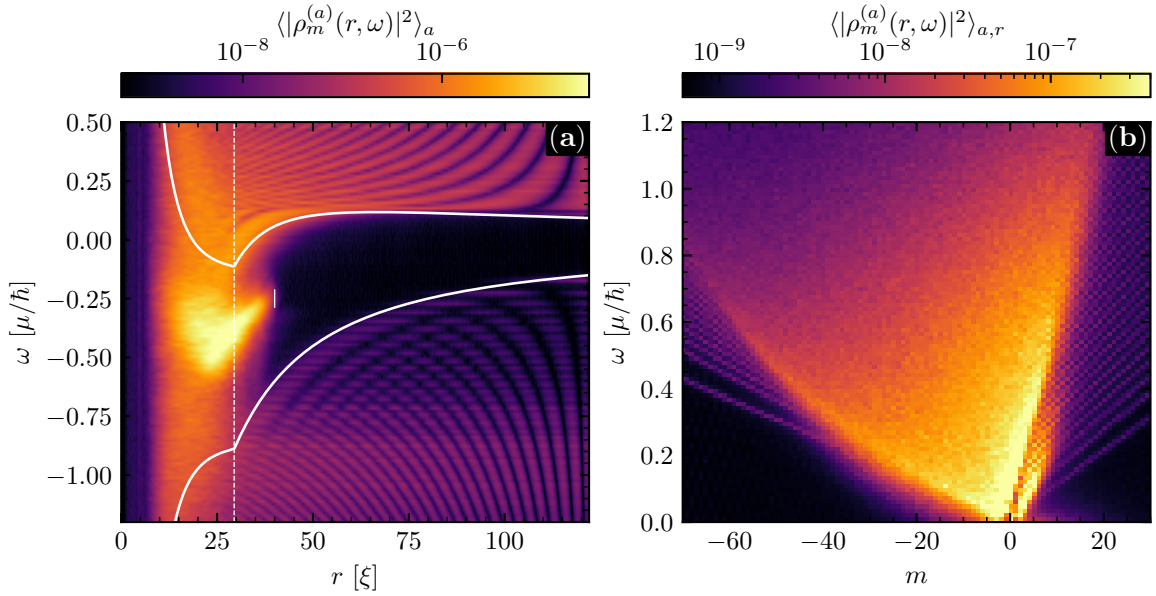

Figure 3.6 (Simulation results) Panel **(a)**: ensemble-averaged squared amplitudes for $m = \pm 15$, white lines show the turnover frequencies $\omega^{\pm}(r)$ for the average Rankine radius $R = 29.45$ (vertical white dashed line). Panel **(b)**: radially averaged spectrum from $r_a = 40$ (see white vertical solid line segment in left panel) to the boundary $r_B = 121.5$.

where r_1, r_2, r_3 are the (sorted) solutions to $\omega^{\pm} = \omega$ for the frequency considered. Note, however, that the background ρ_0, v_0 is different from that of chapter 2. The resonance condition for the A-modes takes the form of a separated O-mode, i.e. $\cos(\Phi_{1B} + \pi/4) = 0$. The frequencies which solve the resonance condition are shown in figure 3.5 as horizontal lines in panel (a) and dots in panel (b).

VII. The observed spectrum

Armed with the analytic predictions summarised by figure 3.5, we now shift our focus towards the numerical simulations. Using the approach outlined in section IV (see equation (3.20)), we obtain a spectrum of (complex) amplitudes $\rho_m^{(a)}(\omega, r)$ for each realisation $a = 1, \ldots, 51$, azimuthal number m, frequency ω and radius r.

The ensemble-averaged result is shown in figure 3.6, in the same form as the predictions in figure 3.5. Panel (a) illustrates the radial dependence of the sound in different frequencies for $m = -15$. Superimposing the turnover frequencies from our model (white solid lines), we see that the data is in excellent agreement with our prediction for $r > R$, since $\omega^{\pm}$ correctly separates the propa-

gating and evanescent regions of the system. Inside the core, amplitudes are seemingly uniformly distributed, other than a low-negative-frequency region of very large amplitudes where we expected the modes to be evanescent. This region corresponds to slowly co-rotating modes associated with the movement of vortices inside the core. As seen in the previous chapter, there is an intricate interplay between the vortex (cavity mode) and the sound-field outside (phonon mode). That is, we may expect this signal to partly consist of a remnant of the initial instability of the multiply wound vortex discussed in chapter 2, and partly a numerical artefact due to the misinterpretation of the density depressions around individual vortices as sound-waves. In any case, a detailed study of this signal relies on the movement of individual vortices and their coupling to the surrounding density fluctuations, which is beyond the scope of this investigation.

Focussing on the emitted sound, we consider the radially averaged spectrum on the interval $r \in [r_a, r_B]$, where $r_a = 40$ is chosen to be a couple of healing lengths outside the final core size[*]. The result is figure 3.6(b), which is in excellent agreement with the predicted spectrum in figure 3.5(b). However, whereas the O-mode resonance frequencies are clearly excited (see faint straight lines in figure 3.6(b)), there are no resonant A-modes visible. That is, the orange region in figure 3.5(b) appears featureless in figure 3.6(b).

To understand what is going on, let us return to figure 3.6(a). For the propagating ($\omega \geqslant \omega^+$ or $\omega \leqslant \omega^-$) outer regions ($r > R$), the turnover frequencies $\omega^\pm$ and outer potential boundary r_B form an effective cavity. Following the discussion of the phase space 3.4, a discrete spectrum of resonant frequencies emerges only when both boundaries in the cavity are well defined. In figure 3.6(a) we observe that if this cavity lies entirely outside the cluster core, i.e. the O-modes in figures 3.4 and 3.5, then both boundaries of the cavity are well defined resulting in a curved checkerboard pattern of high and low wave amplitudes (see region around $r = 75$ and $\omega = -0.5$ in figure 3.6(a)). The result is the aforementioned discrete set of resonant O-mode frequencies visible in figure 3.6(b). If, on the other hand, part of the cavity is inside the core, i.e. I-mode or A-mode in figure 3.5, then only the boundary condition at r_B is well defined. The result is the formation of standing waves, but not a discretization of frequencies. This suggests that, for our choice of parameters, the model fails for $r < R$ since the studied ω-range is sensitive to the movement of individual vortices. The absence of features in the core region of 3.6(a) can then be understood as a consequence of the scattering across both frequencies (due to the time-dependence of vortex movement) and azimuthal numbers (due to features in azimuthal direction).

In our simulations, and in experiments, dissipation acts on energies, meaning that higher frequencies are damped more than lower frequencies. Therefore, the majority of the sound energy escaping the cluster ought to reside in the frequencies delimiting the A-modes from the O-modes in figure 3.5. Consequently, the peak in amplitude for co-rotating frequencies depends on the core size, and therefore on the time, the waves were emitted from the core. In comparison, the peaks at

[*]It was confirmed that such an average remains unchanged for variations of r_a when $r_a \geqslant r_{sr}^{(0)}$, other than the expected effects from the standing wave patterns.

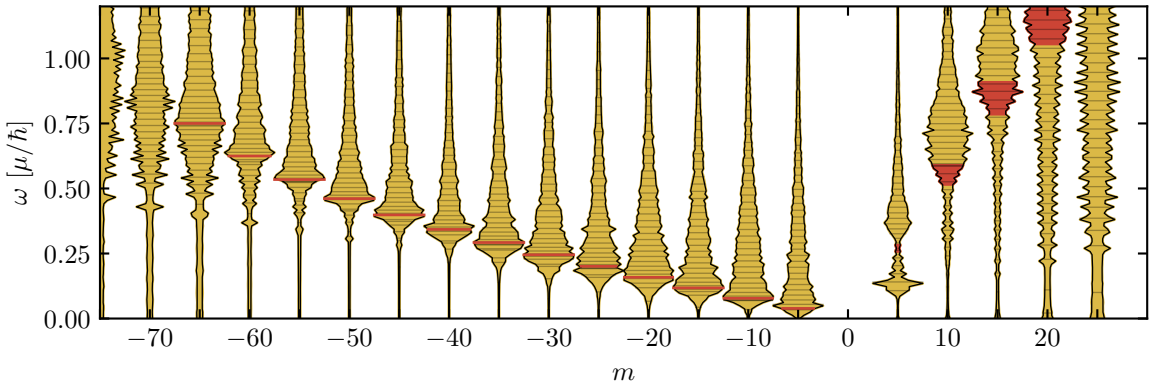

Figure 3.7 (Sound-ring spectrum) Relative (squared) amplitudes of the radially averaged spectrum $\langle|\rho_m^{(a)}(t,r)|^2\rangle_{a,r}$ for a selection of azimuthal modes. The thickness of each vertical band is proportional to the amplitudes of the corresponding slice in figure 3.6(b). Thin horizontal lines are drawn at the resonant frequencies and thick red lines are drawn at the sound-ring frequencies ω_{sr} for the counter-rotating ($m < 0$) modes. For the co-rotating ($m > 0$) modes, the range of turnover frequencies at the Rankine radius R, i.e. $\omega^+(R)$, is drawn (red bands) for estimated range $R \in [26.2, 32.7]$.

the sound-ring frequencies remain constant and are thus well resolved. This result is independent of the validity of the model inside the core. In figure 3.7, the (relative) amplitudes from figure 3.6(b) is plotted for a selection of azimuthal modes m, where the thickness of each (orange) band is proportional to the mode amplitude at that frequency. We see that for $m < 0$, where the sound-ring exists, the spectrum is clearly peaked at the sound-ring frequencies ω_{sr} (red horizontal lines). In comparison, on the co-rotating side, where there is no sound-ring, the amplitudes have a wider peak, somewhat above the band of delimiting frequencies $\omega^+(R)$ for the range of core sizes R within the analysis window. Crucially, due to the expansion of the core R over time and the finite speed of the wave, the population of these frequencies depend on the core size R at the time of departure, when the core was even smaller than the initial size within the analysed time window. That is, at a given time t and radius r, the expected peak is not located at $\omega^+(R(t))$, but rather at $\omega^+(R(t-\Delta t))$, where Δt is the time it took the wave to propagate from $R(t-\Delta t)$ to r.

This is in contrast to the sound-ring frequencies ω_{sr}, which, when they exist, do not depend on the core size. Instead, the sound ring is static and located well outside the core, providing a consistent lower threshold on the counter-rotating frequencies needed for the waves to escape the cluster.

VIII. Conclusion

In this chapter, we introduced the notion of sound rings to describe the wave dynamics of a compact vortex cluster. By comparing with numerical simulations of the SGPE, we verified that the sound ring of the average flow field is a strong signal in the measured spectrum. This complements recent progress in black hole physics, where the gravitational waveform produced during binary mergers is determined by the light-ring of the average one-body spacetime. In our case, the sound ring plays a central role since it exists in a region of the flow which is highly symmetric and non-evolving at early times. The resulting signal is, therefore, independent of the non-linear vortex dynamics inside the cluster, provided the vortices are packed close enough together so that the cluster radius is smaller than the sound-ring, i.e. $R < r_{sr}$.

The findings are expected to be of interest in 2d-quantum turbulence. In a confined system such as a trapped atomic condensate, the number of possible vortex configurations is bounded, and the entropy reaches a maximum at a finite value of the energy [134]. Larger energy can then be reached only by lower entropy creating clustering of vortices of the same sign. Therefore, the injection of energy into such a two-dimensional flow will promote the formation of vortex clusters and sound rings. A coarse-grained velocity field of ℓ same-sign vortices will induce a sound-ring of radius $r_{sr} \sim \ell$, see equation (3.27), in which a strong wave signal is localised around ω_{sr} in the frequency domain. This could be checked in current experimental, and numerical studies of two-dimensional quantum turbulence in which vortex clustering can be induced by evaporative heating, i.e. the annihilation of vortex-antivortex pairs [155, 156, 166].

Although we do not observe a discrete spectrum of modes which probe the inside of the cluster, these modes are expected to be excited for larger vortex clusters with $\ell \gtrsim 100$. In this limit, the discretization of circulation in the underlying micro-structure is also expected to be hidden from the long-wavelength modes, which perceive only the average "classical" Rankine background. These considerations may be of interest for the corresponding quantum to classical limit around fluid flows and rotating compact objects exhibiting discrete angular momentum.

Finally, it should be stressed that it is far from obvious that the sound-ring, a relatively simple model, should have such a descriptive power in this system. The relaxation expansion of a vortex cluster is a complex, highly non-linear system. The discovery of the sound-ring phenomenon therefore not only builds intuition but also offers a remarkably simple theoretical description that captures the essential features of a very complicated phenomenon.

Chapter 4

Non-linear Faraday Resonance of Two-Fluid interfaces

The following accounts for the work presented in the preprint *Primary thermalisation mechanism of Early Universe observed from Faraday-wave scattering on liquid-liquid interfaces* [102] by V. S. Barroso, Z. Fifer, S. Erne, A. Avgoustidis, R. J. A. Hill, S. Weinfurtner and myself. This project is a continuation of the proposal presented in [167]. My primary role focused on data analysis, simulation and model building.

While writing this chapter, I realised that the non-linear treatment could be extended to incorporate surface tension to higher order in perturbation theory. In pursuit of this extension, all figures and numerical simulations below are updated to incorporate the extended model.

I. Introduction

In 1831, Michael Faraday published his work on the patterns created by dust on vibrating surfaces [168, 169]. He noted that a similar instability appeared for fluid surfaces upon vibration of the container. In particular, he observed that the fluid surface oscillated with twice the period of the external vibration. This phenomenon, now referred to as Faraday instability or, more generally, parametric resonance, has been studied extensively since then. It is responsible for the rolling of ships at sea [170], the collapse of bridges [171], and for the thermalisation of the early universe after the hypothesised period of cosmological inflation [89]. This thermalisation mechanism, referred to as preheating, is a broad parametric resonance transferring energy from the primordial inflaton field to other fields, eventually thought to result in the hot plasma taken as the initial state of hot big bang cosmology. Unfortunately, the preheating mechanism, obscured by several hundred thousand years of hot plasma, is likely to remain elusive to direct observation for the foreseeable future[†].

In this chapter, we experimentally investigate the Faraday instability arising from a classical two-fluid interface. The results are analysed from the perspective of cosmological preheating, and the tools are motivated by recent adaptations of the statistical machinery from field theories [103, 104]. Using an ensemble of repeated experiments, we test our model against stochastic simulations of

[†]There may be hope in the field of gravitational wave astronomy.

a non-linear model and identify a broadening of primary resonance bands and the appearance of secondary instabilities as predicted by preheating [100].

II. Dynamics of parametrically driven confined Two-fluid Interfaces

In the following section, we seek to introduce the dynamical equations of motion for the interfacial excitations of two immiscible fluids in a closed container oscillating vertically. This will be done in three steps: (1) the introduction of the perturbative, linear dynamics, and relations for the eigenmodes in an annular cylindrical geometry, (2) a discussion of the well-known unstable growth dictated by Floquet theory and (3) the weakly non-linear extension to the linear dynamics, derived in close correspondence to the approach of Miles [172, 173].

We take a phenomenological, effective field theory approach, where we start by considering an oversimplified model and iteratively add the relevant corrections. Two main approximations greatly simplify the calculations. Firstly, we ignore viscous effects and later correct for them by introducing a phenomenological damping parameter. Secondly, we assume the meniscus of the fluid interface to be negligible.

II.1. The linear theory

The dynamics of classical Newtonian fluids are well described by the Navier-Stokes equations [174],

$$\rho(\partial_t + \mathbf{v}\cdot\nabla)\mathbf{v} = \nabla\cdot\mathbf{T} + \mathbf{F} \tag{4.1a}$$

$$\partial_t\rho + \nabla\cdot\rho\mathbf{v} = 0 \tag{4.1b}$$

which are nothing but a formulation of the conservation of mass (4.1b) and momentum (4.1a) in continuous media. Here, ρ is the density and $\mathbf{v}$ the flow velocity of the fluid, $\mathbf{F}$ is the net external force per unit volume acting on the fluid and $\mathbf{T}$ is the stress tensor with indices T_{ij}. The Newtonian stress tensor has an isotropic contribution from the thermodynamic pressure p, and a deviatoric stress proportional to the velocity gradients, with the the viscosity being the constant of proportionality.

We shall assume the fluid to be of constant density ($\nabla\rho = 0$ and $\partial_t\rho = 0$) and to be inviscid (zero viscosity), in which case the stress tensor is defined entirely by the thermodynamic pressure via

$$T_{ij} = -p\delta_{ij}. \tag{4.2}$$

Note, however, that to connect with the experiment in the subsequent sections, it will be necessary to reintroduce an effective damping parameter to the equations of motion. In the inviscid case, the

system (4.1a) and (4.1b) reduces to the incompressible Euler equations, with the substitution (4.2) in (4.1a), and (4.1b) being reduced to $\nabla \cdot \mathbf{v} = 0$.

Next, we shall assume $\mathbf{F}$ to be the conservative, vertical force of gravitation $\mathbf{F} = \rho \nabla g z$. Additionally, we will assume the flow to be irrotational, i.e. $\nabla \times \mathbf{v} = 0$, permitting us to introduce the velocity potential $\mathbf{v} = \nabla \Phi$*. The resulting governing equations are the Bernoulli equation and the incompressibility condition

$$\partial_t \Phi + \frac{1}{2}|\nabla \Phi|^2 + \frac{p}{\rho} - gz = \text{const}, \tag{4.3a}$$

$$\nabla^2 \Phi = 0\,. \tag{4.3b}$$

Next, we need to set boundary conditions for the pressure p and the velocity potential Φ. Let us start with the velocity potential. In regions where the fluid volume is bound by an impenetrable wall with normal vector $\mathbf{n}$, there is no fluid flow in the direction of $\mathbf{n}$. That is, there is an impenetrability condition of the form

$$\mathbf{n} \cdot \nabla \Phi = 0. \tag{4.4}$$

Here, due to microphysical, viscous effects, one often takes also the tangential flow to be vanishing at the boundary, i.e. $\nabla \Phi = 0$.

Next, let us consider a free boundary of the fluid, where the fluid does not touch a hard wall, but rather another fluid. In this case, the surface must move with the fluid it bounds. Denoting this free surface by $\Gamma(\mathbf{r}, t) = 0$, this can be stated as

$$(\partial_t + \mathbf{v} \cdot \nabla)\Gamma = 0. \tag{4.5}$$

Surface tension, which arises due to microscopic cohesive forces, introduces an energy $V_\sigma = \sigma A$ associated with the area A of the two-fluid interface itself (see e.g. Ch. 4.19 in [174]). One consequence is that the stress tensor $\mathbf{T}$ is discontinuous across an interface between two fluids. Denoting the two fluids by $(\pm)$ and the surface normal vector pointing from the heavier fluid $(-)$ to the lighter fluid $(+)$ by $\mathbf{n}$, the stress tensors $\mathbf{T}_\pm$ are related via [175]

$$\mathbf{n} \cdot (\mathbf{T}_- - \mathbf{T}_+) \cdot \mathbf{n} = \sigma \nabla \cdot \mathbf{n} \quad \text{and} \quad \mathbf{n} \cdot (\mathbf{T}_- - \mathbf{T}_+) \cdot \mathbf{t} = \nabla \sigma \cdot \mathbf{t} \tag{4.6}$$

where, σ is the coefficient of surface tension and $\mathbf{t}$ is a unit vector tangent to the interface. In the case of inviscid fluids the above reduces to the familiar Young-Laplace law

$$p_+ - p_- = \sigma \nabla \cdot \mathbf{n} \tag{4.7}$$

*Note that a natural extension of the theory would be, as in chapter V.3, to use the Helmholtz-Hodge decomposition $\mathbf{v} = \nabla \times \boldsymbol{\psi} + \nabla \Phi$ in terms of the velocity potential Φ and the stream function $\boldsymbol{\psi}$, and consider the situation where the flow is mostly irrotational, i.e. $|\nabla \Phi| \gg |\nabla \times \boldsymbol{\psi}|$.

for the pressure difference across a two-fluid interface. Note that the above relations can be split into two different systems. On the one hand, we have the dynamical boundary value problem (4.3b), (4.4) and (4.5), which determines the modes that fit in the system. On the other hand, we have the dynamical system defined by the two equations (4.3a) and (4.7), which determine the equations of motion for the modes that fit in the system.

As noted by Miles [172, 173], both these systems can be formulated as variational principles in such a way that the derivation carries naturally over to nonlinear deformations of the surface. Note, that the inclusion of surface tension as a Lagrangian potential energy as proposed in appendix D of Miles [173], was subject to a corrigendum [176]. This updated approach serves as the foundation for the treatment of surface tension in the following sections.

The dynamical boundary value problem

We shall now focus on the dynamical boundary value problem (4.3b), (4.4) and (4.5), for two immiscible fluids, labelled $(\pm)$, enclosed by an annular cylindrical container. We choose the labelling such that in the resting position, fluid $(-)$ is below fluid $(+)$, i.e. $\rho_- \geqslant \rho_+$. The volumes occupied by the two fluids are referred to as $V_\pm$, with the total volume of the container being $V = V_- \cup V_+$. The inner surface ∂V of the container is subject to the impenetrability condition (4.4), whereas the interface $\Gamma(\mathbf{r}, t) = 0$ between the two fluid volumes V_+ and V_- obeys the dynamical boundary condition (4.5). The result is a dynamical boundary value problem of the form

$$\nabla^2 \Phi_\pm = 0 \text{ in } V_\pm \tag{4.8a}$$

$$\mathbf{n} \cdot \nabla \Phi_\pm = 0 \text{ on } \partial V, \tag{4.8b}$$

$$(\partial_t + \nabla \Phi_\pm \cdot \nabla)\, \Gamma = 0 \text{ on } \Gamma, \tag{4.8c}$$

To start, we choose z to be the direction opposite to gravity and consider the linearised motion of small deviations ξ from a flat $(z = \Gamma)$ interface at rest $(\nabla \Phi_\pm|_\Gamma = 0)$, i.e. $\Gamma = z - \xi$ for $\Phi \ll 1$ and $|\xi(t, \mathbf{r})| \ll h_0^{(\pm)}$, where $h_0^{(\pm)}$ is the average depth of fluid $\pm$. The resulting linearised condition for the free surface (4.8c) takes the form

$$\partial_t \xi = -\partial_z \Phi_\pm. \tag{4.9}$$

Now introduce cylindrical coordinates $(\mathbf{x}, z) = (r, \theta, z)$ and eigenmodes $\psi_k(r, \theta, z)$ of the horizontal Laplacian, i.e. $\nabla^2 \psi_k \equiv \partial_z^2 \psi_k - k^2 \psi_k$, and note that linearity ensures that each ψ_k satisfies the equations of motion independently. Let the container ∂V consist of two horizontal surfaces $z = \pm h_0$ that are equidistant from the resting position of the interface, with vertical walls that are symmetric under z translations. Due to this symmetry, fixing the location of the top/bottom lids of the container to $z = \pm h_0$ amounts to saying that the two fluids partition the volume of

the container equally. By virtue of the translational symmetry of the vertical walls*, we may use the incompressibility condition (4.8a) for ψ_k in the bulk to connect the linearised dynamic boundary condition on the interface (4.9) with the impenetrable horizontal wall (4.8b) at $z = \pm h_0$ to find that $\psi_{k,\pm} = f_k(r,\theta)\cosh(k(z \mp h_0))$. Re-introducing this to (4.9) motivates the mode decomposition

$$\Phi_\pm(t,r,\theta,z) \equiv \sum_a \phi_{\pm,a}(t)\psi_{\pm,a}(r,\theta,z) \quad \text{for} \quad \psi_{\pm,a} \equiv f_a(r,\theta)\frac{\cosh(k_a(z \mp h_0))}{\cosh(k_a h_0)} \tag{4.10a}$$

$$\xi(t,r,\theta,z) \equiv \sum_a \xi_a(t) f_a(r,\theta), \tag{4.10b}$$

for the linearised dynamics, where the extra constant $\cosh(k_a h_0)$ in $\psi_{\pm,a}$ is factored out of $\phi_{\pm,a}$ for future convenience. Note, however, that (4.10) can look deceiving. When the mode functions f_a are introduced to the boundary of the interface Γ, there will be a discretisation of the permitted eigenvalues k_a. This will determine the exact form of the summation over a, which up to this point remains unspecified. Crucially, if the boundary condition at the edge of the interface Γ is not the same as that of Φ, i.e. $\mathbf{n}\cdot\nabla\Gamma = 0$, we cannot generally expect the summation over a in (4.10a) to be the same as that in (4.10b). However, we have not yet specified a boundary condition for ξ on the boundary of the interface Γ. Such a boundary condition is fixed by the contact angle θ_e of the two fluids with the container wall, resulting in a boundary condition of the form [175]

$$\mathbf{n}\cdot\frac{\nabla\Gamma}{|\nabla\Gamma|} = \cos\theta_e \tag{4.11}$$

at the edge of the interface. For $\theta_e \neq \pi$ this gives rise to a meniscus, whose presence is known to source waves when interface waves are parametrically amplified [177, 178]. Because of this, our experiment was prepared (see section III) using materials that minimise the meniscus. We shall therefore use the assumption of a negligible meniscus ($\theta_e = \pi$) for the remainder of this chapter. Mathematically, this assumption is pleasing as it greatly simplifies the derivation due to both Γ and $\Phi_\pm$ now being subjected to the same boundary condition at the edge of the interface. This means that we may now focus on determining the indexing set in equations (4.10a) and (4.10b), without having to worry that these may not be the same.

For the remainder of this chapter, we shall specialise to an annular geometry wherein the vertical walls consist of two nested cylinders, the outer of radius r_1 and the inner of radius r_2. In this case,

*It is the z-translation symmetry that ensures the eventual coefficients in the eigenmode basis to be the same at each horizontal slice $z = \text{const}$.

the mode functions f_a, which obey the Helmholtz equation $(\nabla^2 - k_a^2)f_a = 0$, are given by

$$f_a(r,\theta) \equiv N_a^{-1} R_{m_a}(k_a r)\cos(m_a\theta), \quad \text{for} \tag{4.12a}$$

$$R_m(kr) \equiv Y'_m(kr_1)J_m(kr) - J'_m(kr_1)Y_m(kr) \quad \text{and} \tag{4.12b}$$

$$N_a^2 \equiv \frac{2}{\pi A k_a^2 J'^2_{m_a}(k_a r_2)}\left[\left(1-\frac{m_a^2}{k_a^2 r_2^2}\right)J'^2_{m_a}(k_a r_1) - \left(1-\frac{m_a^2}{k_a^2 r_1^2}\right)J'^2_{m_a}(k_a r_2)\right] \tag{4.12c}$$

where J_m and Y_m are Bessel functions of the first and second kind, respectively, derivatives with respect to r are denoted by a prime, i.e. $' = \partial_r$, and $A \equiv \pi(r_2^2 - r_1^2)$ is the area of the interface at rest. Here, we have introduced the azimuthal numbers $m_a \in \mathbb{Z}^+$, which are confined to integer values due to angular periodicity $f_a(r,\theta) = f_a(r,\theta+2\pi)$ in (4.12a). The azimuthal number m_a can be thought of as fixing the number of wave crests along a circle. The constant N_a serves as a normalization constant, as in equation (68) of Ziener [179], with respect to the L_2 inner product $(\cdot,\cdot)$ to ensure orthonormality

$$(f_a(\mathbf{x}), f_b(\mathbf{x})) \equiv \frac{1}{A}\int d^2x f_a(\mathbf{x})f_b(\mathbf{x}) = \delta_{m_a,m_b}\delta_{k_a,k_b} \equiv \delta_{ab}\,, \tag{4.13}$$

of the mode functions*. Here, and in what follows, δ_{ab} are the Kronecker delta symbols.

Whereas m_a is discretized by azimuthal periodicity, k_a is discretised by the boundary condition (4.8b) or, equivalently, (**??**), at r_2. That is, k_a are the values of k for which†

$$Y'_m(kr_1)J'_m(kr_2) = Y'_m(kr_2)J'_m(kr_1)\,. \tag{4.14}$$

Note that the set $\{k_a\}_a$ of values k that satisfy this condition generally depends on the azimuthal number m. There is no closed-form solution of (4.14), although approximations exist (see e.g [180] and [181]). As a result, we determine $k_{a\,a}$ through the numerical solution of equation (4.14).

Before returning our focus to the determination of the linearised dynamics of ξ, we will benefit from the observation that using the decomposition (4.10), along with the orthonormality relation (4.13), allows us to write the linearised relation (4.9) as

$$\dot{\xi}_a(t) = \mp\phi_{\pm,a}(t)T_a \quad \text{for } T_a \equiv k_a\tanh(k_a h_0)\,. \tag{4.15}$$

The equations of motion

The natural next step in the derivation of the linearised equations of motion for the modes ξ_a and $\phi_{\pm,a}$ would now be to linearise the Bernoulli equation (4.3a), at the interface $z = \xi$. Then, using our expression for the mode functions ξ_a and $\phi_{\pm,a}$ from (4.10), along with the observation

*Here, the area A is introduced in the denominator to adimensionalize the inner product and the mode functions f_a explicitly.

†The is nothing special about the outermost radius r_2 here. In this case, the innermost radius r_1 was used to obtain the form (4.12b) for R_m. If, instead, one were to use r_2 in determining the coefficients in (4.12b), then k_a would instead be discretised from invoking (4.8b) at r_1.

that (4.15) requires $\phi_{+,a} = -\phi_{-,a}$, to consider the difference across the interface. The pressure difference can be used to summon the Young-Laplace condition from (4.7). After using the orthonormality relations (4.13) to separate the modes, we would find the dynamical system

$$\dot{\xi}_a(t) = \mp\phi_{\pm,a}(t)T_a \quad \text{and} \quad \dot{\phi}_{\mp,a} = \frac{(\rho_\mp - \rho_\pm)g - \sigma k_a^2}{\rho_\mp + \rho_\pm}\xi_a. \tag{4.16}$$

However, as mentioned in the beginning of this section, we shall focus on the approach of Miles [172, 173], including the surface tension as in the corrigenda [176] (see also [182]). The reason that we choose this path, is the mathematical convenience of the Lagrangian formalism when we consider the nonlinear extension of the model in section II.3.

In the presence of a single conservative vertical force $\mathbf{f} = -g(t)\mathbf{e}_z$, the dynamics of the system may be formulated* in terms of a Lagrangian of the form [172, 173, 176, 182]

$$L = L_+ + L_- - V_\sigma \tag{4.17a}$$

$$L_\pm = \rho_\pm \iiint_{V_\pm} dV \left[\frac{1}{2}|\nabla\Phi_\pm|^2 - gz\right] \tag{4.17b}$$

$$V_\sigma = \sigma \iint (|\nabla\Gamma| - 1)\,dA, \tag{4.17c}$$

where $L_\pm$ are the effective Lagrangians for the top (+) and bottom (−) fluids, and V_σ is the interaction energy due to tensile forces on Γ, with strength controlled by the surface tension σ. Note that the integrals (4.17b) are nothing but the kinetic energy $\frac{1}{2}\rho_\pm|\mathbf{v}_\pm|^2$ minus the gravitational potential energy $\rho_\pm gz$ of each fluid. The expression in (4.17c) introduces an energy proportional to the area $\iint|\nabla\Gamma|dA$ of the interface, with proportionality σ, mentioned in the beginning of the section when introducing surface tension. The factor -1 in the integrand ensures that the surface energy V_σ is 0 for a flat fluid interface. In terms of the mode decomposition (4.10), the Lagrangian (4.17), to leading order in $|\xi| \ll |h_0|$ and $\phi_\pm \ll 1$, takes the form (see appendix D for details)

$$L \simeq A\sum_a \frac{\rho_- + \rho_+}{2T_a}\left[\dot{\xi}_a^2 - \omega_a^2\xi_a^2\right] + \text{const} \quad \text{for } \omega_a^2 \equiv \frac{(\rho_- - \rho_+)g + \sigma k_a^2}{\rho_+ + \rho-}T_a, \tag{4.18}$$

where (4.15) has been used to eliminate all appearances of $\phi_{\pm,a}$. Clearly, this is the same system as found with standard perturbation theory in (4.16), i.e. the modes ξ_a behave as harmonic oscillators with frequencies ω_a. Note that the Lagrangian (4.18) remains valid if the entire system is placed on a vertically oscillating platform. Indeed, if the vertical position is parametrised by $z = z_s(t)$, then the effective gravity becomes $g \mapsto g_{eff}(t) \equiv g + f(t)$ for $f(t) = \ddot{z}_s$, where g is the usual vertical gravitational acceleration.

*Note that the time dependence of the force can either be included as an effective gravity $g \mapsto g + g(t)$, or it can be taken as a time-dependent fluid volume $V_\pm(t)$ in the integration domain.

Up to this point, we have assumed the fluids to be perfectly inviscid. As a first approach, we can include dissipation phenomenologically by introducing a Rayleigh dissipation function

$$R_\gamma \equiv \sum_a (R_a^+ + R_a^-) \quad \text{for} \quad R_a^\pm \simeq \sum_a A\gamma_a \frac{\rho_\pm}{T_a}\dot{\xi}_a^2, \tag{4.19}$$

in (4.18), as suggested by Miles [172]. Here, the dissipation function R_γ is responsible for a generalised non-conservative force $-\partial_{\xi_a} R_\gamma$, modifying the equations of motion for the conservative Lagrangian system (4.18) through

$$\frac{d}{dt}\frac{\partial L}{\partial \dot{\xi}_a} - \frac{\partial L}{\partial \xi_a} = -\frac{\partial R_\gamma}{\partial \dot{\xi}_a}. \tag{4.20}$$

The dissipation function (4.19) is written in terms of the contributions from the top (R_a^+) and bottom (R_a^-) fluids, where we have assumed the dissipation to be diagonal, i.e. absence of cross-terms $\dot{\xi}_a\dot{\xi}_b$ for $a \neq b$. Moreover, the phenomenological damping parameter γ_a, which accounts for all viscous effects in the single-mode dynamics, has been introduced*.
The resulting equation of motion for the interface modes ξ_a is in the form of a damped harmonic oscillator equation,

$$\ddot{\xi}_a + 2\gamma_a\dot{\xi}_a + \omega_a^2(t)\xi_a = 0, \quad \text{where} \tag{4.21a}$$

$$\omega_a^2(t) \equiv \frac{(\rho_- - \rho_+)g_{eff}(t) + \sigma k_a^2}{\rho_- + \rho_+} k_a \tanh(k_a h_0)\,, \tag{4.21b}$$

subjected to a time-dependent vertical force $f(t) = g_{eff}(t) - g$. We shall now focus on the case of parametric amplification, which is the instability that may arise in the case of a periodic vertical force $f(t)$.

If $f(t)$ is periodic and vertical, the linear dynamics (4.21) takes a form comparable to that of cosmological preheating (1.3), where the interfacial modes ξ_a correspond to the amplified matter field, and the vertical oscillation plays the role of the inflaton field. A pleasing consequence of this is that in an experiment, alternative inflationary models may be investigated by modifying the vertical force. However, a comparison of this kind is beyond the scope of this text. Instead, we shall focus on the non-linear regime in the hydrodynamical context. Towards the end of this chapter, we shall see that even in its nonlinear description, the hydrodynamical equations capture the essential features of the preheating mechanism.

II.2. Charting the instability

An unstable behavior arises in the linear dynamics (4.21) when the system is subjected to a vertically oscillating force $f(t) \equiv F_0 \cos(\omega_d t)$ of amplitude F_0. In this case the linear dynamics (4.21) takes

*The interested reader is invited to consult the appendix of our paper [102], where an analytical model for the phenomenological damping parameters γ_a is introduced.

the form of the well-known Mathieu equation [183]. Let us start by writing equation (4.21) in matrix form as a damped Hill's equation

$$\frac{d}{dt}\begin{bmatrix}\xi_a\\ \dot{\xi}_a\end{bmatrix} = D(t)\begin{bmatrix}\xi_a\\ \dot{\xi}_a\end{bmatrix} \quad \text{for} \quad D(t) \equiv \begin{bmatrix}0 & 1\\ -\omega_a(t) & -2\gamma_a\end{bmatrix}, \tag{4.22}$$

where D is periodic with period $T \equiv 2\pi/\omega_d$, i.e. $D(t) = D(t+T)$. This equation can be solved for arbitrary initial conditions by considering the system $\dot{C} = D(t)C$ where C is a 2×2 matrix that starts as the identity matrix, i.e. $C(0) = \mathbb{I}$. A solution $C(t)$, referred to as the fundamental solution matrix, to this equation is such that at any given time t, it maps an initial condition $(\xi_0, \dot{\xi}_0)^T$ to the evolved state $(\xi(t), \dot{\xi}(t))^T$. From Floquet theory, it follows that stability of the system (4.22) is achieved if, and only if, every eigenvalue λ_n of $C(T)$ has modulus less than or equal to one ($|\lambda_n| \leqslant 1$), see e.g. [184]. This can be seen from the realisation that for any initial condition $\mathbf{x}_0 = (\xi_0, \dot{\xi}_0)^T$, the solution at integer increments of the driving period T is given as powers of $C(T)$, i.e. $\mathbf{x}(nT) = C^n(T)\mathbf{x}_0$ for $n \in \mathbb{N}$. Moreover, provided that the damping γ_a in (4.22) is constant, the determinant of $C(T)$, which can be identified with the Wronskian, is conserved, thus leading to the observation that $\det C(T) = 1$. It follows that the eigenvalues λ of $C(T)$ are given by $2\lambda = t_C \pm \sqrt{t_C^2 - 4}$, which takes real values when the trace $t_C \equiv \mathrm{tr}C(T)$ has magnitude $|t_C| \geqslant 2$, and complex for $|t_C| < 2$. Since, $\det C(T) = \lambda_1\lambda_2 = 1$ must include at least one $|\lambda| > 1$ for distinct and real eigenvalues, the case $|t_C| \geqslant 2$ is unstable, whereas $|t_C| < 2$ is stable since $|\lambda_1| = |\lambda_2|$.

Writing $C(T) \equiv e^{AT}$, i.e. A is the matrix logarithm of $C(T)$, permits defining $\mathbf{p}(t) \equiv e^{-At}\mathbf{x}(t)$ which is a periodic function with period T. This result is commonly referred to as Floquet's theorem, and the implication for our case is that the solutions to (4.22) can be written

$$\xi_a(t) = e^{i\alpha_a t}Q(t) \quad \text{for} \quad Q(t) \equiv \sum_{n\in\mathbb{Z}} c_n e^{in\omega_d t} \tag{4.23}$$

where $Q(t)$ is some periodic function with period T, α_a is a potentially complex number referred to as the Floquet exponent, and $c_n \in \mathbb{C}$ are constants in a Fourier series. In general, we shall write $\alpha_a \equiv \omega_\alpha - i\lambda_a$, where λ_a is the growth rate of the unstable growth. The real part ω_a of the Floquet exponent α_a can be shown to either be $\omega_\alpha = \omega_d/2$, referred to as subharmonic response, or $\omega_\alpha = 0$, referred to as harmonic response [183, 185].

The result of this stability analysis is shown in Figure 4.1(a), where (4.22) has been used to compute the spectrum of $C(T)$ numerically, using a Runge-Kutta-4 (RK4) scheme (see B.1.1), for a range of driving frequencies $\omega_d = 2\omega_0$ and amplitudes F_0 of the external force $f(t) = F_0\cos(\omega_d t)$. The Figure exhibits the familiar [183] tongues (orange regions) of instability at integer multiples of half the driving frequency $\omega_0 \equiv \omega_d/2$, where odd multiples correspond to the subharmonic response, and the even multiples the harmonic response.

For a given set of fluid parameters, the eigenvalues k can be found by solving the discretization condition (4.14) for each azimuthal number m directly. However, as suggested by Ziener [179],

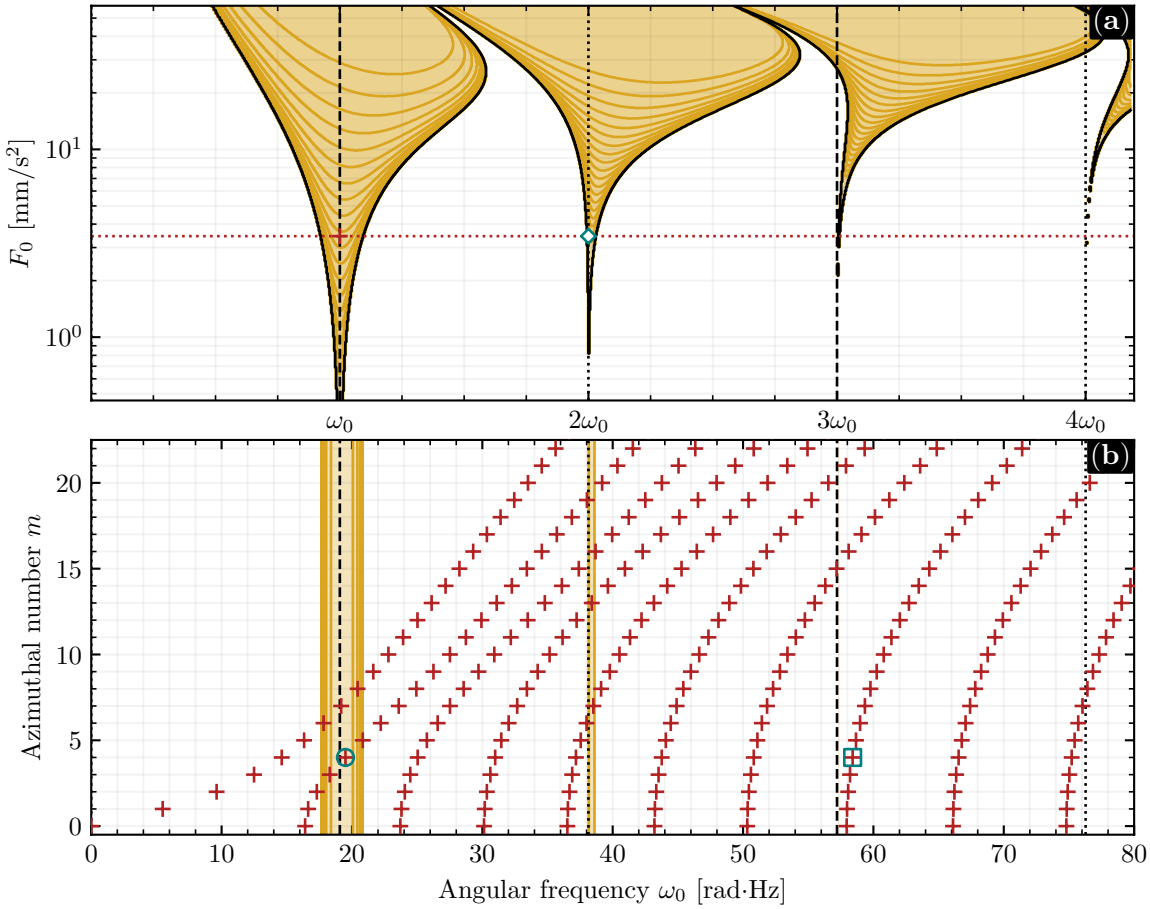

Figure 4.1 (Instability regions) Panel **(a)**: Stability plot for linear shaker system (4.22) at given resonant frequency ω_0 and shaker amplitude F_0, i.e. with vertical force $f(t) = F_0 \cos(2\omega_0 t)$. The white regions are always stable, while the orange regions may exhibit instabilities for sufficiently low values of the damping γ. The orange lines in these regions correspond to 19 different values of damping γ with log-linear spacing from 0.015 to 15.84. The black lines are the stability boundaries for $\gamma = 0$. The values in the experimental realisation are marked as a blue diamond. Panel **(b)** The eigenfrequencies $\omega_{m,k}$ for the modes in the system for $r_1 = 2\text{cm}$, $r_2 = 4\text{cm}$ and $h_0 = 17.5\text{mm}$ are drawn as red crosses as a function of azimuthal number m. For a given azimuthal number m, the red crosses count the number of zero-crossings of $R_m(kr)$ from left to right starting from 0. The expected dominant $m = 4$ mode is highlighted with a blue circle and the non-linear secondary mode with a blue square. In both panels, vertical black lines are drawn at integer multiples of half the driving frequency, dashed for odd multiples (subharmonic), and dotted for even (harmonic). The driving frequency (first vertical dotted line) is that of the experimental setup.

a more convenient numerical approach for determining k is to write the radial part of horizontal Laplacian* for a given azimuthal number m,

$$\widehat{D}\phi = -k^2\phi \quad \text{for} \quad \widehat{D} \equiv \partial_r^2 + \frac{1}{r}\partial_r + \frac{m^2}{r^2}, \tag{4.24}$$

and diagonalise a finite-difference formulation of $\widehat{D}$ with Neumann boundary condition at r_1 and r_2 (see Eq. (60) of Ziener [179]). By using the experimental parameters, which will be introduced later, this method results in a spectrum of $k \in \mathcal{K}_m$ for each m that can be inserted into (4.21b) to give the eigenfrequencies ω_a for each mode $a = (k_a, m_a)$ in the system. The resulting spectrum is shown as red crosses in panel (b) of figure 4.1. Note that discrete k values that solve (4.14) can be ordered by the number of zero crossings in the radial function, i.e. the number of solutions to $R_m(kr) = 0$. Therefore, we shall hereby refer to $k \in \mathcal{K}_m$ as k_n where the label $n = 0, 1, \ldots$ counts the number of zero crossings of $R_m(k_n r)$. That is, an eigenmode f_a of the system is determined by a pair of integers $a = (m, n) \in \mathbb{Z}^+ \times \mathbb{Z}^+$, where m is the azimuthal number, and n is the number of radial zero-crossings.

II.3. Corrections in the Nonlinear regime

We have now seen that instabilities arise from the linear system (4.21), in which modes are expected to grow exponentially over time, see equation (4.23). However, in a realistic setup, this exponential growth must eventually be halted as the excitations ξ of the interface approaches a size comparable to the container. Note that in this regime, it is not always given that the notion of a single-valued interface survives. For example, the waves may collapse into disconnected bubbles, or the two fluids may mix, blurring the notion of the interface altogether. Assuming such complications to be absent, we maintain the notion of an interface $z = \xi(t, r, \theta)$ and pursue the onset of nonlinearities. From the modelling perspective, what happens is that the assumption $|\xi| \ll h_0$, which was used to linearise the equations of motion for the free surface, is violated. In this section, we extend the approach introduced by Miles [172, 173] to two-fluid interfaces with surface tension. The strategy is to consider the weakly non-linear regime, in which the linear dynamics (4.21) receives higher order terms in ξ. It is the appearance of such higher-order terms that must be responsible for preventing the unbounded growth of modes in the system. The key insight is that the boundary value problem (4.8), which remains valid in the non-linear regime, can be re-formulated as a variational principle for $\Phi_\pm$, referred to as Dirichlet's variational principle. The functional whose stationarity implies

*Here, the horizontal Laplacian refers to the Laplacian $\nabla^2 = r^{-1}\partial_r r \partial_r + r^{-2}\partial_\theta^2$ in the (r, θ)-plane.

(4.8) is the Dirichlet action [172] (see appendix D for the full story)

$$S_\pm = \frac{1}{A}\iiint_{V_\pm} \frac{1}{2}(\nabla\Phi_\pm)^2 dV_\pm - \frac{1}{A}\iint \dot{\xi}\,\Phi_\pm|_{\Gamma=0}\,dA \tag{4.25}$$

$$= \frac{1}{2}\varphi_{\pm,a}K^{(\pm)}_{ab}\varphi_{\pm,b} - \dot{\xi}_a D^{(\pm)}_{ab}\varphi_{\pm,b} \tag{4.26}$$

for each fluid ($\pm$) separately. In the final equality (4.26), summation over repeated indices is implicit. Here, the coefficients of a decomposition into the linear eigenmodes (4.10) had been used as generalised coordinates to introduce the two matrices

$$K^{(\pm)}_{ab} \equiv \iiint_{V_\pm} dV_\pm \nabla\psi_{\pm,a}\cdot\nabla\psi_{\pm,b} \quad \text{and} \quad D^{(\pm)}_{ab} \equiv (f_a, \psi_{\pm,b}(r,\theta,\xi))\,, \tag{4.27}$$

where $(\cdot,\cdot)$ refers to the L_2 inner product introduced in (4.13).

Invoking the stationarity of (4.25) with respect to variations in $\phi^{(j)}_b$ then gives a matrix relation $K_{a,b}\phi^{(j)}_b = \dot{\xi}_a D_{a,b}$, that serves as a natural extension of the linear relation (4.15). The strategy is to expand $\mathfrak{L}^{\pm}_{ab} = (K^{-1})_{ac}D_{cb}$ in powers of ξ_a, resulting in non-linear relationship between ϕ_a and $\dot{\xi}_a$ in powers of ξ_a, that should reduce to (4.15) in the limit $|\xi| \ll h_0$ to leading order. The result, in correspondence with equation (2.14) of Miles [172], can be written (see appendix D for details)

$$\frac{L}{A} = \frac{L_0}{A} + \sum_a \frac{\Sigma\rho}{2T_a}\left(\dot{\xi}_a^2 - \omega_a^2(t)\xi_a^2\right) \tag{4.28}$$

$$+ \frac{\Delta\rho}{2}\sum_{abc}\xi_c\mathcal{A}_{cba}\dot{\xi}_a\dot{\xi}_b + \sum_{abcd}\frac{\Sigma\rho}{4}\xi_d\xi_c\left[\mathcal{A}_{dcba}\dot{\xi}_a\dot{\xi}_b + \frac{\sigma\mathcal{M}_{cabd}}{2\Sigma\rho}\xi_a\xi_b\right], \tag{4.29}$$

$$\text{for} \quad \Delta\rho \equiv \rho_- - \rho_+ \quad \text{and} \quad \Sigma\rho \equiv \rho_- + \rho_+, \tag{4.30}$$

where $L_0 \equiv -\frac{1}{2}A\Sigma\rho g h_0^2 - \sigma A$ is a constant and the coefficients

$$\mathcal{A}_{dcb} \equiv \left(2T_bT_c - k_b^2 - k_c^2 + k_d^2\right)\frac{\mathcal{C}_{bcd}}{2T_bT_c}, \tag{4.31a}$$

$$\mathcal{A}_{dfcb} \equiv -\frac{T_b+T_c}{T_bT_c}\mathcal{D}_{fdbc} + \sum_e \frac{\mathcal{C}_{dce}\mathcal{C}_{fbe}}{2T_bT_cT_e}\left(k_e^2 + k_c^2 - k_d^2\right)\left(k_b^2 + k_e^2 - k_f^2\right), \tag{4.31b}$$

$$\mathcal{C}_{abc} \equiv (f_a, f_bf_c)\,, \tag{4.31c}$$

$$\mathcal{D}_{abcd} \equiv (f_af_b, \nabla f_c\cdot\nabla f_d)\,, \tag{4.31d}$$

$$\mathcal{M}_{abcd} \equiv (\nabla f_a\cdot\nabla f_b, \nabla f_c\cdot\nabla f_d) \tag{4.31e}$$

are constants for a given geometry. Hence, and in what follows, we shall abbreviate $T_a \equiv k_a\tanh(k_ah_0)$.

When parametrically amplified, multiple modes ξ_c may experience growth simultaneously, c.f. Figure 4.1. However, as the growth continues, one mode, hereby denoted ξ_b, will grow more rapidly than all the others. If so, this mode b eventually establishes dominance over all other modes, i.e. $|\xi_b| \gg |\xi_a|$ for all $a \neq b$. In that case, one may approximate the equations of motion that follow from (4.28) supplied with the dissipation function (4.19) by (see appendix D for details)

$$\ddot{\xi}_a + 2\gamma_a\dot{\xi}_a + \omega_a^2\xi_a + \tilde{\rho}T_a\mathcal{A}_{bba}\xi_b\ddot{\xi}_b + \frac{1}{2}\tilde{\rho}T_a(2\mathcal{A}_{bba} - \mathcal{A}_{abb})\dot{\xi}_b^2 + A_{ab}\xi_b\dot{\xi}_b^2 - M_{ab}\xi_b^3 + \frac{1}{4}T_a\left(\mathcal{A}_{bbba} + \mathcal{A}_{bbab}\right)\xi_b^2\ddot{\xi}_b \simeq 0, \tag{4.32a}$$

$$\text{for} \quad A_{ab} \equiv \frac{1}{4}T_a\left(2\mathcal{A}_{bbba} + 2\mathcal{A}_{bbab} - \mathcal{A}_{babb} - \mathcal{A}_{abbb}\right) \quad \text{and} \quad M_{ab} \equiv T_a\frac{\sigma\mathcal{M}_{bbba}}{2\Sigma\rho}, \tag{4.32b}$$

for any mode a, where $\tilde{\rho} \equiv \Delta\rho/\Sigma\phi$. To leading order, the non-dominant modes $a \neq b$ evolve according to the linear equations (4.21a), but are subject to non-linear sourcing by the dominant mode ξ_b. The non-linear evolution equation for the dominant mode gives a form equivalent to performing the substitution $a = b$ in (4.32), i.e.

$$\ddot{\xi}_b + 2\gamma_b\left(1 - A_{bb}\xi_b^2\right)\dot{\xi}_b + \left(\omega_b^2 - 2M_{bb}\xi_b^2 + A_{bb}\left[\dot{\xi}_b^2 - \omega_b^2\xi_b^2\right]\right)\xi_b \simeq 0. \tag{4.33a}$$

This non-linear evolution containing effective self-interaction terms offers insight into the mechanism responsible for preventing the growth of the unstable mode once it has reached a certain magnitude. When the amplitude ξ_b^2 grows, the natural frequency shifts and the effective damping is modified, which eventually brings the parametric amplification to a halt. An approximate estimate of this amplitude threshold $\xi_{b,\mathrm{thr}}$ can be found from $|A_{bb}\xi_{b,\mathrm{thr}}^2| \simeq 1$, i.e. when nonlinear effects become of order unity. Numerical computation of the coefficient A_{bb}, with $b = (m, n) = (4, 1)$, gives $\xi_{b,\mathrm{thr}} \simeq 4.7\mathrm{mm}$ for the geometry considered.

There are no quadratic terms in the non-linear effective self-interaction dynamics (4.33). One consequence is that the interfacial height is manifestly symmetric under change of sign in $\xi_b \to -\xi_b$, i.e. it remains insensitive to the difference between up and down. Indeed, the nonlinear dynamics (4.33) is qualitatively similar to what one would have found by a phenomenological expansion of γ_b and ω_b from (4.21a) that obeys this symmetry. Note also that the absence of quadratic corrections to the non-linear dynamics means that the effective Lagrangian for the dominant mode corresponds to a ϕ^4-type theory.

III. Experimental realisation

The experiment consists of an annular cylindrical container, with Nylon walls and lids made of machined acrylic, with inner radius $r_1 = 20\mathrm{mm}$ and outer radius $r_2 = 40\mathrm{mm}$ of height

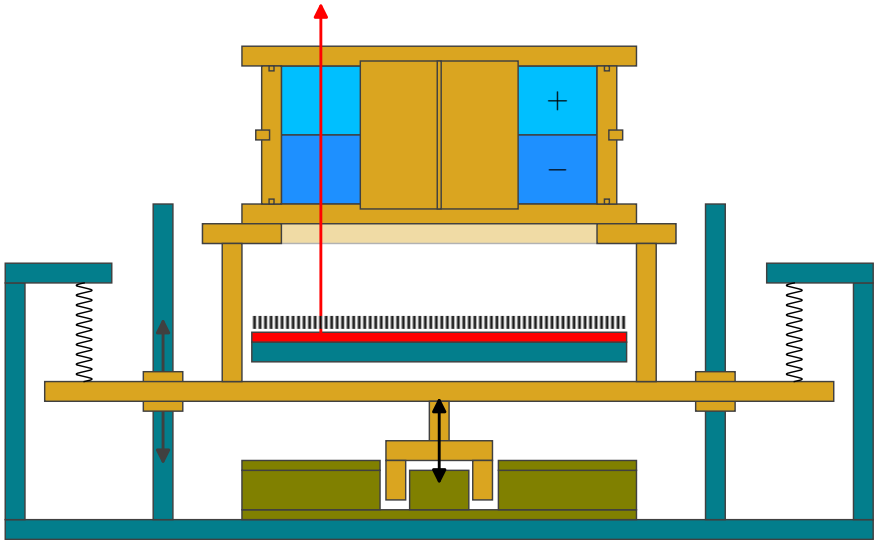

Figure 4.2 (Experimental Setup) A platform (orange) is suspended by springs and guided vertically by air bearings. The vertical movement of the platform is excited by an electromagnetic driver (green). On top of the suspended platform is an annular cylindrical basin filled with equal amounts of two immiscible fluids. The top and bottom lids of the container are transparent, and an illuminated (red) checkerboard pattern is mounted on the rigid (blue) platform and is visible through the top of the basin.

$2h_0 = 35\text{mm}$ (see Figure 4.2). The container is filled with an aqueous potassium carbonate solution (fluid $-$) and ethanol-water solution (fluid $+$) of equal amounts. The measured densities of the two fluids are $\rho_- = 1276(10)\text{kg/m}^3$ and $\rho_+ = 907(7)\text{kg/m}^3$, with surface tension $\sigma = 2.5(10) \times 10^{-3}\text{N/m}$. The basin rests on a platform (orange in Figure 4.2) that is guided by pneumatic bearings and suspended by springs. Attached to the platform is an electromagnetic driver (green in Figure 4.2) whose oscillation supplies a vertical force. The springs are chosen so that the spring-mass system has a resonant frequency that matches the frequency of the force applied by the driver. Attached to the container are a thermometer and an accelerometer. The latter is used to measure the off-axis motion of the platform, which serves to align the base (turquoise in Figure 4.2). Using the accelerometer, the frequency $\omega_d \equiv 2\omega_0 = 6.07(2\pi)\text{Hz}$ (see blue diamond in figure 4.1(a)) and amplitude $F_0 = 0.352g = 3.45\text{m/s}^2$ of the driving force $f(t)$ is measured (See Figure 4.3).

The driving force $f(t)$ starts at time $t_0 = 0$ and and stops at $t_{stop} = 26.36\text{s}$, after having completed 160 periods. The transients in the spring-mass system leads to a period of about 4s for the acceleration of the container to reach a constant value after t_0 and t_{stop} (see Figure 4.3).

After the driving force is turned off at t_{stop}, the system is set to relax over a period of 93.6 sec-

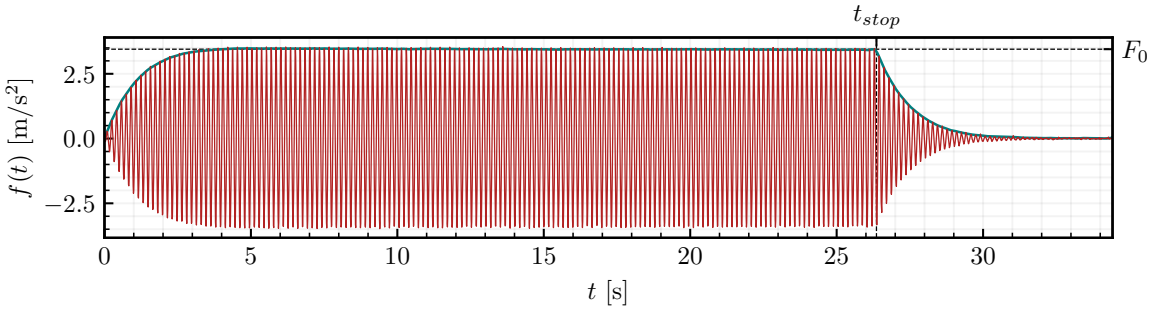

Figure 4.3 (Driving force) The measured vertical acceleration (red curve) of the container in a single experiment is plotted with its upper envelope (blue curve). The time $t_{stop} = 26.36\text{s}$ at which the driving force is turned off is highlighted (vertical dashed line), as well as the constant amplitude $F_0 = 3.45\text{m/s}^2$ (black dashed line).

onds, before the process is restarted after a total of 120 seconds has passed. This process is repeated 1500 times, over a total duration of 49 hours and 47 minutes. During the first 35 seconds of each realisation the interface $z = \xi(t, r, \theta)$ is recorded. The result is a collection of 1500 measurements $\{\xi_i(t, r, \theta)\}_{i=1}^{1500}$ for $t \in [0, 35]$s.

To reconstruct the interface, a two-dimensional Fourier Transform Profilometry (FTP) method [186–188], was used. The fundamental principle of this method is that when a periodic pattern, in this case an illuminated cartesian checkerboard pattern, mounted on the rigid platform, is observed through the interface, then local deformations of the pattern are proportional to the surface gradient. This permits recovery of the surface gradients, which can be integrated to obtain the full height fields $\{\xi_i(t, r, \theta)\}_{i=1}^{1500}$. Note, however, that due to a meniscus, which we have assumed to be absent in the modelling, the reconstruction method breaks down near the walls of the container. For this reason, a trustworthy height field $\xi(t, r, \theta)$ can only be obtained in the radial window $r \in [22\text{mm}, 38\text{mm}]$. Due to these missing points in the reconstruction, the dominant amplitudes ξ_b cannot be extracted using the orthonormality relation. Instead, the reconstructed height fields $\xi(t, r, \theta)$ are decomposed into azimuthal numbers and separated into positive and negative frequencies, i.e.

$$\xi(t, r, \theta) = \sum_{m\in\mathbb{Z}} \xi_m e^{im\theta} \propto \sum_{m\in\mathbb{Z}} e^{im\theta} \int d\omega \left[b_{m,\omega} e^{-i\omega t} + b^*_{m,\omega} e^{i\omega t} \right]. \tag{4.34}$$

Here, the constant of proportionality is chosen such that the amplitude $b_{m,\omega}$ aligns with the theoretical amplitudes ξ_b from the mode decomposition (4.10) with (4.12). That is, for a fixed radius r_0, the (complex) amplitudes $b_{m,\omega}$ are related to the mode amplitudes ξ_b through $4\text{Re}(b_{m_b,\omega_b}) = \xi_b N_b^{-1} R_{m_b}(k_b r_0)$*.

*Here, the factor $4\times$ comes from the factors $1/2$ contained in the $\cos(m\theta)$ and the (implicit) $\cos(\omega t)$ in the

The modulus of the resulting 1500 amplitudes for $b_{m,\omega}(t, r_0)$ for $m = 4$ and $\omega = \omega_0$ are shown in panel (a) of Figure 4.4 for the fixed radius $r_0 \simeq 24\text{mm}$. The figure shows the time evolution of the ensemble as it passes four different regimes: (1) The time before the amplitudes have grown beyond the noise floor of the detection method, (2) The steady exponential growth expected from Floquet theory, (3) the non-linear regime in which the unusually large modes have reached the plateau $\xi_{b,\text{thr}}$ and (4) the damped stage after the shaker, and thus the instability, has been turned off.

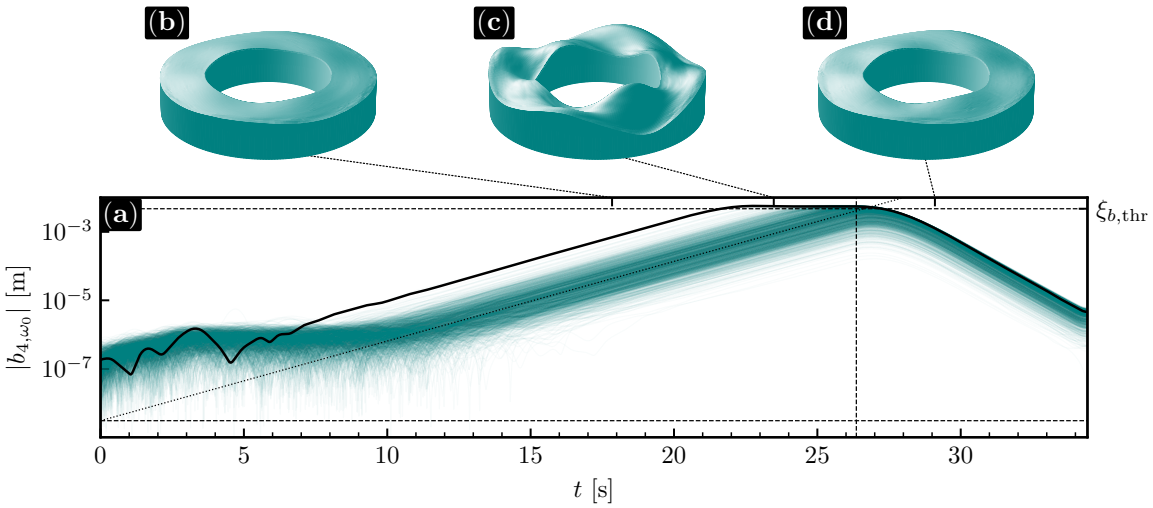

Figure 4.4 (Experimental Data) Panel **(a)**: The instantaneous amplitudes $|b_{m,\omega}|$ for $m = 4$ and $\omega = \omega_0$ (half the driving frequency) for all 1500 realisations (blue). An exceptionally non-linear realisation is highlighted in solid black. The non-linear threshold $\xi_{b,\text{thr}}$ and the average equilibrium amplitude $\xi_{b,\text{ns}}$ (see Eq. (4.36)) for the selected value of σ_η are drawn as dashed black lines. A dotted black line is drawn to indicate the evolution $\xi_{b,\text{ns}} e^{\lambda_E t}$ from initial amplitude $\xi_{b,\text{ns}}$, where λ_E is the average growth rate. A vertical black dashed line is drawn to indicate the time $t_{stop} = 26.36\text{s}$ at which the driving force was switched off. Panels **(b),(c),(d)**: The reconstructed interface is rendered at three instances $t = 17.84\text{s}$ (b), $t = 23.48\text{s}$ (c) and $t = 29.1\text{s}$ (d) for the exceptionally non-linear run. Note that the rendering is shown only for the trusted radii, i.e. $22\text{mm} \leqslant r \leqslant 38\text{mm}$, and that the top fluid is rendered transparent.

A rendering* of the full height field $z = \xi(t, r, \theta)$ measured in one of the experiments is shown for three different temporal snapshots, $t = 17.84\text{s}, 23.48\text{s}$ and 29.1s, in panels (b), (c) and (d) of

eigenmode definitions.

*The rendering is chosen such that the coloring is proportional to the (squared) dot product between the surface normal and unit vector pointing away for a light-source.

figure 4.4 respectively. These three snapshots, which correspond to regions (2), (3) and (4), show a dominant $m = 4$ mode (see four crests at r_1 in panel (c)) with one zero-crossing in excellent agreement with the prediction from the numerical Floquet analysis presented in figure 4.1 (see the blue circle in panel (b)).

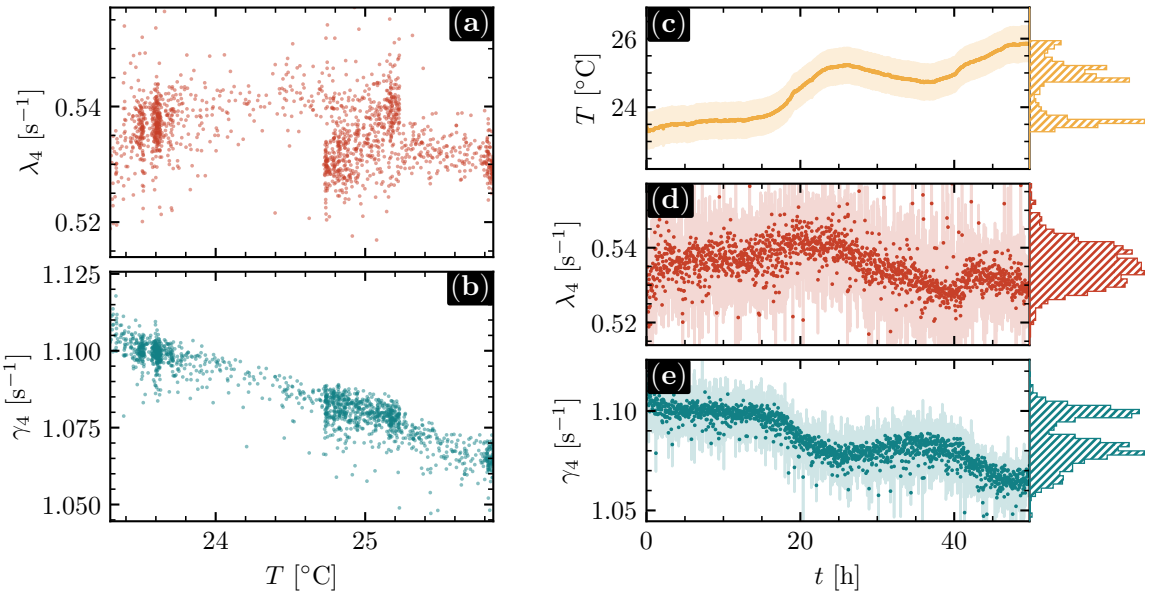

Figure 4.5 (Thermal drift) Panels **(a)** and **(b)**: The measured growth rates λ_4 (panel (a)) and decay rates γ_4 (panel (b)) for the all realisations versus the temperature T. It is clear that the damping γ_4 is anti-correlated with temperature T. Panels **(c)**,**(d)** and **(e)**: The temperature T (panel (c)), growth rate λ_4 (panel (d)) and damping γ_4 (panel (e)) versus the time t of the full repeated experiment. In each panel of the three panels, the corresponding distribution is shown on the right side.

In each experimental realization $\xi(t)$, the growth rate λ_4 and decay rate γ_4 can be extracted from the data by finding, and fitting, linear segments of $\ln|b_{4,\omega_0}(t)|$. The result of this procedure is shown in Figure 4.5. Panels (a) and (b) depict the variation of λ_4 and γ_4 with temperature T, and panels (c), (d) and (e) show the time dependence of these quantities. In panel (c) there are non-Gaussian temperature variations, varying with the time of day. We see that whereas the growth rate λ_4 of the $m = 4$ mode is relatively insensitive to temperature, the damping decreases linearly with temperature. This is expected as the damping scales with viscosity, which is inversely proportional to the temperature.

IV. Numerically Simulated Stochastic Evolution

To compare the experimental results with the non-linear models, we consider numerical simulations of equations (4.32) and (4.33) subject to the measured vertical force $f(t)$. The measured accelerations $f(t)$ are needed for two reasons: (1) the transients (see Figure 4.3) affects the dynamics, and (2) there is some, although small, variation in $f(t)$ from experiment to experiment.

A naive numerical implementation of the non-linear dynamics (4.32) and (4.33) is, however, problematic as one would need knowledge of the initial state of the interface at rest. Moreover, during the ramp-up period of the driving force $f(t)$ (see Figure 4.3), the driving force is too small for the instability to appear (see Figure 4.1) which, in combination with the phenomenological damping γ_b, leads to an unrealistic damped evolution during this period.

This conundrum is resolved by the observation that there is no such thing as an interface at rest. Instead, for sufficiently small amplitudes ξ, the dissipation due to γ_b is kept at bay by some fluctuating, stochastic influence $\eta(t, \mathbf{x})$. To model this, let us introduce a Langevinian stochastic term $\eta(t, \mathbf{x})$ on the right side of equations (4.32) and (4.33).

To see how the initial state of the interface is determined through the inclusion of such a noise term, imagine that the driving force $f(t) = 0$ is turned off so that the system is left to relax towards its equilibrium state. In this state, the amplitudes are expected to be very small, so that the evolution of the system is well described by the linear dynamics (4.21a). Over long time scales, the acceleration $\ddot{\xi}_b$ is negligible*, in which case the system becomes over-damped and can be formulated as stochastic process (see e.g. [158])

$$2\gamma_a d\xi_a = -\omega_a^2 \xi_a dt + \sigma_\eta dB_t, \tag{4.35}$$

where the noise η has been assumed to be featureless white noise with standard deviation σ_η permitting us to write $d\eta = \sigma_\eta dB_t$ where dB_t is a Wiener process, i.e. $dB_t^2 \simeq dt$ (see e.g. chapter 4 of Gardiner [158]). Equilibrium is reached when ensemble averages $\langle F(\xi_b)\rangle$ are constant for any function F. This can be turned into a differential equation for the probability density function, resulting in a central Gaussian with standard deviation σ_ξ given by $4\gamma_b\omega_b^2\sigma_\xi^2 = \sigma_\eta^2$. The average amplitude of mode ξ_b is therefore expected to be

$$\xi_{b,ns} \equiv \langle|\xi_b|\rangle = \frac{\sigma_\eta}{\sqrt{2\pi\gamma_b}\omega_b}, \tag{4.36}$$

prior to turning the driving force on. Note that if the equilibrium (4.36) was of a thermal nature, the Gaussian distribution should take the form of a Boltzmann distribution with the quadratic form of the Hamiltonian that follows from (4.18) in the overdamped limit. However, this is found not to match the experimental data. That is, the initial state is not well approximated by thermal excitations alone. Instead, the background noise is assumed to be significantly affected by external noise sources.

*Here, long time is taken to mean large in comparison with the natural period $2\pi/\omega_b(0)$ of the considered mode.

Now let $\xi_{b,n} \equiv \xi_b(n\Delta t)$ and consider a deterministic timestep $\xi_{b,n} \mapsto \xi_{b,n+1}$ performed using a Runge-Kutta-4 (RK4) scheme (see B.1.1). After the step, we supply the stochastic contribution by $\xi_{b,n+1} \mapsto \xi_{b,n+1} + \eta(t)\Delta t$, where η is sampled from a central Gaussian distribution with variance* $\sigma_\eta^2/\Delta t$.

For a given geometry, measured driving force $f(t)$, and set of fluid parameters, a simulation using the stochastic model therefore only depends on a single parameter σ_η, which is related to the excitation of the interface at rest. However, to model the initial non-Gaussianity, which we shall discuss in the next section, there is a need for a variation in the effective noise σ_η from experiment to experiment. To match the initial distribution over experimental realisations, we consider a data-driven ansatz $\sigma_\eta \propto |b_{m,\omega}(t_0)|$ at some reference time t_0 chosen in the early linear regime†. Finally, white gaussian noise is added to the simulated distributions ξ_b to mimic the detection noise relevant at early times.

V. The Statistical Approach

As seen in section IV, the naive treatment of the noise predicts a Gaussian equilibrium distribution for the mode amplitudes. However, we shall see that the ensemble starts off with a slight non-gaussianity. Moreover, during the early growth, the modes evolve linearly with (4.21a), for which the shape of the distribution remains effectively unchanged. This can be seen in panel (a) of figure 4.6, for which the fixed-time distribution of the experimentally observed amplitudes $\mathrm{Re}[b_{4,\omega_0}]$ is depicted at four different times, with a fitted Gaussian distribution shown as a black dashed line for comparison. The first (red) is at $t = 7\mathrm{s}$, where the distribution is given by the gaussian white noise from the detection method. The next (orange) is in the middle of the linear regime, at $t = 17.84\mathrm{s}$, where the distribution is found to be more sharply peaked (leptokurtic) than a Gaussian. This distribution remains approximately unchanged until the early non-linear period (green) at $t = 23.48\mathrm{s}$. Finally, after the non-linear period, when the system has entered the damped regime (blue), the distribution is changed and has attained a skewness. The four selected times are highlighted with vertical dashed lines in panels (b), (c) and (d) of figure 4.6.

In panel (b) of figure 4.6, the averaged square amplitude $\langle |b_{4,\omega_0}|^2 \rangle$ is drawn (blue line) as a function of time. Here, and in all that follows, averages over experimental realisations are referred to as $\langle \cdot \rangle$. For the numerically simulated data, averages $\langle \cdot \rangle$ are computed over repeated runs. For comparison, the corresponding values $\langle |\xi_b^{(\mathrm{sim})}|^2 \rangle$ are drawn (red line) together with the experimental data. The agreement of the two curves confirms that the stochastic non-linear simulations IV accurately predict the ensemble-averaged amplitude of the dominant mode.

*Note that if the simulation samples from a distribution with standard deviation σ each timestep of duration Δt, then the parameter σ_η as defined in the stochastic process (4.35) is given by $\sigma_\eta = \sigma\sqrt{\Delta t}$.

†This can not be too early, as the signal is swamped by detection noise at early times, which is, as we shall see, perfectly gaussian.

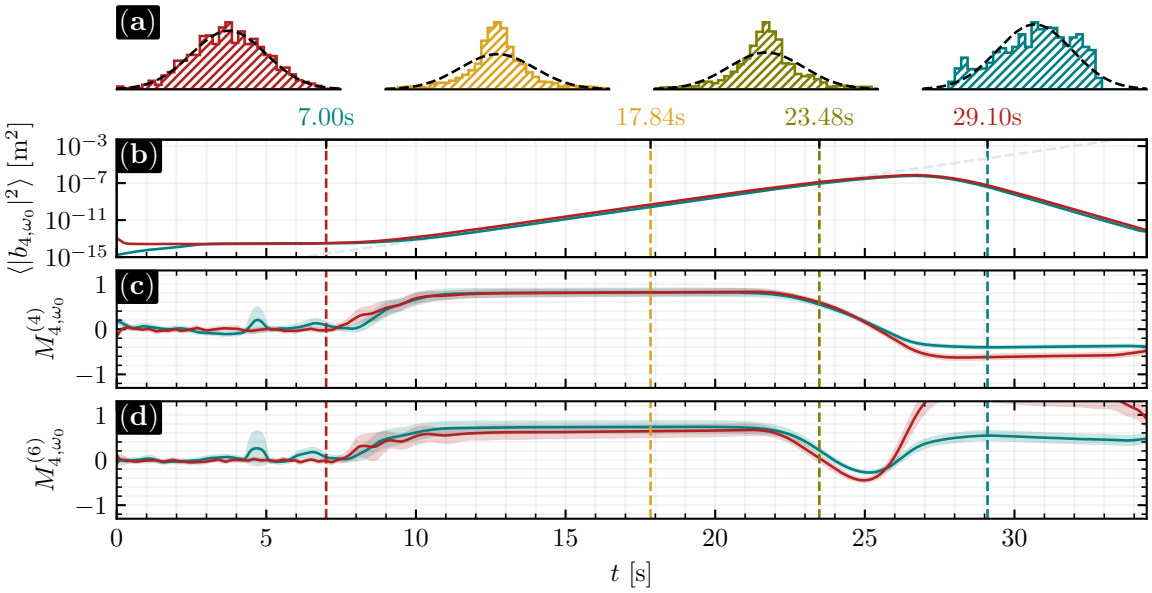

Figure 4.6 (Ensemble evolution) Panel **(a)**: Ensemble distributions of (the real part of) the instantaneuous amplitudes $\mathrm{Re}[b_{m,\omega_0}(t)]$ of the dominant $m = 4$ mode at four different times; the noise-floor (red), the log-linear unstable growth (orange), the non-linear period (green) and the decay (blue). Panel **(b)**: The average squared amplitudes $\langle |b_{4,\omega_0}(t)| \rangle$ for experiment (blue) and simulation (red). Panels **(c)** and **(d)**, exhibit the statistical measures $M^{(2n)}_{m,\omega}$ for $n = 2, 3$ computed on both experimental data (blue) and using numerical simulations (red), both with bootstrapped bands of one standard deviation.

To investigate the distributional properties of the ensemble more quantitatively, we take inspiration from the statistical machinery of Quantum Field Theory (QFT). In a recent study, a roadmap on how to extract an effective QFT description purely from experimental data was presented [103]. Here, the central quantities are higher-order equal-time correlation functions, which can be used to determine the effective action [104]. This effective description is, however, developed with quantum many-body systems in mind, and a dedicated study is needed to determine exactly how these methods, e.g. the recovery of a diagrammatic description from [103], would carry over to the case of classical fluid interfaces. Taking inspiration from these works, we consider the generating functional, or characteristic function,

$$Z[J] \equiv \left\langle \exp\left(i \int J(s) X(s) \, ds \right) \right\rangle , \tag{4.37}$$

where $X(s)$ is a random variable with auxiliary function $J(s)$ for each state s. In our case, this corresponds to $J(s)X(s)ds = s_a(t)\xi_a(t)dt$ with $s \in \mathbb{Z}^+ \times \mathbb{R}$. The significance of the gener-

ating functional $Z[J]$ lies mainly in its ability to generate all statistical moments, or full correlation functions, by taking functional derivatives $\delta/\delta J$ with respect to the currents of interest, i.e.

$$\langle X(s_1)...X(s_n)\rangle \equiv (-i)^n \frac{\delta^n Z[J]}{\delta J(s_1)...\delta J(s_n)}\bigg|_{J=0}. \tag{4.38}$$

Similarly, the logarithm $\ln(Z)$ generates all cumulants, which are also called n-point functions or (connected) correlation functions $\langle X(s_1)...X(s_n)\rangle_C$. Here, the n'th order cumulants can be expressed in terms of the n first moments via (see e.g. [158])

$$\left\langle \prod_{j=1}^{n} X(s_j) \right\rangle_C = \sum_{p\in P_n} (-1)^{|p|-1}(|p|-1)! \prod_{B\in p} \left\langle \prod_{i\in B} X(s_i) \right\rangle, \tag{4.39}$$

where $\{X(s_i)\}_i$ are random variables, $p \in P_n$ is a partition of n elements into $|p|$ subcollections, $B \in p$ is one of these subcollections and $i \in B$ are the elements of B.

Since (4.37) factorizes over independent variables, the cumulants $\langle X_1...X_n\rangle_C$, being coefficients in the series expansion of $\ln(Z)$, must vanish if, and only if, all variables $X_1, ..., X_n$ are independent. That is, if modes evolve independently, then the only non-zero cumulants are those involving equal modes at equal times, i.e. $\langle |b_{m,\omega}(t)|^n\rangle_C$. Since moments generally increase in magnitude as the order increases, i.e. $\langle X^{2n}\rangle \geqslant \langle X^n\rangle^2$, the n^{th} cumulant scales with the n^{th} moment. To eliminate this scaling, let us consider the quantities

$$M^{(2n)}_{m,\omega}(t,r) \equiv \frac{\langle \left(b^*_{m,\omega} b_{m,\omega}\right)^n\rangle_C}{\langle \left(b^*_{m,\omega} b_{m,\omega}\right)^n\rangle}, \tag{4.40}$$

hereby referred to as relative cumulants. Crucially, for a normally distributed classical ensemble, the cumulant is zero for all $n > 1$ so that the quantities $M^{(2n)}_{m,\omega}$ vanish entirely in this case [189]. That is, the deviation of $M^{(2n)}_{m,\omega}$ from zero is a measure of the non-gaussianity of the ensemble. In QFT, the cumulant in equation (4.40) is referred to as the full correlation function, whereas the moment is its connected part. The latter vanishes for non-interacting (quadratic) fields, and it is the fundamental quantity for studying particle scattering and decay processes [190].

The quantity $M^{(2n)}_{m,\omega}$ with $m = 4$ and $\omega = \omega_0$ (dominant mode) is exhibited for both experimental and simulated data in panels (c) and (d) of figure 4.6 for $n = 2$ and $n = 3$ respectively. As expected, the white detection noise during the early period up to about $t = 8$s is Gaussian, so that $M^{(2n)}_{m,\omega}$ is zero there. Thereafter, when the mode amplitudes have grown out of the detector noise, the relative cumulants take a constant non-zero value, indicating a residual non-gaussianity from the early period. When the exceptionally large modes enter the non-linear regime around $t = 22$s, the distribution changes considerably. Conceptually, what is going on is that as the ensemble reaches the non-linear threshold, the upper tail of the distribution is deformed by the non-linear threshold, leading to a deformation of the initially symmetric distribution.

The behaviour of the higher order cumulants exhibited in panels (b),(c) and (d) of figure 4.6 are in good agreement with the numerical predictions based on the stochastic non-linear model. That is, the effective model recovers both the average behaviour and the behaviour of the ensemble averages.

VI. The Emergence of Secondaries

We have now seen that the system consistently displays the exponential amplification, stagnation period and subsequent decay of the resonant $m = 4$ mode, with wavenumber $k_1/(2\pi) \approx 0.35\,\mathrm{cm}^{-1}$ corresponding to one zero-crossing. Next, we turn our focus towards the excitation of other modes as the dominant mode ξ_b turns non-linear. Here, the relevant equation of motion is the sourced linear oscillator in equation (4.32), for which a numerical study of the coefficients shows that the main contributions should lie in the $m = 4$ mode at other wavenumbers k.

This presents a difficulty in the data analysis as the breakdown of the detection method near the boundaries of the system prevents accurate decomposition of the $m = 4$ mode into the respective Bessel modes. This is further complicated by the fact the dominant $b = (m, k) = (4, k_1)$ mode is, as expected, parametrically amplified at all integer multiples of ω_0 (see e.g. [183]), meaning that frequency-filtering is insufficient. Instead, we consider the radial Fourier spectrum $\tilde{b}_{m,\omega}(t, k_r)$ at different frequency bands ω and radial wavenumbers k_r.

In panel (a) of figure 4.7 this quantity is displayed for two different modes (blue) together with the corresponding ξ_a and ξ_b from numerical simulations (red). The first mode (solid blue) is the dominant mode, which is found from considering $\tilde{b}_{m,\omega}(t, k_r)$ the primary resonance band ω_0 and filtered at around the value for $k_r = k_{r,1} \approx 1/2\mathrm{cm}$ for which the mode $(4, k_1)$ with one zero-crossing is peaked (see blue circle in panel (b) of figure 4.1). The second, subdominant mode, is taken at the third resonance band $3\omega_0$ and with $k_r = k_{r,2} \approx 2/\mathrm{cm}$, where $k_{r,2}$ is where the mode $(4, k_7)$ with seven zero-crossings is peaked (see blue square in figure 4.1(b)). Here the numerical simulations are based on non-linear self-interactions (4.33) for the dominant mode (solid red) ξ_b with $b = (4, k_1)$ as usual, and non-linear sourcing (4.32) for the subdominant (dashed red) ξ_a for $a = (4, k_7)$.

We observe that experiment and simulation are in good agreement and that the subdominant mode $a = (4, k_7)$ is amplified at a much larger rate than the dominant modes $b = (4, k_1)$. Here, it should be stressed that the exponential growth of a is not the result of parametric resonance, as this would result in a growth rate comparable to that of the primary resonance b. In fact, at early times around $t = 18\mathrm{s}$, the subdominant mode exhibits a contribution from parametric resonance as the log-linear slope is parallel with the dominant one in this period.

The similarity between cosmic preheating and the interfacial dynamics of our two fluids lies in the parametric amplification of field modes resulting from an oscillating background source and the eventual breakdown of the instabilities. In fact, the linear dynamics for the two-fluid system

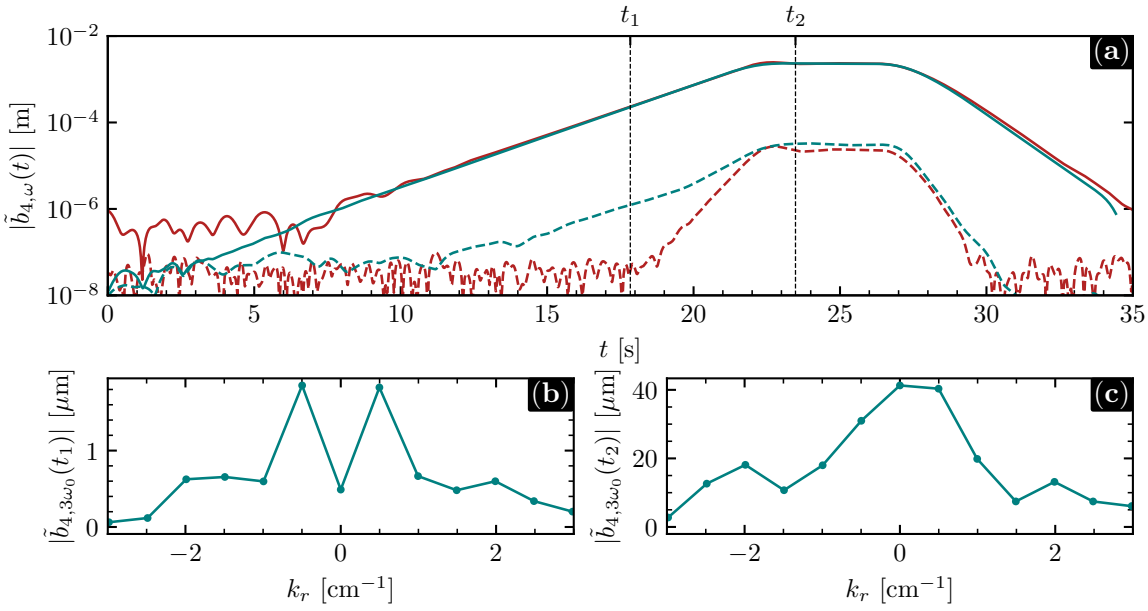

Figure 4.7 (Secondaries) Panel **(a)**: Radial Fourier transform of experimentally (blue) reconstructed instantaneous amplitudes $\tilde{b}_{4,\omega}(t, k_r)$ in comparison with the results $\xi_a^{(\mathrm{sim})}$ and $\xi_b^{(\mathrm{sim})}$ from numerical simulations (red). The dominant mode, $\xi_b^{(\mathrm{sim})}$ for the simulation and $\tilde{b}_{4,\omega_0}(t, k_{r,1})$ for the experimental data is drawn as solid lines. The secondary modes $\xi_a^{(\mathrm{sim})}$ and $\tilde{b}_{4,3\omega_0}(t, k_{r,2})$ are drawn as dashed lines. Dashed light blue lines are drawn to emphasise the log-linear growth of the experimental data. These curves have growth rates $\lambda_0 = 0.52/\mathrm{s}$ (top) and $\lambda_1 = 1.48/\mathrm{s} \approx 2.85\lambda_0$ (bottom). Panels **(b)** and **(c)**: The radial Fourier spectrum of the instantaneous amplitudes $\tilde{b}_{4,\omega}(t, k_r)$ are drawn at times $t_1 = 17.84\mathrm{s}$ (b) and $t_2 = 23.48\mathrm{s}$ (c).

(4.21a), which is a damped Mathieu equation, takes a similar mathematical form to the evolution of a scalar field coupled to an oscillating inflaton field in simple models for Cosmological Preheating (see e.g. [88]).

In their investigation of parametric resonance from the perspective of quantum field theory, Berges & Serreau [100] identified a signature of preheating as the scattering from the primary instabilities into the secondary instabilities, with the latter appearing at an integer multiple of the frequency, and growth rate, of the former. In our case, this corresponds to the mode $(4, k_7)$ at $3\omega_0$ (dashed line in figure 4.7) having a growth rate that is an integer multiple of the rate at which the mode $(4, k_1)$ at ω_0 grows. The growth rates (faint dashed blue lines in 4.7) of the two experimentally (blue lines in 4.7) observed modes are found to be $\lambda_0 \approx 0.52/\mathrm{s}$ (primary) and $\lambda_1 \approx 1.48/\mathrm{s} = 2.85\lambda_0$ (secondary). This is close to, but not quite, the ratio of $3:1$ which is expected from preheating. However, as mentioned above, the experimental amplitudes are not easily

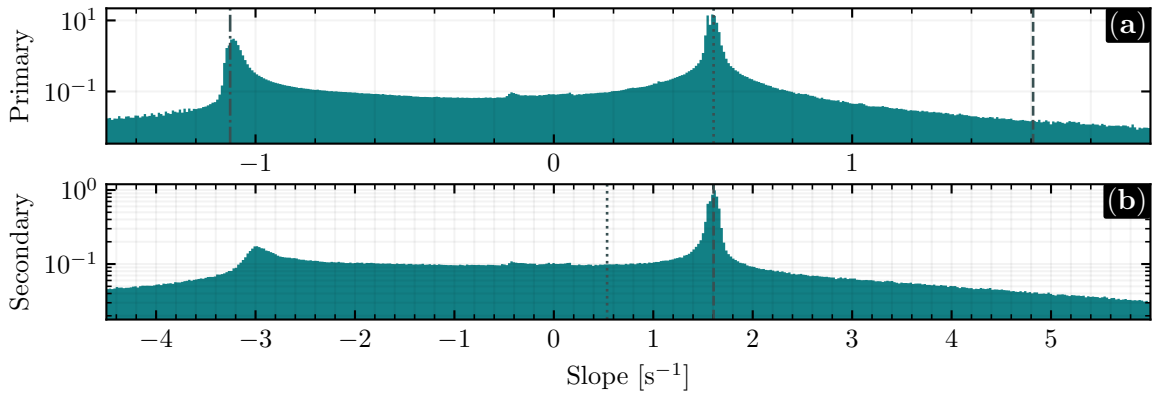

Figure 4.8 (Simulated Slopes) The normalised distribution of log-linear growth/decay rates of the primary and secondary instability is shown in panels **(a)** and **(b)** respectively. The secondary instability, or subdominant mode, has a growth rate (vertical dashed line) three times as large as that of the primary or dominant mode (vertical dotted line). In panel (a), the decay rate γ is marked as a dot-dashed vertical line.

separated in k, meaning that these slopes are expected to be somewhat inaccurate. Having demonstrated that the numerical model faithfully captures all the essential features of the experimental data, we may compute the ratio of secondary to primary slopes produced by the simulations. For simulations with zero detection noise, the result of this analysis is a ratio of 3.06, which is in excellent agreement with the integer prediction from preheating (see figure 4.8). Indeed, we could have anticipated this result by inspecting the nonlinear dynamics for the subdominant mode in (4.32). For a subdominant mode in the same azimuthal channel m as the primary, we have $\mathcal{A}_{bba} = \mathcal{A}_{abb} = 0$, for which the subdominant mode ξ_a enters linearly, while the dominant mode ξ_b enters as cubic terms, i.e. $\mathcal{O}(\xi_b^3, \dot{\xi}_b\xi_b^2, \ldots)$. That is, if ξ_b scales with $e^{\lambda_0 t}$, then ξ_a scales with $(e^{\lambda_0 t})^3$.

Another feature of cosmological preheating is a broadening of the primary resonance band accompanying the population of the secondary [99], which signals the onset of the non-perturbative regime. We can observe this broadening around $|k_r| = k_{r,1}$ in figure 4.7 as the radial Fourier spectrum transitions from relatively sharp peaks at time $t_1 = 17.86s$ in panel (b) to broad peaks in panel (c) at time $t_2 = 23.48s$. Note that the shoulders at $|k_r| = k_{r,2}$ represents the secondary.

VII. Summary and Conclusion

In this chapter, we have revisited the well-known phenomenon of parametric resonance, or Faraday instability, in two-fluid systems. We considered a collection of carefully prepared repeated experiments, and discussed the four different stages experienced by the amplified wave: (1) Its initial

stochastic amplitude in equilibrium (not necessarily thermal), (2) the exponential growth predicted by the linear dynamics when a vertically oscillating force is applied, (3) the fully non-linear period, where the mode is prevented from further growth and instead stagnates at a threshold amplitude and (4) a period of damped exponential decay in absence of the applied force. Here our focus was on the transition from (2) to (3), where we constructed an analytical model to capture the dynamics of the weakly nonlinear regime. To synthetically replicate the experimental data, we considered a numerical simulation of a stochastic extension of the nonlinear dynamics. We demonstrated that this model not only fits a single experiment, but that it captures the behaviour of the entire ensemble of experimental realisations, and it correctly predicts the excitation of secondary instabilities. Finally, we commented on the similarity with the preheating scenario during cosmological inflation. In particular, we saw how the emergence of secondary instabilities is accompanied by a broadening of the primary resonance, and that the instability grows at an integer multiple of the rate of the primary instability.

Moreover, by extending the non-linear model introduced by Miles [172, 173], to incorporate two-fluid interfaces with deep surface tension, i.e. higher-order nonlinear terms due to surface tension, we discovered an effective equation of motion for nonlinear self-interactions in (4.33), along with the sourced oscillator dynamics of subdominant modes (4.32). This self-interaction model can be seen as a classical ϕ^4-type effective field theory, and as such, represents a platform for experimentally simulating classical aspects of such theories.

From the perspective of fluid dynamics, the topics encountered in this chapter opens several interesting avenues for further investigation. Firstly, since the instability acts as an amplifier, the ensemble resulting from repeated experiments offers an indirect probe of the equilibrium fluctuations of the interface at rest.

Secondly, with our state-of-the-art experimental setup, we were able to monitor not just a single parametrically amplified mode, but also the subdominant modes that are sourced by the growth of the dominant mode. This is interesting as experiments of this kind may permit a time-resolved study of the onset of turbulence, see e.g. [191].

Chapter 5

Holographic Surface Measurements

This chapter presents the theoretical foundation and first experimental testing of a digital holography approach to measuring spatiotemporal deformations of fluid interfaces. The idea is being patented [106]. The technique has been developed in collaboration with V. Barroso, S. C. Ajithkumar, T. Kent and S. Weinfurter. I have played a central role in all aspects of this project. The adaptions of the method will be used in the next generation of the experiments presented in the previous chapter, as well as in a series of superfluid ^{4}He experiments that are currently being prepared.

I. Introduction

The need for fast and accurate measurements of surfaces has exploded with the advent of automatic production lines and progress in computer vision. One popular approach to such measurements is using the strategy of binocular vision, i.e. correlating images taken from slightly displaced vantage points [192], a method referred to as Digital Image Correlation (DIC). A popular, computationally inexpensive alternative is the so-called Fourier Transform Profilometry (FTP) method [186, 193, 194], which exploits the local deformations of periodic patterns on a surface. However, these methods can be inconvenient for fluid interfaces as one is often required to make the fluid opaque, e.g. by adding contaminants to it, for standard approaches to work. A popular alternative is to exploit the deflection of rays as they escape the fluid from underneath. Here, a particularly useful strategy is to monitor the local deformations of randomised, or periodic, backdrop patterns, referred to as Free-Surface Synthetic Schlieren (FS-SS) [188], or Fast Checkerboard Demodulation (FCD) [187] respectively. The FCD method's accuracy and domain of validity can be appreciated in figure 4.4 of the previous chapter 4, as this was the method implemented to reconstruct the fluid interface in the experiment. The FCD method, however, rests on the assumption that the fluid interface is sufficiently deformed for a camera to detect the refractive deflections of the rays. Therefore, long wavelength deformations, and very low amplitudes, are not easily measured with this approach. An example of this breakdown of the FCD method for low amplitudes can be seen for times $t < 10s$ in Figure 4.4 of the previous chapter. Moreover, the constant of proportionality between transverse ray displacement and surface gradients scales with the difference in refractive index. Hence, the sensitivity of FCD is drastically reduced by interfaces delimiting media of similar refractive index.

Over the last two decades, an intriguing avenue for high-precision profilometry has appeared

in the field of Digital Holography (DH) [195–202]. Holography, the complete reconstruction of the optical wavefront using diffraction theory, was introduced by Gabor in 1948 [203]. In the following years, Gabor demonstrated the ability to extract three-dimensional information from a two-dimensional hologram to regain focus and spatial resolution [204, 205]. The basic observation of holography is contained in the following argument. Consider two optical fields E_1 and E_2, whose superposition results in an intensity

$$\tilde{I} = |E_1 + E_2|^2 = |E_1|^2 + |E_2|^2 + E_1 E_2^* + E_1^* E_2. \tag{5.1}$$

Curiously, if this intensity pattern $\tilde{I}$ is printed on a film and illuminated by one of the beams that created it, then the result $E_1\tilde{I}$ contains a term $E_2|E_1|^2$ which is a complete reconstruction of the other (complex) three-dimensional optical field E_2. This is in stark difference from conventional photography, which captures only optical intensities and is therefore blind to the phase of the optical field. It is in this sense that holography is linked with the ability to store three-dimensional information on a two-dimensional surface.

The first successful image reconstruction by digital holography appeared in 1967 [206]. However, it was not until 1994 that Schnars and Jüptner introduced the first ever digitally reconstructed hologram using a CCD camera [207], based on the off-axis method proposed by Leith [208]. Henceforth, Cuche et al. introduced the possibility of using Digital Holography (DH) as a quantitative phase measurement [209], now called off-axis digital holography. The method of off-axis holography can be summarised in the context of equation (5.1). By observing that if the two rays E_1 and E_2 are not parallel, then the two last terms, referred to as the twins, receive a spatial frequency which enables them to be separated in the Spatial-Frequency Domain (SFD) from the first two terms. In fact, one may imagine a collection of $n > 2$ optical fields in equation (5.1), for which the principle of holography remains valid. This approach, which is typically used in conjunction with the off-axis method, is referred to as Multiplexed Off-Axis Digital Holography [210–214].

In this chapter, we search for a holographic approach to measuring fluid interfaces in the regime where the aforementioned techniques of fluid profilometry fail. That is, in the regime of small surface gradients $|\nabla h| \ll 1$ and similar refractive indices. The idea is to exploit the deformation of the phase-front of coherent light impinging on the surface. In particular, we exploit the multitude of optical rays born from the partial reflection of the interface (see Figure 5.1) similar to that of the Digital Holographic Reflectometry introduced by Colomb [215, 216]. However, we shall see that by making the bottom of the fluid tiltable, the superposition of rays constitutes intensities that can be seen as multiplexed off-axis holograms.

II. Theoretical considerations

In this section, we will build the necessary theory for the experiment piece by piece. Starting from a WKB ansatz, we see how the classical ray-tracing relations from geometrical optics emerge. These

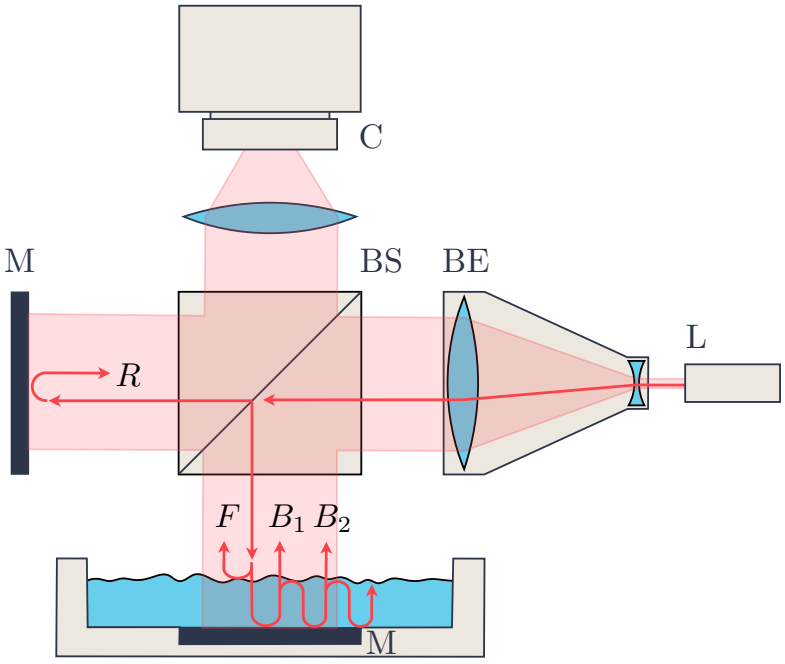

Figure 5.1 (Schematic of experimental setup) A laser source (L) emits a collimated optical beam that expands to the desired diameter by passing through a Beam Expander (BE). A $50-50$ non-polarizing Beam Splitter (BS) divides the beam into two: a probe going through the fluid sample and a reference, both reflecting from adjustable mirrors (M). The reflected trajectories recombine in the beam splitter, and the resulting beam is captured by a camera (C). The reference beam is labelled R, the beam that reflects off the free surface is labelled F, and the beams that reflect back and forth inside the fluid j times are labelled B_j.

are used to obtain an approximate relation for the intensity of coherent light returning from a fluid surface. We discuss how the returning light consists of an infinite number of rays, and that these can be separated in k-space by introducing an adjustable submerged mirror.

II.1. A multitude of rays

Consider a collection of (complex) propagating electromagnetic waves that are traversing a medium which is homogeneous on length scales comparable to the wavelength λ. Within the geometrical optics limit, the electric field strengths can be written

$$\mathbf{E}_n(t,\mathbf{r}) = E_0\mathbf{A}_n \exp\left(i\Phi_n - i\omega t\right) \quad \text{for} \quad \Phi_n(t,\mathbf{r}) \equiv \int_{\gamma_n} \mathbf{k}\cdot d\mathbf{r}, \tag{5.2}$$

where ω is the angular frequency and $\mathbf{A}_n$ is a complex, dimensionless, two-dimensional vector whose length gives the relative amplitude with respect to the reference amplitude E_0, and with the direction along the axis of polarization. Here, each phase Φ_n depends on the path γ_n travelled by the phase-fronts of the ray $\mathbf{E}_n$. For a superposition of rays $\{\mathbf{E}_n\}$ of the form (5.2) at same frequency ω, the (time-averaged) intensity is given by

$$I(t,\mathbf{r}) \equiv I_0 + I_0 \sum_{n\neq k} A_{nk}(t,\mathbf{r}) e^{i\Phi_{nk}(t,\mathbf{r})}, \tag{5.3}$$

for $\mathbf{A}_n^\dagger \mathbf{A}_m \equiv A_{nm}$ and $\Phi_{nm} \equiv \Phi_n - \Phi_m$, and the sum runs over all distinct values of n and k. Here, and in what follows, the conjugate transpose is denoted by a superscript $\dagger$. We choose $I_0 \equiv \frac{1}{2}\varepsilon c|E_0|^2$ to be the average total intensity so that $|E_0|$ is defined through the relation $\sum_n |\mathbf{E}_n|^2 \equiv |E_0|^2$ or, equivalently, $\sum_n |\mathbf{A}_n|^2 = 1$.

From equation (5.3), it is clear that for any two distinct rays n and k with unequally varying phases ($\Phi_{nk} \neq 0$ and $|\nabla\Phi_{nk}| \neq 0$), the intensity I must fluctuate locally in space. Due to the short wavelengths of optical light, the resulting intensity distributions, commonly referred to as interferograms or interference patterns, are highly sensitive to relative changes along or of the paths travelled by the conspiring beams.

Within the geometrical optics approximation, the trajectories followed by rays are given by the stationarity of phases $\Phi_n - \omega t$ of the form (5.2). The result takes the form of a Hamiltonian system (see appendix A) with the dispersion relation $\omega = \omega(\mathbf{x},\mathbf{k})$ as effective Hamiltonian [163], i.e.

$$\frac{d\mathbf{x}}{dt} = \nabla_k \omega \quad \text{and} \quad \frac{d\mathbf{k}}{dt} = -\nabla\omega. \tag{5.4}$$

In an isotropic medium, where the frequency depends only on the magnitude $k = |\mathbf{k}|$ of the wave-vector, the ray moves along $\mathbf{k}$, i.e. $d\mathbf{r} \propto \mathbf{k}$, and stationarity of the phase Φ_n is equivalent to Fermat's principle, i.e. that rays take the quickest route between any two points.

Indeed, a ray that passes through an infinitesimal distance dz of an isotropic medium with refractive index n attains a phase $d\Phi = k_0 n dz$, where $k_0 = 2\pi/\lambda$ is the wave-number, with corresponding wavelength λ, of the ray in vacuum. Consequently, to determine the contribution to the phase Φ_n of a ray from traversing a homogeneous medium, we only need the lengths of their trajectories.

To model the geometry in Figure 5.1, we now consider the rays as they leave the beam splitter (BS), and let z be the direction of the incident beam, i.e. the optical axis (see Figure 5.2). We shall assume the incident beam is aligned with the direction of gravity, so that the fluid interface can be written $z = h(t,\mathbf{r})$, with $h = \text{const}$ when the fluid is at rest. Here, t is time and $\mathbf{r} \equiv x\mathbf{e}_x + y\mathbf{e}_y$ are coordinates for the transverse, horizontal plane. Submerged under the interface is a tilted plane mirror with surface $z = -\mathbf{m}_b \cdot \mathbf{r}$. Here, $\mathbf{m}_b$ determines the normal vector $\mathbf{n}_b \propto \mathbf{e}_z + \mathbf{m}_b$ of the mirror. We shall assume the tilt to be small, i.e. $|\mathbf{m}_b| \ll 1$, for which $\mathbf{m}_b$ can be interpreted as

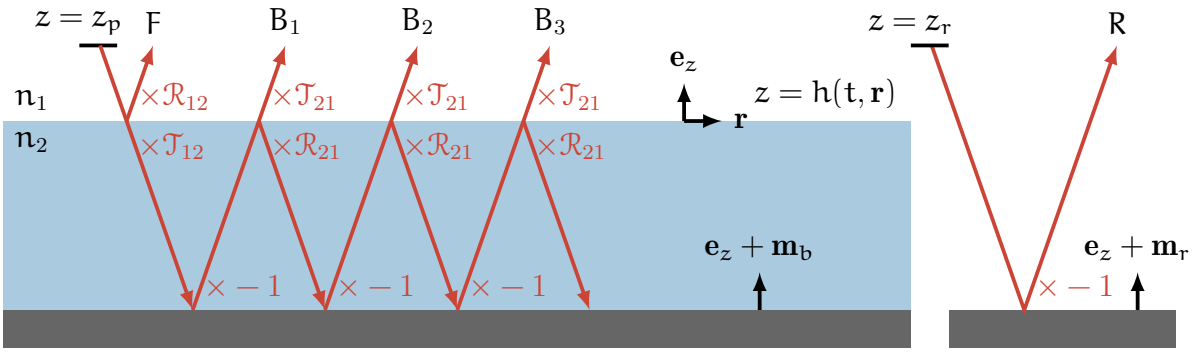

Figure 5.2 (Geometry of rays) The three different types of rays R, F and B_n are illustrated. The incoming beam starts at an altitude $z = z_p$ in the probe beam (left), and $z = z_r$ in the reference arm (right). The probe beam reflects partially off the free surface $z = h$ with reflection coefficient $\mathcal{R}_{12}$ resulting in the beam labelled F. The transmitted component is trapped inside the fluid, creating a new transmitted ray B_n for every reflection n off the submerged mirror. The relative amplitudes of these rays are given by $-\mathcal{T}_{12}\mathcal{T}_{21}\mathcal{R}_{21}^n$. In the experiment, the angle of incidence on the surface is negligible, and the normal vectors of the submerged mirror ($\mathbf{e}_z + \mathbf{m}_b$) and reference mirror ($\mathbf{e}_z + \mathbf{m}_r$) are rotated relative to that of the free surface ($\mathbf{e}_z$), i.e. $|\mathbf{m}_r|, |\mathbf{m}_b| \neq 0$.

the (vectorial) angle of rotation of the mirror from the optical axis. That is, $\mathbf{m}_b$ is a vector in the transverse (horizontal) plane, where $\mathbf{m}_b = 0$ corresponds to the submerged mirror being parallel with the undisturbed fluid interface $z = \text{const}$.

The reference beam, labelled R in Figure 5.1, can be modelled similar to the geometry above, but with the absence of the interface h. That is, we label the optical axis z and denote the surface of the reference mirror by $z = -\mathbf{m}_r \cdot \mathbf{r}$, with $|\mathbf{m}_r| \ll 1$. As for the submerged mirror, this determines the surface normal of the reference mirror through $\mathbf{n}_r \propto \mathbf{e}_z + \mathbf{m}_r$.

We shall assume the two mirrors to be perfectly reflecting. However, an incident ray on the fluid interface h is generally partially transmitted, and partially reflected. At the interface, the background on which the rays propagate changes suddenly, leading to a violation of the WKB assumption (5.2) that a phase changes over much smaller scales than the background. To relate amplitudes on either side of the interface, we return to electrodynamics, where the projections of the electric and magnetic field amplitudes must be continuous across an un-charged surface [217]. The result is the well-known Fresnel equations, which for normal incidence take the form

$$\mathbf{E}_i = \mathcal{R}_{12}\mathbf{E}_r + \mathcal{T}_{12}\mathbf{E}_t \quad \text{for} \quad \mathcal{R}_{12} \equiv \frac{n_1 - n_2}{n_2 + n_1} \quad \text{and} \quad \mathcal{T}_{12} \equiv 1 + \mathcal{R}_{12}. \tag{5.5}$$

Here $\mathbf{E}_i$ is the incident beam, from a medium with refractive index n_1 towards a medium with n_2, and $\mathbf{E}_r$ and $\mathbf{E}_t$ are the reflected and transmitted rays respectively. Note that the reflection off a

perfect mirror is included in the relation (5.5). Indeed, if we let $n_2 \to \infty$, then the surface becomes a perfect mirror with a coefficient of reflection equal to -1. It should also be observed that the relations (5.5) conserve the flow of power, contrary to what one would think at first glance. This is because the medium traversed by the transmitted ray is different, so that the transmitted power T is related to the coefficient $\mathcal{T}_{12}$ of transmission by $T \equiv \mathcal{T}_{12} n_2/n_1$.

The consequence of the partial reflection of the fluid interface is that the fluid acts as a cavity, producing a new returning ray B_n for every reflection $n = 1, \dots$ off the submerged mirror (see Figure 5.2).

For small surface gradients $|\nabla h| \ll 1$ and tilts $|\mathbf{m}_b|, |\mathbf{m}_r| \ll 1$, the leading order expression (5.2) for the accumulated phase becomes a matter of accounting for the vertical distances. The result can be conveniently written as

$$\Phi_F = 2k_0 n_1 L_{0h}, \quad \Phi_R = 2k_0 n_1 L_{0r}, \quad \text{and} \quad \Phi_{B_j} = 2k_0 (n_1 L_{0h} + j n_2 L_{hb}) \tag{5.6a}$$

$$\text{for} \quad L_{0h} \equiv z_p - h(t, \mathbf{r}), \quad L_{hb} \equiv h(t, \mathbf{r}) + \mathbf{m}_b \cdot \mathbf{r}, \quad \text{and} \quad L_{0r} \equiv z_r + \mathbf{m}_r \cdot \mathbf{r}\,. \tag{5.6b}$$

Note that the expression (5.6) for the phases rests on the assumption that the horizontal deflection of rays is negligible. Therefore, the domain of validity of a method based on these expressions starts exactly where the FCD method [186–188], which exploits the ray displacements, starts failing.

From the intensity (5.3) interference patterns are formed by phase differences between any pair of rays. Using the leading order expressions (5.6), we find

$$\Phi_{RF} = 2k_0 n_1 \left(h + \mathbf{m}_r \cdot \mathbf{r} + \Delta z\right), \tag{5.7a}$$

$$\Phi_{RB_j} = 2k_0 \left[(n_1 - j n_2) h + (n_1 \mathbf{m}_r - j n_2 \mathbf{m}_b) \cdot \mathbf{r} + n_1 \Delta z\right], \tag{5.7b}$$

$$\Phi_{FB_j} = 2k_0 n_2 \left[j h + j \mathbf{m}_b \cdot \mathbf{r}\right], \tag{5.7c}$$

$$\Phi_{B_\ell B_j} = 2k_0 n_2 \left[(\ell - j) h + (\ell - j) \mathbf{m}_b \cdot \mathbf{r}\right], \tag{5.7d}$$

where $\Delta z \equiv z_r - z_p$ is the difference in arm length of the reference beam z_r and the probe beam z_p (see Figure 5.2). The corresponding amplitudes are found by invoking the Fresnel relation (5.5) at each interaction with the free surface, and can be expressed in terms of $\mathcal{R}_{21} \geqslant 0$. The result can be written

$$A_{RF} = \mathcal{R}_{21} \tag{5.8a}$$

$$A_{RB_j} = (1 - \mathcal{R}_{21}^2) \mathcal{R}_{21}^{j-1} \tag{5.8b}$$

$$A_{FB_j} = (1 - \mathcal{R}_{21}^2) \mathcal{R}_{21}^{j} \tag{5.8c}$$

$$A_{B_\ell B_j} = (1 - \mathcal{R}_{21}^2)^2 \mathcal{R}_{21}^{\ell + j - 2}, \tag{5.8d}$$

for $j \in \mathbb{N}$. Note that if the setup 5.1 is modified to make distinct polarizations of the reference beam and probe beams, e.g. by using a polarizing beam splitter, then the amplitudes (5.8) must be

modified. For example, if the two arms are linearly polarized with relative rotation angle θ_p, then the amplitudes A_{RF} and A_{RB_j} in (5.8) attain an additional suppression factor $\cos\theta_p$.

In all the above, we have implicitly assumed the beams to be perfectly coherent. Realistic laser sources, however, have a finite coherence length. To take this into account, the amplitudes (5.8) would be suppressed by a function that varies with the difference of the lengths (5.6) in units of the coherence length (see e.g. [215]).

Because $\mathcal{R}_{21}$ is typically small ($\mathcal{R}_{21} \simeq 14.16\%$ for air-water interfaces), the RB_1 interferogram has the largest amplitude. The sensitivity of its phase to variations in the height, $\partial_h \Phi_{RB_1} = 2k_0(n_1 - n_2)$, however, is the smallest. The most phase-sensitive of the $j = 1$ interferograms is FB_1, with $\partial_h \Phi_{FB_1} = 2k_0 n_2$. In general, all phases in (5.7) are related to the interfacial height h through $\Phi_{ab} \simeq 2k_0 \alpha_{ab} h$, where $\alpha_{ab} = \alpha_1 n_1 - \alpha_2 n_2$ with integer coefficients $\alpha_1, \alpha_2 \in \mathbb{Z}$. In terms of the wavelength λ of the laser, the variations $\delta\Phi_{ab}$ due to deformations of the interface h is given by

$$\left(\frac{\delta\Phi_{ab}}{2\pi}\right) = \alpha_{ab}\left(\frac{h}{\lambda/2}\right) \quad \text{for} \quad \alpha_{ab} = \begin{cases} n_1 & \text{for RF} \\ j n_2 & \text{for } FB_j \\ n_1 - j n_2 & \text{for } RB_j \end{cases}. \tag{5.9}$$

That is, the fringes of the intensity pattern are shifted by a full period in regions where the height h is elevated by $\lambda/2\alpha_{ab}$. If, for example, the incident light is green with $\lambda = 532\text{nm}$ and the fluid is water, then a local elevation by 266nm of the height would shift the RF fringes by exactly one period. Because shifts in the fringes can be observed well below a full period, we expect the method to be sensitive to height fluctuations of the order of $\mathcal{O}(10\text{nm})$. Note, however, that if the interface delimits media of similar refractive index, i.e. $|n_2 - n_1| \ll 1$, then the RB_1-phase becomes less sensitive. This separation of the scales probed by the different holograms in the limit $n_2 \to n_1$ enables extending the domain of applicability. Note, however, that care must be taken as the limit has implications for the reflection and transmission coefficients (5.5).

The intensity contributed by the three interferograms RF, RB_1 and FB_1 have distinct external influences. For example, inhomogeneities in the bulk of the surrounding gas, from changes in the composition of the gas, the temperature, or from sound waves, are picked up by RF and RB_1, but not by FB_1, which only probes the fluid bulk. For transparent fluids, FB_1 is expected to have the largest signal-to-noise ratio, provided the reflection coefficient $|\mathcal{R}|$ is not too small.

Now imagine inspecting the spatial Fourier spectrum of the combined intensity (5.3) for phases given by (5.7). By virtue of the distinct tilts $\mathbf{m}_r$ and $\mathbf{m}_b$ of the reference and bottom mirrors respectively, the interferograms separate into spatial carrier frequencies (see figure 5.3).

The formation of phase differences of the form (5.7) in a superposition (5.3) is the main ingredient in Multiplexed Off-axis Digital Holography. Here, the idea of off-axis digital holography becomes more clear. It is the formation of interference between two optical beams, with phase difference $\Phi_{ab} = \Phi_a - \Phi_b$, with relatively tilted phase fronts, i.e. $|\nabla\Phi_{ab}| \approx \mathbf{k}_{ab} \neq 0$, The signal,

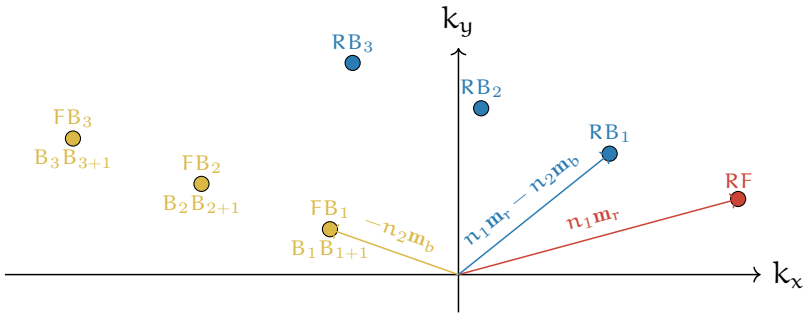

Figure 5.3 (Separation of Carrier Peaks) The separation of spatial carrier frequencies $\mathbf{k} = (k_x, k_y)$ that results from small tilts $\mathbf{m}_b$ and $\mathbf{m}_r$ of the submerged mirror and reference mirror respectively. Each node represents a hologram specified by the label. The holograms are categorised into three groups (yellow, blue and red). Yellow holograms are independent of the configuration of the reference mirror $\mathbf{m}_r$, the red hologram is independent of the submerged mirror $\mathbf{m}_b$ and the blue nodes respond to adjustments in both mirrors.

which for us is the deformations of the interfacial height h, then appears as modulations of the spatial carrier $\mathbf{k}_{ab}$, which for us is a superposition of $n_1\mathbf{m}_r$ and $n_2\mathbf{m}_b$. By introducing a tilt $\mathbf{m}_b$ of the submerged mirror, the collection of partially reflected rays separate into isolated off-axis holograms formed by any pair of rays. With this simple step, i.e. adjustability of the submerged mirror, we may use a basic Michelson interferometer in Figure 5.1 to perform simultaneous, independent measurements of the surface by virtue of the multiplexing in (5.7).

II.2. Production of synthetic data with Numerical Phase-tracing

The first step toward experimental realisation is to mimic the setup numerically as realistic as possible. We keep the assumption of homogeneity of the bulk and ray optics, but with the inclusion of non-linear deflections. This can be done numerically by iteratively propagating a mesh of rays through the mathematical formulation of the setup in Figure 5.1.

The geometry is formulated analytically as in section II.1 (see Figure 5.2) by introducing two separate geometries, the first contains only a reference mirror, defined by the relation $z = -\mathbf{m}_r \cdot \mathbf{r}$. The other contains a submerged mirror $z = -\mathbf{m}_b \cdot \mathbf{r}$ and a fluid interface $z = h(\mathbf{r})$, which we shall take to be of the form

$$h(\mathbf{r}) = h_0 + A\left[\cos(\mathbf{k}_1 \cdot \mathbf{r}) + \cos(\mathbf{k}_2 \cdot \mathbf{r})\right], \tag{5.10}$$

for $A = 250\text{nm}$, $h_0 = 3\text{mm}$, $\mathbf{k}_1 = (-2, 2)/\text{cm}$ and $\mathbf{k}_2 = (1, 1/2)/\text{cm}$.

The simulation is initiated with a linearly spaced Cartesian mesh of 1536×1536 two-dimensional locations $\mathbf{r}_{ij} \in \mathbb{R}^2$ in the (x, y) plane, and at a fixed altitude $z = z_0$. The resulting

three-dimensional locations $\mathbf{x}_{ij} = z_0\mathbf{e}_z + \mathbf{r}_{ij}$ are taken as the initial locations of the rays, and all rays start facing perfectly downward, i.e. with initial direction $\mathbf{d}_{ij} = -\mathbf{e}_z$. In addition to a position $\mathbf{x}_{ij}$ and a direction $\mathbf{d}_{ij}$ of propagation, each ray is initialised with a phase $\phi_{ij} = 0$, unit (relative) amplitude $A_{ij} = 1$ and refractive index $n_{ij} = n_1$ of the current medium. Each ray is then simulated independently using the following algorithm.

Step (1) For each mathematical surface $F_k(\mathbf{x}) = 0$ in the geometry, solve the equation $F_k(\mathbf{x}_{ij} + s_k\mathbf{d}_{ij}) = 0$ for s_k is numerically, and determine the $k = k_0$ with smallest non-negative value s for s_k, and label F_{k_0} as the current surface. If there are no solutions s_k, choose $s = (z_0 - \mathbf{x}_{ij}\cdot\mathbf{e}_z)/(\mathbf{d}_{ij}\cdot\mathbf{e}_z)$ to propagate the ray back to z_0, and move to step (4) after this step. Update the position $\mathbf{x}_{ij} \mapsto \mathbf{x}_{ij} + s\mathbf{d}_{ij}$ and the phase $\phi_{ij} \mapsto \phi_{ij} + k_0 n_{ij} s|\mathbf{d}_{ij}|$.

Step (2) Compute the normal vector $\mathbf{n} \equiv \nabla F_{k_0}/|\nabla F_{k_0}|$ of the current surface and find the reflected $\mathbf{d}^r_{ij}$ and refracted $\mathbf{d}^t_{ij}$ directions about the surface normal using Snell's law, i.e.

$$\mathbf{d}^r_{ij} = \mathbf{d}_{ij} - 2c\mathbf{n} \quad \text{and} \quad \mathbf{d}^t_{ij} = r\mathbf{d}_{ij} - \left(rc + \sqrt{1 - r^2(1-c^2)}\right)\mathbf{n} \tag{5.11}$$

where $c \equiv \mathbf{n}\cdot\mathbf{d}_{ij}$ and $r = n_a/n_b$ is the current refractive index n_a divided by the refractive index n_b behind the surface. Duplicate the current ray, assign the (reflected) direction $\mathbf{d}^r_{ij}$ to the duplicate, and reduce the amplitude by the Fresnel reflection coefficient*, i.e. $A_{ij} \mapsto \mathcal{R}_{ab}A_{ij}$. Pass the duplicate to step (3). Update the refractive index $n_a \mapsto n_b$, direction $\mathbf{d}_{ij} \mapsto \mathbf{d}^t_{ij}$ and amplitude $A_{ij} \mapsto \mathcal{T}_{ab}\,A_{ij}$ of the current ray and pass it to step (3). Here $\mathcal{T}_{ab}$ is the Fresnel transmission coefficient.

Step (3) If the amplitude is sufficiently large, i.e. $|A_{ij}| > \varepsilon$ for some ε (the chosen value here is $\varepsilon = 5\times10^{-4}$), send the ray back to step (1). If not, discard the ray.

Step (4) Wait for all rays to reach this step. When they do, move to step (5).

Step (5) Use the (x, y) coordinates of the current position $\mathbf{x}_{ij}$ to interpolate the amplitudes A_{ij} and phases ϕ_{ij} to the original transverse coordinate $\mathbf{r}_{ij}$. Then use equation (5.3) for rays $A_{ij}e^{i\phi_{ij}}$ to compute the intensity I_{ij}. The value of the resulting image Y_{ij} at pixel (i, j) is chosen by sampling from a Poisson distribution with mean γI_{ij} (here we use $\gamma = 100$).

The result from this algorithm is a single image Y_{ij} of the expected intensity in the idealised situation of homogeneous bulk, but with taking the deflection of rays fully into account. An example of a simulated image is shown for the interface (5.10) delimiting air ($n_1 = 1$) from water ($n_2 = 1.33$) in panel (a) of Figure 5.4. The spatial Fourier transform of this image, shown in panel 5.4(b), confirms the anticipated separation of carriers, or multiplexing, from the leading-order phase relations

*Technically, the polarization averaged Fresnel relations for general angle of incidence is used here, but for the purpose of the specific example discussed here, this is the same relations as those for normal incidence, i.e. (5.5).

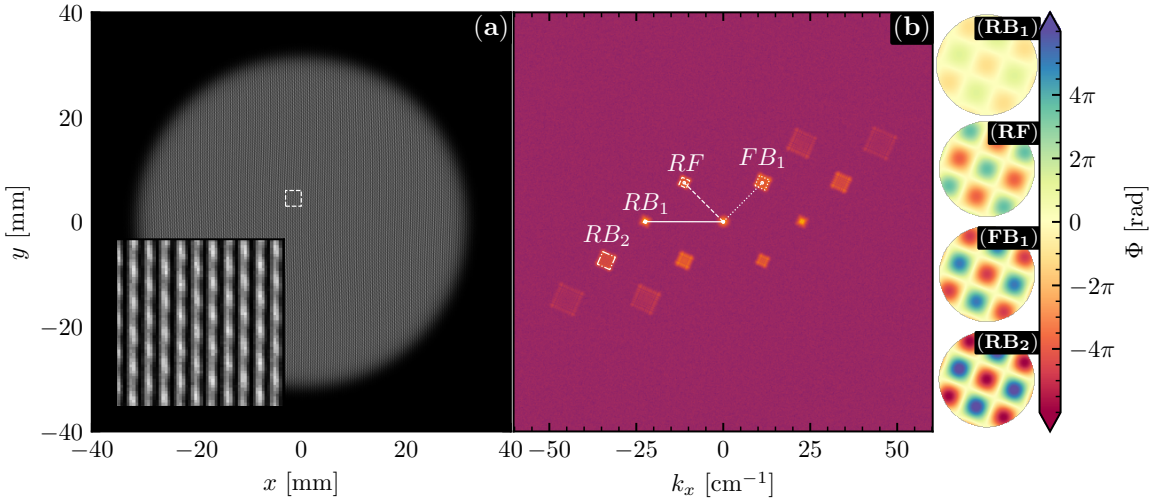

Figure 5.4 (Phase-tracing) Panel **(a)**: Numerically simulated intensity Y_{ij} with an inset highlighting an expanded region (white dashed rectangle) of the image. Panel **(b)**: The spatial Fourier transform $\hat{Y}_{ij}$ of the simulated intensity, where the brightness of each pixel is proportional to the logarithmic amplitude $\ln|\hat{Y}_{ij}|$. White lines are drawn to illustrate the carrier frequencies $2k_0(n_1\mathbf{m}_r - n_2\mathbf{m}_b)$ (solid white), $2k_0n_1\mathbf{m}_r$ (dashed white) and $2k_0n_2\mathbf{m}_b$ (dotted white) of the three holograms RB_1, RF and FB_1. The predicted modulation area for each peak is highlighted as a rectangular region. The differences of simulated phase fields are shown in the four panels on the right with a shared colorbar. The visibly correlated, spatial dependence of the phases is proportional to the height-field $h(\mathbf{r})$ in (5.10).

(5.7). As predicted, the three holograms RB_1, RF and FB_1 are located at $2k_0(n_1\mathbf{m}_r - n_2\mathbf{m}_b)$ (solid white), $2k_0n_1\mathbf{m}_r$ (dashed white) and $2k_0n_2\mathbf{m}_b$ (dotted white) respectively.

The contribution from a hologram to a spatial frequency $\mathbf{k}$ is generally given by the local linearization $\nabla\Phi$ of the phase Φ. If the phase Φ is of the form (5.7), then the k-space region of excited amplitudes near each carrier peak $\mathbf{k}_m$ is given by $\mathbf{k}_m + C\nabla h$ for some constant C. The corresponding areas, found from considering maxima of ∇h from (5.10), are shown for the three holograms RB_1, RF and FB_1 as white rectangles in panel 5.4(b). These are in good agreement with the simulated data. Note that the strongest signal, which is the RB_1 hologram (solid white line), has the smallest modulation area. This is due to the prefactor $|n_2 - n_1| < 1$ in (5.7b), which reduces the response $\partial_h\Phi_{RB_1}$ of the phase Φ_{RB_1} to excitations of the interface h. The true phases from the ray-tracing algorithm are shown in the four panels labelled RB_1, RF, FB_1 and RB_2 in Figure 5.4. Notice that the phase from the RF hologram is anti-correlated with all the other holograms and that all the phases respond differently to the height field $h(\mathbf{r})$. Here, the RB_1-phase has the lowest amplitude, and the RB_2 has the largest.

II.3. Procedure for recovery of the phase fields

In this section, we investigate how the different phase fields can be reconstructed from the digital image alone. Our strategy shall focus on recovering information from the synthetic data exhibited in Figure 5.4, for which the true height field is known. Before doing this, however, we should investigate the theory. Here, we take the canonical approach, which in the digital holography community is referred to as the Angular Method [195], and Fourier Demodulation [186] in the fluid profilometry community.

Consider a digital image Y_{ij} indexed by a cartesian mesh of pixel locations $\mathbf{r}_{ij}$ and formed from capturing intensities of the form (5.3). That is, $Y_{ij} = \widehat{\Gamma}[I(\mathbf{r}_{ij})] + \delta Y_{ij}$ where δY_{ij} is a stochastic variable that describes the noise in the image, $\mathbf{r}_{ij}$ is the spatial (pixel) coordinate, and $\widehat{\Gamma}$ is a function that transforms physical intensities to pixel values. To start, consider the idealised case of $\widehat{\Gamma}$ being a linear operator, i.e. $\widehat{\Gamma}[A+B] = \widehat{\Gamma}[A]+\widehat{\Gamma}[B]$, and assume all phase differences $\Phi_{ab} = \Phi_a - \Phi_b$ to have small variations $\phi^{(ab)}(t,\mathbf{r})$ around a stationary planar phase $\mathbf{k}_{ab}\cdot\mathbf{r}$ as is the case for equations (5.7). That is, $\Phi_{ab}(t,\mathbf{r}) = \phi^{(ab)}(t,\mathbf{r}) + \mathbf{k}_{ab}\cdot\mathbf{r}$, so that

$$Y_{ij} \equiv \tilde{Y}_{ij} + \delta Y_{ij} = Y_0 + \sum_n B_n \exp\left[i\mathbf{k}_n\cdot\mathbf{r}_{ij} + i\phi_{ij}^{(n)}\right] + \delta Y_{ij} \tag{5.12}$$

for amplitudes $B_n = Y_0 A_n$ with $Y_0 \equiv \widehat{\Gamma}[I_0]$. Here Y_0 is the pixel value corresponding to the spatially averaged intensity I_0. Here, the sum runs over all ordered pairs of distinct labels $a \neq b$, e.g. $n = RF$ or $n = RB_1$, as in (5.3). Since each pair of indices $a \neq b$ enters twice, once with Φ_{ab} and once with $\Phi_{ba} = -\Phi_{ab}$, the image Y_{ij} in (5.12) is real-valued. Now imagine a Fourier filter F_m around a single carrier peak $\mathbf{k}_m$, i.e. $F_m \equiv \mathcal{F}^{-1}G_m(\mathbf{k})\mathcal{F}$, where $\mathcal{F}$ is a two-dimensional, spatial Fourier transform with inverse $\mathcal{F}^{-1}$, and $G_m(\mathbf{k})$ is some function only taking non-zero values nearby $\mathbf{k}_m$. The role of the filter F_m is to isolate each modulated plane wave in equation (5.12), meaning that ideally, we have

$$F_m[Y]_{ij} = B_m \exp\left[i\mathbf{k}_m\cdot\mathbf{r}_{ij} + i\phi_{ij}^{(m)}\right] + F_m[\delta Y]_{ij}. \tag{5.13}$$

This equation forms the essential ingredient in Fourier demodulation, see e.g. Wildeman [187]. Using the Fourier filter F_m, we have extracted a complex signal whose only deviation from a complex plane wave, other than the noise, is due to the spatial variations of $\phi_{ij}^{(m)}$. Then, if the noise is small, i.e. $F[\delta Y]_{ij} \ll \tilde{Y}_{ij}$, the complex phase $\operatorname{Im}\log F[Y]_{ij}$ of the filtered image $F[Y]_{ij}$ takes the form

$$\begin{aligned} \operatorname{Im}\log F_m[Y]_{ij} &= \mathbf{k}_m\cdot\mathbf{r}_{ij} + \phi_{ij}^{(m)} - \operatorname{Re}[\delta\phi_{ij}^{(m)}] + \mathcal{O}\left(\left|\delta\phi_{ij}^{(m)}\right|^2\right) \\ \text{where} \quad \delta\phi_{ij}^{(m)} &\equiv i\frac{F_m[\delta Y]_{ij}}{\tilde{Y}_{ij}^{(m)}}. \end{aligned} \tag{5.14}$$

Assuming no variation in the carrier $\mathbf{k}_m$, and δY_{ij} to be a central random variable, i.e. $\langle \delta Y_{ij} \rangle \approx 0$, then the ensemble-averaged phase $\langle \phi_{ij}^{(m)} \rangle$ is found from the relation

$$\langle \phi_{ij}^{(m)} \rangle = \operatorname{Im} \log F_m[Y]_{ij} - \mathbf{k}_m \cdot \mathbf{r}_{ij} \tag{5.15}$$

with the small fluctuations about it being given by

$$\operatorname{Re}\left[\delta\phi_{ij}^{(m)}\right] \equiv -\frac{2}{B_m} \operatorname{Im}\left[\frac{F_m[\delta Y]_{ij}}{e^{i\mathbf{k}_m \cdot \mathbf{r}_{ij} - i\phi_{ij}^{(m)}}}\right]. \tag{5.16}$$

Provided that an ideal filter F_m can be constructed, equation (5.15) informs us how to recover the phase fields $\{\phi_{ij}^{(m)}\}_m$ from the image Y_{ij}, and equation (5.16) sets the level of the noise. Here, we should note, in passing, that the noise is inversely proportional to the amplitude B_m and is generally dependent on the details of the filter F_m.

We shall refer to the demodulation scheme (5.15) as *absolute* reconstruction. In some cases, it can be convenient to consider instead the relative change in the phases $\phi_{ij}^{(m)}$ in the image Y_{ij} with respect to those of some reference image Y_{ij}^0, see e.g. the demodulation scheme of Wildeman [187] for a discussion. This approach, which we shall refer to as *relative* reconstruction, can be written

$$\langle \Delta\phi_{ij}^{(m)} \rangle = \operatorname{Im} \log \left(F_m[Y]_{ij} F_m[Y^0]_{ij}^* \right), \tag{5.17}$$

where $*$ is the complex conjugate. The relative reconstruction has the pleasing property of being relatively insensitive to the exact location of the carrier $\mathbf{k}_m$. More importantly, any persistent defects in the phase fronts are eliminated in the product $F_m[Y]_{ij} F_m[Y^0]_{ij}^*$, making the reconstruction more robust. In what follows, the reconstruction strategy chosen is assumed to be absolute unless otherwise stated.

Armed with the demodulation method (5.15), the only thing needed to recover the phases from Figure 5.4 is to decide on a function $G_m(\mathbf{k})$ in the definition of the Fourier filter F_m. Here, the simplest and perhaps most natural choice would be a top-hat filter centred at the carrier $\mathbf{k}_m$ with some radius r_k, i.e. $G_m(\mathbf{k}) = 2$ for $|\mathbf{k} - \mathbf{k}_m| \leqslant r_k$ and 0 otherwise[*]. However, the reconstruction can be improved by using a Raised-Cosine filter

$$G_m(\mathbf{k}) = H_{b,r_k}(|\mathbf{k} - \mathbf{k}_m|) \quad \text{for} \tag{5.18a}$$

$$H_{b,r_k}(x) \equiv \begin{cases} 1 & \text{for } |x| \leqslant \frac{1-b}{2} r_k \\ \frac{1}{2}\left[1 + \cos\left(\frac{\pi}{b r_k}\left[|x| - \frac{1-b}{2} r_k\right]\right)\right] & \text{for } \frac{1-b}{2} r_k \leqslant |x| \leqslant \frac{1+b}{2} r_k \\ 0 & \text{for } |x| \geqslant \frac{1+b}{2T} \end{cases}. \tag{5.18b}$$

[*]The value two here is to compensate for the prefactor $\frac{1}{2}$ in the complex plane waves of real harmonic functions.

We may now construct the phases from the simulated image Y_{ij} exhibited in Figure 5.4. The procedure is as follows. First, compute the two-dimensional Fourier transform $\hat{Y}_{ij}$ of Y_{ij} and locate the carrier peaks $\mathbf{k}_m$, i.e. the local maxima of $|\hat{Y}_{ij}|$. Then, choose a filter size r_k that is large enough to contain the entire peak, but not so large that it includes other amplitudes, and use this to construct a cosine filter $G_m(\mathbf{k})$ according to (5.18) around each peak $\mathbf{k}_m$. The chosen filter sizes r_k and centred at the carrier peaks $\mathbf{k}_m$ are shown as dotted white circles in panel (a) of Figure 5.5.

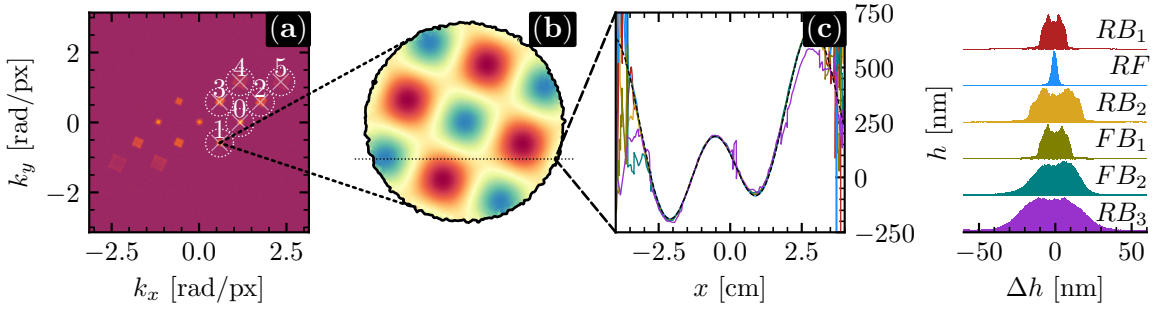

Figure 5.5 (Reconstructed artificial data) Panel **(a)**: The logarithmic amplitudes $\log|\hat{Y}_{ij}|$ of the Fourier transform $\hat{Y}_{ij}$ of the synthetic image Y_{ij} in Figure 5.4(a). The six carrier peaks $\mathbf{k}_m$ chosen are labelled 0-5, and (dotted white) circles are drawn to highlight the size r_k of the filter (5.18). Panel **(b)**: The unwrapped, reconstructed phase field $\phi_{ij}^{(m)}$ for the chosen peak $m = 1$. This matches the true phase field in panel (RF) from Figure 5.4. A horizontal line indicates the slice depicted in panel (c). Panel **(c)**: The reconstructed height fields h of a linear slice are shown (thin coloured) for all the six carriers from panel (a). A black line is drawn on top to indicate the true height field (5.10). The colour of each line is labelled by the histograms on the right, which show, for each of the carriers, the distribution of deviations $\Delta h = h - h_t$ of the reconstructed height h from the true height h_t.

For each filter F_m, we may then apply the reconstruction (5.15) to obtain a wrapped phase field $\phi_{ij}^{(m)} + 2\pi a_{ij}$, where $a_{ij} \in \mathbb{Z}$ are unknown integers due to the phases only being retrievable modulo 2π. By performing a spatial phase-unwrapping, as in [218], the 1536×1536 unknown integers a_{ij} can be reduced to a single integer $a \in \mathbb{Z}$, whose precise value would, in principle, depend on the average total depth h_0 of the fluid (see equation (5.10)). The resulting phase, for the carrier peak labelled (1) in Figure 5.5(a) and RF in Figure 5.4(b), is shown in panel (b) of Figure 5.5. This should be compared with the true, or exact, phase difference Φ_{RF} exhibited in panel (RF) of Figure 5.4.

Using the phase fields $\phi_{ij}^{(m)}$ along with the knowledge of which hologram in Figure 5.5(a) corresponds to which of the theoretically predicted phases(5.7), the height fields h, which should coincide for all holograms, can be estimated. Let us consider a single hologram, for example the one labelled 1 in 5.5(a), to illustrate the process. We know this is the RF hologram from the synthetic

image 5.4, but we can also discover this by revisiting the predicted carrier locations in Figure 5.3. The RF hologram is a neighbour of the largest-amplitude hologram RB_1, and it is at the end of the straight line, in k-space, that avoids the origin but passes through all the holograms RB_j. Having identified $\phi_{ij}^{(m)}$ for $m = 1$ with the RF hologram, we visit the phases (5.7) to conclude that the predicted height is given by $h_{ij}^{\mathsf{RF}} = (2k_0 n_1)^{-1}\phi_{ij}^{(1)}$ in this case. A horizontal slice (black line in 5.5(b)) of the reconstructed height h_{ij}^{RF} is shown in panel (c) of Figure 5.5 as a blue line (see histogram to the right).

A similar line of reasoning can be used to obtain, in this case six, height fields (all shown in panel (c) of Figure 5.5) for each peak $0, 1, 2, 3, 4$ and 5 corresponding to the holograms, RB_1 (red), RF (blue), RB_2 (orange), FB_1 (green), FB_2 (teal) and RB_3 (purple) respectively. Note, however, that since absolute heights cannot be recovered, the knowledge of the parameter $h_0 = 3mm$ from (5.10) is used to bring all the heights to the same level. On top of the reconstructed height h_{ij}, the true height (5.10) is drawn in black. Other than some defects in the reconstruction of the very low-amplitude hologram RB_3, all reconstructed heights are found to be in excellent agreement with the true height field.

To investigate the error from reconstruction, we consider the difference $\Delta h = h - h_t$ of the reconstructed height field h and the true height field h_t (5.10). The distribution of this quantity across all pixels is shown in to the right in Figure 5.5. Here, the RF hologram is found to have the smallest error ($\mathcal{O}(0.5\mathrm{nm})\,\Delta h$, whereas RB_3 has the largest error ($\mathcal{O}(25\mathrm{nm})$.

To understand how the error varies from hologram to hologram, we should first observe that there are two* main competing factors. On the one hand, when inspecting the prediction (5.16) for the noise, we see that the error in the phase scales linearly with the size of the filter $F_m[\delta Y]$, which in our case is equal for all holograms, and inversely with the amplitude B_m. From this alone, we would conclude that the phase of the RB_1 hologram, which has the largest amplitude c.f. (5.8), will exhibit the least noise. On the other hand, when considering the translation of phases to heights h in (5.7), the RB_1-phase Φ_{RB_1} responds the least to the height, with $h \propto \Phi_{\mathsf{RB}_1}/(n_2 - n_1)$, meaning that the phase-noise is amplified the most when estimating the height. That is, the distribution of errors in the right panels of Figure 5.5 is in accordance with the predictions.

At this point, it should be commented that a shortcut exists when one is not interested in the full spatial dependence of the interface $h(t, \mathbf{r})$, but only in the evolution of the overall, spatially averaged height $\overline{h}(t)$. In that case, the Fourier demodulation (5.15) is not necessary. Indeed, since any modulation of a carrier peak $\mathbf{k}_m \equiv \nabla\Phi_m$ is caused by gradients ∇h of the height field, the overall height $\overline{h}(t)$ must be proportional to the phase of the Fourier amplitude $\mathcal{F}[Y](\mathbf{k}_m)$ exactly at the carrier $\mathbf{k}_m$. That is, the overall phase $\overline{\phi}_{ij}^{(m)}$ may be obtained from the substitution $F_m[Y]_{ij} \mapsto \mathcal{F}[Y]_{ij}(\mathbf{k}_m)$, bypassing the demodulation altogether. Note, however, that the phase can only be

*There is a third, important but complicated factor influencing the error that is omitted from the arguments presented here. That is the horizontal displacement of the phase-fields, due to both the tilted mirrors and the surface gradients.

recovered modulo 2π. One can, therefore, not measure the full depth $\overline{h}(t)$ using the above scheme, since only the wrapped phase fields can be recovered.

Note that the adjustability of a submerged mirror is what provides separate recovery of the different phases, but it is still possible to use the method without it. Indeed, without the mirror $\mathbf{m}_r$ altogether, the RF-hologram would remain. In fact, any sufficiently flat surface underneath the fluid has the potential to act as a mirror. That is, although an actual mirror is desirable, it can, in principle, be replaced with any flat surface. If the mirror is present but perfectly parallel with the undisturbed interface, i.e. $\mathbf{m}_r = 0$, then the holograms RB_j and RF all modulate the same carrier $\propto n_1\mathbf{m}_r$. A naive reconstruction would then hinge on the dominant amplitude of the RB_1 hologram, which is certainly the case for similar refractive index $n_2 \to n_1$. Alternatively, one may use a fitting procedure as in [215, 216] to disentangle the different phases that co-inhabit the carrier $n_1\mathbf{m}_r$.

To determine if a tilted submerged mirror is feasible in a specific situation, consider the following. Take, for example, the FB_1 beam whose carrier is $\mathbf{k}_{FB_1} \equiv \nabla\Phi_{FB_1} = 2k_0n_2\mathbf{m}_b$ according to (5.7). In an image of the intensity (5.3), the fringes due to this carrier has wavelength $L_{FB_1} \equiv 2\pi/|\mathbf{k}_{FB_1}|$. Denoting the physical width of a pixel in the image by px, e.g. $\mathrm{px} = \mathrm{mm}/100$, we have

$$|\mathbf{m}_b| = 2 \times 10^{-3} \left(\frac{\lambda}{532\mathrm{nm}}\right) \left(\frac{n_2}{1.33}\right)^{-1} \left(\frac{L}{10\mathrm{px}}\right)^{-1} \left(\frac{\mathrm{px}}{\mathrm{mm}/100}\right)^{-1}. \tag{5.19}$$

That is, for an image with resolution $\mathrm{px} = \mathrm{mm}/100$ to exhibit a fringe of FB_1 over a width of 10 pixels using a light-source with wavelength $\lambda = 532\mathrm{nm}$, the mirror submerged under a fluid with refractive index $n_2 = 1.33$ would have to be tilted two milliradians off-axis. Note here that a resolution of $\mathrm{px} = \mathrm{mm}/100$ corresponds to imaging a $2\mathrm{cm}$ wide region with resolution 2000×2000. This is, in practical situations, a high resolution and a small region. The point is that in many practical situations, the tilt $\mathbf{m}_b$ of the bottom mirror is of the order of magnitude one would expect it to be in the first place. In other words, the tilt needed from the submerged mirror is practically feasible, and often sufficiently small for it to have negligible effects on the dynamical deformations of the interface.

III. Experimental realisation

The experimental setup depicted in 5.1 is realised with caged, non-polarising, one-inch optical components using a green ($\lambda = 532\mathrm{nm}$) laser* with power $0.9\mathrm{mW}$. The basin is made from machined acrylic with a square cross-section of inner dimensions $89\mathrm{mm} \times 89\mathrm{mm}$ and bottom thickness of

*Collimated Laser-Diode-Pumped DPSS Laser Module, (ThorLabs CPS532-C2).

16.45mm. A cylindrical hole is made in the bottom to fit a broadband mirror inside, and a camera* with focus at infinity, is used to image the output beam.

The camera is connected to a computer running a custom-built Graphical User Interface. The app provides a live view of the images from the camera, along with various analysis pipelines on the fly. For example, this includes monitoring the spatial Fourier transform of the camera footage live. In the spatial Fourier transform view, the user can select carrier peaks and monitor the reconstructed phases $\phi_{ij}^{(m)}$.

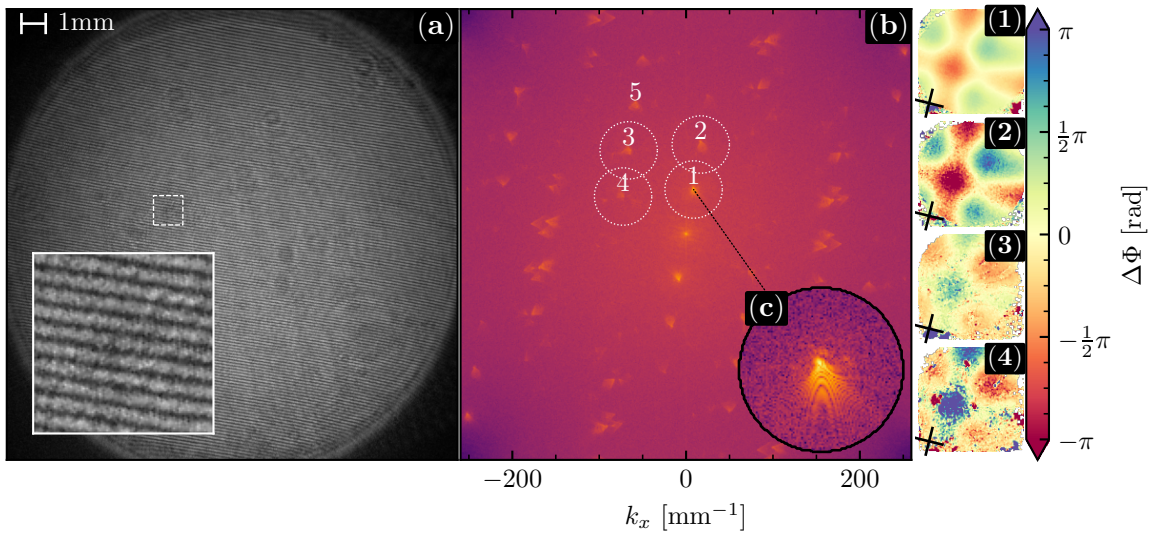

Figure 5.6 (Experimental realisation) Panel **(a)**: The experimentally imaged intensity Y_{ij} in grayscale. A magnification of the region indicated by the white dashed rectangle is shown in the inset. Panel **(b)**: The logarithmic amplitude $\ln|\hat{Y}|$ of the spatial Fourier transform $\hat{Y}$ of the image in panel (a). The locations of four holograms are labelled 1-6, and a scaled view of the peak labelled 1 is shown in panel **(c)**. For each of the four carriers 1-4, the corresponding demodulated phases are shown in panels **(1-4)**. Panels **(1-4)**: The reconstructed phases for the four carrier frequencies highlighted in panel (b) is shown in the regions where the carrier is sufficiently present ($|F_m[Y]_{ij}| \geqslant 1$px). In the lower left corner of each panel, a black cross is drawn to indicate the orientation of the square fluid container.

A representative image captured by the camera, with the basin filled with water, is shown in panel (a) of Figure 5.6. In panel (b) of Figure 5.6, the Fourier transform of the image in panel (a) is shown. Here, the first striking difference from the synthetic data is the much larger number of peaks than expected. Most of these can be attributed to a new family of holograms, also co-linear in k-space, that arises due to partial reflections from the beam-splitter. Consequentially, almost all

*Basler ace (acA2440-75um).

peaks appearing in panel (b) of 5.6 carry information about the height field. However, most of these additional holograms behave as lower-amplitude replicas of the already established families RF, RB_j and FB_j.

The large number of peaks appearing in the experimental data of Figure 5.6(b) introduces a complication not encountered in the simulated image. It is not at all clear which peaks should be associated with which of the predicted phases (5.7). On the one hand, the inclusion of reflections from the beam splitter, or other surfaces in the setup, introduces new holograms. On the other hand, discretization and saturation in the digital image is, for example, expected to create harmonics, appearing at integer multiples of each carrier frequency.

When performing the experiment, the identity of the peaks can be revealed via a simple test: if the reference beam R is blocked, then only the FB_j holograms should remain. This test was performed on the data exhibited in Figure 5.6, with the result that, out of the labelled peaks, only the one labelled 3 remained. Hence suggesting the identification of the peak 3 with FB_1. Likewise, the most prominent peak, which is the carrier labelled 1, can be attributed to RB_1. This peak identification was further supported by monitoring the response of the carrier locations when the two mirrors are independently tilted. That is, when adjusting the submerged mirror, only the carrier of the RF hologram remains fixed*. Likewise, an adjustment of the reference mirror leaves only the FB_j family fixed.

Although the carrier peaks can be identified when performing the experiment, all the information should be contained within a single image. However, labelling the peaks is much less straightforward than one might think. To illustrate the ambiguities that may arise when identifying the carriers using only a single image, let us attempt to label the peaks in Figure 5.6(b). To ease notation, we shall denote the location of each labelled peak in Figure 5.6(b) by $\mathbf{p}_a$, where a is the label appearing in Figure 5.6(b). First, naively comparing Figure 5.6(b) with the anticipated carrier locations 5.3 suggests that holograms should reveal themselves by belonging to two straight lines. One of the lines would be inhabited by the FB_j family, given by the line passing $\mathbf{p}_1$ and $\mathbf{p}_2$. The other would contain the RB_j and RF families, spanned by the peaks $\mathbf{p}_3$ and $\mathbf{p}_4$. From this, we would conclude that peak 1 should be labelled FB_1, peak 2 as FB_2, 4 as RF and 3 as RB_1. However, such an identification would be premature. For example, $\mathbf{p}_1$ is the brightest peak, which is responsible for the most prominent fringes in Figure 5.6(a). Being the brightest peak, the amplitude relations (5.8) suggests identifying $\mathbf{p}_1$ with RB_1, and not FB_1. This would mean that $\mathbf{p}_2$ is an unexpected hologram, appearing either as a harmonic of the RB_1-hologram, or as a genuine new hologram introduced by the partial reflections of the beam splitter. Playing along with this labelling, the natural candidates from RF and FB_1 would be $\mathbf{p}_3$ and $\mathbf{p}_4$. From the geometrical placement of the carriers in Figure 5.3, we expect the carrier for FB_1 to give RB_2 when added to that of RB_1, and to give RF when subtracted. Therefore, if we associate the peak $\mathbf{p}_4$ with FB_1, then $\mathbf{p}_3 \simeq \mathbf{p}_4 + \mathbf{p}_1$ would be RB_2, but RF would be absent. On the other hand, if we associate $\mathbf{p}_3$ with FB_1, then $-\mathbf{p}_4$ could be

*Note that an adjustment of the submerged mirror excites waves on the surface. Therefore, the RF also responds to the tilt, but returning quickly to its initial carrier after the initial perturbation is sufficiently damped.

RF, in which case $\mathbf{p}_5 \simeq \mathbf{p}_1 + \mathbf{p}_3$ would correspond to RB_2. This would mean that the higher order holograms such as FB_2 and RB_3 are absent, or greatly displaced. This is plausible as these holograms are expected to have very low amplitudes (c.f. (5.8)). Note, however, that multiple alternative identifications can be entertained. For example by instead identifying $\mathbf{p}_5$ with RF. At this point, it is clear that peak identification is, in itself, a formidable problem.

During the experiment, the table on which the experiment rests was tapped regularly to ensure the presence of waves on the water surface. Due to the square cross-section of the basin, the resulting interfacial waves should be resonant modes similar to those of the height field (5.10), with orthogonal wave-vectors $\mathbf{k}_1$ and $\mathbf{k}_2$. In 5.6(b), the holograms do not appear as extended rectangular regions as in the synthetic data 5.4, which can be seen in the magnification of peak 1 shown in panel (c) of Figure 5.6. This suggests, at first glance, that the aforementioned orthogonality of waves on the interface is absent. However, this can be identified with an overall curvature of the surface (perhaps due to a meniscus?), which can be eliminated by using the relative reconstruction scheme (5.17). Taking the previous image, captured a time $s/60$ earlier, as the reference image Y^0_{ij} in (5.17), we obtain the four phases exhibited in panels (1-4) of 5.6. These phases, or rather the changes in phase over one 60^{th} of a second, all exhibit a clearly correlated signal consisting of orthogonal waves. In each panel, a black cross is drawn to highlight the independently measured* orientation of the fluid container. The alignment of the phase deformations with the walls of the fluid container further validates the claim that the field independently measured by the separately reconstructed phase fields is, indeed, the interfacial height h.

In what follows, we shall consider two quantitative tests of the method. Firstly, we shall investigate the phase ratios, which may enable automatic peak identification, and comment on the possibility of measuring the refractive index as part of the experiment. Secondly, we shall validate the predicted heights, i.e. the constants of proportionality between the phases (5.7) and the height h, by changing the volume of the fluid by a known amount.

III.1. Peak Identification

Using the procedure outlined in section II.3, one may recover M phases $\{\phi^{(m)}_{ij}\}_{m=1}^{M}$ from a single image Y_{ij}. However, it is not always straightforward to identify these phases with those anticipated in (5.7). In this section, we shall discuss some promising approaches to this problem.

Firstly, in both the data analysis and when conducting the experiment, the RB_1 beam is easily identified using (5.8): it is the most prominent peak in k-space, i.e. the dominant plane wave in the image Y_{ij} (see e.g. Figure 5.4). Because amplitudes vary with the details of the experimental setup, however, one may benefit from verifying the identification by confirming that the modulation is the smallest. This follows from the pre-factor $\partial_h \Phi_{RB_1} = 2k_0(n_2 - n_1)$ in (5.7) being the smallest.

*This measurement is performed by aligning a striped transparency with the container, and determining the carrier $\mathbf{k}_m$ of the resulting image in the usual way.

When conducting the experiment, there are two simple tests one may perform to identify the interferograms. While monitoring the k-space of the image live, perform a small adjustment of the reference mirror. Then the RF and RB_j holograms will change their carrier location, whereas the FB_j and $B_\ell B_j$ holograms remain fixed. To single out the RF-peak, one may subsequently adjust the submerged mirror $\mathbf{m}_b$, to which all but the RF hologram should respond. Another simple test that can be performed during the experiment is to cover the reference arm, which ought to leave only the peaks associated with the FB_j and $B_\ell B_j$ beams.

If manipulating the experimental setup is not possible, the holograms may, in most circumstances, be identified directly from the reconstructed phases $\phi_{ij}^{(m)}$. From equations (5.7), the constants of proportionality between the phases $\phi_{ij}^{(m)}$ and the interface h are all of the form $2k_0\alpha_m$ for some linear combination α_m of n_1 and n_2 with integer coefficients. Here, one approach to the identification problem would be to inspect the ratios $\phi_{ij}^{(a)}/\phi_{ij}^{(b)}$ for all distinct pairs $a \neq b$ of reconstructions, and compare the fit results to the anticipated ratios n_a/n_b calculated from the knowledge of the refractive indices n_1 and n_2. However, this approach is both problematic due to potential zero-divisions in the ratios, and due to differences in the constant terms in the phases. Moreover, when armed with more than two distinct holograms, the ratios of phases, which (ideally) depend only on n_1 and n_2, are over-specified. Therefore, it is possible to perform a measurement of the refractive indices as part of the experiment.

The collection of reconstructed phases $\{\phi_{ij}^{(m)}\}_{m=1}^{M}$ can be seen as an M-dimensional vector field $\mathbf{p} = \sum_m \phi_{ij}^{(m)}(t,\mathbf{x})\mathbf{e}_m$. Assume that the phases were collected from a configuration in which the height field h was changing, either in space or time. Any spatial or temporal fluctuation of the height $h \mapsto h+\delta h$ results in a fluctuation $\mathbf{p} \mapsto \mathbf{p}+2k_0\mathbf{v}\delta h$ for a constant vector $\mathbf{v} = \sum_m \alpha_m \mathbf{e}_m$ which depends only on the refractive indices. That is, the vector $\mathbf{p}$ always responds to variations in h along the same axis $\mathbf{v}$, and this axis determines all the phase ratios. More generally, we may consider the spectrum $C\mathbf{v}_k = \lambda_k \mathbf{v}_k$ of the covariance matrix $C_{ab} = \langle X_{ij}^{(a)} X_{ij}^{(b)} \rangle$ for the centralised variables $X_{ij}^{(a)} \equiv \phi_{ij}^{(a)} - \langle \phi_{ij}^{(a)} \rangle$. Here, the average $\langle\cdot\rangle$ is purposefully left unspecified, as the preferred choice, e.g. average over space (pixels) or time (frames), will generally depend on the specific scenario considered. Assuming all phases measure the same interface, there is one eigenvector $\mathbf{v}_k$ of C_{ab} with eigenvalue λ_k much larger than the others, hereby referred to as the principal component. Note that this technique is commonly referred to as Principal Component Analysis (PCA) [219, 220]. In our case, the principal component is precisely the aforementioned vector $\mathbf{v}$. How consistently variations in the entire data $\mathbf{p}$ can be represented by the single field h is captured by the normalised eigenvalues $\mathrm{sg}_k \equiv |\lambda_k|/\sum_a |\lambda_a|$, where λ_k is the eigenvalue of the principal component. The quantity sg_k takes values from 0 to 1, where $\mathrm{sg}_k = 0$ would imply that there is no variation in the data at all, and $\mathrm{sg}_k = 1$ that all the variation in the data is entirely along the principal component $\mathbf{v}$.

In light of equation (5.7), the principal component $\mathbf{v}$ fixes the ratios of the phase fields, leaving only $|\mathbf{v}|$ as a free variable. Consequentially, we only need to identify one phase prefactor from equa-

tions (5.7) to obtain them all. Since the RB_1 beam can, in most situations, be easily identified, the information needed to transform the M reconstructed phases into estimates of the height field is thus obtained.

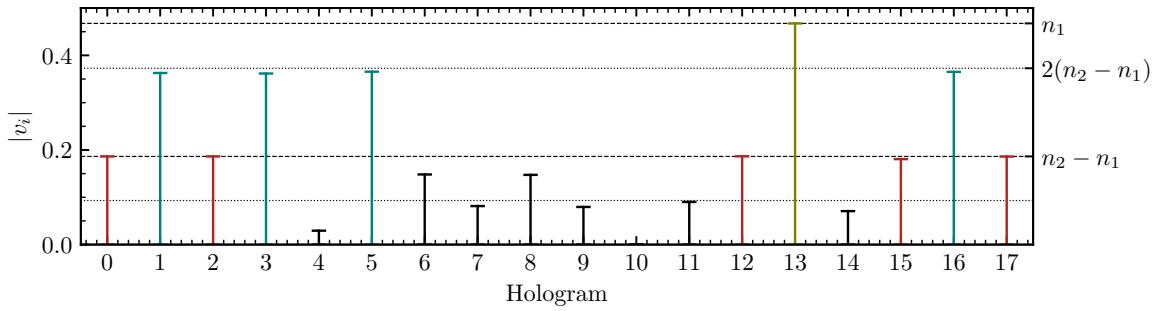

Figure 5.7 (Phase Ratios) The phase prefactors v_i predicted from a temporal PCA with $sg_k = 97\%$ are shown. There is no successfully reconstructed FB_1 beam, but the RF beam (13/green) is present. Most holograms are equivalent to RB_1 (red), or its doubling $\widetilde{RB}_1$ (blue). Prefactors corresponding to holograms that could not be reconstructed consistently are coloured black.

An example of the entries v_i of a principal component $\mathbf{v}$ is shown in Figure 5.7. The details of this experiment will be discussed in the next section. Here, the averages $\langle\cdot\rangle$ used in the PCA are taken across time. The holograms are sorted by amplitude, so that 0 corresponds to the brightest peak, 1 to the second brightest, and so on. In Figure 5.7, the 17 holograms considered are divided into four categories. First, the brightest peak, hologram 0, can be identified with RB_1. All holograms that respond similarly (0,2,12,15,17) to variations in the height as the RB_1 hologram are coloured red. As such, the red holograms can be associated with the prefactor $n_2 - n_1$ in the entries of the principal component. The second brightest peak, hologram 1, responds twice as much as RB_1 to variations in the height. Every hologram with this response (1,3,5,16) is coloured blue in Figure 5.7. Note that these holograms, hereby referred to as the doublings $\widetilde{RB}_1$ of RB_1, are not expected from the theory. It is, however, not hard to imagine extensions of the theory that would incorporate the doublings. For example, including the additional reflections from the beam splitter would naturally produce candidates for $\widetilde{RB}_1$ at the right locations. Regardless of the model, it is clear that the doublings can equally well be used to measure the interface. In Figure 5.7, there is a single hologram, number 13 (green), with a height-response much larger than the others. The response of this hologram is consistent with the label RF. The holograms (4,6,7,8,9,10,11,14) that do not fall into the aforementioned categories, i.e. RB_1, $\widetilde{RB}_1$ and RF, are coloured black in Figure 5.7. The phases of these holograms are only weakly correlated with the height field.

III.2. Varying depth by injecting a known volume

To test of the validity of the reconstruction, consider the response of phases Φ_a of the form (5.7) to changes in the volume of the fluid. All phases in (5.7) can be written $\Phi_a = \Phi_{a0} + 2k_0 n_a h$, where Φ_{a0} is independent of the interface h, and n_a is some function of the refractive indices n_1 and n_2 of the fluid and the surrounding gas. The constant cross-sectional area A of the container (see figure 5.1) means that changes dV in the volume V of the fluid is related to changes $d\Phi_a$ in the phase Φ_a through

$$d\Phi_a \simeq \frac{2k_0 n_a}{A} dV. \tag{5.20}$$

Based on this observation, we aim to inject a known amount of fluid into the basin slowly and compare the predicted change in height $\Delta h_v(t)$ from the supplied volume $V(t)$ with the measured overall change height $\overline{h}(t)$ from the spatially averaged phase $\Phi_a(t)$ of a single hologram.

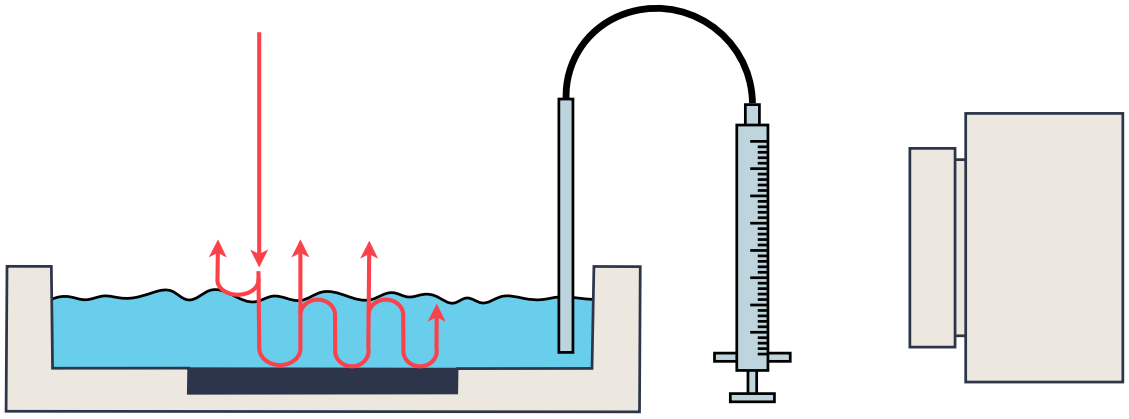

Figure 5.8 (Supplied volume schematic) The spatially averaged heights predicted from different holograms are monitored while the basin is slowly being injected with fluid. A camera keeps track of the volume in the syringe, which is used to independently predict the change in interfacial height resulting from movement of the syringe piston.

This is done by attaching a 1mL syringe to a capillary tube pointing into the bottom of the fluid (see figure 5.8). The syringe is slowly driven by a remote-controlled mechanical device set to produce an even in/out-flux of water. The syringe volume is monitored by a camera*. By cross-correlating images along the syringe-piston axis and measuring the result in units of the separation of the increment indicators, a detailed curve of the volume over time is obtained. The measured volume $V(t)$ is shown (black line) in panel (a) of figure 5.9, where the initial linear injection period is measured to have flux rate 12.3μL/sec. This is sufficiently small for temporal phase-unwrapping

*The two image sequences of the cameras are synchronized by time-stamping.

to be possible (see (5.7)) at the chosen acquisition rate of 60fps. During the first 75 seconds of the experiment, volume is injected at a constant rate. Then, after a 5s period of rest, the volume is withdrawn at approximately the same rate, but with regular brief pauses.

The resulting holographic data consists of a series of 8193 images with resolution 1024×1024. From the initial image, 20 holograms are identified by locating the most prominent carrier peaks (see panel (b) of figure 5.9). These are hereby labelled $a = 0, \ldots, 19$ by their order when sorted by decreasing amplitude. The collection of unwrapped phases $\Phi_a(t)$ for each hologram is found to be consistent with a single principal component, having significance sg_k of 97.4%, from applying the PCA introduced in section III.1. Indeed, identifying the phase $\Phi_0(t)$ with the RB_1 interferogram for which the prefactor $n_a = n_2 - n_1$ is known, the relation 5.20 may be used to obtain consistent measurements of the overall height using 10 of these 20 holograms. These curves, shown as coloured lines in figure 5.9(a), are all found to match the independently measured syringe volume (black line).

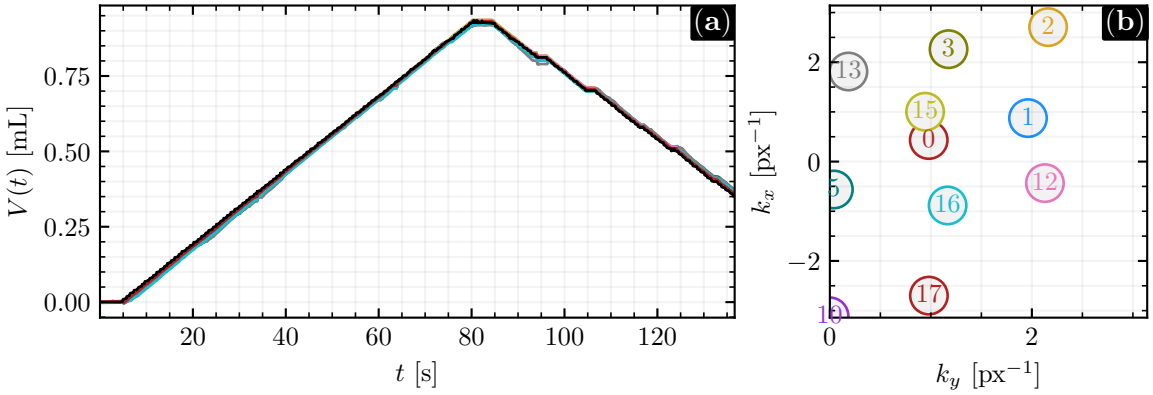

Figure 5.9 (Known Volume) Panel **(a)**: The volume $V(t)$ added to the basin over time during the experiment. The black line is the independently measured ejected volume from the syringe, and the overlapping coloured lines are inferred changes in volume using the 10 holograms with carrier frequencies shown in panel **(b)**.

Note that although 10 holograms could be consistently used to recover the correct volume in the basin independently, this does not mean that these are all distinct phases from (5.7). Indeed, when inspecting the principal component, shown in Figure 5.7 in the previous section, we saw that all except one of the weights are an integer multiple of the same prefactor.

IV. Summary and Conlusion

In this chapter, we have demonstrated the use of digital holography to measure waves on fluid surfaces. First, in section II, we found analytical predictions (5.7) for the phase differences associated

with three families, R, F and B_j, of rays. Crucially, all these phases are proportional to the interfacial height, meaning each offers an independent measurement of the surface, provided that they can be separately recovered. We discussed how introducing a gentle tilt of the two mirrors resulted in the desired separation of the holograms in the spatial Fourier domain.

Next, we shifted focus towards a numerical simulation of an idealised optical setup. The simulated images were found to be in excellent agreement with the predicted separation of peaks, and the phases could be reconstructed using standard Fourier demodulation techniques. We then introduced a simple experimental realisation of the principle. Here, we discussed the additional challenges that appear in realistic data, emphasising the large number of unanticipated holograms that can appear due to additional reflecting surfaces and discretization effects. We argued that rather than presenting a problem for the method, these additional holograms can be used to reconstruct the surface. We saw how the holograms could be identified using Principal Component Analysis (PCA), and argued that this approach has the potential for extracting the values for the refractive indices of the media as part of the experiment.

Finally, we considered a simple test of the method, wherein the volume of the measured fluid was adjusted while the surface was monitored. The change in fluid volume deduced from 10 distinct holograms was in excellent agreement with an independent measurement of the volume.

It is clear that the method is flexible and has wide applicability. Perhaps the most appealing feature is that spatial defects in the amplitude of the optical beam are relatively unimportant. Due to the multiplexing, the technique can be realised with basic optical components, and is expected to be applicable also in situations where more intricate optical setups are impractical. For example, ongoing investigations into the possibility of using the device to measure refractive index, evaporation rates, and coefficients of thermal expansion have proven promising.

Chapter 6

Conclusion

In this thesis, we have investigated a variety of phenomena, in a variety of physical situations, ranging from quantum vortices in two-dimensional BECs, to classical two-fluid systems and optical profilometry. Our initial motivation came from analogue gravity, where previous studies have suggested that astrophysical phenomena are more universal and robust than anticipated from mathematical analogies. Motivated by this, we set out to investigate astrophysical effects from the perspective of the simulators when pushed further into incalculable regimes. In doing so, we discovered novel tools and effects in each respective system. This brings us back to a claim made in the introduction; that when an analogy is formed, it opens a two-way bridge between different fields of physics. It seems, then, that if one of the systems exhibits an interesting phenomenon, then that phenomenon is interesting in both systems. Let us briefly revisit the results of this thesis, and comment on what we have learned from the perspective of the analogy.

In chapters 2 and 3, we investigated the dynamics of quantum vortices in two-dimensional BECs. A quantized vortex of charge ℓ constitutes a rotating flow $v_\theta = \ell/r$ around it. Therefore, from the perspective of the analogy, a quantised vortex can be thought of as a rotating spacetime with discretized circulation, and without a horizon (c.f. (1.2)).

In the first part, chapter 2, we studied the dynamical instability of the multiply charged vortex in the context of rotational superradiance. In black hole physics, rotational superradiance is a mechanism wherein incident waves are amplified at the expense of the rotational energy of the black hole. At first glance, it is therefore unclear how superradiance would proceed in a system where the rotation is of a discrete and topological nature. As it turns out, the supperradiance mechanism results in an instability that tears multiply charged vortices apart. In the first part of chapter 2, we investigated the details of this process. Here, we saw that the instability could be interpreted as a perpetual amplification of negative energy modes near the vortex core due to an interaction with positive energy modes outside. In particular, we found that it is this negative energy mode in the core that guides and splits the multiply charged vortex. Moreover, our approach naturally connected the instability in open and closed systems. In closed systems, we saw that the vortex could be stabilised[†].

In the last half of chapter 2 we studied the fate of the doubly-quantised vortex in detail using nonlinear simulations. Here, we discovered a new phenomenon that may occur in small systems at

[†]Technically, we only investigated the stability of the doubly wound ($\ell = 2$) vortex. For vortices with higher charge, there will be more candidates for the instability, and one would expect stabilisation to be impossible for sufficiently large ℓ.

very low temperatures. Instead of decaying fully into two separate vortices, the vortex splits into two phase singularities that perpetually switch from spiralling outwards, to spiralling inwards. We saw that this process could be interpreted as a nonlinear phase-shift in the growing mode, transforming it into a decaying mode, and that the process can be seen as a perpetual release and re-absorption of compressible energy. Finally, we concluded that the effect should have observable consequences also in dissipative systems, making it relevant in experiments.

From these investigations, it is clear that the superradiance mechanism is responsible for relevant and interesting physics in the simulator. In particular, the consequences of superradiance are, due to the instability that arises, rather different from those of a rotating black hole. In light of this, a particularly interesting system to further investigate this link would be one where circulation is quantized, as in the quantum vortex case, but the effective spacetime exhibits a horizon, as in the black hole case. It has been argued that in such systems, the instability is stabilised. If the instability is absent, we are again faced with the conundrum of how rotational energy can be harvested from a system where rotation is topological. For example, if waves are continually superradiated off such a system, it must continually shed rotational energy. It stands to reason that, perhaps, if the superradiance mechanism is not somehow prevented, that the vortex will eventually lose one quantum of rotation. One system that exhibits such features is a draining bathtub flow of superfluid.

In chapter 3, we investigated a system closely related to the preceding chapter, namely the decay of dense vortex clusters. Here, the motivation came from the ringdown process for the relaxation of compact astrophysical objects. When these astrophysical objects are excited, they can relax through the emission of long-lived, decaying waves referred to as Quasi-Normal Modes (QNMs). These waves, which are ingoing at the horizon, and outgoing at infinity, are, in most cases, intimately connected to the existence of circular trajectories of light, or light rings. In this context, light rings can be thought of as unstable fixed points in the radial phase space for the waves. A wave excited at a light ring is trapped by the geometry and will leak out slowly. It is in this sense that the waves emanating from the light ring are often taken as approximations of the QNM spectrum.

Being a relaxation process, however, the ringdown is conceptually related to the strive of a compact astrophysical object towards its equilibrium state. Therefore, it is not clear how the process is modified if there is no equilibrium, and the background on which waves propagate is instead evolving.

The relaxation of the vortex cluster represents an interesting platform to investigate these effects. Since a cluster of high charge is energetically unstable, any dissipative mechanism may expand the cluster. The result is the dissipative expansion of a vortex cluster investigated in chapter 3. Curiously, while the core expands, the flow outside the vortex cluster is kept relatively fixed. The consequence was that the light-ring, or rather the sound-ring in this case, was kept intact. The significance of the sound-ring, however, appeared as something quite different from the black hole case. Whereas the ringdown process for black holes is related to the late relaxation following an excitation in the past, the sound-ring was continually excited by the escaping waves produced by the dynamically evolving vortices in the core. The sound-ring revealed itself not only as a relaxation channel, but as an

emergent, geometrical feature that was independent of the vortex configurations in the core. Based on this observation, we were able to predict the main features of the radiated spectrum of (counter-rotating) sound using only one parameter; the net charge ℓ of the cluster. That such a simple model can be used to predict features in a system of such complexity, is not at all obvious. Such a model is, for example, expected to be of relevance for investigations into quantum turbulence. Here, the sound-ring is an example of how the astrophysical phenomena can, often serendipitously, lead to the discovery of effects that are relevant in the field of the simulator. Returning to the gravitational perspective, the sound-ring offers the following lessons. Firstly, our results suggests that light-ring physics remains predictive also when the background is evolving. Secondly, although the absence of a horizon changes the consequences and interpretation of waves emanating from the light-ring, aspects of the mechanism remain relevant and predictive also in this case. Finally, light-ring physics seems relatively insensitive to the discretization of circulation. On this final point, it should be stressed that whereas the light-ring remains predictive in the case of discretized circulation, it seems likely that the phenomenon should affect the vortex configurations. For example, in the case of the decaying vortex cluster, the sound-ring existed only in the counter-rotating part of the spectrum. Since we interpreted the sound-ring mechanism as a blocking-mechanism of escaping waves, is it tempting to entertain the idea that this suppression of counter-rotating radiation can somehow be related to the reduction in rotational energy of the cluster.

In chapter 4, we shifted focus toward the parametric amplification of classical two-fluid interfaces. In particular, we experimentally investigated the well-known Faraday instability experienced by a two-fluid interface upon vertical oscillation of its container. We presented an extended model for the nonlinear dynamics, which incorporates two-fluid interfaces and higher order effects from surface tension. To compare the experimental data with theory, we considered numerical simulations of a phenomenological stochastic extension of the nonlinear dynamics. This model was shown to not only reproduce the behaviour of a single experimental realisation but of the entire experimental ensemble. We did this by introducing a measure of non-Gaussianity of the ensemble, which to my knowledge, is a technique new to classical fluid dynamics. Moreover, we saw, in both theory, numerical simulation and experiment, how the resonant mode turning nonlinear led to the amplification of modes that would otherwise have been unable to grow. This is particularly interesting as it opens the possibility for monitoring the appearance of secondary instabilities over time. Such a time-dependent cascade of one mode into many can, for example, may help to shed light on the nature of turbulence.

Finally, we commented on the similarities with cosmological preheating. In particular, the nonlinear effects, such as the emergence of secondaries and the broadening of resonance bands, remain consistent with the preheating mechanism. Interestingly, this hints that aspects of the analogy may indeed remain applicable when extrapolated into the nonlinear regime, which is not all obvious. More generally, this system represents a promising, new, classical context, in which cosmological preheating can be placed under experimental scrutiny.

In the final body of this work, chapter 5, we investigated a new technique for measuring fluid

interfaces using the principles of holography. Here, the key idea is to exploit the multitude of rays that appear due to partial reflections from the interface, along with a gentle tilt of the bottom face of the fluid, to enable multiple independent measurements of the interface simultaneously. The first prototype of a device implementing this principle confirms the applicability of the method. The detection method presented in chapter 5 may be used when further investigating the relationship between parametric amplification of two-fluid interfaces and cosmological preheating discussed in chapter 4. This can, perhaps in combination with the currently used Fourier Checkerboard Demodulation (FCD) method, permit monitoring the interfacial waves all the way from the equilibrium fluctuations of the interface at rest, to the nonlinear regime.

Work is in progress for setting up a draining bathtub flow in superfluid ^{4}He. Such a flow represents a black hole simulator with topological and quantum features, and as such, can help elucidate how gravitational phenomena are modified by such features. It is in anticipation of this coming series of experiments that all the efforts of this work is united. Here, an adaptation of the holographic detection scheme will be implemented to recover the surface fluctuations of the superfluid. This will enable investigation of the superradiance mechanism as well as the ringdown process in the system. The same detection scheme will be used to repeat the preheating experiments, both in further investigations of the classical setup and in the superfluid.

The superfluid simulator is bound to offer lessons on wave phenomena in spacetimes with discrete and topologically non-trivial features. Who knows, perhaps observable consequences of quantum features of spacetime will be revealed. Most certainly, however, these experiments will offer lessons on the extent, robustness and universality of the various astrophysical phenomena. One thing is certain: as we strive to push the simulated phenomena further into uncharted territory, we will also learn about the physics of the simulator.

Appendix A

WKB scattering and resonances

In this appendix, I present different aspects and techniques surrounding the Wentzel–Kramers–Brillouin (WKB) approximation for wave solutions of partial differential equations, which focus on the rotationally symmetric case. Parts of the formalism is unique, but it rests heavily on that of Patrick [221, 222] and Tracy [163].

A.1. Introduction

The WKB approximation is a special case of multiscale expansion in which one considers oscillatory functions f with a phase varying much faster than the amplitude. That is, the amplitude varies slowly compared to the phase or, equivalently, the characteristic scale over which the background varies is much larger than the local wavelength. When plane waves are exact solutions of the underlying equations, such as for wave equations in a homogeneous medium, the WKB method is exact. In such cases, the equations of motion determine a relation between the wavevector $\mathbf{k}$ and the frequency ω of the waves called the dispersion relation. In an inhomogeneous medium, the dispersion relation appears as the leading order solution in the WKB expansion and gives the relation between the local values of $\mathbf{k}$ and ω.

The text is structured as follows. First, in section A.2, a WKB expansion for a class of systems is investigated to leading, and next-to-leading order. In section A.3, a Hamiltonian system for the local wavefronts is constructed. The resulting, particle-like dynamics is used to investigate what it takes for waves to stagnate. Then, in A.4, we construct transfer matrices that relate WKB amplitudes on different sides of stagnation points, where the method breaks. The analysis is specialised for a radial coordinate. Finally, we discuss the different types of phenomena such as superradiance, quasi-bound states and tunnelling in depth.

A.2. The WKB expansion

Suppose you have a differential equation for f for which the highest derivative is small. You may then expand the equation using

$$f \simeq A e^{i\Phi/\varepsilon} \text{ with } \partial \mapsto \varepsilon\partial \text{ and } \Phi = \sum_{n=0}^{\infty} \varepsilon^n \Phi_n \tag{A.1}$$

and separate different powers of ε as $\varepsilon \to 0$. Here, the symbol ∂ refers to any first-order partial differential operator.

In this section, we shall consider a general system of coupled equations of the form

$$D_t M_1 = \hat{K}_1(-i\nabla) M_2 \tag{A.2a}$$

$$D_t M_2 = \hat{K}_2(-i\nabla) M_1, \tag{A.2b}$$

where $D_t = \partial_t + \mathbf{v}\cdot\nabla$ is the convective derivative, and $\hat{K}_a$ is assumed to be expandable in $-i\nabla$, i.e. an arbitrary smooth function f

$$\hat{K}_a(-i\nabla) f = \sum_n \frac{K_a^{(n)}}{n!} (-i\nabla)^n f, \tag{A.3}$$

where the coefficients $K_a^{(n)}$ may depend on the spatial coordinate. Note that if $f = Ae^{i\Phi/\varepsilon}$ then, to linear order in ε,

$$e^{-\frac{i\Phi}{\varepsilon}} K_a(-i\varepsilon\nabla) A e^{\frac{i\Phi}{\varepsilon}} \simeq \left(A - i\varepsilon \nabla A\cdot\nabla_k\right) K_a(\mathbf{k}) \text{ for } \mathbf{k} \equiv -i\nabla\Phi. \tag{A.4}$$

To invoke the WKB approximation, we introduce a change of variables $M_n = A_n e^{i\Phi/\varepsilon}$ for $n \in \{1, 2\}$. Note that this does not require the two functions M_n to have the same phase, but rather that difference in phase of M_1 and M_2 varies slowly, i.e. on the same scale as A_n. Introducing the short-hand notation $K_a = \hat{K}_a(-i\nabla\Phi)$, we have

$$-iA_a\Omega + A_b K_a + \varepsilon\left[-D_t A_a + i\nabla A_b\cdot\nabla_k K_a\right] = 0 \tag{A.5}$$

where $\Omega \equiv iD_t\Phi$. To leading order, we have the dispersion relation

$$\Omega^2 = -K_b K_a \text{ with } A_a = A_b \frac{K_a}{i\Omega}, \tag{A.6}$$

and the linear equation demands

$$D_t A_a = i\nabla A_b\cdot\nabla_k K_a. \tag{A.7}$$

By using the dispersion relation (A.6) the linear order equation (A.7) can be written in the suggestive form

$$\frac{\partial_t R + \nabla \cdot R\mathbf{v}_g}{R} = \nabla \cdot \mathbf{v} + \frac{\Omega}{2}\left[\frac{\nabla \cdot \nabla_k K_a}{K_a} + \frac{\nabla \cdot \nabla_k K_b}{K_b}\right] \tag{A.8}$$

for $R \equiv A_a A_b$, where $\mathbf{v}_g \equiv \nabla_k \Omega - \mathbf{v}$ is the group speed. That is, R is conserved along the group flow $\mathbf{v}_g$ if the background is incompressible $\nabla \cdot \mathbf{v} = 0$, and there is no cross-terms, i.e. $\nabla \cdot \nabla_k K_b = 0$ for $b = 1, 2$. For rotationally symmetric and time-invariant amplitudes, we find

$$\nabla \cdot R\mathbf{v}_g = 0. \tag{A.9}$$

Let us consider some examples from the main text. First, in chapter 3, we constructed an effective linear system (see (3.22)) that can be matched with (A.2) by identifying

$$\begin{aligned} D_t \delta\rho &= -\rho_0 \nabla^2 \delta\phi\,, \\ D_t \delta\phi &= -\left(1 - \frac{\nabla^2}{4\rho_0}\right)\delta\rho \end{aligned} \quad \Longleftrightarrow \quad \begin{aligned} M_1 &= \delta\rho \\ M_2 &= \delta\phi \\ K_1(\mathbf{k}) &= \rho_0 \mathbf{k}^2 \\ K_2(\mathbf{k}) &= -\left(1 + \frac{\mathbf{k}^2}{4\rho_0}\right). \end{aligned} \tag{A.10}$$

That is, the comoving dispersion relation takes the form

$$\Omega^2 = \left(\omega_D^{\pm} - \frac{m v_\theta}{r}\right)^2 = F(\mathbf{k})\mathbf{k}^2 \text{ for } F(k) \equiv \rho_0 + \frac{1}{4}\mathbf{k}^2 \tag{A.11}$$

which matches that of (3.24). Moreover, the amplitudes obey the conservation law (A.9), which takes the form

$$\partial_r \left(r F^{-1} \Omega v_g^r \mathcal{A}^2\right) = 0 \quad \text{with} \quad \mathcal{B} = -i F^{-1} \Omega \mathcal{A}, \tag{A.12}$$

for the amplitudes $\mathcal{A}$ and $\mathcal{B}$ defined in (3.23).

Another example is the (corrected) WKB expansion of equations (2.16), from chapter 2. Here, we argue that by introducing variables $\delta\Phi \equiv \delta\tilde{\Phi}/\sqrt{\rho}$ and $\delta\rho \equiv \delta\tilde{\rho}/\sqrt{\rho}$, the WKB expansion becomes well behaved. When supplied with the vortex density relation (2.10), i.e. $\nabla^2\sqrt{\rho} = [\ell^2 + 2r^2(\rho - 1)]\sqrt{\rho}/r^2$, the resulting equation matches the general form (A.2), with

$$\begin{aligned} D_t \delta\tilde{\rho} &= \left[-\nabla^2 + \frac{\nabla^2\sqrt{\rho}}{\sqrt{\rho}}\right]\delta\tilde{\Phi} \\ D_t \delta\tilde{\Phi} &= -\frac{1}{4}\left[4\rho - \nabla^2 + \frac{\nabla^2\sqrt{\rho}}{\sqrt{\rho}}\right]\delta\tilde{\rho} \end{aligned} \quad \Longleftrightarrow \quad \begin{aligned} M_1 &= \delta\tilde{\rho} \\ M_2 &= \delta\tilde{\Phi} \\ K_1(\mathbf{k}) &= \mathbf{k}^2 + \frac{\ell^2}{r^2} + 2(\rho - 1) \\ K_2(\mathbf{k}) &= -\frac{1}{4}\left[4\rho + \mathbf{k}^2 + \frac{\ell^2}{r^2} + 2(\rho - 1)\right] \end{aligned} \tag{A.13}$$

which, results in the form displayed in (2.29), i.e.

$$\Omega^2 = F(k)k^2, \qquad F(k) \equiv \rho + \tfrac{1}{4}k^2, \tag{A.14}$$

$$k^2 \equiv p^2 + \widetilde{m}^2/r^2, \qquad \widetilde{m}^2 \equiv m^2 + \ell^2 + 2r^2(\rho - 1). \tag{A.15}$$

In particular, we recover relation for the amplitudes (A.12).

A.3. Eikonal Ray-Tracing

In this section, I discuss how to use the leading order equation in a WKB expansion, as in (A.6), to construct a Hamiltonian system local dynamics of solutions. We shall write $\sqrt{-K_1K_2} = c(k)k$ so that the dispersion relation can be written in the form $\Omega_d^2 = c^2k^2$, where c can be interpreted as the speed of propagation. Our Hamiltonian system is constructed by following a trajectory of constant phase (see e.g. [163]), where the dispersion relation is imposed as a Lagrange multiplier constraint, i.e.

$$\delta \int_{\lambda_0}^{\lambda_1} \left[k_i \frac{dx^i}{d\lambda} - \omega \frac{dt}{d\lambda} + H \right] d\lambda \overset{!}{=} 0 \text{ with } H \equiv \frac{1}{2}\Omega^2 - \frac{1}{2}\Omega_d^2 \tag{A.16}$$

where the $1/2$ factor is introduced for convenience and λ parametrises the trajectory. The symbol δ signals infinitesimal change of the trajectory in the variational calculus sense. The resulting dynamics is that of an Hamiltonian flow

$$\dot{\mathbf{x}} = -\nabla_k H, \quad \dot{\mathbf{k}} = \nabla H \tag{A.17a}$$

$$\dot{t} = \partial_\omega H, \quad \dot{\omega} = -\partial_t H \tag{A.17b}$$

$$\text{with } \Omega = \pm\Omega_d. \tag{A.17c}$$

Here, without loss of generality, we have $\dot{t} = \Omega_d$ and therefore time t is related to the parametrisation λ of the trajectory through $\partial_t = \Omega_d^{-1}\partial_\lambda$. This means that $\dot{\mathbf{x}} = \Omega_d \mathbf{v}_g$, where, as before, $\mathbf{v}_g$ is the group speed. That is, as it should, the location $\mathbf{x}$ of a wave-packet moves with the group speed. One consequence of this is that a wave-front stagnates spatially $\dot{\mathbf{x}} = 0$ whenever $\nabla_k H = 0$. At these points the phase does not accumulate much faster than the amplitudes, casting doubt upon the validity of the WKB approximation. Note also that we may write $\partial_t \mathbf{k} = -\nabla\omega$, meaning that the direction of propagation is refracted by spatial variations in the frequency.

We note that in polar coordinates $\mathbf{x} = (r, \theta)$ we may write the phase as $d\Phi \equiv k_r dr + m d\theta - \omega dt$. In that case, the system (A.17) can be written

$$\dot{r} = -\partial_{k_r} H, \quad \dot{k}_r = \partial_r H \tag{A.18a}$$

$$\dot{\theta} = -\partial_m H, \quad \dot{m} = \partial_\theta H \tag{A.18b}$$

$$\dot{t} = \partial_\omega H, \quad \dot{\omega} = -\partial_t H \tag{A.18c}$$

$$\text{with } \Omega = \Omega_d \tag{A.18d}$$

from which it is clear that rotational symmetry, i.e. $\partial_\theta H = 0$, results in conservation of azimuthal number m, and time-translation symmetry, i.e. $\partial_t H = 0$, results in the conservation of frequencies ω. Note that the conservation of m is associated with an angular velocity $\dot{\theta} \equiv -\partial_m H$. In this case, we may introduce $\Omega_d = \omega_d + \mathbf{v}\cdot\mathbf{k}$ to observe that ω_d acts as the effective Hamiltonian for the radial phase space, i.e.

$$\frac{dr}{dt} = \frac{\partial \omega_d}{\partial k_r} \qquad \text{and} \qquad \frac{dk_r}{dt} = -\frac{\partial \omega_d}{\partial r}. \tag{A.19}$$

Here, we observe that turning points are given by radial stagnation $\partial\omega_d/\partial k_r = 0$. Note also that the time it takes a wave to traverse a curve γ is

$$dr = \frac{\partial \omega_d}{\partial k_r} dt \implies \int dt = \frac{\partial}{\partial \omega_d} \int k_r \frac{\partial \omega_d}{\partial k_r} dt = \partial_{\omega_d} \int k_r \, dr, \tag{A.20}$$

which is the equivalent of the energy-derivative of phase space area of a closed orbit is the time.

A.4. Beyond WKB: Transfer Matrices and Resonances

At the turning points, where $\nabla_{\mathbf{k}}\omega = 0$, one encounters problems. The radial derivative of the amplitude diverges, and therefore violates the WKB assumption of a phase varying much faster than the amplitude. We note, however, that all other quantities can remain linearized, so that we have $\mathcal{H}\phi = 0$ where $\mathcal{H}$ is the Hamiltonian H from (A.16) but where $\mathbf{k}$ is kept as a differential operator, i.e. $\mathbf{k} = -i\nabla$. Close to a turning point $\mathbf{x}_0$, we then have

$$\mathcal{H} \simeq \mathcal{H}_0 + (\partial_i H)(x^i - x_0^i) + (\partial_{k_i} H)(k^i - k_0^i) \tag{A.21}$$

$$+ \frac{1}{2}(\partial_{k_j}\partial_{k_i} H)(k_i - k_i^0)(k_j - k_j^0) \tag{A.22}$$

$$+ \frac{1}{2}(\partial_j \partial_i H)(x^i - x_0^i)(x^j - x_0^j) + (\partial_{k_i}\partial_i H)(x^i - x_0^i)(k_j - k_j^0) \tag{A.23}$$

$$= (\partial_i H)(x^i - x_0^i) + \frac{1}{2}(\partial_{k_j}\partial_{k_k} H)(-i\nabla_k - k_k^0)(-i\nabla_j - k_j^0) + \mathcal{O}((\mathbf{x}-\mathbf{x}_0)^2, (\mathbf{k}-\mathbf{k}_0)^3) \tag{A.24}$$

in the case of axial symmetry, it suffices to expand only the radial phase space, so that

$$\mathcal{H} \simeq (\partial_r H)(r - r_0) + \frac{1}{2}(\partial_{k_r}^2 H)_0(-i\partial_r - k_r)^2 \tag{A.25}$$

$$= (\partial_r H)(r - r_0) + \frac{1}{2}(\partial_{k_r}^2 H)(k_r^2 + 2k_r i\partial_r - \partial_r^2)$$

so if $\partial^2_{k_r} H \neq 0$ at the turning point, then the equation $\mathcal{H}\phi = 0$ takes the form

$$-\partial_r^2\phi + 2ik_r\partial_r\phi + \left[k_r^2 + Q(r - r_0)\right]\phi = 0 \text{ for } Q \equiv 2\frac{\partial_r H}{\partial^2_{k_r} H} \tag{A.26}$$

which simplifies greatly when factoring out a plane wave by introducing $\phi \equiv A\exp(ik_r r)$. Then the above equation takes the form $\partial_r^2 A - Q(r - r_0)A = 0$. With the substitution

$$z \equiv Q^{1/3}(r - r_0) \tag{A.27}$$

this is the Airy equation $\partial_z^2 A = zA$, whose solutions are the Airy functions of the first (Ai) and second (Bi) kind. Therefore, the solution to the wave equation around a turning point (r, k_r) is

$$\phi = e^{ik_r r}\left[C_1 Ai(z) + C_2 Bi(z)\right]. \tag{A.28}$$

The Airy functions are rarely nice to work with, but in this case, we are only interested in using them to glue the WKB modes on each side of the turning point together. Therefore, it suffices to observe the asymptotics

$$Ai(z) \simeq \frac{1}{2\sqrt{\pi}|z|^{1/4}}\begin{cases} e^{-\frac{2}{3}z^{\frac{3}{2}}} \text{ for } z \to \infty \\ 2\cos\left(-\frac{2}{3}(-z)^{\frac{3}{2}} + \frac{\pi}{4}\right) \text{ for } z \to -\infty \end{cases} \tag{A.29}$$

$$Bi(z) \simeq \frac{1}{2\sqrt{\pi}|z|^{1/4}}\begin{cases} 2e^{\frac{2}{3}z^{\frac{3}{2}}} \text{ for } z \to \infty \\ 2\sin\left(-\frac{2}{3}(-z)^{\frac{3}{2}} + \frac{\pi}{4}\right) \text{ for } z \to -\infty \end{cases} \tag{A.30}$$

We now need to match this with the WKB solution close to this point. First note that (A.25) can be inverted to inform us that if $\mathcal{H} = 0$, then $k_r = k_{r0} \mp Q^{\frac{1}{3}}(-z)^{\frac{1}{2}}$, and so

$$\int k_r dr = k_{r0} r \pm \frac{2}{3}(-z)^{\frac{3}{2}} + \text{const.} \tag{A.31}$$

Knowing this, we use the perturbed Hamiltonian combined with (A.9) to estimate the WKB solution ϕ near the turning point. The result is

$$\phi_\mp \simeq |z|^{-\frac{1}{4}}\exp\left[i\int k_r dr\right] \simeq |z|^{-\frac{1}{4}} e^{ik_{r0}r \pm \frac{2}{3}i(-z)^{\frac{3}{2}}} = |z|^{-\frac{1}{4}} e^{ik_{r0}r \pm \frac{2}{3}z^{\frac{3}{2}}}. \tag{A.32}$$

Since both phases and amplitudes match, we can justify only looking at the phase on both sides on the turning point. We first match at $z \sim -\infty$. If $A_\pm$ are the coefficients of WKB modes $\sim e^{\pm\frac{2}{3}i(-z)^{\frac{3}{2}}}$, and C and D are the coefficients on $Ai(z)$ and $Bi(z)$ respectively, then we must have

$$A_+ e^{\frac{2}{3}i(-z)^{\frac{3}{2}}} + A_- e^{-\frac{2}{3}i(-z)^{\frac{3}{2}}} = 2C\cos\left(-\frac{2}{3}(-z)^{\frac{3}{2}} + \frac{\pi}{4}\right) + 2D\sin\left(-\frac{2}{3}(-z)^{\frac{3}{2}} + \frac{\pi}{4}\right) \tag{A.33}$$

which can be written in matrix form as

$$\begin{bmatrix} A_+ \\ A_- \end{bmatrix} = e^{-\frac{\pi i}{4}} \begin{bmatrix} 1 & i \\ i & 1 \end{bmatrix} \begin{bmatrix} C \\ D \end{bmatrix}. \tag{A.34}$$

Similarly, the matching requirement $z \sim \infty$ with WKB amplitudes labelled $B_\pm$, is

$$B_+ e^{\frac{2}{3}z^{\frac{3}{2}}} + B_- e^{-\frac{2}{3}z^{\frac{3}{2}}} = CAi(z) + DBi(z) \sim D2e^{\frac{2}{3}z^{\frac{3}{2}}} + Ce^{-\frac{2}{3}z^{\frac{3}{2}}} \tag{A.35}$$

which can be written in matrix form as

$$\begin{bmatrix} C \\ D \end{bmatrix} = \frac{1}{2} \begin{bmatrix} 0 & 2 \\ 1 & 0 \end{bmatrix} \begin{bmatrix} B_+ \\ B_- \end{bmatrix}. \tag{A.36}$$

At the end of the day, we can relate the amplitudes $A_\pm$ at the $z < 0$ side of the turning point to the amplitudes $B_\pm$ on the $z > 0$ side of the turning point

$$\begin{bmatrix} A_+ \\ A_- \end{bmatrix} = M \begin{bmatrix} B_+ \\ B_- \end{bmatrix} \text{ for } M \equiv e^{-\frac{\pi i}{4}} \frac{1}{2} \begin{bmatrix} i & 2 \\ 1 & 2i \end{bmatrix}$$

where M is the linear transformation that maps WKB amplitudes $B_\pm$ at $z > 0$ to amplitudes $A_\pm$ at $z < 0$. Next, we will benefit from transforming these relations back from z as defined in (A.27) into the radial coordinate r. First, observe that

$$k_r = -i\partial_r \left(\mp \frac{2}{3} i(-z)^{\frac{3}{2}} \right) = -i\partial_r \left(\pm \frac{2}{3} z^{\frac{3}{2}} \right) = \mp i\sqrt{Q(r - r_0)}, \tag{A.37}$$

meaning that there are four different cases, corresponding to the signs Q and z,

$$k_r = \begin{cases} \begin{cases} k_r^\pm & \equiv \pm\sqrt{|Q|(r_0 - r)} \text{ for } r < r_0 \text{ has } z < 0 \\ \tilde{k}_r^\mp & \equiv \mp i\sqrt{|Q|(r - r_0)} \text{ for } r > r_0 \text{ has } z > 0 \end{cases} & \text{for } Q > 0 \\ \begin{cases} k_r^\pm & \equiv \pm\sqrt{|Q|(r - r_0)} \text{ for } r > r_0 \text{ has } z < 0 \\ \tilde{k}_r^\pm & \equiv \pm i\sqrt{|Q|(r_0 - r)} \text{ for } r < r_0 \text{ has } z > 0 \end{cases} & \text{for } Q < 0 \end{cases} \tag{A.38}$$

Here, $k_r^\pm$ refers to propagating modes with positive $(+)$ and negative $(-)$ radial wavenumber k_r. Likewise, $\tilde{k}_r^\pm$ refers to the evanescent modes that grow $(-)$ and decay $(+)$ with radius r. To match, we note that $z < 0$ whenever $Q > 0$ and $r < r_0$ or $Q < 0$ and $r > r_0$. Then, for $Q > 0$ we may associate $A_\mp$ above with the propagating WKB modes $k_r^\pm$, and $B_\pm$ with the evanescent WKB modes $\tilde{k}_r^\mp$ (notice the different sign). For $Q < 0$, the direction of z is opposite to that of r so M maps inner amplitudes to outer amplitudes, and M^{-1} maps outer amplitudes to inner amplitudes. That is, M^{-1} maps outer amplitudes $A_\pm$ corresponding to $k_r^\pm$ into inner amplitudes $B_\pm$ corresponding to $\tilde{k}_r^\pm$.

Staying with this notation, we may depict the transition as a graphical mnemonic (with radius growing towards the right)

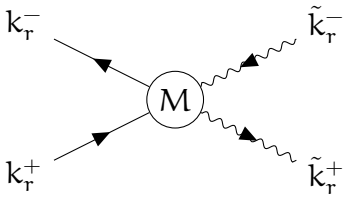

$$M \equiv \frac{1}{2} e^{-\frac{\pi i}{4}} \begin{bmatrix} i & 2 \\ 1 & 2i \end{bmatrix}$$

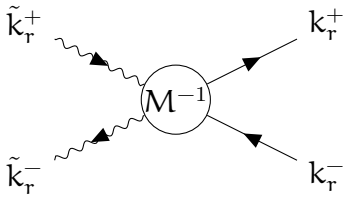

$$M^{-1} \equiv \frac{1}{2} e^{-\frac{\pi i}{4}} \begin{bmatrix} 2 & 2i \\ i & 1 \end{bmatrix}$$

for $Q > 0$ and $Q < 0$ respectively. Here, arrows point to the right if the phase – real or imaginary part – increases with radius, and the left if it decreases. That is, arrows on propagating lines indicate the direction of increasing phase with r, i.e. the direction of propagation of a positive frequency (and positive branch of the dispersion relation) modes. The arrows on the evanescent modes indicate the direction in which the mode decays.

We note that if we define the matrix F by $F(a, b) = (b, a)$ – i.e. the flipping matrix – then MF flips the right arms of the diagram (swaps column vectors of M), and FM flips the left arms of the diagram (swaps row vectors of M). It may therefore be convenient to define the matrices $T \equiv FMF$ and $\tilde{T}$ such that the diagrams take consistent "arrow conventions":

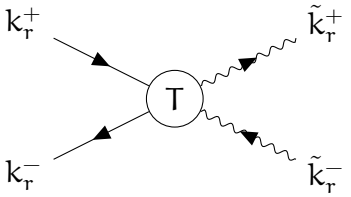

$$T \equiv FMF = \frac{1}{2} e^{-\frac{\pi i}{4}} \begin{bmatrix} 2i & 1 \\ 2 & i \end{bmatrix}$$

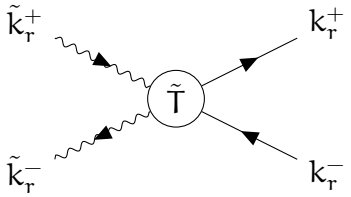

$$\tilde{T} \equiv M^{-1} = \frac{1}{2} e^{-\frac{\pi i}{4}} \begin{bmatrix} 2 & 2i \\ i & 1 \end{bmatrix} \tag{A.39}$$

These matrices transfer amplitudes, from just outside to just inside a turning point.

One immediate consequence of these expressions is that the absence of an incoming evanescent mode $\tilde{k}_r^+$ from the left is equivalent to imposing the boundary condition $A_- = iA_+$ at the innermost turning point. Likewise, the absence of an incoming evanescent mode $\tilde{k}_r^-$ from the right is equivalent to imposing the boundary condition $A_+ = iA_-$ on the outermost turning point. Therefore, perfect reflections of oscillatory modes off a turning point contribute with a phase-shift of $\pi/2$.

The arrow convention in (A.39) is consistent in that the top line always points outwards, while the bottom line always points inwards. However, we can only interpret the arrows causally, i.e. the

direction of propagation, when positive frequencies are considered. For negative (comoving) frequencies, the outward-pointing oscillatory line, for example, is in fact travelling inwards. Therefore, care should be taken when imposing boundary conditions of diagrams of the form (A.39).

When taken together with the WKB propagator,

$$\mathcal{W}_{ab} \equiv \begin{bmatrix} \mathcal{W}^{+}_{ab} & 0 \\ 0 & \mathcal{W}^{-}_{ab} \end{bmatrix}$$
$$\text{for } \mathcal{W}^{\pm}_{ab} \equiv Q^{\pm}_{ab} e^{\pm i S_{ba}} \text{ with } S_{ba} \equiv \int_{r_b}^{r_a} k_r \, dr \text{ and } Q^{\pm}_{ab} \equiv \frac{A^{\pm}(r_b)}{A^{\pm}(r_a)}, \tag{A.40}$$

we have all the ingredients needed to relate WKB amplitudes on one boundary of the system to another. We shall, in most of what follows, assume that $Q^{+}_{ab} = Q^{-}_{ab} \equiv Q_{ab}$. That is, the change in amplitude of a WKB mode as it propagates from r_b to r_a is independent of the direction of propagation. Under these assumptions, the WKB propagator (A.40) can be written

$$\mathcal{W}_{ab} \equiv Q_{ab} \begin{bmatrix} e^{-iS_{ab}} & 0 \\ 0 & e^{iS_{ab}} \end{bmatrix}. \tag{A.41}$$

We shall now consider a range of frequently encountered scenarios.

A.4.1. Case I: Bound states

Typically, the need for this formalism appears when hunting resonant frequencies. The simplest, purely geometric, resonance is a single well, separated by infinite evanescent regions of on either side. This corresponds to a diagram of the form

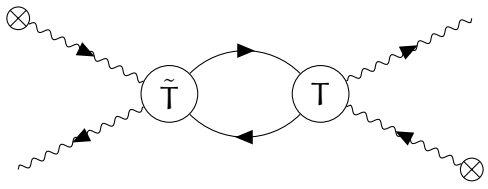

(A.42)

Here, the symbol $\otimes$ is placed on dangling legs of the diagram to indicate the absence of amplitude in the channel. Here, $\otimes$ is placed on the two evanescent sources, indicating that we are interested in situations where there are no incoming amplitudes.

Labelling the two turning points 1 and 2, from left to right, the resonance condition can be written

$$\begin{bmatrix} 0 \\ \tilde{b}_{-} \end{bmatrix} = \tilde{T} \mathcal{W}_{21} T \begin{bmatrix} \tilde{B}_{+} \\ 0 \end{bmatrix}$$

Here, the operator $\tilde{T}\mathcal{W}_{21}T$, which maps evanescent amplitudes on the right to evanescent amplitudes on the left, can be written

$$\tilde{T}\mathcal{W}_{21}T = \frac{e^{-\frac{\pi i}{2}}}{4}\begin{bmatrix}2 & 2i\\ i & 1\end{bmatrix}\begin{bmatrix}\mathcal{W}_{12}^{+} & 0\\ 0 & \mathcal{W}_{12}^{-}\end{bmatrix}\begin{bmatrix}2i & 1\\ 2 & i\end{bmatrix} = \frac{1}{4i}\begin{bmatrix}2 & 2i\\ i & 1\end{bmatrix}\begin{bmatrix}2i\mathcal{W}_{12}^{+} & \mathcal{W}_{12}^{+}\\ 2\mathcal{W}_{12}^{-} & i\mathcal{W}_{12}^{-}\end{bmatrix} = \begin{bmatrix}2\alpha & \beta\\ -\beta & \alpha/2\end{bmatrix}$$
$$\text{for } \alpha \equiv \frac{\mathcal{W}_{12}^{+} + \mathcal{W}_{12}^{-}}{2} \text{ and } \beta \equiv \frac{\mathcal{W}_{12}^{+} - \mathcal{W}_{12}^{-}}{2i}$$

Therefore, if the oscillatory loop between r_1 and r_2 is isolated, i.e. absence of evanescent sources $\tilde{b}_+ = \tilde{B}_- = 0$, then the evanescent amplitudes must be related through

$$0 = 2\alpha\tilde{B}_+ \text{ and } \tilde{b}_- = -\beta\tilde{B}_+.$$

The only way to produce a non-trivial solution is by having $\alpha = 0$. To investigate what this means, we may summon the relation (A.41) to recognise that in this case, one has

$$\alpha = Q_{12}\cos(S_{12}) \quad \text{and} \quad \beta = -Q_{12}\sin(S_{12}). \tag{A.43}$$

That is, the resonance condition takes the form of a Bohr-Sommerfeld quantization criterion from the old quantum theory, i.e.

$$\cos\left(\int_{r_1}^{r_2} k_r(\omega, m, r)dr\right) = 0. \tag{A.44}$$

A.4.2. Case II: Tunneling

Another frequently encountered case is the opposite of the previous scenario, i.e. a barrier separating two oscillatory regions. We may depict the scenario as follows

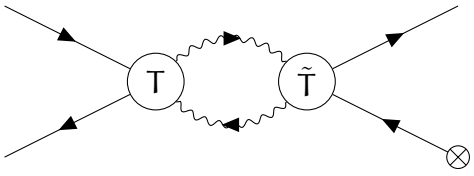

(A.45)

Here, we shall investigate the reflection and transmission of a mode trying to escape from the left, hence the $\otimes$ on in incoming node from the right. The relevant quantity is

$$T\tilde{\mathcal{W}}_{12}\tilde{T} = \frac{1}{4}e^{-\frac{\pi i}{2}}\begin{bmatrix}2i & 1\\ 2 & i\end{bmatrix}\begin{bmatrix}\tilde{\mathcal{W}}_{21}^{+} & 0\\ 0 & \tilde{\mathcal{W}}_{21}^{-}\end{bmatrix}\begin{bmatrix}2 & 2i\\ i & 1\end{bmatrix} = \frac{4+\gamma}{4X}\tilde{\mathcal{W}}_{12}^{+}\begin{bmatrix}X & i\\ -i & X\end{bmatrix} \text{ for } X \equiv \frac{4+\gamma}{4-\gamma} \tag{A.46}$$

where $\gamma \equiv \tilde{W}_{12}^{-}/\tilde{W}_{12}^{+}$ has been introduced. Considering an outward-propagating oscillatory mode with unit amplitude, we may introduce the relative reflected $\mathcal{R}$ and transmitted $\mathcal{T}$ portions of the incident wave. That is

$$\begin{bmatrix} 1 \\ \mathcal{R} \end{bmatrix} = \frac{4+\gamma}{4X}\tilde{W}_{12}^{+}\begin{bmatrix} X & i \\ -i & X \end{bmatrix}\begin{bmatrix} \mathcal{T} \\ 0 \end{bmatrix} \tag{A.47}$$

for which we find

$$\mathcal{T} = \frac{4}{4\tilde{W}_{12}^{+} + \tilde{W}_{12}^{-}} \quad \text{and} \quad \mathcal{R} = \frac{1}{i}\frac{4\tilde{W}_{12}^{+} - \tilde{W}_{12}^{-}}{4\tilde{W}_{12}^{+} + \tilde{W}_{12}^{-}}. \tag{A.48}$$

Using the WKB propagator (A.41) we find

$$\gamma = \frac{1}{4}e^{-2\tilde{S}_{21}} \quad \text{for} \quad \tilde{S}_{ba} \equiv \int_{r_b}^{r_a} |k_r| dr, \tag{A.49}$$

where one generally has $\tilde{S}_{ba} = iS_{ba}$ for evanescent modes. The expressions for the reflected amplitude $\mathcal{R}$ and the transmitted $\mathcal{T}$ are therefore

$$i\mathcal{R} = \frac{1}{X} = \frac{4 - e^{-2\tilde{S}_{12}}}{4 + e^{-2\tilde{S}_{12}}} \text{ and } \mathcal{T} = \frac{1}{Q_{12}}\frac{4e^{-\tilde{S}_{12}}}{4 + e^{-2\tilde{S}_{12}}} \tag{A.50}$$

As expected, the transmitted amplitude, referred to as the tunnelling amplitude, is exponentially suppressed by the phase difference $\tilde{S}_{12}$ accumulated from points 1 to 2. Note also the presence of the geometric factor Q_{12} caused by the physical width of the barrier. We also observe that the reflection coefficient's multiplicative factor of i indicates that the effective scattering imposes a $\pi/2$ phase shift on the reflected oscillatory modes. Moreover, since $X > 1$ we always have $|\mathcal{R}| < 1$. That is, the reflected amplitude never exceeds the incident amplitude. However, this changes for negative frequencies since (A.47) must then be modified to incorporate the flipped direction propagation with respect to the arrows in the diagram. If the right side of the barrier is a negative frequency mode, then the two outer amplitudes (0 and $\mathcal{T}$) in (A.47) must be interchanged. The result is that $i\mathcal{R} = X$, which means that now, one has $|\mathcal{R}| > 1$ instead. That is, the incident wave returns amplified. Finally, we may observe that the same argument holds for scattering from the outside, with ($i\mathcal{R} = X$) or without ($i\mathcal{R} = 1/X$) negative frequencies inside.

A.4.3. Case III: Quasi-Bound States

One natural extension to the Bound-State scenario is to include an outer, oscillatory region. The result, which can be depicted as follows

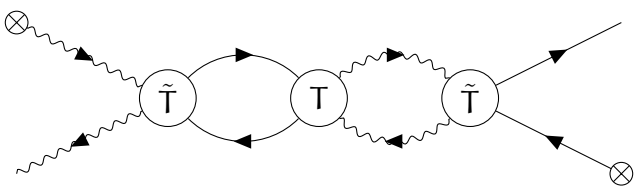

(A.51)

is a combination of the two previous cases. Following the same procedure and assumptions as in the previous case, we find

$$\tilde{T}\mathcal{W}_{12}T\tilde{\mathcal{W}}_{23}\tilde{T} = \frac{4+\gamma}{4X}\tilde{\mathcal{W}}^{+}_{23}\frac{1}{2}e^{\frac{-\pi i}{4}}\begin{bmatrix}2 & 2i\\ i & 1\end{bmatrix}\begin{bmatrix}\mathcal{W}^{+}_{12} & 0\\ 0 & \mathcal{W}^{-}_{12}\end{bmatrix}\begin{bmatrix}X & i\\ -i & X\end{bmatrix} \tag{A.52}$$

$$= \left(1+\frac{\gamma}{4}\right)\frac{1}{X}\mathcal{W}^{-}_{12}\tilde{\mathcal{W}}^{+}_{23}e^{\frac{-\pi i}{4}}\begin{bmatrix}gX+1 & i(X+g)\\ \frac{i}{2}(gX-1) & \frac{1}{2}(X-g)\end{bmatrix} \text{ for } g \equiv \frac{\mathcal{W}^{+}_{12}}{\mathcal{W}^{-}_{12}} = e^{-2iS_{12}} \tag{A.53}$$

where points 1, 2, 3 refer to the three turning points sorted by increasing radius, and X and γ are defined as in (A.46), but for the region $r \in [r_2, r_3]$. It follows that nontrivial solutions exist provided that $gX + 1 = 0$, i.e.

$$e^{2iS_{12}} + X = 0 \quad \text{for} \quad X \equiv \frac{4+e^{-2\tilde{S}_{23}}}{4-e^{-2\tilde{S}_{23}}}. \tag{A.54}$$

or, equivalently

$$4\cot S_{12} = ie^{-2\tilde{S}_{23}}. \tag{A.55}$$

Clearly, if the phases S_{12} and $\tilde{S}_{23}$ are real, then the only way to solve (A.55) is if $\tilde{S}_{23} \to \infty$, which results in case I. The resonance condition (A.55) does, however, exhibit solutions if one permits complex frequencies $\omega \in \mathbb{C}$. Solutions of this kind are not oscillating like normal modes, as their amplitude oscillation is exponentially damped or amplified over time. Therefore, resonant modes of this kind is often referred to as being Quasi-Normal, or Quasi-Bound.

A.4.4. Case IV: Double well

An important, further extension of Case III is the situation in which there is an outer boundary, with boundary condition B, that reflects escaping modes back into the Quasi-Bound State loop:

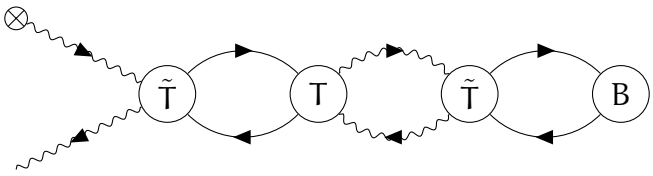

(A.56)

We have essentially already computed this – all that remains is to append a propagator $\mathcal{W}_{34}$ to the right of the previous case (A.52), and to fix a boundary condition, labelled B, at the outermost point 4. Using $A_- = \nu A_+$ for B, we find

$$\begin{bmatrix}0\\ b_+\end{bmatrix} = \left(1+\frac{\gamma}{4}\right)\frac{1}{X}\mathcal{W}^{-}_{12}\tilde{\mathcal{W}}^{+}_{23}e^{\frac{-\pi i}{4}}\begin{bmatrix}gX+1 & i(X+g)\\ \frac{i}{2}(gX-1) & \frac{1}{2}(X-g)\end{bmatrix}\begin{bmatrix}\mathcal{W}^{+}_{34}A_+\\ \mathcal{W}^{-}_{34}\nu A_+\end{bmatrix} \tag{A.57}$$

resulting in the resonance condition

$$e^{2iS_{12}} + i\nu e^{2iS_{34}} + \left(1 + i\nu e^{2iS_{12}} e^{2iS_{34}}\right) X = 0, \tag{A.58}$$

or, alternatively

$$4\cot(S_{12})\cot(S_{34} + \eta + \pi/4) = e^{-2\tilde{S}_{23}} \tag{A.59}$$

where we have assumed $|\nu| = 1$ for which we may write $\nu \equiv e^{2i\eta}$ with $\eta \in \mathbb{R}$. That is, ν is a parameterisation of a perfectly reflecting boundary condition.

To investigate if this makes sense, let us first consider the case of a strong separation $\tilde{S}_{23} \sim \infty$. Then either $\cot(S_{21}) = \infty$ or $\cot(S_{34} + \eta + \pi/4) = \infty$. That is, $\cos(S_{12}) = 0$ or $\cos(S_{43} + \eta + \pi/4) = 0$, which is what we expect from two isolated wells, i.e. the case 1 calculation.

Equation (A.59) is, in a certain sense, the limiting behaviour of equation (A.54). For when a realistic mode travels, there will always be some loss of energy. If the outer region is large, i.e. $\Phi_{43} \mapsto \infty$, then even the tiniest dissipative contribution $k_r^{\pm} \mp \mapsto k_r^{\pm} \mp i\varepsilon$ for $\varepsilon \ll 1$ will result in $e^{2i\Phi_{43}} \to 0$. Then, equation (A.58) asymptotes to the form of (A.54). Note also that for relatively large systems, only S_{34} will depend on the system size.

Appendix B

Numerical Methods

B.1. General tools

In this section, I briefly list a set of standard numerical tools used throughout this text.

B.1.1. Runge-Kutta-4 (RK4) Scheme

Runge-Kutta-4 (RK4) is a method for numerically approximating solutions to differential equations of the form

$$\frac{dy}{dt} = f(t, y). \tag{B.1}$$

For discrete time-steps $t_{n+1} = t_n + \Delta t$ and $y_n \equiv y(t_n)$, RK4 is given by

$$y(t_n + \Delta t) = y(t_n) + \tfrac{1}{6}\left(k_1 + 2k_2 + 2k_3 + k_4\right)\Delta t \tag{B.2}$$

$$k_1 \equiv f(t_n, y_n) \tag{B.3}$$

$$k_2 \equiv f(t_n + \tfrac{1}{2}\Delta t, y_n + \tfrac{1}{2}k_1) \tag{B.4}$$

$$k_3 \equiv f(t_n + \tfrac{1}{2}\Delta t, y_n + \tfrac{1}{2}k_2) \tag{B.5}$$

$$k_4 \equiv f(t_n + \Delta t, y_n + k_3). \tag{B.6}$$

This is a fourth-order method, i.e. the error scales as $\mathcal{O}(\Delta t^4)$. The RK4 scheme is e.g. used, together with a stochastic step, in the simulations of chapter 4.

B.1.2. Bisection method

Given some function $f(x)$, for which we know that $f(a)f(b) < 0$, the mid-point method recursively searches for a point $c \in [a, b]$ for which $f(c) = 0$. The idea is to introduce a recursive function $\mathrm{bisect}(a, b, f, N)$ which continually subdivides the interval $[a, b]$ (N times), always throwing away the half of $[a, b]$ where the function f has equal sign on the endpoints. That is

$$\mathrm{bisect}(a, b, f, N) = \begin{cases} \frac{a+b}{2} & \text{if } N = 0 \\ \mathrm{bisect}\left(a, \frac{a+b}{2}, f, N-1\right) & \text{if } f\left(\frac{a+b}{2}\right) f(a) < 0 \text{ and } N \neq 0\,. \\ \mathrm{bisect}\left(\frac{a+b}{2}, b, f, N-1\right) & \text{otherwise} \end{cases} \tag{B.7}$$

B.1.3. Construction of numerical stencils

Consider a function $f : \mathbb{R} \to \mathbb{R}$ that has been discretized on a set of points x_i with uniform spacing $\Delta x \equiv x_{i+1} - x_i$. Writing $f_i \equiv f(x_i)$, we may observe that the first N terms in a Taylor series of f_{k+l} around x_k can be interpreted as a matrix operation

$$f_{k+l} = \sum_{n=0}^{N-1} \frac{l^n \Delta x^n}{n!} \partial_x^n f_k + \mathcal{O}(\Delta x^N) = A_{l,n} \partial_x^n f_k + \mathcal{O}(\Delta x^N) \quad \text{for} \quad A_{l,n} \equiv \frac{l^n}{n!} \Delta x^n, \tag{B.8}$$

mapping the N first derivatives, to the N first locations. This means that if we write $\mathbf{f} \equiv \sum_n f_n \mathbf{e}_n$ and $\mathbf{D} f_k \equiv \sum_n \mathbf{e}_n \partial_x^n f(x_k)$, then the n^{th} derivative of f at x_k may be approximated as a linear combination of f_{k+l} for at least $n+1$ different l's, i.e. $\mathbf{D} f_k = A^{-1} \mathbf{f}_k$. There is freedom in the choice of values for l. For example, one may consider consecutive points $l = k + j$ for $j \in J_m^a \equiv \{a - m, ..., a + m\}$, where a sets the shift from the centre and $N = 1 + 2m$ is the number of points used. Then

$$\begin{aligned} \partial_x^n f(x_k) &= D_{k,i}^{(n)} f_i + \mathcal{O}(\Delta x^{N-n}) \\ \text{for} \quad D_{k,i}^{(n)} &\equiv \sum_{j \in J_m^a} \Delta_{n,j}^{(m;a)} \delta_{k+j,i} \quad \text{and} \quad \Delta_{n,l}^{(m;a)} \equiv A_{n,k+l}^{-1}, \end{aligned} \tag{B.9}$$

where $\delta_{a,b}$ are the Kronecker delta symbols. Here, the matrix $D_{k,i}^{(n)}$ is the finite difference matrix approximating the n^{th} derivative of f with the stencil matrix $\Delta_{n,l}^{(m;a)}$. The matrix $\Delta_{n,l}^{(m;a)}$ determines the weights on f_{k+l} for $l \in J_m^a$ needed in the linear relation of f_i's that would, when summed, result in an approximation of $\partial_x^n f_k$. For example, the 3 and 5-point centred ($a = 0$) stencil matrices are

$$\begin{pmatrix} f_k \\ \partial f_k \\ \partial^2 f_k \end{pmatrix} \approx \Delta^{(1;0)} \begin{pmatrix} f_{k-1} \\ f_k \\ f_{k+1} \end{pmatrix} \quad \text{for} \quad \Delta^{(1;0)} \equiv \frac{1}{2} \begin{pmatrix} 0 & 2 & 0 \\ -1 & 0 & 1 \\ 2 & -4 & 2 \end{pmatrix} \tag{B.10}$$

$$\begin{pmatrix} f_k \\ \partial f_k \\ \partial^2 f_k \\ \partial^3 f_k \\ \partial^4 f_k \end{pmatrix} \approx \Delta^{(2;0)} \begin{pmatrix} f_{k-2} \\ f_{k-1} \\ f_k \\ f_{k+1} \\ f_{k+2} \end{pmatrix} \quad \text{for} \quad \Delta^{(2;0)} \equiv \frac{1}{12} \begin{pmatrix} 0 & 0 & 12 & 0 & 0 \\ 1 & -8 & 0 & 8 & -1 \\ -1 & 16 & -30 & 16 & -1 \\ -6 & 12 & 0 & -12 & 6 \\ 12 & -48 & 72 & -48 & 12 \end{pmatrix} \tag{B.11}$$

where $\Delta x = 1$ has been set for notational convenience. Naively implementing (B.9) can, however, be problematic. Since the matrix derivative $D_{k,i}^{(n)}$ is determined by convolution of the stencil matrix $\Delta_{n,j}^{(m;a)}$ with the identity matrix, the dimensionality of $\mathbf{f}$ must, in general, be larger than of $\partial_x^n \mathbf{f}$. This is caused by the non-locality of the derivative and makes the evaluation of derivatives at the

boundaries of f ambiguous. In the case of the points J^a_m, one is left with $2m$ values for f_i that are unspecified. We now consider the case of N_p points $x_0, \ldots, x_{N_p-1}$, and split the matrices $\Delta^{(n;a)}_{k,i}$ in the three parts $\Delta^{(n;a)} = [L^{(n;a)}, D^{(n;a)}, R^{(n;a)}]$, where $L^{(n;a)}_{i,j} \equiv \Delta^{(n;a)}_{i,j}$ for $j < m$ encodes the left boundary, $D^{(n;a)}_{i,j-m} \equiv \Delta^{(n;a)}_{i,j}$ for $N_p + m > j > m$ and $R^{(n,a)}_{i,j-N_p-m} \equiv \Delta^{(n;a)}_{i,j}$ for $j > N_p + m$. What remains is to determine how to map $L^{(n;a)}$ and $R^{(n;a)}$ into $D^{(n;a)}$ using a generic boundary condition. One possible approach is to use a range of relatively shifted stencils to estimate the same derivative.

$$\begin{pmatrix} S^{(n;0)}_{-m} & S^{(n;0)}_{1-m} & \cdots & S^{(n;0)}_{m-1} & S^{(n;0)}_{m} \\ 0 & S^{(n;1)}_{-m} & \cdots & S^{(n;1)}_{m-2} & S^{(n;1)}_{m-1} \\ \vdots & \vdots & \ddots & \vdots & \vdots \\ 0 & 0 & \cdots & S^{(n;a-1)}_{-m} & S^{(n;a-1)}_{1-m} \\ 0 & 0 & \cdots & 0 & S^{(n;a)}_{-m} \end{pmatrix} \begin{pmatrix} f_{k_0-m} \\ f_{k_0-m+1} \\ \vdots \\ f_{k_0+m-1} \\ f_{k_0+m} \end{pmatrix} = \begin{pmatrix} 1 \\ 1 \\ \vdots \\ 1 \\ 1 \end{pmatrix} \partial^n_x f_{k_0} \tag{B.12}$$

If k_0 is a boundary point, with $\partial^n_x f_{k_0} = 0$, then the matrix may be split to solve for f_{k_0-i} for $i > 0$ in terms of f_{k_0+i} for $i \geqslant 0$. That is

$$\underbrace{\begin{pmatrix} S^{(n;0)}_{0} & S^{(n;0)}_{1} & \cdots & S^{(n;0)}_{m} \\ S^{(n;1)}_{-1} & S^{(n;1)}_{2} & \cdots & S^{(n;1)}_{m-1} \\ \vdots & \vdots & \ddots & \vdots \\ S^{(n;a)}_{-a} & S^{(n;a)}_{1-a} & \cdots & S^{(n;a)}_{m-1-a} \end{pmatrix}}_{\equiv A} \begin{pmatrix} f_{k_0} \\ f_{k_0+1} \\ \vdots \\ f_{k_0+m} \end{pmatrix} = - \underbrace{\begin{pmatrix} S^{(n;0)}_{-m} & S^{(n;0)}_{1-m} & \cdots & S^{(n;0)}_{-1} \\ 0 & S^{(n;1)}_{-m} & \cdots & S^{(n;1)}_{-2} \\ \vdots & \vdots & \ddots & \vdots \\ 0 & 0 & \cdots & S^{(n;a)}_{-1-a} \end{pmatrix}}_{\equiv B} \begin{pmatrix} f_{k_0-m} \\ f_{k_0-m+1} \\ \vdots \\ f_{k_0-1} \end{pmatrix} \tag{B.13}$$

such that $-B^{-1}A$ maps f_i for $i \geqslant k_0$ to f_i for $i < k_0$. That is, the map $L^{(n;a)} \mapsto -L^{(n;a)}B^{-1}A$ results in a contribution to the upper left corner of $D^{(n;a)}$ that accounts for the boundary conditions at the left boundary. An analogous procedure can be used to map $R^{(n;a)}$ into the lower right corner of $D^{(n;a)}$ provided that the boundary condition on the right is $\partial^n_x f = 0$ for some n.

One convenient property of this approach is that boundary conditions may be imposed near, but not exactly at, the numerical boundaries. This is illustrated in Figure B.1, where the stencils are tested on unshifted (left) and shifted (right) boundary conditions. In both cases, the boundary condition is $\partial^0_x f = 0$ (Dirichlet) on the left and $\partial^1_x f = 0$ (Neumann) on the right. In both cases, the eigenvectors (with small eigenvalues) of the boundary-adjusted matrices $D^{(2;0)}$ are shown in comparison with the corresponding theoretical eigenmodes of ∂^2_x.

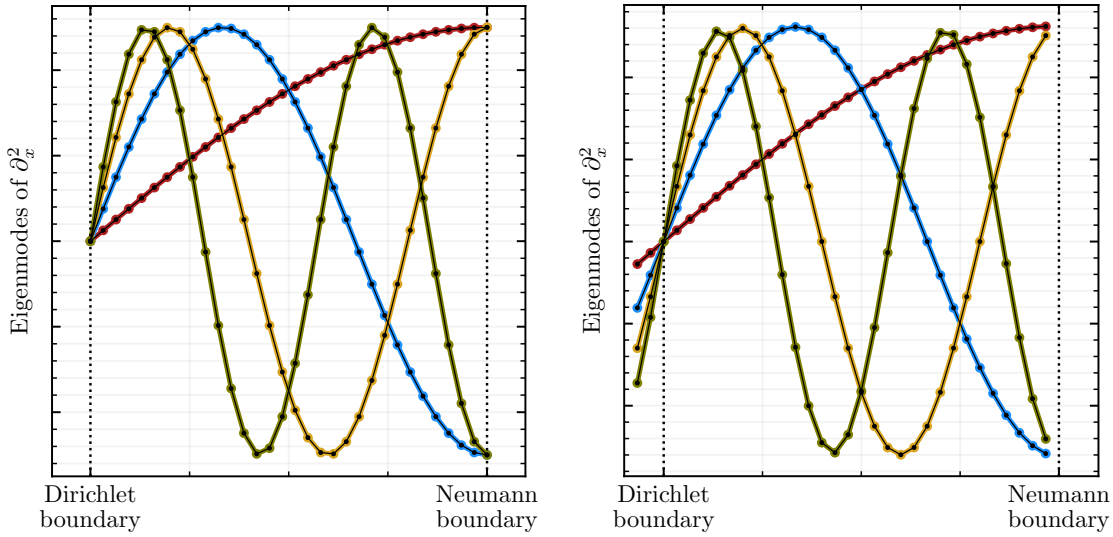

Figure B.1 (Stencil design) Examples of interpolated boundary conditions in stencil construction using a 16x16 matrix. These are eigenvectors of the discretized ∂_x^2 matrix. The black lines are the theoretical lines $\phi = \sin(\omega_n(n - n_0))$ for $\omega_n = \pi(2n+1)/2$.

B.2. Atomic Condensates

B.2.1. Numerical estimates of Vortex Profiles

In this section, two numerical strategies for obtaining the ground-state density surrounding a multiply wound vortex are detailed. There are two numerical complications with solving (2.10) directly: (1) the spatial separation of boundary conditions, with one of them at infinity and (2) the sensitivity of the equation to initial conditions.

Shooting method

Based on the asymptotic expansion (2.11), we may make an initial guess for the numerical value of $Y_0 = \sqrt{\rho_0}$ at a very small radius $r = \varepsilon \ll 1$ and use equation (2.10) to evolve this to a radius r_∞ using a finite difference scheme. That is, we solve

$$\partial_r \begin{pmatrix} Y \\ Z \end{pmatrix} = \begin{pmatrix} Z \\ -\frac{1}{r}Z - \left(2 - \frac{\ell^2}{r^2}\right) Y + 2Y^3 \end{pmatrix} \tag{B.14}$$

with $Y(\varepsilon) = Y_0 J_\ell(\varepsilon)$ with $Z(\varepsilon) = Y_0 J'_\ell(\varepsilon)$. Using a Taylor expansion of (2.10) around $r \to \infty$ we find

$$Y_\infty(r) \overset{\infty}{\sim} 1 - \frac{\ell^2}{4r^2} - \left(1 + \frac{\ell^2}{8}\right)\frac{\ell^2}{4r^4} - \left(8 + 2\ell^2 + \frac{\ell^4}{16}\right)\frac{\ell^2}{8r^6} + \mathcal{O}\left(\frac{1}{r^8}\right), \tag{B.15}$$

which is used to estimate the asymptotic value for Y and Z at r_∞. We then solve (B.14) iteratively using RK4 (see B.1.1), where the initial guess Y_0 is updated each step using the bisection method (see B.1.2) based on the sign of $Y_\infty(r_\infty) - Y_n(r_\infty; Y_0)$, where $Y_n(r_\infty; Y_0)$ is the numerically obtained value for Y using the guess Y_0. Due to the instability of (B.14), the density is then stiched together, using a linear ramp function, from the asymptotic (2.11) at small radii, to the numerical solution Y_n at intermediate radii, and to the asymptotic (B.15) at large radii.

Damped matrix evolution

A convenient alternative to the above approach is found by considering the GPE (2.4) under imaginary time. The background density $\rho \equiv |\Psi|^2$ can be found from fixing the phase $\Psi \equiv \sqrt{\rho} e^{i\ell\theta}$ and evolving the modulus $\sqrt{\rho}$ in imaginary time $\tau \equiv it$, i.e.

$$\partial_\tau \sqrt{\rho} = \left(\frac{1}{2}\partial_r^2 + \frac{1}{2r}\partial_r - \frac{\ell^2}{2r^2} - V(r) + 1 - \rho\right)\sqrt{\rho}. \tag{B.16}$$

Using B.1.3 the radial derivatives ∂_r and ∂_r^2 may be represented as matrices, with a Dirichlet boundary condition ($\rho(0) = 0$) at the origin. The boundary condition at the outermost radius r_B generally depends on the potential $V(r)$. If $V(r_B) \gg 1$ then a Dirichlet condition may be used. If $V = 0$ and the boundary is far from the core, i.e. $r_B \gg \ell$, then the boundary condition may be approximated as Neumann at r_B.

B.2.2. Numerical Simulation of BdG

When linearizing the adimensionalised GPE using $\Psi \mapsto \Psi_0 + \delta\psi$, for $|\delta\psi| \ll |\Psi_0|$, we are left with the Bogoliubov de-Gennes (BdG)quation

$$i\partial_t \begin{bmatrix} \delta\psi \\ \delta\psi^* \end{bmatrix} = \begin{bmatrix} \widehat{H} & \Psi_0^2 \\ -(\Psi_0^*)^2 & -\widehat{H} \end{bmatrix} \begin{bmatrix} \delta\psi \\ \delta\psi^* \end{bmatrix} \text{ for } \widehat{H} \equiv -\frac{1}{2}\nabla^2 + U - 1 + 2|\Psi_0|^2. \tag{B.17}$$

This is, by design, a linear system, meaning that it may in principle be exactly solved using a spectral evolution. First note that the system takes a nice form if $\delta\psi$ carries the phase of Ψ_0, i.e. if $\Psi =$

$\sqrt{\rho}e^{i\Phi}$ then $\delta\psi = \psi e^{i\Phi}$. Then

$$i\partial_t \underbrace{\begin{bmatrix}\delta\psi\\ \delta\psi^*\end{bmatrix}}_{\equiv|\psi(t)\rangle} = \begin{bmatrix}\mathcal{D}_+ & \rho\\ -\rho & -\mathcal{D}_-\end{bmatrix}\begin{bmatrix}\delta\psi\\ \delta\psi^*\end{bmatrix} \equiv \widehat{L}\begin{bmatrix}\delta\psi\\ \delta\psi^*\end{bmatrix} \text{ for } \mathcal{D}_\pm \equiv e^{\mp i\Phi}\widehat{H}e^{\pm i\Phi}, \tag{B.18}$$

which is the case of the BdG presented in equation (2.12). From factorising $\widehat{L} = PDP^{-1}$ numerically, where D is a diagonal matrix, any initial state $\mathbf{u}(t_0)$ can be evolved to a time Δt later by applying $\mathbf{u}(t_0+\Delta t) = P\exp(-iD\Delta t)P^{-1}\mathbf{u}(t_0)$.

The numerical simulations of the BdG are used to determine the boundary conditions in section IV.2 of chapter 2 in two different scenarios: (1) the reflection of a BdG wave off a hard wall with step-approximated background with Neumann boundary conditions and (2) the reflection of a BdG wave off a hard wall with true/exact background density.

B.2.3. The (S)GPE solver

There is a wide variety of numerical strategies devised for solving the GPE numerically (see e.g. [223]). One particularly popular family of schemes are the so-called Time-Splitting Pseudo-Spectral Methods [224]. These methods, which rely on splitting the time-evolution operator into parts that are diagonal in different function bases, tend to be both computationally efficient and benefit from explicit conservation of the norm.

The key realisation to these methods is that for small time-steps Δt, the time step can be performed using a state-dependent time evolution operator

$$\psi(t+\Delta t,\mathbf{x}) = e^{i\Delta t H(\mathbf{x},\psi)}\psi(t,\mathbf{x}) \text{ for } H(\mathbf{x},\psi) = (1-i\gamma)\left(-\frac{1}{2}\nabla^2 + U - 1 + |\Psi|^2\right). \tag{B.19}$$

Note that this is the time evolution operator for the dGPE, which reduces the conservative GPE when setting $\gamma = 0$. In particular, $H(\mathbf{x},\psi)$ is a sum of a non-local derivative term, K, which depends on space only through the spatial derivatives, and a spatially dependent scalar term V. Defining,

$$K(\nabla^2) \equiv i\Delta t\,(1-i\gamma)\,\frac{1}{2}\nabla^2 \tag{B.20}$$

$$V(\mathbf{x}) \equiv -i\Delta t\,(1-i\gamma)\left[U(\mathbf{x}) - 1 + |\Psi(\mathbf{x})|^2\right] \tag{B.21}$$

the goal is then to split the exponentiated operator

$$e^{K+V} = e^K e^V e^{-\frac{1}{2}[K,V]} e^{-\frac{1}{6}(2[V,[K,V]-[K,[K,V]])}\ldots \tag{B.22}$$

using the Zassenhaus formula [225]. The key realisation is that K and V and of the order Δt, meaning that for small timesteps, the nested commutators in (B.22) become increasingly suppressed. For

example, to leading order, one has $e^{K+V} = e^K e^V$, which corresponds to the two-split methods. Note that in some cases, an ambiguity arises from there being multiple available states ϕ to the spatial step e^V (see e.g. [226]). Armed by the factorization of the exponentiated derivative e^K and spatial term e^V, all that remains is to evaluate K in a function basis that permits a closed-form expression for the exponentiated derivatives. If periodicity of the state Ψ is enforced by setting the potential $U \gg 1$ in a sufficiently large region around the numerical boundary, then a Fourier basis $\exp(i\mathbf{k}\cdot\mathbf{x})$ may be used. This is particularly convenient due to the efficient numerical Fast-Fourier Transform (FFT) algorithm, which drastically reduces the computational cost. These schemes are referred to as Fourier Pseudo-Spectral Time-Splitting methods. Denoting a spatial Fourier transform by $\mathcal{F}$, with inverse $\mathcal{F}^{-1}$, the two-split Fourier pseudo-spectral method can be summarised as follows:

$$\Psi_1 = e^V \Psi(t_0, \mathbf{x}) \tag{B.23}$$

$$\Psi(t_0 + \Delta t, \mathbf{x}) = \mathcal{F}^{-1} \exp[K(-\mathbf{k}^2)]\mathcal{F}\Psi_1 \tag{B.24}$$

where ∇^2 is replaced by $-\mathbf{k}^2$ in K. An implementation of (B.23) for $\gamma = 0$ gives a discrete numerical estimate, with error $\mathcal{O}(\Delta t)$, for the state evolved according to the GPE (2.4). For $\gamma \neq 0$, the evolution is that of the dGPE (2.65). The full stochastic evolution, i.e. the SGPE (3.1),

$$i\partial_t \Psi = \left[-\frac{1}{2}\nabla^2 + U - 1 + |\Psi|^2\right] + \eta \tag{B.25}$$

can be obtained by supplying the noise after the timestep, i.e.

$$\Psi_1 = e^V \Psi(t_0, \mathbf{x}) \tag{B.26}$$

$$\Psi_2 = \mathcal{F}^{-1} \exp K(-\mathbf{k}^2)\mathcal{F}\Psi_1 \tag{B.27}$$

$$\Psi(t_0 + \Delta t, \mathbf{x}) = \Psi_2 + s(\mathbf{x})\Delta t. \tag{B.28}$$

Here, $s(\mathbf{x})$ is sampled from a central, complex gaussian distribution at each spatial location.

To implement the above algorithms, the coordinate $\mathbf{x}$ is discretised into linearly spaced cartesian pixels $\mathbf{x}_{ij}$. In this case, the spatial Fourier transform $\mathcal{F}$ must be replaced with the pseudo-spectral Fast-Fourier Transform (FFT).

Conservation

To ensure the validity of the numerical GPE simulations, the energy is monitored. The full energy decomposition discussed around Equation (2.60) in chapter 2 is shown in Figure B.2 for the same dataset (see 2.5). Here, the total energy is $955.18905 \pm 9.6 \times 10^{-5}$, with relative variations of 10^{-7}.

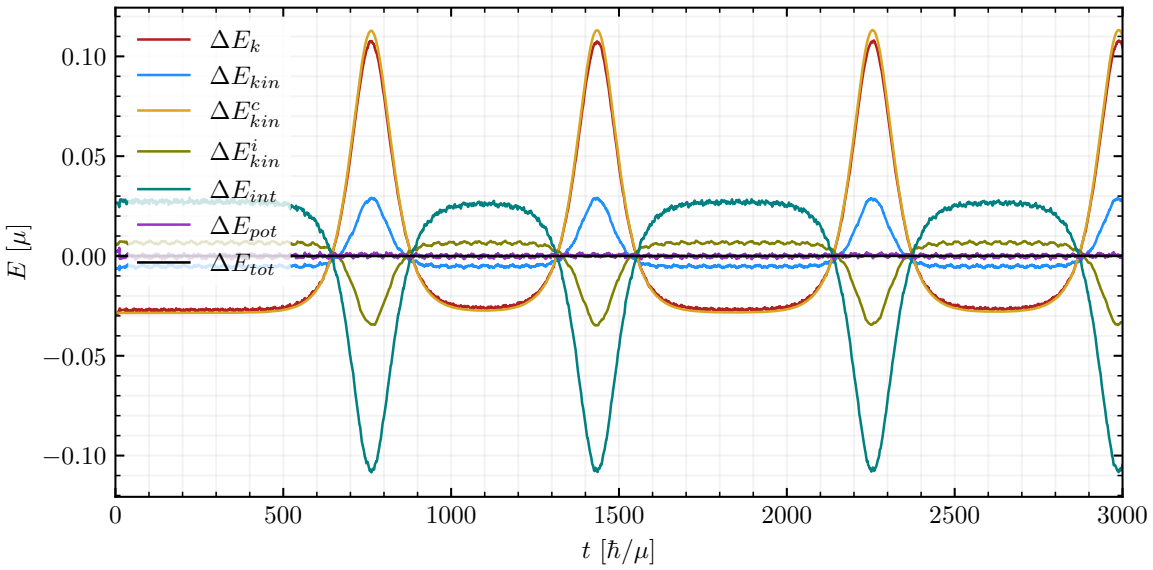

Figure B.2 (Evolution of energy components) The different energy components discussed around (2.60) is shown relative to the initial energy.

Boundary Conditions

Numerical simulations of the GPE are used to inspect the boundary condition at the potential boundary in comparison with the BdG, see section IV.2 in chapter 2. Here, the one-dimensional GPE is initialised with the Thomas-Fermi density $\Psi = 1 - U$ and iterated under the influence of damping ($\gamma = 1/100$) and with potential of the form (2.51) substituting $|x|$ for the radial coordinate r. The resulting state is used as background, to which a gaussian pulse is added. This state is evolved with the GPE using the scheme outlined in B.2.3, resulting in a time-dependent density $\rho = |\Psi|^2$, as depicted in Figure 2.3.

B.2.4. The Vortex Tracker

To extract the vortex trajectories within a numerical simulation $\Psi^k_{nm} = \Psi(t_k, x_n, y_m)$, the problem is first split into two parts: (1) Locating all the vortex locations $\mathbf{r}_i$ in a single frame k and (2) obtaining the optimal matching of vortex locations across neighbouring temporal snapshots k.

For part (1), consider a finite difference evaluation of $C_{i,j} \equiv \nabla \times \mathbf{v}_{i,j}$ for $\mathbf{v} = \mathrm{Im}(\nabla\Psi/\Psi)$. Then, the extrema of $C_{i,j}$ gives the vortex locations. Alternatively, writing $\mathbf{v}_{i,j} = v^y_{i,j}\mathbf{e}_x + v^y_{i,j}\mathbf{e}_y$ one may consider the convolution

$$\tilde{C}_{ij} \equiv v_x \star \cos\phi(x,y) + v_y \star \sin\phi(x,y) \quad \text{for} \quad \phi(x,y) = \arctan(y/x) \tag{B.29}$$

where $\star$ denotes a spatial convolution, which corresponds to estimating the circulation around nested circles at each point. Here v_x and v_y are already discretized, whereas there is freedom in the discretization of x and y. We choose $x \mapsto x_n$ and $y \mapsto y_n$ to be central, i.e. $x_n = n - N/2$ for $n = 0, \ldots, N$ and $y_n = n - N/2$ for $n = 0, \ldots, N$, with $N = 4$. The approach based on $\tilde{C}_{i,j}$ matches well with the approach based on $C_{i,j}$, but with slightly better resolution. Finally, suppose that (i_n, j_n) for $n = 1, 2, \ldots$ are the pixel locations of the local extrema of $\tilde{C}_{i,j}$. If $\mathbf{r}_{i,j} = (x_{i,j}, y_{i,j})$ are the physical coordinates corresponding to the pixels (i, j), then a sub-pixel resolution estimate for the vortex locations $\mathbf{r}_n$ can be found by taking the weighted average of $(\sum \mathbf{r}_{i,j}|\tilde{C}_{i,j}|)/(\sum |\tilde{C}_{i,j}|)$, where the sum runs over immediate neighbours of i_n, j_n.

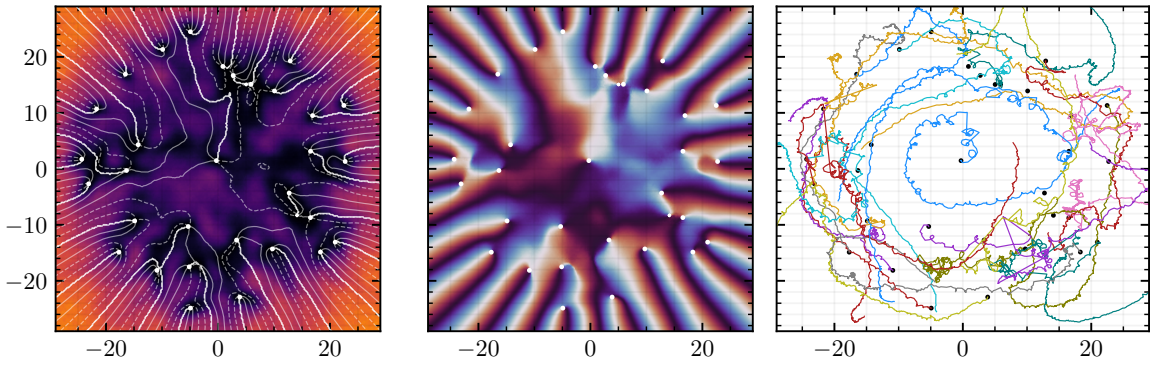

Figure B.3 (Vortex tracking)

The result of this procedure is a collection $\{\mathbf{r}_n^k\}_{n=1}^{N_v}$ of N_v vortex locations $\mathbf{r}_n^k$ at each time-frame k. To match the vortices across time-frames, the indices n are shuffled so as to minimise the trace of $D_{nm} = |\mathbf{r}_n^k - \mathbf{r}_m^{k+1}|^2$. However, nucleation and annihilation of vortex pairs, as well as the decay of multiply charged vortices, complicates the matching of vortices across time frames. To incorporate this, the shuffling of indices across timeframes is performed backwards in time and is avoided if the minimal distance $\min_n |\mathbf{r}_n^k - \mathbf{r}_m^{k+1}|$ far exceeds the characteristic distance travelled by vortices across time frames. An example of the vortex trajectories extracted from a simulation is shown in Figure B.3.

Appendix C

A view on the point-vortex model

In this appendix, we consider derivation of the point-vortex model from the phase ansatz

$$\phi = \sum_i \ell_i \arctan\left(\frac{y - y_i}{x - x_i}\right) \tag{C.1}$$

in the context of the Gross-Pitaevskii equation. Here, the ansatz (C.1) should be seen as a simple model that captures the essential topology of a two-dimensional condensate with vortices, of windings ℓ_j, at locations $\mathbf{r}_j = (x_j, y_j)$. One essential feature not contained in the phase (C.1) is the modification due to boundaries. However, for an impenetrable boundary with normal vector $\mathbf{n}$, i.e. $\mathbf{n} \perp \nabla\phi = 0$, one may add additional fictitious "ghost vortices" to the phase ansatz (C.1) to ensure the boundary condition to be obeyed, see e.g. [146].

Our strategy is to impose (C.1) on the GPE in hydrodynamic form, i.e.

$$\partial_t \phi + G + \frac{1}{2}(\nabla\phi)^2 = 0 \tag{C.2a}$$

$$\partial_t \rho + \nabla \cdot (\rho \nabla \phi) = 0 \tag{C.2b}$$

$$G[\rho] \equiv \rho + U - 1 - \frac{\nabla^2\sqrt{\rho}}{2\sqrt{\rho}}. \tag{C.2c}$$

which depends implicitly on the vortex coordinates $\mathbf{r}_i = x_i\mathbf{e}_x + y_i\mathbf{e}_y$ from (C.1) through the quantities

$$\partial_t \phi = -\sum_j \ell_j \frac{(x - x_j)\partial_t y_j - (y - y_j)\partial_t x_j}{(x - x_j)^2 + (y - y_j)^2} = \sum_j \ell_j \frac{\Delta\mathbf{r}_j}{|\Delta\mathbf{r}_j|^2} \cdot R\partial_t \Delta\mathbf{r}_j \tag{C.3}$$

$$\nabla\phi = \sum_j \ell_j \frac{\mathbf{e}_y(x - x_j) - \mathbf{e}_x(y - y_j)}{(x - x_j)^2 + (y - y_j)^2} = \sum_j \ell_j R \frac{\Delta\mathbf{r}_j}{|\Delta\mathbf{r}_j|^2} \tag{C.4}$$

$$(\nabla\phi)^2 = \sum_{i,j} \ell_i\ell_j \frac{(x - x_i)(x - x_j) + (y - y_i)(y - y_j)}{[(x - x_i)^2 + (y - y_i)^2]\,[(x - x_j)^2 + (y - y_j)^2]} = \sum_{i,j} \ell_i\ell_j \frac{\Delta\mathbf{r}_i \cdot \Delta\mathbf{r}_j}{|\Delta\mathbf{r}_i|^2|\Delta\mathbf{r}_j|^2} \tag{C.5}$$

$$\text{with} \quad R \equiv \begin{bmatrix} 0 & -1 \\ 1 & 0 \end{bmatrix} \quad \text{and} \quad \Delta\mathbf{r}_i \equiv \mathbf{r} - \mathbf{r}_i \quad \text{and} \quad \nabla^2\phi = 0. \tag{C.6}$$

where the spatial coodinate $\mathbf{r} \equiv (x, y)$ has been introduced. Using these relations, equation (C.2a) takes the form

$$G - \sum_j \frac{\ell_j \Delta \mathbf{r}_j}{|\Delta \mathbf{r}_j|^2} \cdot \left[R\partial_t \mathbf{r}_j - \frac{1}{2} \sum_i \frac{\ell_i \Delta \mathbf{r}_i}{|\Delta \mathbf{r}_i|^2} \right] = 0 \tag{C.7}$$

where $R^T = -R$ is the transpose of R. In the limit $\mathbf{r} \to \mathbf{r}_n$, this equation is divergent. As $\mathbf{r} \to \mathbf{r}_n$, then divergent terms must obey the equation independently, and so

$$2\Delta \mathbf{r}_n \cdot \left[R\partial_t \mathbf{r}_n - \sum_{i \neq n} \frac{\ell_i \Delta \mathbf{r}_{ni}}{|\Delta \mathbf{r}_{ni}|^2} \right] = \frac{1}{\ell_n} \left(2|\Delta \mathbf{r}_n|^2 G[\rho] + \ell_n^2 \right) \tag{C.8}$$

where the vortex separation $\Delta \mathbf{r}_{ni} \equiv \mathbf{r}_n - \mathbf{r}_i$ has been introduced. Here, the left side of the equation is linear in the direction $\Delta \mathbf{r}_n$ from which we approach the vortex $\mathbf{r}_n$, and the term in the bracket depends only on the vortex coordinates $\mathbf{r}_i$, and not $\mathbf{r}$. The term on the right side depends only on the distance $\Delta \mathbf{r}_n$ through the density ρ. Therefore, if G is rotationally symmetric, the two sides of the equation must vanish independently in the limit $\Delta \mathbf{r}_n \to 0$. Here, it is pleasing to note that in the case of a central multiply wound vortex in a free region ($U = 0$), we rediscover the divergent term from the relation (2.10) discussed in chapter 2. As for the left hand side of (C.8), we are free to choose any direction of $\Delta \mathbf{r}_n$ when taking the limit, to the term in the bracket must vanish independently of $\Delta \mathbf{r}_n$. The resulting expression, which is valid when G is rotationally symmetric, is exactly the point-vortex dynamics (see e.g. [146])

$$\partial_t \mathbf{r}_n = -\sum_{i \neq n} R \frac{\ell_i \Delta \mathbf{r}_{ni}}{|\Delta \mathbf{r}_{ni}|^2}. \tag{C.9}$$

Here, we should recall that equation (C.9) is in dimensional units. Re-introducing the length unit $\xi = \hbar/\sqrt{m\mu}$ and time unit $\tau = \hbar/\mu$ from (2.2) into (C.9), is equivalent to setting $\ell_j \mapsto \hbar \ell_j / m$.

When expressing vectors the vectors $\mathbf{r}_j = x_j \mathbf{e}_x + y_j \mathbf{e}_y$ as complex numbers, e.g. $z_j \equiv x_j + i y_j$, and realising that the rotation matrix R can be identified with i, the point-vortex model (C.9) takes the particularly slick form

$$\left(\frac{dz_n}{dt} \right)^* = \sum_{k \neq n} \frac{i\ell_k}{z_n - z_k}. \tag{C.10}$$

Let us consider the case of only two vortices z_1 and z_2 with windings ℓ_1 and ℓ_2. Clearly, the relevant degrees of freedom are relative $D \equiv (z_1 - z_2)/2$ and collective motions $C \equiv (z_1 + z_2)/2$, so

$$\left(\frac{dC}{dt} \right)^* = \frac{i(\ell_2 - \ell_1)}{4D} \qquad \text{and} \qquad \left(\frac{dD}{dt} \right)^* = \frac{i(\ell_2 + \ell_1)}{4D}. \tag{C.11}$$

Therefore, if the two vortices are counter-rotating and equally charged, i.e. $\ell_2 \equiv \ell = -\ell_1$, then there is no relative motion ($D = \mathrm{const}$) and the vortex pair travels collectively with

$$\frac{dC}{dt} = -v\frac{iD}{|D|} \quad \text{for} \quad v \equiv \frac{\ell}{2|D|} \tag{C.12}$$

That is, they travel in a direction perpendicular to the line defined by their positions and at a constant speed inversely proportional to their separation.

If the two vortices are co-rotating and equally charged, i.e. $\ell_2 \equiv \ell = \ell_1$, then there is no collective motion ($C = \mathrm{const}$) and the two vortices orbit the point C at radius $|D|$, i.e.

$$\frac{dD}{dt} = -i\Omega_{pv}D \quad \text{for} \quad \Omega_{pv} \equiv \frac{\ell}{2|D|^2}\,. \tag{C.13}$$

This is the expression for the Point-vortex orbital frequency used in e.g. Figure 2.8. Note, however, that here $|D|$ is the radius (with center C) of oscillation, whereas $s = 2|D|$ is the vortex separation used in chapter 2.

Appendix D

Derivation of non-linear two-fluid interface dynamics

In this section, the derivation of the non-linear interfacial dynamics of a vertically oscillated two-fluid interface is presented. The calculations follow those of Miles [172, 173] closely, but with two main differences. First, the contribution from surface tension is considered differently. Whereas Miles [173] proposes to add surface tension perturbatively to linear order, it is here taken into account from the start, leading to additional quartic terms in the final Lagrangian. The second difference is the explicit inclusion of the lighter fluid resting on top of the interface.

Consider two inviscid fluids, with densities $\rho_- < \rho_+$, occupying volumes $V_\pm$. The fluids are assumed to be immiscible, i.e. $V_+ \cap V_- = 0$, with flow fields $\mathbf{v}_\pm \equiv \nabla\Phi_\pm$ given in terms of velocity potentials $\Phi_\pm$. The boundary separating the two fluids is referred to as Γ and assumed to be single-valued in the vertical coordinate, i.e. $z = h(t, \mathbf{r})$, where $\mathbf{r} = (r, \theta)$ is the horizontal coordinate. Each fluid has kinetic energy density $\rho_\pm \nabla|\Phi_\pm|^2$, whereas the potential energy density is dictated by the hydro-static pressure, i.e. $g\rho_\pm z$. In addition to the self-energies of the two fluids, there is energy due to tensile forces in the shape of the interface. This energy is proportional to the surface area of the interface Γ, with the proportionality constant being the surface tension σ. That is, the Lagrangian for the system can be written

$$L = L_+ + L_- - V_\sigma \tag{D.1}$$

$$L_\pm = \rho_\pm \iiint_{V_\pm} dV \left[\frac{1}{2}|\nabla\Phi_\pm|^2 - gz\right] \tag{D.2}$$

$$V_\sigma = \sigma \iint (|\nabla\Gamma| - 1)\, dA, \tag{D.3}$$

Here, we are armed with Dirichlet's variational principle

$$S_\pm = \frac{1}{A}\iiint_{V_\pm} \frac{1}{2}(\nabla\Phi_\pm)^2 dV_\pm - \frac{1}{A}\iint \dot{\xi}\, \Phi_\pm|_{\Gamma=0}\, dA \tag{D.4}$$

whose stationarity with respect to variations $\delta\Phi_\pm$ in $\Phi_\pm$ for a given interface $z = \xi$ fixes the boundary-value problem (4.8). Our strategy is to use the linear eigenmodes ξ_α and $\phi_{\pm,\alpha}$ from

(4.10) as generalised coordinates for ξ and $\Phi_\pm$. Introducing this in the Dirichlet action (D.4) results in

$$S_\pm = \frac{1}{2}\varphi_{\pm,a}K^{(\pm)}_{ab}\varphi_{\pm,b} - \dot{\xi}_a D^{(\pm)}_{ab}\varphi_{\pm,b} \tag{D.5}$$

for

$$K^\pm_{ab} \equiv \iiint_{V_\pm} dV_\pm \nabla\psi_{\pm,a}\cdot\nabla\psi_{\pm,b} \quad \text{and} \quad D^\pm_{ab} \equiv (f_a, \psi_{\pm,b}(r,\theta,\xi))\,. \tag{D.6}$$

Here, stationarity of (D.5) with respect to variations in $\phi_{\pm,a}$ yields $K^\pm_{ab}\phi_{\pm,b} = \dot{\xi}_b D^\pm_{ba}$ which can be perturbatively inverted to eliminate $\phi_{\pm,a}$ from the non-linear Lagrangian (D.1).

We start by considering the expansion of $D^\pm_{ab}$, which can be written

$$\begin{aligned} D^\pm_{ab} &\equiv (f_a, \psi_{j,b}(\mathbf{x},\xi)) \\ &\simeq (f_a,\psi_{j,b}(\mathbf{x},0)) + (f_a,\xi\partial_z\psi_{j,b}(\mathbf{x},0)) + \frac{1}{2}\left(f_a,\xi^2\partial_z^2\psi_{j,b}(\mathbf{x},0)\right) \\ &= \delta_{ab} \mp \sum_c \xi_c T_b \underbrace{(f_a, f_c f_b)}_{C_{abc}} + \frac{1}{2}\sum_{c,d}\xi_c\xi_d k_b^2 \underbrace{(f_a, f_c f_d f_b)}_{C_{abcd}} \end{aligned} \tag{D.7}$$

where $\partial_z\psi_{j,b}(\mathbf{x},0) = \mp f_b T_b$ with $T_b \equiv k_b\tanh(k_b h_0)$ and $\partial_z^2\psi_{j,b}(\mathbf{x},0) = f_b k_b^2$.

For $K^\pm_{ab}$, first write $K^\pm_{ab} = K_{0,ab} + \delta K^\pm_{ab}$ where $K^\pm_{0,ab}$ is $K^\pm_{ab}$ integrated to the resting position $z = 0$. Writing $\psi_{\pm,a} \equiv f_a\chi_{\pm,a}$ for $\chi_{\pm,a} = \cosh(k_a(z\mp h_0))/\cosh(k_a)$, we have

$$K^\pm_{0,ab} = \mp\frac{1}{A}\iint_S dA\int_{\pm h_0}^0 dz\,\nabla\psi_{\pm,a}\cdot\nabla\psi_{\pm,b} \tag{D.8}$$

$$= \mp\frac{1}{A}\left(\iint_S dA\,\nabla f_a\cdot\nabla f_b\right)\frac{\int_{\pm h_0}^0 dz\cosh(k_a(z\mp h_0))\cosh(k_b(z\mp h_0))}{\cosh(k_a h_0)\cosh(k_b h_0)} \tag{D.9}$$

$$\mp k_a k_b (f_a, f_b)\frac{\int_{\pm h_0}^0 dz\sinh(k_a(z\mp h_0))\sinh(k_b(z\mp h_0))}{\cosh(k_a h_0)\cosh(k_b h_0)} \tag{D.10}$$

Invoking Green's theorem gives

$$\frac{1}{A}\iint_S dA\,\nabla f_a\cdot\nabla f_b = -\frac{1}{A}\iint_S dA\,f_a\nabla^2 f_b = k_b^2(f_a,f_b) = k_b^2\delta_{ab}, \tag{D.11}$$

so that $K^\pm_{0,ab} = \delta_{ab}T_a$ is a diagonal matrix with diagonal entries $T_a \equiv k_a\tanh(k_a h_0)$. Writing

$$G_\pm(\mathbf{x},z) \equiv \nabla\psi_{\pm,a}\cdot\nabla\psi_{\pm,b} = \chi_a\chi_b\nabla f_a\cdot\nabla f_b + f_a f_b\partial_z\chi_{\pm,a}\partial_z\chi_{\pm,b} \tag{D.12}$$

and using that $\chi_{\pm,a}(z=0)=1, \chi'_{\pm,a}(z=0)=\mp T_a$ and $\chi''_{\pm,a}(z=0)=-k_a^2$, where $'$ denotes vertical derivatives, i.e. $'=\partial_z$, we find

$$K^{\pm}_{ab} \equiv K^{\pm}_{0,ab} + \frac{1}{A}\iint_S dA \int_0^{\xi} G_{\pm}(\mathbf{x},z) \simeq K^{\pm}_{0,ab} \mp (G_{\pm}(\mathbf{x},0),\xi) \mp \frac{1}{2}\left(\xi^2, \partial_z G_{\pm}(\mathbf{x},0)\right) \tag{D.13}$$

$$= T_a\delta_{ab} \mp \sum_c \xi_c \left(\nabla f_a \cdot \nabla f_b, f_c\right) \mp T_a T_b \sum_c \xi_c \left(f_a f_b, f_c\right) \tag{D.14}$$

$$+ \frac{1}{2}\left(k_a^2 T_b + k_b^2 T_a\right) \sum_{cd} \xi_c\xi_d \left(f_c f_d, f_a f_b\right) + \frac{1}{2}(T_a+T_b) \sum_{cd} \xi_c\xi_d \left(f_c f_d, \nabla f_a \cdot \nabla f_b\right) \tag{D.15}$$

at this point, we benefit from introducing

$$\mathcal{C}_{abc} \equiv (f_a, f_b f_c) \tag{D.16a}$$

$$\mathcal{C}_{abcd} \equiv (f_a f_b, f_c f_d) = \frac{1}{k_c^2}(\mathcal{D}_{abcd} + \mathcal{D}_{dabc} + \mathcal{D}_{dbac}) \tag{D.16b}$$

$$\mathcal{D}_{abc} \equiv (f_a, \nabla f_b \cdot \nabla f_c) = k_b^2 \mathcal{C}_{abc} - \mathcal{D}_{cab} = \frac{1}{2}(k_b^2 + k_c^2 - k_a^2)\mathcal{C}_{abc} \tag{D.16c}$$

$$\mathcal{D}_{abcd} \equiv (f_a f_b, \nabla f_c \cdot \nabla f_d) \tag{D.16d}$$

$$\mathcal{M}_{abcd} \equiv (\nabla f_a \cdot \nabla f_b, \nabla f_c \cdot \nabla f_d) \tag{D.16e}$$

for which the coefficients $K^{\pm}_{ab}$ and $D^{\pm}_{ab}$ take the form

$$K^{\pm}_{ab} = \delta_{ab} T_a \mp \sum_c \left(\mathcal{D}_{cab} + T_a T_b \mathcal{C}_{abc}\right) \xi_c \tag{D.17}$$

$$+ \sum_{cd} \frac{1}{2}\left[(k_a^2 T_b + k_b^2 T_a)\mathcal{C}_{abcd} + (T_a+T_b)\mathcal{D}_{cdab}\right] \xi_c\xi_d \tag{D.18}$$

$$D^{\pm}_{ab} = \delta_{ab} \mp \sum_c \xi_c T_b \mathcal{C}_{abc} + \frac{1}{2}\sum_{cd} \xi_c\xi_d k_b^2 \mathcal{C}_{abcd} \tag{D.19}$$

Using that $K^{\pm}_{ab}\phi_{\pm,b} = \dot{\xi}_b D^{\pm}_{ba}$ we now search for $L^{\pm} \equiv (K^{\pm})^{-1}D$, which can be done order by order. That is, if $K = K_0 + K_1 + K_2$ are orders of the expansion of K, then we postulate a matrix $G = G_0 + G_1 + G_2$ such that $GK = \mathbb{I}$. The result is

$$G_0 = K_0^{-1}, \quad G_1 = -G_0 K_1 G_0, \quad G_2 = -G_0 K_2 G_0 + G_0 K_1 G_0 K_1 G_0, \quad \ldots \tag{D.20}$$

and so on. Since $(K^{\pm})^{-1}_{ab} \simeq \delta_{ab} T_a^{-1}$ to leading order, it can be identified with G_0. We find

$$(G_0)_{ab} = \delta_{ab} T_a^{-1} \tag{D.21a}$$

$$(G_1)_{ab} = -\frac{1}{T_a T_d} \sum_{cd} \delta_{ac} (K_1)_{cd} \delta_{db} = \pm \sum_c \left(\frac{\mathcal{D}_{cab}}{T_a T_b} + \mathcal{C}_{abc} \right) \xi_c \tag{D.21b}$$

$$(G_2)_{ab} = -\frac{1}{T_a T_b} (K_2)_{ab} + \frac{1}{T_a T_b} \sum_e \frac{1}{T_e} (K_1)_{ae} (K_1)_{eb} \tag{D.21c}$$

$$= -\sum_{cd} \frac{\xi_c \xi_d}{2 T_a T_b} \left[(k_a^2 T_b + k_b^2 T_a) \mathcal{C}_{abcd} + (T_a + T_b) \mathcal{D}_{cdab} \right] \tag{D.21d}$$

$$+ \sum_{cde} \xi_c \xi_d \left(\frac{\mathcal{D}_{cae} \mathcal{D}_{deb}}{T_a T_b T_e} + \frac{\mathcal{C}_{ebc} \mathcal{D}_{dae}}{T_a} + \frac{\mathcal{C}_{eac} \mathcal{D}_{dbe}}{T_b} + T_e \mathcal{C}_{aec} \mathcal{C}_{ebd} \right) \tag{D.21e}$$

This permits computing the matrix product $L^{\pm} \equiv (K^{\pm})^{-1} D^{\mathsf{T}}$ order by order, i.e.

$$(L_0^{\pm})_{ab} = \sum_c (G_0)_{ac} \mathcal{D}^0_{bc} = T_a^{-1} \delta_{ab} \tag{D.22a}$$

$$(L_1^{\pm})_{ab} = \sum_c \left[(G_0)_{ac} D^1_{bc} + (G_1)_{ac} D^0_{bc} \right] = \pm \sum_c \xi_c \frac{\mathcal{D}_{cab}}{T_a T_b} \tag{D.22b}$$

$$(L_2^{\pm})_{ab} = \sum_c \left[(G_0)_{ac} \mathcal{D}^2_{bc} + (G_1)_{ac} \mathcal{D}^1_{bc} + (G_2)_{ac} \mathcal{D}^0_{bc} \right] \tag{D.22c}$$

$$= \sum_{cd} \xi_c \xi_d \left[-\frac{k_b^2}{2 T_b} \mathcal{C}_{bacd} - \frac{T_a + T_b}{2 T_a T_b} \mathcal{D}_{cdab} + \sum_e \frac{\mathcal{D}_{dbe}}{T_a T_b T_e} \left(\mathcal{D}_{cae} + T_a T_e \mathcal{C}_{eac} \right) \right]. \tag{D.22d}$$

This matches equation (2.14) of Miles [172] for the bottom fluid ($-$) and, crucially, depends only on the fluid position $\pm$ through the linear term. That is, we have now found the matrix $L^{\pm}_{ab} \equiv L_0^{\pm} + L_1^{\pm} + L_2^{\pm}$ that maps $\dot{\xi}_b$ to $\phi_{\pm,a}$, i.e. $\phi_{\pm,a} = L^{\pm}_{ab} \dot{\xi}_b$, which follows from the stationarity of the Dirichlet action.

Next, we focus on the Lagrangian (D.1), where we first note that

$$\frac{V_\sigma}{A} = \frac{1}{A} \sigma \iint_A dA |\nabla \Gamma| = \frac{\sigma}{A} \iint_A dA \sqrt{1 + (\nabla \xi)^2} \tag{D.23}$$

$$\simeq \sigma + \frac{\sigma}{2} \sum_a k_a^2 \xi_a^2 - \frac{\sigma}{8} \sum_{abcd} \xi_a \xi_b \xi_c \xi_d \mathcal{M}_{abcd} \tag{D.24}$$

Next, we consider the Lagrangians of the bulk piece by piece

$$\frac{L_\pm}{A} = \frac{1}{A}\rho_\pm \sum_{ab} \iiint_{V_\pm} dV_\pm \left[\frac{1}{2}\phi_{\pm,a}\phi_{\pm,b}\nabla\psi_{\pm,a}\cdot\nabla\psi_{\pm,b} - gz\right] \tag{D.25}$$

$$= \frac{1}{2}\rho_\pm \sum_{abc} \dot{\xi}_b\dot{\xi}_c L^\pm_{ac} D^\pm_{ba} \pm \frac{1}{2}\rho_\pm \sum_a g\xi_a^2 - \frac{1}{2}\rho_\pm g h_0^2 \tag{D.26}$$

for which we need to perform one last matrix product:

$$\sum_a L^\pm_{ac} D^\pm_{ba} = \frac{\delta_{cb}}{T_c} \mp \sum_d \xi_d \mathcal{A}_{dcb} + \frac{1}{2}\sum_{fd} \xi_d\xi_f \mathcal{A}_{dfcb}, \tag{D.27}$$

where

$$\mathcal{A}_{dcb} \equiv \left(\mathcal{C}_{bcd} - \frac{\mathcal{D}_{dbc}}{T_b T_c}\right) = \left(2T_bT_c - k_b^2 - k_c^2 + k_d^2\right)\frac{\mathcal{C}_{bcd}}{2T_bT_c} \tag{D.28}$$

$$\mathcal{A}_{dfcb} \equiv -\frac{T_b+T_c}{T_bT_c}\mathcal{D}_{fdbc} + \sum_e \frac{\mathcal{C}_{dce}\mathcal{C}_{fbe}}{2T_bT_cT_e}\left(k_e^2 + k_c^2 - k_d^2\right)\left(k_b^2 + k_e^2 - k_f^2\right) \tag{D.29}$$

Note that up to this point, there has been no need to assume equal depths $z = \pm h_0$ of the two fluids. In fact, the above relations can easily be extended to uneven depths by setting $\pm h_0 \to \pm h_0^\pm$ with $h_0^- \neq h_0^+$, i.e. $T_a \mapsto T_a^\pm$. In the case of equal depths, however, the Lagrangian becomes exceptionally simple

$$\frac{L}{A} = \frac{L_0}{A} + \sum_a \frac{\Sigma\rho}{2T_a}\left(\dot{\xi}_a^2 - \omega_a^2(t)\xi_a^2\right) \tag{D.30a}$$

$$+ \frac{\Delta\rho}{2}\sum_{abc}\xi_c\mathcal{A}_{cba}\dot{\xi}_a\dot{\xi}_b + \sum_{abcd}\frac{\Sigma\rho}{4}\xi_d\xi_c\left[\mathcal{A}_{dcba}\dot{\xi}_a\dot{\xi}_b + \frac{\sigma\mathcal{M}_{cabd}}{2\Sigma\rho}\xi_a\xi_b\right] \tag{D.30b}$$

$$\text{for} \quad \Delta\rho \equiv \rho_- - \rho_+ \quad \text{and} \quad \Sigma\rho \equiv \rho_- + \rho_+ \tag{D.30c}$$

where $L_0 \equiv -\frac{1}{2}A\Sigma\rho g h_0^2 - \sigma A$ is a constant.

Armed with the nonlinear Lagrangian (D.30a) to quartic order in ξ_a, we now consider the case of a single dominating mode ξ_b in the system. That is $|\xi_b| \gg |\xi_a|$ for all $a \neq b$. We may then perturb the Lagrangian around ξ_b, keeping only linear contributions from ξ_a. This will provide us with an effective nonlinear self-interaction for the dominant mode to leading order, and a source

equation for the subdominant mode ξ_a as it evolves in the presence of the dominant mode ξ_b.

$$\frac{L}{A} = \frac{L_0}{A} + \frac{\Sigma\rho}{2T_b}\left(\dot{\xi}_b^2 - \omega_b^2\xi_b^2\right) + \frac{\Delta\rho}{2}\mathcal{A}_{bbb}\xi_b\dot{\xi}_b^2 + \frac{\Sigma\rho}{4}\left[\mathcal{A}_{bbbb}\xi_b^2\dot{\xi}_b^2 + \frac{\sigma\mathcal{M}_{bbbb}}{2\Sigma\rho}\xi_b^4\right] \tag{D.31}$$

$$+ \sum_{a\neq b}\left[\frac{\Sigma\rho}{2T_a}\left(\dot{\xi}_a^2 - \omega_a^2\xi_a^2\right) + \frac{\Delta\rho}{2}\left(2\mathcal{A}_{bba}\xi_b\dot{\xi}_a\dot{\xi}_b + \mathcal{A}_{abb}\xi_a\dot{\xi}_b^2\right)\right] \tag{D.32}$$

$$+ \sum_{a\neq b}\frac{\Sigma\rho}{4}\left[\left(\mathcal{A}_{bbba} + \mathcal{A}_{bbab}\right)\xi_b^2\dot{\xi}_a\dot{\xi}_b + \left(\mathcal{A}_{babb} + \mathcal{A}_{abbb}\right)\xi_a\xi_b\dot{\xi}_b^2 + 4\frac{\sigma\mathcal{M}_{bbba}}{2\Sigma\rho}\xi_a\xi_b^3\right] \tag{D.33}$$

Before approaching the equations of motion, we will benefit from the observation that $\mathcal{C}_{abc}$ is an off-diagonal tensor, i.e. $\mathcal{C}_{aaa} = 0$, which follows from the azimuthal integral. Then

$$\frac{L}{A} = \frac{L_0}{A} + \frac{\Sigma\rho}{2T_b}\left(\dot{\xi}_b^2 - \omega_b^2(t)\xi_b^2\right) + \frac{\Sigma\rho}{4}\left[\mathcal{A}_{bbbb}\xi_b^2\dot{\xi}_b^2 + \frac{\sigma\mathcal{M}_{bbbb}}{2\Sigma\rho}\xi_b^4\right] \tag{D.34}$$

$$+ \sum_{a\neq b}\left[\frac{\Sigma\rho}{2T_a}\left(\dot{\xi}_a^2 - \omega_a^2(t)\xi_a^2\right) + \frac{\Delta\rho}{2}\left(2\mathcal{A}_{bba}\xi_b\dot{\xi}_a\dot{\xi}_b + \mathcal{A}_{abb}\xi_a\dot{\xi}_b^2\right)\right] \tag{D.35}$$

$$+ \sum_{a\neq b}\frac{\Sigma\rho}{4}\left[\left(\mathcal{A}_{bbba} + \mathcal{A}_{bbab}\right)\xi_b^2\dot{\xi}_a\dot{\xi}_b + \left(\mathcal{A}_{babb} + \mathcal{A}_{abbb}\right)\xi_a\xi_b\dot{\xi}_b^2 + 4\frac{\sigma\mathcal{M}_{bbba}}{2\Sigma\rho}\xi_a\xi_b^3\right] \tag{D.36}$$

To leading order, the equation of motion for the dominant mode then takes the form

$$\left(1 + \mathcal{A}_b\xi_b^2\right)\ddot{\xi}_b + 2\gamma_b\dot{\xi}_b + \left(\omega_b^2(t) + \mathcal{A}_b\dot{\xi}_b^2 - \mathcal{M}_b\xi_b^2\right)\xi_b \tag{D.37}$$

where the prefactor of $\ddot{x}_b$ may be perturbatively inverted to give

$$\ddot{\xi}_b + 2\gamma_b\left(1 - \mathcal{A}_b\xi_b^2\right)\dot{\xi}_b + \left(\omega_b^2 + \mathcal{A}_b\left[\dot{\xi}_b^2 - \omega_b^2\xi_b^2\right] - \mathcal{M}_b\xi_b^2\right)\xi_b \simeq 0 \tag{D.38}$$

with the definitions $\mathcal{A}_b \equiv \frac{1}{2}T_b\mathcal{A}_{bbbb}$ and $\mathcal{M}_b \equiv T_b\sigma\mathcal{M}_{bbbb}/\Sigma\rho$. Here, the Rayleigh dissipation function has been used to reintroduce the equations to a phenomenological damping γ_b.

Similarly, the equation of motion for the subdominant mode ξ_a, is found to be

$$\ddot{\xi}_a + 2\gamma_a\dot{\xi}_a + \omega_a^2\xi_a + \tilde{\rho}T_a\mathcal{A}_{bba}\xi_b\ddot{\xi}_b + \frac{1}{2}\tilde{\rho}T_a(2\mathcal{A}_{bba} - \mathcal{A}_{abb})\dot{\xi}_b^2 \tag{D.39}$$

$$+ A_{ab}\xi_b\dot{\xi}_b^2 + \frac{1}{4}T_a\left(\mathcal{A}_{bbba} + \mathcal{A}_{bbab}\right)\xi_b^2\ddot{\xi}_b - \frac{1}{2}M_{ab}\xi_b^3 \tag{D.40}$$

where

$$A_{ab} \equiv \frac{1}{4} T_a \left(2\mathcal{A}_{bbba} + 2\mathcal{A}_{bbab} - \mathcal{A}_{babb} - \mathcal{A}_{abbb}\right) \tag{D.41}$$

$$M_{ab} \equiv T_a \frac{\sigma \mathcal{M}_{bbba}}{2\Sigma\rho}. \tag{D.42}$$

When the subdominant mode ξ_a is in the same m as the dominant mode ξ_b, then $\mathcal{A}_{bba} = \mathcal{A}_{abb} = 0$ so that

$$\ddot{\xi}_a + 2\gamma_a \dot{\xi}_a + \omega_a^2 \xi_a + A_{ab} \xi_b \dot{\xi}_b^2 + \frac{1}{4} T_a \left(\mathcal{A}_{bbba} + \mathcal{A}_{bbab}\right) \xi_b^2 \ddot{\xi}_b - M_{ab} \xi_b^3 \simeq 0 \tag{D.43}$$

which reduces to the equation of motion for the dominant mode when $b = a$.

Bibliography

[1] P. Bartha, "Analogy and Analogical Reasoning," in *The Stanford Encyclopedia of Philosophy*, E. N. Zalta, Ed., Summer 2022, Metaphysics Research Lab, Stanford University, 2022.

[2] A. E. Shapiro, "Light, pressure, and rectilinear propagation: Descartes' celestial optics and Newton's hydrostatics," *Studies in History and Philosophy of Science Part A*, vol. 5, no. 3, pp. 239–296, 1974, ISSN: 0039-3681. DOI: 10.1016/0039-3681(74)90002-8.

[3] J. Priestley, *The History and Present State of Electricity: With Original Experiments*, The third edition, corrected and enlarged. London: Printed for C. Bathurst, and T. Lowndes ... J. Rivington, and J. Johnson ... S. Crowder, G. Robinson, and R. Baldwin ... T. Becket, and T. Cadell ..., 1775.

[4] J. C. Maxwell, *The Scientific Papers of James Clerk Maxwell*, W. D. Niven, Ed., ser. Cambridge Library Collection - Physical Sciences. Cambridge: Cambridge University Press, 2011, vol. 1, ISBN: 978-1-108-01225-6. DOI: 10.1017/CBO9780511698095.

[5] H. Marmanis, "Analogy between the Navier–Stokes equations and Maxwell's equations: Application to turbulence," *Physics of Fluids*, vol. 10, no. 6, pp. 1428–1437, 1998, ISSN: 1070-6631. DOI: 10.1063/1.869762.

[6] G. Rousseaux, S. Seifer, V. Steinberg, and A. Wiebel, "On the Lamb vector and the hydrodynamic charge," *Exp Fluids*, vol. 42, no. 2, pp. 291–299, 2007, ISSN: 1432-1114. DOI: 10.1007/s00348-006-0238-2.

[7] E. Rutherford, "LXXIX. The scattering of α and β particles by matter and the structure of the atom," *The London, Edinburgh, and Dublin Philosophical Magazine and Journal of Science*, vol. 21, no. 125, pp. 669–688, 1911, ISSN: 1941-5982. DOI: 10.1080/14786440508637080.

[8] E. Schrödinger, "An Undulatory Theory of the Mechanics of Atoms and Molecules," *Phys. Rev.*, vol. 28, no. 6, pp. 1049–1070, 1926. DOI: 10.1103/PhysRev.28.1049.

[9] M. Steiner, "The Application of Mathematics to Natural Science," *The Journal of Philosophy*, vol. 86, no. 9, pp. 449–480, 1989. DOI: 10.2307/2026759.

[10] J. D. Bekenstein, "Black Holes and Entropy," *Phys. Rev. D*, vol. 7, no. 8, pp. 2333–2346, 1973. DOI: 10.1103/PhysRevD.7.2333.

[11] J. M. Bardeen, B. Carter, and S. W. Hawking, "The four laws of black hole mechanics," *Commun.Math. Phys.*, vol. 31, no. 2, pp. 161–170, 1973, ISSN: 1432-0916. DOI: 10.1007/BF01645742.

[12] S. W. Hawking, "Black hole explosions?" *Nature*, vol. 248, no. 5443, pp. 30–31, 1974, ISSN: 00280836. DOI: 10.1038/248030a0.

[13] S. Wuppuluri and F. A. Doria, *The Map and the Territory: Exploring the Foundations of Science, Thought and Reality*. Springer, 2018, ISBN: 978-3-319-72478-2.

[14] P. W. Evans and K. P. Y. Thébault, "On the limits of experimental knowledge," *Philosophical Transactions of the Royal Society A: Mathematical, Physical and Engineering Sciences*, vol. 378, no. 2177, p. 20 190 235, 2020. DOI: 10.1098/rsta.2019.0235.

[15] A. Einstein, "Die Feldgleichungen der Gravitation," *Sitzungsberichte der Königlich Preußischen Akademie der Wissenschaften (Berlin*, pp. 844–847, 1915.

[16] K. Schwarzschild, "Über das Gravitationsfeld eines Massenpunktes nach der Einsteinschen Theorie," *Sitzungsberichte der Königlich Preußischen Akademie der Wissenschaften (Berlin*, pp. 189–196, 1916.

[17] S. Chandrasekhar, "The highly collapsed configurations of a stellar mass," *Monthly Notices of the Royal Astronomical Society*, vol. 91, pp. 456–466, 1931, ISSN: 0035-8711. DOI: 10.1093/mnras/91.5.456.

[18] D. Finkelstein, "Past-Future Asymmetry of the Gravitational Field of a Point Particle," *Phys. Rev.*, vol. 110, no. 4, pp. 965–967, 1958. DOI: 10.1103/PhysRev.110.965.

[19] J. D. Bekenstein, "Generalized second law of thermodynamics in black-hole physics," *Phys. Rev. D*, vol. 9, no. 12, pp. 3292–3300, 1974. DOI: 10.1103/PhysRevD.9.3292.

[20] C. Barceló, S. Liberati, and M. Visser, "Analogue Gravity," *Living Rev. Relativ.*, vol. 14, no. 1, p. 3, 2011, ISSN: 1433-8351. DOI: 10.12942/lrr-2011-3.

[21] S. Hawking, "Gravitationally Collapsed Objects of Very Low Mass," *Monthly Notices of the Royal Astronomical Society*, vol. 152, no. 1, pp. 75–78, 1971, ISSN: 0035-8711. DOI: 10.1093/mnras/152.1.75.

[22] A. M. Green and A. R. Liddle, "Critical collapse and the primordial black hole initial mass function," *Phys. Rev. D*, vol. 60, no. 6, p. 063 509, 1999. DOI: 10.1103/PhysRevD.60.063509.

[23] W. G. Unruh, "Experimental Black-Hole Evaporation?" *Phys. Rev. Lett.*, vol. 46, no. 21, pp. 1351–1353, 1981. DOI: 10.1103/PhysRevLett.46.1351.

[24] ——, "Sonic analogue of black holes and the effects of high frequencies on black hole evaporation," *Phys. Rev. D*, vol. 51, no. 6, pp. 2827–2838, 1995. DOI: 10.1103/PhysRevD.51.2827.

[25] C. Barceló, S. Liberati, and M. Visser, "Analogue Gravity," *Living Reviews in Relativity*, vol. 8, no. 1, 2005, ISSN: 1433-8351. DOI: 10.12942/lrr-2005-12.

[26] T. Jacobson, "Black-hole evaporation and ultrashort distances," *Phys. Rev. D*, vol. 44, no. 6, pp. 1731–1739, 1991. DOI: 10.1103/PhysRevD.44.1731.

[27] T. Jacobson, "Black hole radiation in the presence of a short distance cutoff," *Phys. Rev. D*, vol. 48, no. 2, pp. 728–741, 1993. DOI: 10.1103/PhysRevD.48.728.

[28] R. Brout, S. Massar, R. Parentani, and P. Spindel, "Hawking radiation without trans-Planckian frequencies," *Phys. Rev. D*, vol. 52, no. 8, pp. 4559–4568, 1995. DOI: 10.1103/PhysRevD.52.4559.

[29] S. Corley, "Computing the spectrum of black hole radiation in the presence of high frequency dispersion: An analytical approach," *Phys. Rev. D*, vol. 57, no. 10, pp. 6280–6291, 1998. DOI: 10.1103/PhysRevD.57.6280.

[30] S. Liberati, S. Sonego, and M. Visser, "Unexpectedly large surface gravities for acoustic horizons?" *Class. Quantum Grav.*, vol. 17, no. 15, pp. 2903–2923, 2000, ISSN: 0264-9381. DOI: 10.1088/0264-9381/17/15/305.

[31] W. Gordon, "Zur Lichtfortpflanzung nach der Relativitätstheorie," *Annalen der Physik*, vol. 377, no. 22, pp. 421–456, 1923, ISSN: 1521-3889. DOI: 10.1002/andp.19233772202.

[32] C. Barceló, S. Liberati, and M. Visser, "Refringence, field theory and normal modes," *Class. Quantum Grav.*, vol. 19, no. 11, pp. 2961–2982, 2002, ISSN: 0264-9381. DOI: 10.1088/0264-9381/19/11/314.

[33] U. Leonhardt and P. Piwnicki, "Relativistic Effects of Light in Moving Media with Extremely Low Group Velocity," *Phys. Rev. Lett.*, vol. 84, no. 5, pp. 822–825, 2000. DOI: 10.1103/PhysRevLett.84.822.

[34] C. Barceló, S. Liberati, and M. Visser, "Analogue gravity from field theory normal modes?" *Classical and Quantum Gravity*, vol. 18, no. 17, pp. 3595–3610, 2001, ISSN: 1361-6382. DOI: 10.1088/0264-9381/18/17/313.

[35] R. Schützhold and W. G. Unruh, "Gravity wave analogues of black holes," *Phys. Rev. D*, vol. 66, no. 4, p. 044 019, 2002. DOI: 10.1103/PhysRevD.66.044019.

[36] G. Rousseaux, C. Mathis, P. Maïssa, T. G. Philbin, and U. Leonhardt, "Observation of negative-frequency waves in a water tank: A classical analogue to the Hawking effect?" *New Journal of Physics*, vol. 10, no. 5, p. 053 015, 2008, ISSN: 1367-2630. DOI: 10.1088/1367-2630/10/5/053015.

[37] T. G. Philbin, C. Kuklewicz, S. Robertson, S. Hill, F. Konig, *et al.*, "Fiber-Optical Analog of the Event Horizon," *Science*, vol. 319, no. 5868, pp. 1367–1370, 2008, ISSN: 1095-9203. DOI: 10.1126/science.1153625.

[38] O. Lahav *et al.*, "Realization of a Sonic Black Hole Analog in a Bose-Einstein Condensate," *Phys. Rev. Lett.*, vol. 105, no. 24, p. 240 401, 2010. DOI: 10.1103/PhysRevLett.105.240401.

[39] F. Belgiorno *et al.*, "Hawking Radiation from Ultrashort Laser Pulse Filaments," *Phys. Rev. Lett.*, vol. 105, no. 20, p. 203 901, 2010. DOI: 10.1103/PhysRevLett.105.203901.

[40] H. Nguyen, D. Gerace, I. Carusotto, D. Sanvitto, E. Galopin, *et al.*, "Acoustic Black Hole in a Stationary Hydrodynamic Flow of Microcavity Polaritons," *Physical Review Letters*, vol. 114, no. 3, 2015, ISSN: 1079-7114. DOI: 10.1103/physrevlett.114.036402.

[41] M. Člověčko, E. Gažo, M. Kupka, and P. Skyba, "Magnonic Analog of Black- and White-Hole Horizons in Superfluid He3-B," *Physical Review Letters*, vol. 123, no. 16, 2019, ISSN: 1079-7114. DOI: 10.1103/physrevlett.123.161302.

[42] S. Weinfurtner, E. W. Tedford, M. C. J. Penrice, W. G. Unruh, and G. A. Lawrence, "Measurement of stimulated Hawking emission in an analogue system," *Phys. Rev. Lett.*, vol. 106, p. 021 302, 2011. DOI: 10.1103/PhysRevLett.106.021302.

[43] J. Drori, Y. Rosenberg, D. Bermudez, Y. Silberberg, and U. Leonhardt, "Observation of Stimulated Hawking Radiation in an Optical Analogue," *Physical Review Letters*, vol. 122, no. 1, 2019, ISSN: 1079-7114. DOI: 10.1103/physrevlett.122.010404.

[44] L.-P. Euvé, F. Michel, R. Parentani, T. G. Philbin, and G. Rousseaux, "Observation of Noise Correlated by the Hawking Effect in a Water Tank," *Phys. Rev. Lett.*, vol. 117, no. 12, p. 121 301, 2016. DOI: 10.1103/PhysRevLett.117.121301.

[45] J. Steinhauer, "Observation of quantum Hawking radiation and its entanglement in an analogue black hole," *Nature Physics*, vol. 12, no. 10, pp. 959–965, 2016, ISSN: 1745-2481. DOI: 10.1038/nphys3863.

[46] J. R. Muñoz de Nova, K. Golubkov, V. I. Kolobov, and J. Steinhauer, "Observation of thermal Hawking radiation and its temperature in an analogue black hole," *Nature*, vol. 569, no. 7758, pp. 688–691, 2019, ISSN: 1476-4687. DOI: 10.1038/s41586-019-1241-0.

[47] W. G. Unruh, "Notes on black-hole evaporation," *Phys. Rev. D*, vol. 14, no. 4, pp. 870–892, 1976. DOI: 10.1103/PhysRevD.14.870.

[48] S. Biermann *et al.*, "Unruh and analogue Unruh temperatures for circular motion in $3+1$ and $2+1$ dimensions," *Phys. Rev. D*, vol. 102, no. 8, p. 085 006, 2020. DOI: 10.1103/PhysRevD.102.085006.

[49] C. Gooding *et al.*, "Interferometric Unruh Detectors for Bose-Einstein Condensates," *Phys. Rev. Lett.*, vol. 125, no. 21, p. 213 603, 2020. DOI: 10.1103/PhysRevLett.125.213603.

[50] Y. B. Zel'Dovich, "Generation of Waves by a Rotating Body," *Soviet Journal of Experimental and Theoretical Physics Letters*, vol. 14, p. 180, 1971, ISSN: 0021-3640.

[51] S. A. Teukolsky and W. H. Press, "Perturbations of a rotating black hole. III. Interaction of the hole with gravitational and electromagnetic radiation.," *The Astrophysical Journal*, vol. 193, pp. 443–461, 1974, ISSN: 0004-637X. DOI: 10.1086/153180.

[52] W. H. Press and S. A. Teukolsky, "Floating Orbits, Superradiant Scattering and the Black-hole Bomb," *Nature*, vol. 238, no. 5361, pp. 211–212, 1972, ISSN: 1476-4687. DOI: 10.1038/238211a0.

[53] A. A. Starobinsky, "Amplification of waves reflected from a rotating "black hole"." *Sov. Phys. JETP*, vol. 37, no. 1, pp. 28–32, 1973.

[54] A. A. Starobinskil and S. M. Churilov, "Amplification of electromagnetic and gravitational waves scattered by a rotating "black hole"," *Sov. Phys. JETP*, vol. 65, no. 1, pp. 1–5, 1974.

[55] R. Penrose and R. M. Floyd, "Extraction of Rotational Energy from a Black Hole," *Nature Physical Science*, vol. 229, no. 6, pp. 177–179, 1971, ISSN: 2058-1106. DOI: 10.1038/physci229177a0.

[56] T. Torres, S. Patrick, A. Coutant, M. Richartz, E. W. Tedford, *et al.*, "Rotational superradiant scattering in a vortex flow," *Nature Physics*, vol. 13, pp. 833–836, 2017. DOI: 10.1038/nphys4151.

[57] D. Faccio and E. M. Wright, "Superradiant Amplification of Acoustic Beams via Medium Rotation," *Phys. Rev. Lett.*, vol. 123, no. 4, p. 044 301, 2019. DOI: 10.1103/PhysRevLett.123.044301.

[58] M. Cromb, G. M. Gibson, E. Toninelli, M. J. Padgett, E. M. Wright, and D. Faccio, "Amplification of waves from a rotating body," *Nat. Phys.*, vol. 16, no. 10, pp. 1069–1073, 2020, ISSN: 1745-2481. DOI: 10.1038/s41567-020-0944-3.

[59] M. C. Braidotti, D. Faccio, and E. M. Wright, "Penrose Superradiance in Nonlinear Optics," *Phys. Rev. Lett.*, vol. 125, no. 19, p. 193 902, 2020. DOI: 10.1103/PhysRevLett.125.193902.

[60] M. C. Braidotti *et al.*, "Measurement of Penrose Superradiance in a Photon Superfluid," *Phys. Rev. Lett.*, vol. 128, no. 1, p. 013 901, 2022. DOI: 10.1103/PhysRevLett.128.013901.

[61] L. Giacomelli and I. Carusotto, "Ergoregion instabilities in rotating two-dimensional Bose-Einstein condensates: Perspectives on the stability of quantized vortices," *Phys. Rev. Research*, vol. 2, no. 3, p. 033 139, 2020. DOI: 10.1103/PhysRevResearch.2.033139.

[62] S. Patrick, A. Geelmuyden, S. Erne, C. F. Barenghi, and S. Weinfurtner, "Quantum vortex instability and black hole superradiance," *Phys. Rev. Research*, vol. 4, no. 3, p. 033 117, 2022. DOI: 10.1103/PhysRevResearch.4.033117.

[63] ——, *Origin and evolution of the multiply-quantised vortex instability*, 2021. DOI: 10.48550/arXiv.2111.02567. arXiv: 2111.02567 [cond-mat, physics:hep-ph, physics:hep-th, physics:physics].

[64] T. A. S. Cardoso and M. Richartz, *Dissipative Quantum Vortices and Superradiant Scattering*, 2022. arXiv: 2209.02613 [cond-mat, physics:gr-qc].

[65] T. Torres, M. Lloyd, S. R. Dolan, and S. Weinfurtner, *Wave focusing by submerged islands and gravitational analogues*, 2022. DOI: 10.48550/arXiv.2202.05926. arXiv: 2202.05926 [gr-qc, physics:hep-th, physics:physics].

[66] T. Torres, S. Patrick, M. Richartz, and S. Weinfurtner, "Quasinormal Mode Oscillations in an Analogue Black Hole Experiment," *Phys. Rev. Lett.*, vol. 125, no. 1, p. 011 301, 2020. DOI: 10.1103/PhysRevLett.125.011301.

[67] C. V. Vishveshwara, "Scattering of Gravitational Radiation by a Schwarzschild Black-hole," *Nature*, vol. 227, no. 5261, pp. 936–938, 1970, ISSN: 1476-4687. DOI: 10.1038/227936a0.

[68] LIGO Scientific and Virgo Collaborations *et al.*, "Tests of General Relativity with GW150914," *Phys. Rev. Lett.*, vol. 116, no. 22, p. 221 101, 2016. DOI: 10.1103/PhysRevLett.116.221101.

[69] M. Giesler, M. Isi, M. A. Scheel, and S. A. Teukolsky, "Black Hole Ringdown: The Importance of Overtones," *Phys. Rev. X*, vol. 9, no. 4, p. 041 060, 2019. DOI: 10.1103/PhysRevX.9.041060.

[70] C. M. Wilson, G. Johansson, A. Pourkabirian, M. Simoen, J. R. Johansson, *et al.*, "Observation of the dynamical Casimir effect in a superconducting circuit," *Nature*, vol. 479, no. 7373, pp. 376–379, 2011, ISSN: 1476-4687. DOI: 10.1038/nature10561.

[71] J.-C. Jaskula, G. B. Partridge, M. Bonneau, R. Lopes, J. Ruaudel, *et al.*, "Acoustic Analog to the Dynamical Casimir Effect in a Bose-Einstein Condensate," *Phys. Rev. Lett.*, vol. 109, no. 22, p. 220 401, 2012. DOI: 10.1103/PhysRevLett.109.220401.

[72] J. Braden, M. C. Johnson, H. V. Peiris, A. Pontzen, and S. Weinfurtner, "New Semiclassical Picture of Vacuum Decay," *Physical Review Letters*, vol. 123, no. 3, 2019, ISSN: 1079-7114. DOI: 10.1103/physrevlett.123.031601.

[73] D. Pîrvu, J. Braden, and M. C. Johnson, "Bubble clustering in cosmological first order phase transitions," *Phys. Rev. D*, vol. 105, no. 4, p. 043 510, 2022. DOI: 10.1103/PhysRevD.105.043510.

[74] J. Braden, M. C. Johnson, H. V. Peiris, A. Pontzen, and S. Weinfurtner, *Mass Renormalization in Lattice Simulations of False Vacuum Decay*, 2022. DOI: 10.48550/arXiv.2204.11867. arXiv: 2204.11867 [astro-ph, physics:gr-qc, physics:hep-ph, physics:hep-th].

[75] T. P. Billam, K. Brown, and I. G. Moss, "False-vacuum decay in an ultracold spin-1 Bose gas," *Phys. Rev. A*, vol. 105, no. 4, p. L041301, 2022. DOI: 10.1103/PhysRevA.105.L041301.

[76] A. Friedman, "Über die Krümmung des Raumes," *Z. Physik*, vol. 10, no. 1, pp. 377–386, 1922, ISSN: 0044-3328. DOI: 10.1007/BF01332580.

[77] A. Friedmann, "Über die Möglichkeit einer Welt mit konstanter negativer Krümmung des Raumes," *Z. Physik*, vol. 21, no. 1, pp. 326–332, 1924, ISSN: 0044-3328. DOI: 10.1007/BF01328280.

[78] E. Hubble, "A Relation between Distance and Radial Velocity among Extra-Galactic Nebulae," *Proceedings of the National Academy of Science*, vol. 15, pp. 168–173, 1929, ISSN: 0027-8424. DOI: 10.1073/pnas.15.3.168.

[79] A. A. Penzias and R. W. Wilson, "A Measurement of Excess Antenna Temperature at 4080 Mc/s.," *The Astrophysical Journal*, vol. 142, pp. 419–421, 1965, ISSN: 0004-637X. DOI: 10.1086/148307.

[80] R. H. Dicke, P. J. E. Peebles, P. G. Roll, and D. T. Wilkinson, "Cosmic Black-Body Radiation.," *The Astrophysical Journal*, vol. 142, pp. 414–419, 1965, ISSN: 0004-637X. DOI: 10.1086/148306.

[81] P. Collaboration *et al.*, "Planck 2015 results. XIII. Cosmological parameters," *Astronomy & Astrophysics, Volume 594, id.A13, 63 pp.*, vol. 594, p. 63, 2016, ISSN: 0004-6361. DOI: 10.1051/0004-6361/201525830.

[82] A. H. Guth, "Inflationary universe: A possible solution to the horizon and flatness problems," *Phys. Rev. D*, vol. 23, no. 2, pp. 347–356, 1981. DOI: 10.1103/PhysRevD.23.347.

[83] A. D. Linde, "A new inflationary universe scenario: A possible solution of the horizon, flatness, homogeneity, isotropy and primordial monopole problems," *Physics Letters B*, vol. 108, no. 6, pp. 389–393, 1982, ISSN: 0370-2693. DOI: 10.1016/0370-2693(82)91219-9.

[84] A. Albrecht and P. J. Steinhardt, "Cosmology for Grand Unified Theories with Radiatively Induced Symmetry Breaking," *Phys. Rev. Lett.*, vol. 48, no. 17, pp. 1220–1223, 1982. DOI: 10.1103/PhysRevLett.48.1220.

[85] A. A. Starobinsky, "A new type of isotropic cosmological models without singularity," *Physics Letters B*, vol. 91, no. 1, pp. 99–102, 1980, ISSN: 0370-2693. DOI: 10.1016/0370-2693(80)90670-X.

[86] L. F. Abbott, E. Farhi, and M. B. Wise, "Particle production in the new inflationary cosmology," *Physics Letters B*, vol. 117, no. 1, pp. 29–33, 1982, ISSN: 0370-2693. DOI: 10.1016/0370-2693(82)90867-X.

[87] J. H. Traschen and R. H. Brandenberger, "Particle production during out-of-equilibrium phase transitions," *Phys. Rev. D*, vol. 42, no. 8, pp. 2491–2504, 1990. DOI: 10.1103/PhysRevD.42.2491.

[88] L. Kofman, A. Linde, and A. A. Starobinsky, "Reheating after Inflation," *Phys. Rev. Lett.*, vol. 73, no. 24, pp. 3195–3198, 1994. DOI: 10.1103/PhysRevLett.73.3195.

[89] ——, "Towards the theory of reheating after inflation," *Physical Review D - Particles, Fields, Gravitation and Cosmology*, vol. 56, no. 6, pp. 3258–3295, 1997, ISSN: 15502368. DOI: 10.1103/PhysRevD.56.3258.

[90] S. Weinfurtner, "Analogue model for an expanding universe," *Gen Relativ Gravit*, vol. 37, no. 9, pp. 1549–1554, 2005, ISSN: 1572-9532. DOI: 10.1007/s10714-005-0135-7.

[91] S. Weinfurtner and M. Visser, "On the phenomenon of emergent spacetimes:An instruction guide for experimental cosmology," in *Proceedings of From Quantum to Emergent Gravity: Theory and Phenomenology — PoS(QG-Ph)*, vol. 43, SISSA Medialab, 2008, p. 044. DOI: 10.22323/1.043.0044.

[92] P. Jain, S. Weinfurtner, M. Visser, and C. W. Gardiner, "Analog model of a Friedmann-Robertson-Walker universe in Bose-Einstein condensates: Application of the classical field method," *Phys. Rev. A*, vol. 76, no. 3, p. 033 616, 2007. DOI: 10.1103/PhysRevA.76.033616.

[93] R. Schützhold, M. Uhlmann, L. Petersen, H. Schmitz, A. Friedenauer, and T. Schätz, "Analogue of Cosmological Particle Creation in an Ion Trap," *Phys. Rev. Lett.*, vol. 99, no. 20, p. 201 301, 2007. DOI: 10.1103/PhysRevLett.99.201301.

[94] X. Busch, R. Parentani, and S. Robertson, "Quantum entanglement due to a modulated dynamical Casimir effect," *Phys. Rev. A*, vol. 89, no. 6, p. 063 606, 2014. DOI: 10.1103/PhysRevA.89.063606.

[95] S. Eckel, A. Kumar, T. Jacobson, I. B. Spielman, and G. K. Campbell, "A Rapidly Expanding Bose-Einstein Condensate: An Expanding Universe in the Lab," *Phys. Rev. X*, vol. 8, no. 2, p. 021 021, 2018. DOI: 10.1103/PhysRevX.8.021021.

[96] M. Wittemer, F. Hakelberg, P. Kiefer, J.-P. Schröder, C. Fey, *et al.*, "Phonon Pair Creation by Inflating Quantum Fluctuations in an Ion Trap," *Phys. Rev. Lett.*, vol. 123, no. 18, p. 180 502, 2019. DOI: 10.1103/PhysRevLett.123.180502.

[97] A. Prain, S. Vezzoli, N. Westerberg, T. Roger, and D. Faccio, "Spontaneous Photon Production in Time-Dependent Epsilon-Near-Zero Materials," *Phys. Rev. Lett.*, vol. 118, no. 13, p. 133 904, 2017. DOI: 10.1103/PhysRevLett.118.133904.

[98] J. Steinhauer *et al.*, "Analogue cosmological particle creation in an ultracold quantum fluid of light," *Nat Commun*, vol. 13, no. 1, p. 2890, 2022, ISSN: 2041-1723. DOI: 10.1038/s41467-022-30603-1.

[99] T. V. Zache, V. Kasper, and J. Berges, "Inflationary preheating dynamics with two-species condensates," *Physical Review A*, vol. 95, no. 6, 2017. DOI: 10.1103/physreva.95.063629.

[100] J. Berges and J. Serreau, "Parametric Resonance in Quantum Field Theory," *Phys. Rev. Lett.*, vol. 91, no. 11, p. 111 601, 2003. DOI: 10.1103/PhysRevLett.91.111601.

[101] Z. Fifer, T. Torres, S. Erne, A. Avgoustidis, R. J. A. Hill, and S. Weinfurtner, "Analog cosmology with two-fluid systems in a strong gradient magnetic field," *Phys. Rev. E*, vol. 99, no. 3, p. 031 101, 2019. DOI: 10.1103/PhysRevE.99.031101.

[102] V. S. Barroso *et al.*, *Primary thermalisation mechanism of Early Universe observed from Faraday-wave scattering on liquid-liquid interfaces*, 2022. DOI: 10.48550/arXiv.2207.02199. arXiv: 2207.02199 [astro-ph, physics:gr-qc, physics:physics].

[103] T. V. Zache, T. Schweigler, S. Erne, J. Schmiedmayer, and J. Berges, "Extracting the Field Theory Description of a Quantum Many-Body System from Experimental Data," *Phys. Rev. X*, vol. 10, no. 1, p. 011 020, 2020. DOI: 10.1103/PhysRevX.10.011020.

[104] M. Prüfer *et al.*, "Experimental extraction of the quantum effective action for a non-equilibrium many-body system," *Nat. Phys.*, vol. 16, no. 10, pp. 1012–1016, 2020, ISSN: 1745-2481. DOI: 10.1038/s41567-020-0933-6.

[105] A. Geelmuyden, S. Erne, S. Patrick, C. F. Barenghi, and S. Weinfurtner, "Sound-ring radiation of expanding vortex clusters," *Phys. Rev. Research*, vol. 4, no. 2, p. 023 099, 2022. DOI: 10.1103/PhysRevResearch.4.023099.

[106] A. Geelmuyden, S. Weinfurtner, and V. S. Barroso, "Optical Path Length Characterisation," 2214343.2.

[107] Bose, "Plancks Gesetz und Lichtquantenhypothese," *Zeitschrift für Physik*, vol. 26, no. 1, pp. 178–181, 1924. DOI: 10.1007/bf01327326.

[108] A. Einstein, "Quantentheorie des einatomigen idealen Gases," in *Albert Einstein: Akademie-Vorträge*, John Wiley & Sons, Ltd, 2005, pp. 237–244, ISBN: 978-3-527-60895-9. DOI: 10.1002/3527608958.ch27.

[109] M. H. Anderson, J. R. Ensher, M. R. Matthews, C. E. Wieman, and E. A. Cornell, "Observation of Bose-Einstein Condensation in a Dilute Atomic Vapor," *Science*, vol. 269, no. 5221, pp. 198–201, 1995. DOI: 10.1126/science.269.5221.198.

[110] M. R. Andrews *et al.*, "Propagation of Sound in a Bose-Einstein Condensate," *Phys. Rev. Lett.*, vol. 79, no. 4, pp. 553–556, 1997. DOI: 10.1103/PhysRevLett.79.553.

[111] C. F. Barenghi and N. G. Parker, "A primer on quantum fluids," *arXiv:1605.09580 [cond-mat, physics:physics]*, 2016. DOI: 10.1007/978-3-319-42476-7. arXiv: 1605.09580 [cond-mat, physics:physics].

[112] Y. Shin *et al.*, "Dynamical Instability of a Doubly Quantized Vortex in a Bose-Einstein Condensate," *Phys. Rev. Lett.*, vol. 93, no. 16, p. 160 406, 2004. DOI: 10.1103/PhysRevLett.93.160406.

[113] T. Isoshima *et al.*, "Spontaneous Splitting of a Quadruply Charged Vortex," *Phys. Rev. Lett.*, vol. 99, no. 20, p. 200 403, 2007. DOI: 10.1103/PhysRevLett.99.200403.

[114] M. Okano, H. Yasuda, K. Kasa, M. Kumakura, and Y. Takahashi, "Splitting of a Quadruply Quantized Vortex in the Rb Bose-Einstein Condensate," *J Low Temp Phys*, vol. 148, no. 3, pp. 447–451, 2007, ISSN: 1573-7357. DOI: 10.1007/s10909-007-9405-y.

[115] H. Pu, C. K. Law, J. H. Eberly, and N. P. Bigelow, "Coherent disintegration and stability of vortices in trapped Bose condensates," *Phys. Rev. A*, vol. 59, no. 2, pp. 1533–1537, 1999. DOI: 10.1103/PhysRevA.59.1533.

[116] R. Brito, V. Cardoso, and P. Pani, *Superradiance – the 2020 Edition*. 2020, vol. 971. arXiv: 1501.06570.

[117] M. Visser, *The Kerr spacetime: A brief introduction*, 2008. DOI: 10.48550/arXiv.0706.0622. arXiv: 0706.0622 [astro-ph, physics:gr-qc, physics:hep-th].

[118] T. Torres, S. Patrick, M. Richartz, and S. Weinfurtner, "Analogue black hole spectroscopy; or, how to listen to dumb holes," *Class. Quantum Grav.*, vol. 36, no. 19, p. 194 002, 2019, ISSN: 0264-9381. DOI: 10.1088/1361-6382/ab3d48.

[119] C. Gooding, S. Weinfurtner, and W. G. Unruh, "Superradiant scattering of orbital angular momentum beams," *Phys. Rev. Research*, vol. 3, no. 2, p. 023 242, 2021. DOI: 10.1103/PhysRevResearch.3.023242.

[120] J. D. Bekenstein and M. Schiffer, "The many faces of superradiance," *Phys. Rev. D*, vol. 58, no. 6, p. 064 014, 1998. DOI: 10.1103/PhysRevD.58.064014.

[121] L. A. Oliveira, V. Cardoso, and L. C. B. Crispino, "Ergoregion instability: The hydrodynamic vortex," *Phys. Rev. D*, vol. 89, no. 12, p. 124 008, 2014. DOI: 10.1103/PhysRevD.89.124008.

[122] L. A. Oliveira, L. J. Garay, and L. C. B. Crispino, "Ergoregion instability of a rotating quantum system," *Phys. Rev. D*, vol. 97, no. 12, p. 124 063, 2018. DOI: 10.1103/PhysRevD.97.124063.

[123] J. L. Friedman and B. F. Schutz, "Gravitational radiation instability in rotating stars.," *The Astrophysical Journal*, vol. 199, pp. L157–L159, 1975, ISSN: 0004-637X. DOI: 10.1086/181872.

[124] S. R. Dolan, "Instability of the massive Klein-Gordon field on the Kerr spacetime," *Phys. Rev. D*, vol. 76, no. 8, p. 084 001, 2007. DOI: 10.1103/PhysRevD.76.084001.

[125] V. Cardoso, P. Pani, M. Cadoni, and M. Cavaglià, "Ergoregion instability of ultracompact astrophysical objects," *Phys. Rev. D*, vol. 77, no. 12, p. 124 044, 2008. DOI: 10.1103/PhysRevD.77.124044.

[126] A. Görlitz *et al.*, "Realization of Bose-Einstein Condensates in Lower Dimensions," *Phys. Rev. Lett.*, vol. 87, no. 13, p. 130 402, 2001. DOI: 10.1103/PhysRevLett.87.130402.

[127] N. Navon, R. P. Smith, and Z. Hadzibabic, "Quantum gases in optical boxes," *Nat. Phys.*, vol. 17, no. 12, pp. 1334–1341, 2021, ISSN: 1745-2481. DOI: 10.1038/s41567-021-01403-z.

[128] L. Salasnich, A. Parola, and L. Reatto, "Effective wave equations for the dynamics of cigar-shaped and disk-shaped Bose condensates," *Physical Review A*, vol. 65, no. 4, p. 043 614, 2002.

[129] C. J. Pethick and H. Smith, *Bose–Einstein Condensation in Dilute Gases*, Second. Cambridge: Cambridge University Press, 2008, ISBN: 978-0-521-84651-6. DOI: 10.1017/CBO9780511802850.

[130] E. P. Gross, "Structure of a quantized vortex in boson systems," *Nuovo Cim*, vol. 20, no. 3, pp. 454–477, 1961, ISSN: 1827-6121. DOI: 10.1007/BF02731494.

[131] L. P. Pitaevskii, "Vortex lines in an imperfect Bose gas," *Sov. Phys. JETP*, vol. 13, no. 2, pp. 451–454, 1961.

[132] E. Madelung, "Quantentheorie in hydrodynamischer Form," *Z. Physik*, vol. 40, no. 3, pp. 322–326, 1927, ISSN: 0044-3328. DOI: 10.1007/BF01400372.

[133] R. P. Feynman, "Chapter II Application of Quantum Mechanics to Liquid Helium," in *Progress in Low Temperature Physics*, C. J. Gorter, Ed., vol. 1, Elsevier, 1955, pp. 17–53. DOI: 10.1016/S0079-6417(08)60077-3.

[134] L. Onsager, "Statistical hydrodynamics," *Nuovo Cim*, vol. 6, no. 2, pp. 279–287, 1949, ISSN: 1827-6121. DOI: 10.1007/BF02780991.

[135] C. D. Andereck, J. Chalups, and W. I. Glaberson, "Tkachenko Waves in Rotating Superfluid Helium," *Phys. Rev. Lett.*, vol. 44, no. 1, pp. 33–36, 1980. DOI: 10.1103/PhysRevLett.44.33.

[136] I. Bloch, J. Dalibard, and W. Zwerger, "Many-body physics with ultracold gases," *Rev. Mod. Phys.*, vol. 80, no. 3, pp. 885–964, 2008, ISSN: 0034-6861, 1539-0756. DOI: 10.1103/RevModPhys.80.885.

[137] C. F. Barenghi, L. Skrbek, and K. R. Sreenivasan, "Introduction to quantum turbulence," *Proceedings of the National Academy of Sciences*, vol. 111, no. supplement_1, pp. 4647–4652, 2014. DOI: 10.1073/pnas.1400033111.

[138] N. Bogolubov, "On the theory of superfluidity," *J. Phys. (USSR)*, vol. 11, pp. 23–32, 1947.

[139] C. Barcelo, S. Liberati, and M. Visser, "Analogue Gravity," Tech. Rep., 2011. DOI: 10.12942/lrr-2005-12. arXiv: gr-qc/0505065.

[140] H. Takeuchi, M. Kobayashi, and K. Kasamatsu, "Is a Doubly Quantized Vortex Dynamically Unstable in Uniform Superfluids?" *J. Phys. Soc. Jpn.*, vol. 87, no. 2, p. 023 601, 2018, ISSN: 0031-9015. DOI: 10.7566/JPSJ.87.023601.

[141] C. Nore, M. Abid, and M. E. Brachet, "Decaying Kolmogorov turbulence in a model of superflow," *Physics of Fluids*, vol. 9, no. 9, pp. 2644–2669, 1997, ISSN: 1070-6631. DOI: 10.1063/1.869473.

[142] ——, "Kolmogorov Turbulence in Low-Temperature Superflows," *Phys. Rev. Lett.*, vol. 78, no. 20, pp. 3896–3899, 1997. DOI: 10.1103/PhysRevLett.78.3896.

[143] S. P. Cockburn and N. P. Proukakis, "The stochastic Gross-Pitaevskii equation and some applications," *Laser Phys.*, vol. 19, no. 4, pp. 558–570, 2009, ISSN: 1555-6611. DOI: 10.1134/S1054660X09040057.

[144] N. P. Proukakis and B. Jackson, "Finite-temperature models of Bose–Einstein condensation," *Journal of Physics B: Atomic, Molecular and Optical Physics*, vol. 41, no. 20, p. 203 002, 2008, ISSN: 1361-6455. DOI: 10.1088/0953-4075/41/20/203002.

[145] O. R. Stockdale *et al.*, "Universal dynamics in the expansion of vortex clusters in a dissipative two-dimensional superfluid," *Phys. Rev. Research*, vol. 2, no. 3, p. 033 138, 2020. DOI: 10.1103/PhysRevResearch.2.033138.

[146] P. K. Newton, *The N-Vortex Problem*, J. E. Marsden and L. Sirovich, Eds., ser. Applied Mathematical Sciences. New York, NY: Springer, 2001, vol. 145, ISBN: 978-1-4419-2916-7 978-1-4684-9290-3. DOI: 10.1007/978-1-4684-9290-3.

[147] N. Parker, "Numerical studies of vortices and dark solitons in atomic Bose-Einstein condensates," Doctoral, Durham University, 2004.

[148] V. Cardoso, A. S. Miranda, E. Berti, H. Witek, and V. T. Zanchin, "Geodesic stability, Lyapunov exponents, and quasinormal modes," *Phys. Rev. D*, vol. 79, no. 6, p. 064 016, 2009. DOI: 10.1103/PhysRevD.79.064016.

[149] LIGO Scientific Collaboration and Virgo Collaboration *et al.*, "Observation of Gravitational Waves from a Binary Black Hole Merger," *Phys. Rev. Lett.*, vol. 116, no. 6, p. 061 102, 2016. DOI: 10.1103/PhysRevLett.116.061102.

[150] LIGO Scientific Collaboration and Virgo Collaboration *et al.*, "GW170817: Observation of Gravitational Waves from a Binary Neutron Star Inspiral," *Phys. Rev. Lett.*, vol. 119, no. 16, p. 161 101, 2017. DOI: 10.1103/PhysRevLett.119.161101.

[151] G. Khanna and R. H. Price, "Black hole ringing, quasinormal modes, and light rings," *Phys. Rev. D*, vol. 95, no. 8, p. 081 501, 2017. DOI: 10.1103/PhysRevD.95.081501.

[152] E. Berti, V. Cardoso, and A. O. Starinets, "Quasinormal modes of black holes and black branes," *Class. Quantum Grav.*, vol. 26, no. 16, p. 163 001, 2009, ISSN: 0264-9381, 1361-6382. DOI: 10.1088/0264-9381/26/16/163001. arXiv: 0905.2975.

[153] M. Modugno, L. Pricoupenko, and Y. Castin, "Bose-Einstein condensates with a bent vortex in rotating traps," *Eur. Phys. J. D*, vol. 22, no. 2, pp. 235–257, 2003, ISSN: 1434-6079. DOI: 10.1140/epjd/e2003-00015-y.

[154] G. Baym, "Tkachenko Modes of Vortex Lattices in Rapidly Rotating Bose-Einstein Condensates," *Phys. Rev. Lett.*, vol. 91, no. 11, p. 110 402, 2003. DOI: 10.1103/PhysRevLett.91.110402.

[155] M. T. Reeves *et al.*, "Turbulent Relaxation to Equilibrium in a Two-Dimensional Quantum Vortex Gas," *Phys. Rev. X*, vol. 12, no. 1, p. 011 031, 2022. DOI: 10.1103/PhysRevX.12.011031.

[156] G. Gauthier *et al.*, "Giant Vortex Clusters in a Two-Dimensional Quantum Fluid," *Science*, vol. 364, no. 6447, pp. 1264–1267, 2019, ISSN: 0036-8075, 1095-9203. DOI: 10.1126/science.aat5718. arXiv: 1801.06951.

[157] B. Jackson, N. P. Proukakis, C. F. Barenghi, and E. Zaremba, "Finite-temperature vortex dynamics in Bose-Einstein condensates," *Phys. Rev. A*, vol. 79, no. 5, p. 053 615, 2009. DOI: 10.1103/PhysRevA.79.053615.

[158] C. W. Gardiner, *Handbook of Stochastic Methods: For Physics, Chemistry and the Natural Sciences*, 3rd ed. edition. Berlin ; New York: Springer, 2004, ISBN: 978-3-540-20882-2.

[159] M. T. Reeves *et al.*, "Turbulent relaxation to equilibrium in a two-dimensional quantum vortex gas," *arXiv:2010.10049 [cond-mat, physics:physics, physics:quant-ph]*, 2022. arXiv: 2010.10049 [cond-mat, physics:physics, physics:quant-ph].

[160] B. Lautrup, *Physics of Continuous Matter: Exotic and Everyday Phenomena in the Macroscopic World*, Second. Boca Raton: CRC Press, 2011, ISBN: 978-0-429-10950-8. DOI: 10.1201/9781439894200.

[161] R. P. Feynman, "Superfluidity and superconductivity," *Reviews of Modern Physics*, vol. 29, no. 2, p. 205, 1957.

[162] G. Krstulovic, M. Brachet, and E. Tirapegui, "Radiation and vortex dynamics in the nonlinear Schrödinger equation," *Physical Review E*, vol. 78, no. 2, p. 026 601, 2008.

[163] E. R. Tracy, A. J. Brizard, A. S. Richardson, and A. N. Kaufman, *Ray Tracing and Beyond: Phase Space Methods in Plasma Wave Theory*. Cambridge: Cambridge University Press, 2014, ISBN: 978-0-521-76806-1. DOI: 10.1017/CBO9780511667565.

[164] S. R. Dolan and A. C. Ottewill, "Wave propagation and quasinormal mode excitation on Schwarzschild spacetime," *Phys. Rev. D*, vol. 84, no. 10, p. 104 002, 2011. DOI: 10.1103/PhysRevD.84.104002.

[165] T. Torres, A. Coutant, S. Dolan, and S. Weinfurtner, "Waves on a vortex: Rays, rings and resonances," *J. Fluid Mech.*, vol. 857, pp. 291–311, 2018. DOI: 10.1017/jfm.2018.752.

[166] S. P. Johnstone, A. J. Groszek, P. T. Starkey, C. J. Billington, T. P. Simula, and K. Helmerson, "Evolution of large-scale flow from turbulence in a two-dimensional superfluid," *Science*, vol. 364, no. 6447, pp. 1267–1271, 2019, ISSN: 0036-8075. DOI: 10.1126/science.aat5793.

[167] Z. Fifer, "Analog cosmology with two-fluid systems," Thesis, University of Nottingham, 2022.

[168] M. Faraday, "XVII. On a peculiar class of acoustical figures; and on certain forms assumed by groups of particles upon vibrating elastic surfaces," *Philosophical Transactions of the Royal Society of London*, vol. 121, pp. 299–340, 1831. DOI: 10.1098/rstl.1831.0018.

[169] ——, *Experimental Researches in Chemistry and Physics*. London: Taylor & Francis, ISBN: 978-0-429-21788-3.

[170] "Ship Hydrostatics and Stability," in *Ship Hydrostatics and Stability (Second Edition)*, A. Biran and R. López-Pulido, Eds., Oxford: Butterworth-Heinemann, 2014, p. i, ISBN: 978-0-08-098287-8. DOI: 10.1016/B978-0-08-098287-8.00014-1.

[171] F. Gazzola, "Brief History of Suspension Bridges," in *Mathematical Models for Suspension Bridges: Nonlinear Structural Instability*, ser. MS&A, F. Gazzola, Ed., Cham: Springer International Publishing, 2015, pp. 1–41, ISBN: 978-3-319-15434-3. DOI: 10.1007/978-3-319-15434-3_1.

[172] J. W. Miles, "Nonlinear surface waves in closed basins," *Journal of Fluid Mechanics*, vol. 75, no. 3, pp. 419–448, 1976, ISSN: 1469-7645, 0022-1120. DOI: 10.1017/S002211207600030X.

[173] ——, "Nonlinear Faraday resonance," *Journal of Fluid Mechanics*, vol. 146, pp. 285–302, 1984, ISSN: 1469-7645, 0022-1120. DOI: 10.1017/S0022112084001865.

[174] P. K. Kundu and I. M. Cohen, *Fluid Mechanics*, 4th ed. Amsterdam ; Boston: Academic Press, 2008, ISBN: 978-0-12-373735-9.

[175] J. W. M. Bush, *Interfacial Phenomena*, 2013.

[176] J. W. Miles, "CORRIGENDA," *Journal of Fluid Mechanics*, vol. 154, pp. 535–535, 1985, ISSN: 1469-7645, 0022-1120. DOI: 10.1017/S0022112085001677.

[177] S. Douady, "Experimental study of the Faraday instability," *Journal of Fluid Mechanics*, vol. 221, pp. 383–409, 1990. DOI: 10.1017/s0022112090003603.

[178] A. Wernet, C. Wagner, D. Papathanassiou, H. W. Müller, and K. Knorr, "Amplitude measurements of Faraday waves," *Phys. Rev. E*, vol. 63, no. 3, p. 036 305, 2001. DOI: 10.1103/PhysRevE.63.036305.

[179] C. H. Ziener, F. T. Kurz, L. R. Buschle, and T. Kampf, "Orthogonality, Lommel integrals and cross product zeros of linear combinations of Bessel functions," *SpringerPlus*, vol. 4, no. 1, p. 390, 2015, ISSN: 2193-1801. DOI: 10.1186/s40064-015-1142-0.

[180] J. McMahon, "On the Roots of the Bessel and Certain Related Functions," *Annals of Mathematics*, vol. 9, no. 1/6, pp. 23–30, 1894, ISSN: 0003-486X. DOI: 10.2307/1967501.

[181] M. Abramowitz, *Handbook of Mathematical Functions, With Formulas, Graphs, and Mathematical Tables*, USA: Dover Publications, Inc., 1974, ISBN: 978-0-486-61272-0.

[182] P. Christodoulides and F. Dias, "Resonant capillary–gravity interfacial waves," *Journal of Fluid Mechanics*, vol. 265, pp. 303–343, 1994, ISSN: 1469-7645, 0022-1120. DOI: 10.1017/S0022112094000856.

[183] I. Kovacic, R. Rand, and S. M. Sah, "Mathieu's equation and its generalizations: Overview of stability charts and their features," *Applied Mechanics Reviews*, vol. 70, no. 2, 2018, ISSN: 00036900. DOI: 10.1115/1.4039144.

[184] R. H. Rand, "Lecture Notes on Nonlinear Vibrations," in 2012.

[185] K. Kumar and L. S. Tuckerman, "Parametric Instability of the Interface Between two Fluids," *Journal of Fluid Mechanics*, vol. 279, pp. 49–68, 1994, ISSN: 14697645. DOI: 10.1017/s0022112094003812.

[186] M. Takeda and K. Mutoh, "Fourier transform profilometry for the automatic measurement of 3-D object shapes," *Appl. Opt., AO*, vol. 22, no. 24, pp. 3977–3982, 1983, ISSN: 2155-3165. DOI: 10.1364/AO.22.003977.

[187] S. Wildeman, "Real-time quantitative Schlieren imaging by fast Fourier demodulation of a checkered backdrop," *Experiments in Fluids*, vol. 59, no. 6, p. 97, 2018, ISSN: 1432-1114. DOI: 10.1007/s00348-018-2553-9.

[188] F. Moisy, M. Rabaud, and K. Salsac, "A synthetic Schlieren method for the measurement of the topography of a liquid interface," *Experiments in Fluids*, vol. 46, pp. 1021–1036, 2009. DOI: 10.1007/s00348-008-0608-z.

[189] J. Marcinkiewicz and A. Zygmund, "On the summability of double Fourier series," *Fundamenta Mathematicae*, vol. 32, no. 1, pp. 122–132, 1939, ISSN: 0016-2736. DOI: 10.4064/fm-32-1-122-132.

[190] M. E. Peskin and D. V. Schroeder, *An Introduction to Quantum Field Theory*. 1995.

[191] M. Gałka *et al.*, *Emergence of isotropy and dynamic scaling in 2D wave turbulence*, 2022. DOI: 10.48550/arXiv.2203.09514. arXiv: 2203.09514 [cond-mat, physics:physics].

[192] M. A. Sutton, J. J. Orteu, and H. Schreier, *Image Correlation for Shape, Motion and Deformation Measurements: Basic Concepts, Theory and Applications*, 2009th edition. New York, N.Y: Springer, 2009, ISBN: 978-0-387-78746-6.

[193] X. Su and W. Chen, "Fourier transform profilometry:: A review," *Optics and Lasers in Engineering*, vol. 35, no. 5, pp. 263–284, 2001, ISSN: 0143-8166. DOI: 10.1016/S0143-8166(01)00023-9.

[194] P. J. Cobelli, A. Maurel, V. Pagneux, and P. Petitjeans, "Global measurement of water waves by Fourier transform profilometry," *Exp Fluids*, vol. 46, no. 6, p. 1037, 2009, ISSN: 1432-1114. DOI: 10.1007/s00348-009-0611-z.

[195] M. K. Kim, "Principles and techniques of digital holographic microscopy," *SR*, vol. 1, no. 1, p. 018 005, 2010, ISSN: 1946-3251. DOI: 10.1117/6.0000006.

[196] G. Di Caprio *et al.*, *Holographic imaging of unlabelled sperm cells for semen analysis: A review*, 2014. DOI: 10.48550/arXiv.1411.7374. arXiv: 1411.7374 [physics].

[197] T. Kreis, "Application of Digital Holography for Nondestructive Testing and Metrology: A Review," *IEEE Transactions on Industrial Informatics*, vol. 12, no. 1, pp. 240–247, 2016, ISSN: 1941-0050. DOI: 10.1109/TII.2015.2482900.

[198] T. Tahara, X. Quan, R. Otani, Y. Takaki, and O. Matoba, "Digital holography and its multidimensional imaging applications: A review," *Microscopy*, vol. 67, no. 2, pp. 55–67, 2018, ISSN: 2050-5698. DOI: 10.1093/jmicro/dfy007.

[199] M. Paturzo *et al.*, "Digital Holography, a metrological tool for quantitative analysis: Trends and future applications," *Optics and Lasers in Engineering*, Optical Tools for Metrology, Imaging and Diagnostics, vol. 104, pp. 32–47, 2018, ISSN: 0143-8166. DOI: 10.1016/j.optlaseng.2017.11.013.

[200] G. Nehmetallah, L. Williams, and T. Nguyen, *Latest Advances in Single and Multiwavelength Digital Holography and Holographic Microscopy*. IntechOpen, 2020, ISBN: 978-1-83969-705-0. DOI: 10.5772/intechopen.94382.

[201] J. Zhang, S. Dai, C. Ma, T. Xi, D. Jianglei, and Z. Jianlin, "A review of common-path off-axis digital holography: Towards high stable optical instrument manufacturing," *Light: Advanced Manufacturing*, 2021. DOI: 10.37188/lam.2021.023.

[202] T. Zeng, T. Zeng, Y. Zhu, Y. Zhu, and E. Y. Lam, "Deep learning for digital holography: A review," *Opt. Express, OE*, vol. 29, no. 24, pp. 40 572–40 593, 2021, ISSN: 1094-4087. DOI: 10.1364/OE.443367.

[203] D. Gabor, "A New Microscopic Principle," *Nature*, vol. 161, no. 4098, pp. 777–778, 1948, ISSN: 1476-4687. DOI: 10.1038/161777a0.

[204] D. Gabor and W. L. Bragg, "Microscopy by reconstructed wave-fronts," *Proceedings of the Royal Society of London. Series A. Mathematical and Physical Sciences*, vol. 197, no. 1051, pp. 454–487, 1949. DOI: 10.1098/rspa.1949.0075.

[205] D. Gabor, "Microscopy by Reconstructed Wave Fronts: II," *Proc. Phys. Soc. B*, vol. 64, no. 6, pp. 449–469, 1951, ISSN: 0370-1301. DOI: 10.1088/0370-1301/64/6/301.

[206] J. W. Goodman and R. W. Lawrence, "Digital image formation from electronically detected holograms," *Appl. Phys. Lett.*, vol. 11, no. 3, pp. 77–79, 1967, ISSN: 0003-6951. DOI: 10.1063/1.1755043.

[207] U. Schnars and W. Jüptner, "Direct recording of holograms by a CCD target and numerical reconstruction," *Appl. Opt., AO*, vol. 33, no. 2, pp. 179–181, 1994, ISSN: 2155-3165. DOI: 10.1364/AO.33.000179.

[208] E. N. Leith and J. Upatnieks, "Reconstructed Wavefronts and Communication Theory*," *J. Opt. Soc. Am., JOSA*, vol. 52, no. 10, pp. 1123–1130, 1962. DOI: 10.1364/JOSA.52.001123.

[209] E. Cuche, F. Bevilacqua, and C. Depeursinge, "Digital holography for quantitative phase-contrast imaging," *Opt. Lett., OL*, vol. 24, no. 5, pp. 291–293, 1999, ISSN: 1539-4794. DOI: 10.1364/OL.24.000291.

[210] C. Yuan, G. Situ, G. Pedrini, J. Ma, and W. Osten, "Resolution improvement in digital holography by angular and polarization multiplexing," *Appl. Opt., AO*, vol. 50, no. 7, B6–B11, 2011, ISSN: 2155-3165. DOI: 10.1364/AO.50.0000B6.

[211] B. Sha, X. Liu, X.-L. Ge, and C.-S. Guo, "Fast reconstruction of off-axis digital holograms based on digital spatial multiplexing," *Opt. Express, OE*, vol. 22, no. 19, pp. 23 066–23 072, 2014, ISSN: 1094-4087. DOI: 10.1364/OE.22.023066.

[212] V. Mico, C. Ferreira, Z. Zalevsky, and J. García, "Spatially-multiplexed interferometric microscopy (SMIM): Converting a standard microscope into a holographic one," *Opt Express*, vol. 22, no. 12, pp. 14 929–14 943, 2014, ISSN: 1094-4087. DOI: 10.1364/OE.22.014929.

[213] M. Rubin, G. Dardikman, S. K. Mirsky, N. A. Turko, and N. T. Shaked, "Six-pack off-axis holography," *Opt. Lett.*, vol. 42, no. 22, p. 4611, 2017, ISSN: 0146-9592, 1539-4794. DOI: 10.1364/OL.42.004611. arXiv: 1904.01446 [physics].

[214] G. Dardikman and N. T. Shaked, "Is multiplexed off-axis holography for quantitative phase imaging more spatial bandwidth-efficient than on-axis holography?" *J. Opt. Soc. Am. A*, vol. 36, no. 2, A1, 2019, ISSN: 1084-7529, 1520-8532. DOI: 10.1364/JOSAA.36.0000A1. arXiv: 1903.12209 [physics].

[215] T. Colomb *et al.*, "Digital holographic reflectometry," *Opt. Express, OE*, vol. 18, no. 4, pp. 3719–3731, 2010, ISSN: 1094-4087. DOI: 10.1364/OE.18.003719.

[216] T. Colomb and Y. Emery, "Digital holographic reflectometry for semi-transparent multilayers topography measurement," in *2012 International Symposium on Optomechatronic Technologies (ISOT 2012)*, 2012, pp. 1–2. DOI: 10.1109/ISOT.2012.6403297.

[217] D. J. Griffiths, *Introduction to Electrodynamics*, 4th edition. Cambridge, United Kingdom ; New York, NY: Cambridge University Press, 2017, ISBN: 978-1-108-42041-9.

[218] M. A. Herráez, D. R. Burton, M. J. Lalor, and M. A. Gdeisat, "Fast two-dimensional phase-unwrapping algorithm based on sorting by reliability following a noncontinuous path," *Appl. Opt., AO*, vol. 41, no. 35, pp. 7437–7444, 2002, ISSN: 2155-3165. DOI: 10.1364/AO.41.007437.

[219] I. T. Jolliffe, *Principal Component Analysis*. 1986.

[220] I. T. Jolliffe, "Principal component analysis: A beginner's guide — II. Pitfalls, myths and extensions," *Weather*, vol. 48, no. 8, pp. 246–253, 1993, ISSN: 1477-8696. DOI: 10.1002/j.1477-8696.1993.tb05899.x.

[221] S. Patrick and S. Weinfurtner, "Superradiance in dispersive black hole analogues," *Phys. Rev. D*, vol. 102, no. 8, p. 084 041, 2020. DOI: 10.1103/PhysRevD.102.084041.

[222] S. Patrick, "Rotational superradiance with Bogoliubov dispersion," *Class. Quantum Grav.*, vol. 38, no. 9, p. 095 010, 2021, ISSN: 0264-9381. DOI: 10.1088/1361-6382/abf1fc.

[223] V. A. Trofimov and N. Peskov, "Comparison of finite-difference schemes for the Gross-Pitaevskii equation," *Mathematical Modelling and Analysis*, vol. 14, no. 1, pp. 109–126, 2009. DOI: 10.3846/1392-6292.2009.14.109-126.

[224] J. Geiser and A. Nasari, "Comparison of splitting methods for deterministic/stochastic Gross–Pitaevskii equation," *Mathematical and Computational Applications*, vol. 24, no. 3, p. 76, 2019. DOI: 10.3390/mca24030076.

[225] T. Kimura, "Explicit description of the Zassenhaus formula," *Progress of Theoretical and Experimental Physics*, vol. 2017, no. 4, 041A03, 2017, ISSN: 2050-3911. DOI: 10.1093/ptep/ptx044.

[226] J. Javanainen and J. Ruostekoski, "Symbolic calculation in development of algorithms: Split-step methods for the Gross–Pitaevskii equation," *Journal of Physics A: Mathematical and General*, vol. 39, no. 12, p. L179, 2006.

Index